NYU WIRELESS TR 2018-001

Technical Report

Channel Modeling and Multi-Cell Hybrid Beamforming for Fifth-Generation Millimeter-Wave Wireless Communications

Shu Sun, Theodore S. Rappaport

ss7152@nyu.edu, tsr@nyu.edu

NYU WIRELESS
NYU Tandon School of Engineering
2 MetroTech Center
Brooklyn, NY 11201

May 6th, 2018

ABSTRACT

Channel Modeling and Multi-Cell Hybrid Beamforming for Fifth-Generation Millimeter-Wave Wireless Communications

The rapid growth of mobile communications and the soaring popularity of smart phones, tablets, and other mobile devices are creating unprecedented challenges for wireless service providers to surmount a global bandwidth crunch. This has also motivated the evolution of wireless communications from the fourth-generation to the fifth-generation (5G). To overcome the bandwidth shortage and to meet the ever increasing data rate demands expected for 5G systems, the millimeter-wave (mmWave) frequency band (usually considered as 30 GHz to 300 GHz) is being explored for cellular communications, where a tremendous amount of raw bandwidth exists. Nevertheless, while the knowledge on mmWave propagation channels in various outdoor environments is being gained via numerous measurement campaigns carried out by both the academia and industry around the world over the past few years, channel modeling for 5G including mmWave systems is still ongoing, and the system performance, especially combined with the multiple-input multiple-output (MIMO) technology, is yet to be fully evaluated.

This thesis investigates some fundamental aspects of 5G channel modeling and the evaluation of mmWave MIMO system performance, with the use of multi-cell multi-user analog-digital hybrid beamforming (HBF) approaches. A practical omnidirectional path loss synthesizing method and systematic study of various

omnidirectional path loss models considered by the standards bodies are first demonstrated, followed by the introduction of a 5G channel simulator, NYUSIM. The thesis then systematically compares the modeling methodology and system performance prediction of two popular channel models developed for 5G systems: the 3rd Generation Partnership Project (3GPP) TR 38.901 Release 14 channel model, and the NYUSIM channel model. Next, focuses on shifted to mmWave MIMO systems, where a novel channel estimation codebook construction strategy is proposed, and multi-cell multi-user system spectral efficiency is examined using the above two channel models and several HBF approaches, leveraging the coordinated multi-point (CoMP) concept. Specifically, eigenvalue densities for mmWave channels coupled with radio-frequency (RF) precoding are derived, which has never been done in the vast literature. Moreover, a general methodology is provided to analytically compute the average (expected) per-cell sum spectral efficiency of a mmWave multi-cell single-stream system using phase-shifter-based analog beamforming and regularized zero-forcing digital beamforming, and the results are validated through numerical simulations.

The investigations in this thesis concludes that *it is vital to develop an accurate channel model applicable for all the potential 5G spectrum, as the channel model has a profound impact on deployment decisions and on various metrics, such as spectrum efficiency, coverage and performance, cell radius, and hardware/signal processing requirements. For instance, compared to NYUSIM, the larger cluster number (i.e., more rich multipath) in the 3GPP model results in more eigen channels and more similar powers among those eigen channels*, thus is advantageous for spatial multiplexing. On the other hand, the real-world measurement-based NYUSIM channel exhibits sparsity and has fewer but stronger dominant eigenmodes, hence

generating higher spectral efficiency when combined with appropriate HBF procedures. Numerical results show that *CoMP based on the signal-to-leakage-plus-noise ratio (SLNR) method provides highest spectral efficiency in most cases (e.g., up to 67% higher spectral efficiency for the weakest 5% of users as compared to the non-CoMP case), thus is worth using in mmWave multi-cell networks.* Furthermore, the benefits of multi-cell base station coordination (as opposed to the no-coordination case) are ultimately governed by the underlying propagation model, as well as the aggregate interference levels proportional to the cell radius and the number of users per cell. Specifically, a *relatively small cell radius (e.g., 50 m) and a small number of users (e.g., three) per cell usually give rise to high per-user spectral efficiency given a constant transmit power for each user.*

Contents

List of Figures

List of Tables

Chapter 1

Introduction

The rapidly increasing demands from consumers for high data rates, ubiquitous connectivity, high-quality video streaming, and low-latency control or communication are driving the development of fifth-generation (5G) wireless communications [1, 2]. Compared to 4G/International Mobile Telecommunications-Advanced (IMT-Advanced) standards, 5G is envisioned to support a higher density of mobile broadband users, better implementation of Internet of Things (IoT), virtual reality, augmented reality, and many other use cases. There is currently no standard for 5G deployments, but the millimeter-wave (mmWave) spectrum (from around 30 gigahertz (GHz) to 300 GHz) is expected to be a key ingredient due to its massive amount of raw available bandwidths [2]. In July 2016, the Federal Communications Commission (FCC) in the United States approved nearly 11 GHz of spectrum above 24 GHz for 5G, including the 28 GHz, 37 GHz, 39 GHz, and 64 - 71 GHz bands [3], which was more than four times larger than the total amount of licensed spectrum currently available for mobile services.

1.1 Technologies Required to Realize 5G

The demand for cellular data traffic continues to outstrip forecasts and is currently growing at a rate of 40-70% per annum [4, 5]. This growth rate implies that relative to current levels, a 1000 times capacity increase within the next decade may be required to be met by the new radio capabilities of the fifth-generation (5G) wireless communications [1, 2, 6, 7, 8, 9, 10, 11, 12]. The capacity gains required by 5G are expected to be provided by:

- Massive multiple-input multiple-output (MIMO) antenna arrays at base stations (BSs) and smaller arrays at the mobile user equipment (UE) [13, 14, 15, 16, 17, 18, 19]
- Increased spectrum bandwidth and use of wideband ($>$ 100 MHz) channels [20, 21]
- Multi-user and three-dimensional (3D) MIMO [22, 23, 24, 25, 26]
- Network densification using smaller cell coverage zones [27, 28, 29, 30]
- New modulation waveforms [31, 32, 33, 34, 35]

A discussion of the above is given in [6] and references therein, but it is clear that new waveforms will offer the smallest capacity increase, while increased spectrum bandwidth and channel bandwidth will provide the largest capacity increases.

1.2 Spectrum Bands Suitable for 5G

Increased spectrum bandwidth cannot come from existing microwave bands which are already congested and allocated for other purposes, thus new millimeter-wave

(mmWave) spectrum bands of 30-300 GHz are being considered for 5G and beyond, since they have ample unused spectrum relative to the microwave bands [4] and are potential candidates for allocation to mobile services. The World Radio Conference in 2015 (WRC-15) approved a number of candidate bands for 5G, which are: 24.25-27.5 GHz, 31.8-43.5 GHz, 45.5-50.2 GHz, 50.4-52.6 GHz, 66-76 GHz, and 81-86 GHz (see Table 1.1). A final list of the bands will be approved by WRC-19. In addition to these bands, spectrum in the unlicensed bands (60 GHz) may also be used [36]. A judicious contribution of spectrum use across all bands is necessary to keep up with capacity demands, and this is likely to include lower ultra-high frequency (UHF)/microwave frequencies for wider area coverage, and high rate mmWave links for both licensed and unlicensed use.

Table 1.1: Candidate spectrum bands for 5G

Group 30	Group 40/50	Group 70/80
24.25-27.5 GHz	37-40.5 GHz	66-76 GHz
	40.5-42.5 GHz	81-86 GHz
31.8-33.4 GHz	42.5-43.5 GHz	
	45.5-47 GHz	
	47-747.2 GHz	
	47.2-50.2 GHz	
	50.4-52.6 GHz	

The WRC-15 candidate bands are carefully chosen in terms of low-loss atmospheric attenuation versus (vs.) frequency as shown in Fig. 1.1. In particular, they avoid the oxygen absorption peaks in Fig. 1.1 that represent molecular oxygen and water vapor loss [38]. The very small wavelengths of mmWave signals combined with advances in CMOS technology enable the fabrication of large numbers of antenna elements to be placed in extremely small dimensions [39, 40, 41, 42, 43, 44], for example, 128 cross-polarized antennas (equal to 256 elements) can be placed

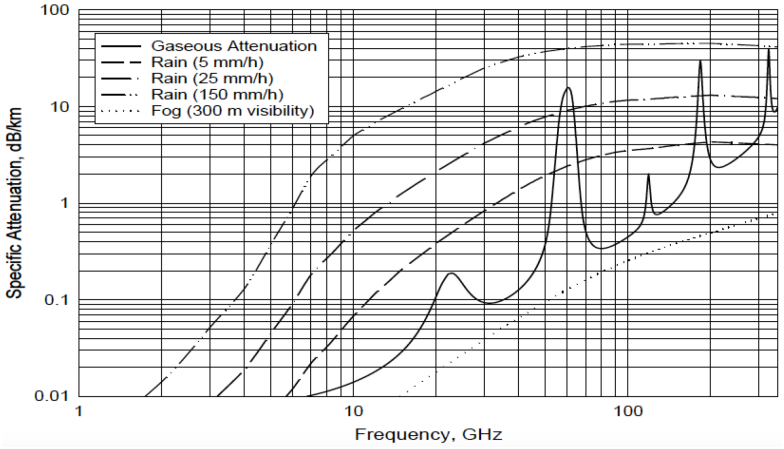

Figure 1.1: Atmospheric attenuation vs. frequency (from [37]).

in a small area of 8 cm x 16 cm. Also, the large relatively unused bandwidths in these bands will enable the allocation of very large spectrum (up to several GHz) per operator in most countries.

1.3 Role of Channel Models in 5G Systems

The radio channel is fundamental to wireless communications [45]. Almost every aspect of wireless communications, ranging from real-world performance prediction, equipment design and system design, antenna architectures, and system performance, to capacity and coverage evaluation, depends upon an accurate understanding of the performance of radio signals when they propagate via a radio channel. The modeling of a radio channel is therefore vital to wireless communications research [46, 47, 48].

1.4 Technical Report Outline

Subsequent to the introduction chapter, the technical report is organized as follows.

Chapter 2 provides a comprehensive background of channel model basics and differences between microwave and mmWave channel modeling, followed by literature review of channel models and simulators, channel estimation, and single-cell and multi-cell beamforming approaches for mmWave MIMO systems.

Chapter 3 presents a practical method for synthesizing omnidirectional received power and path loss from field mmWave measurements using directional horn antennas [49]. The omnidirectional antenna pattern and omnidirectional received power are synthesized by summing the received powers from all measured unique pointing angles obtained at antenna half-power beamwidth step increments. The method is shown to provide accurate results while enhancing the measurement range substantially through the use of directional antennas.

Chapter 4 compares three candidate large-scale propagation path loss models for use over the entire microwave and mmWave radio spectrum: the alpha-beta-gamma (ABG) model, the close-in free space reference distance (CI) model, and the CI model with a frequency-weighted path loss exponent (CIF) [50]. The accuracy and sensitivity of the three path loss models are studied using measured data from 30 propagation measurement data sets from 2 GHz to 73 GHz over distances ranging from 4 m to 1238 m. A series of sensitivity analyses show that the physically-based CI and CIF models offer very similar goodness of fit as compared to the ABG model but with fewer parameters, exhibit more stable model parameter behavior, and yield smaller prediction error in sensitivity tests over a vast range of microwave and mmWave frequencies, scenarios, and distances.

Chapter 5 demonstrates details and applications of a novel channel simulation software named NYUSIM (New York University SIMulator) [51], which can be used to generate realistic temporal and spatial channel responses to support realistic

physical- and link-layer simulations and design for 5G cellular communications. NYUSIM is built upon the statistical spatial channel model for broadband mmWave wireless communication systems developed by researchers at New York University (NYU) [52]. The simulator is applicable for a wide range of carrier frequencies (500 MHz to 100 GHz), radio-frequency (RF) bandwidths (0 to 800 MHz), antenna beamwidths, and operating scenarios, and also incorporates MIMO antenna arrays.

Chapter 6 systematically compares the 3rd Generation Partnership Project (3GPP) TR 38.901 Release 14 channel model and the measurement-based NYUSIM channel model [53], including the line-of-sight (LOS) probability model, large-scale path loss model, outdoor-to-indoor penetration model, clustering methodology, large-scale and small-scale parameters, and their prediction performance for mobile systems. Particularly, the number of clusters in the 3GPP model is over two to four times as large as the maximum number of spatial lobes found through many years of measured data in New York City [2, 52, 54] and implemented in NYUSIM, leading to different channel sparsity levels in the two models. Compared to NYUSIM, the larger cluster number (i.e., more rich multipath) in the 3GPP model results in more eigen channels and more similar powers among those eigen channels, thus is advantageous for spatial multiplexing. On the other hand, the NYUSIM channel exhibits sparsity and has fewer but stronger dominant eigenmodes, hence generating higher spectral efficiency when combined with appropriate analog-digital hybrid beamforming (HBF) procedures. Results show that different channel models can lead to substantially varied predictions on diverse channel performance metrics and hardware requirements, thus it is vital to select an accurate channel model for 5G wireless system performance evaluation.

Chapter 7 presents a novel approach of constructing beamforming dictionary

matrices for mmWave sparse channel estimation using the continuous basis pursuit (CBP) concept [55], and proposes two novel low-complexity algorithms to exploit channel sparsity for adaptively estimating multipath channel parameters. The performance of the proposed CBP-based beamforming dictionary and the two algorithms are verified using NYUSIM. Numerical results show that the CBP-based dictionary offers significantly lower estimation error and higher spectral efficiency than the existing grid-based counterpart, and the proposed algorithms render better performance while requiring less computational effort compared with existing algorithms.

Chapter 8 provides a general methodology to analytically compute the average (expected) per-cell sum spectral efficiency of a mmWave multi-cell single-stream system using phase-shifter-based analog beamforming and regularized zero-forcing digital beamforming [56]. Four analog-digital hybrid beamforming techniques for multi-cell multi-stream mmWave communication are also proposed, in which it is assumed that base stations in different cells share channel state information to cooperatively transmit signals to its home-cell users. Spectral efficiency performance of the proposed hybrid beamforming approaches are investigated and compared using the 3GPP and NYUSIM channel models. Numerical results show that the benefits of base station coordination (as opposed to the no-coordination case) are ultimately governed by the underlying propagation model, as well as the aggregate interference levels proportional to the cell radius and the number of users per cell [56, 57].

Finally, Chapter 9 draws the concluding remarks of the technical report and presents potential future research directions based on the topics of the technical report.

This concludes the outline of the technical report, leading to the publications which have resulted from the work developed in the technical report.

1.5 Publications

The work carried out throughout the technical report has resulted in the following publications:

(1) **S. Sun**, G. R. MacCartney, M. K. Samimi, and T. S. Rappaport, "Synthesizing omnidirectional antenna patterns, received power and path loss from directional antennas for 5G millimeter-wave communications," in *Proceedings of the IEEE Global Communications Conference (GLOBECOM)*, San Diego, CA, 2015, pp. 1-7.

(2) **S. Sun** *et al.*, "Investigation of Prediction Accuracy, Sensitivity, and Parameter Stability of Large-Scale Propagation Path Loss Models for 5G Wireless Communications," *IEEE Transactions on Vehicular Technology*, vol. 65, no. 5, pp. 2843-2860, May 2016.

(3) **S. Sun** and T. S. Rappaport, "Millimeter wave MIMO channel estimation based on adaptive compressed sensing," in *Proceedings of the IEEE International Conference on Communications Workshops (ICC Workshops)*, Paris, France, 2017, pp. 47-53.

(4) **S. Sun**, G. R. MacCartney, and T. S. Rappaport, "A novel millimeter-wave channel simulator and applications for 5G wireless communications," in *Proceedings of the IEEE International Conference on Communications (ICC)*, Paris, France, 2017, pp. 1-7.

(5) T. S. Rappaport, **S. Sun**, and M. Shafi, "Investigation and comparison of 3GPP and NYUSIM channel models for 5G wireless communications," in *Proceedings of the IEEE 86th Vehicular Technology Conference (VTC-Fall)*, Toronto, ON, Canada, 2017, pp. 1-5.

(6) **S. Sun**, T. S. Rappaport, and M. Shafi, "Hybrid beamforming for 5G millimeter-wave multi-cell networks," in *Proceedings of the IEEE Conference on Computer Communications Workshops (INFOCOM WKSHPS)*, Honolulu, HI, USA, Apr. 2018.

(7) **S. Sun**, T. S. Rappaport, M. Shafi, Pan Tang, Jianhua Zhang, and Peter J. Smith, "Propagation models and performance evaluation for 5G millimeter-wave bands," submitted to *IEEE Transactions on Vehicular Technology*, Jan. 2018.

(8) **S. Sun**, T. S. Rappaport, M. Shafi, and H. Tataria, "Analytical framework of hybrid beamforming in multi-cell millimeter-wave systems," submitted to *IEEE Transactions on Wireless Communications*, Feb. 2018.

During my Ph.D. study, I have also contributed to the following publications, which, however, are not included in the technical report:

(9) T. S. Rappaport, **S. Sun**, R. Mayzus, H. Zhao, Y. Azar, K. Wang, G. N. Wong, J. K. Schulz, M. Samimi, and F. Gutierrez, "Millimeter wave mobile communications for 5G cellular: It will work!," *IEEE Access*, vol. 1, pp. 335-349, 2013.

(10) H. Zhao, R. Mayzus, **S. Sun**, M. Samimi, J. K. Schulz, Y. Azar, K. Wang, G. N. Wong, F. Gutierrez, and T. S. Rappaport, "28 GHz millimeter wave

cellular communication measurements for reflection and penetration loss in and around buildings in New York city," in *Proceedings of the IEEE International Conference on Communications (ICC)*, Budapest, Hungary, 2013, pp. 5163-5167.

(11) S. Nie, G. R. MacCartney, **S. Sun**, and T. S. Rappaport, "72 GHz millimeter wave indoor measurements for wireless and backhaul communications," in *Proceedings of the IEEE 24th Annual International Symposium on Personal, Indoor, and Mobile Radio Communications (PIMRC)*, London, UK, 2013, pp. 2429-2433.

(12) M. Samimi, K. Wang, Y. Azar, G. N. Wong, R. Mayzus, H. Zhao, J. K. Schulz, **S. Sun**, F. Gutierrez, and T. S. Rappaport, "28 GHz angle of arrival and angle of departure analysis for outdoor cellular communications using steerable beam antennas in New York city," in *Proceedings of the IEEE 77th Vehicular Technology Conference (VTC Spring)*, Dresden, Germany, 2013, pp. 1-6.

(13) **S. Sun** and T. S. Rappaport, "Multi-beam antenna combining for 28 GHz cellular link improvement in urban environments," in *Proceedings of the IEEE Global Communications Conference (GLOBECOM)*, Atlanta, GA, 2013, pp. 3754-3759.

(14) **S. Sun** and T. S. Rappaport, "Wideband mmWave channels: Implications for design and implementation of adaptive beam antennas," in *Proceedings of the IEEE MTT-S International Microwave Symposium (IMS2014)*, Tampa, FL, 2014, pp. 1-4.

(15) A. Ghosh *et al.*, "Millimeter-Wave Enhanced Local Area Systems: A High-

Data-Rate Approach for Future Wireless Networks," *IEEE Journal on Selected Areas in Communications*, vol. 32, no. 6, pp. 1152-1163, Jun. 2014.

(16) M. R. Akdeniz, Y. Liu, M. K. Samimi, **S. Sun**, S. Rangan, T. S. Rappaport, and E. Erkip, "Millimeter wave channel modeling and cellular capacity evaluation," *IEEE Journal on Selected Areas in Communications*, vol. 32, no. 6, pp. 1164-1179, Jun. 2014.

(17) **S. Sun**, G. R. MacCartney, M. K. Samimi, S. Nie, and T. S. Rappaport, "Millimeter wave multi-beam antenna combining for 5G cellular link improvement in New York city," in *Proceedings of the IEEE International Conference on Communications (ICC)*, Sydney, NSW, 2014, pp. 5468-5473.

(18) S. Nie, G. R. MacCartney, **S. Sun**, and T. S. Rappaport, "28 GHz and 73 GHz signal outage study for millimeter wave cellular and backhaul communications," in *Proceedings of the IEEE International Conference on Communications (ICC)*, Sydney, NSW, 2014, pp. 4856-4861.

(19) **S. Sun**, T. S. Rappaport, R. W. Heath, A. Nix, and S. Rangan, "MIMO for millimeter-wave wireless communications: beamforming, spatial multiplexing, or both?," *IEEE Communications Magazine*, vol. 52, no. 12, pp. 110-121, Dec. 2014.

(20) **S. Sun**, T. S. Rappaport, T. A. Thomas, and A. Ghosh, "A preliminary 3D mm-wave indoor office channel model," in *Proceedings of the International Conference on Computing, Networking and Communications (ICNC)*, Garden Grove, CA, 2015, pp. 26-31.

(21) Q. Li *et al.*, "Validation of a geometry-based statistical mmWave channel

model using ray-tracing simulation," in *Proceedings of the IEEE 81st Vehicular Technology Conference (VTC Spring)*, Glasgow, 2015, pp. 1-5.

(22) T. S. Rappaport, G. R. MacCartney, M. K. Samimi, and **S. Sun**, "Wideband millimeter-wave propagation measurements and channel models for future wireless communication system design," *IEEE Transactions on Communications*, vol. 63, no. 9, pp. 3029-3056, Sep. 2015.

(23) T. A. Thomas, F. W. Vook, and **S. Sun**, "Investigation into the effects of polarization in the indoor mmWave environment," in *Proceedings of the IEEE International Conference on Communications (ICC)*, London, UK, 2015, pp. 1386-1391.

(24) T. A. Thomas, F. W. Vook, E. Visotsky, and **S. Sun**, "System-level performance of different array types for an indoor mmWave system," in *Proceedings of the IEEE 82nd Vehicular Technology Conference (VTC2015-Fall)*, Boston, MA, 2015, pp. 1-5.

(25) **S. Sun**, T. A. Thomas, T. S. Rappaport, H. Nguyen, I. Z. Kovacs and I. Rodriguez, "Path loss, shadow fading, and line-of-sight probability models for 5G urban macro-cellular scenarios," in *Proceedings of the IEEE Globecom Workshops (GC Wkshps)*, San Diego, CA, 2015, pp. 1-7.

(26) G. R. Maccartney, T. S. Rappaport, **S. Sun**, and S. Deng, "Indoor office wideband millimeter-wave propagation measurements and channel models at 28 and 73 GHz for ultra-dense 5G wireless networks," *IEEE Access*, vol. 3, pp. 2388-2424, 2015.

(27) G. R. Maccartney, T. S. Rappaport, M. K. Samimi, and **S. Sun**, "Millimeter-wave omnidirectional path loss data for small cell 5G channel modeling," *IEEE Access*, vol. 3, pp. 1573-1580, 2015.

(28) **S. Sun**, G. R. MacCartney, and T. S. Rappaport, "Millimeter-wave distance-dependent large-scale propagation measurements and path loss models for outdoor and indoor 5G systems," in *Proceedings of the 10th European Conference on Antennas and Propagation (EuCAP)*, Davos, Switzerland, 2016, pp. 1-5.

(29) M. K. Samimi, **S. Sun**, and T. S. Rappaport, "MIMO channel modeling and capacity analysis for 5G millimeter-wave wireless systems," in *Proceedings of the 10th European Conference on Antennas and Propagation (EuCAP)*, Davos, Switzerland, 2016, pp. 1-5.

(30) **S. Sun** *et al.*, "Propagation path loss models for 5G urban micro- and macro-cellular scenarios," in *Proceedings of the IEEE 83rd Vehicular Technology Conference (VTC Spring)*, Nanjing, China, 2016, pp. 1-6.

(31) T. A. Thomas, M. Rybakowski, **S. Sun**, T. S. Rappaport, H. C. Nguyen, I. Z. Kovacs, and I. Rodriguez, "A prediction study of path loss models from 2-73.5 GHz in an urban-macro environment," in *Proceedings of the IEEE 83rd Vehicular Technology Conference (VTC Spring)*, Nanjing, China, 2016, pp. 1-5.

(32) M. K. Samimi, G. R. MacCartney, **S. Sun**, and T. S. Rappaport, "28 GHz millimeter-wave ultrawideband small-scale fading models in wireless channels," in *Proceedings of the IEEE 83rd Vehicular Technology Conference (VTC Spring)*, Nanjing, China, 2016, pp. 1-6.

(33) K. Haneda *et al.*, "5G 3GPP-like channel models for outdoor urban microcellular

and macrocellular environments," in *Proceedings of the IEEE 83rd Vehicular Technology Conference (VTC Spring)*, Nanjing, China, 2016, pp. 1-7.

(34) K. Haneda *et al.*, "Indoor 5G 3GPP-like channel models for office and shopping mall environments," in *Proceedings of the IEEE International Conference on Communications Workshops (ICC)*, Kuala Lumpur, Malaysia, 2016, pp. 694-699.

(35) G. R. MacCartney, S. Deng, **S. Sun**, and T. S. Rappaport, "Millimeter-wave human blockage at 73 GHz with a simple double knife-edge diffraction model and extension for directional antennas," in *Proceedings of the IEEE 84th Vehicular Technology Conference (VTC-Fall)*, Montreal, QC, Canada, 2016, pp. 1-6.

(36) G. R. MacCartney, **S. Sun**, T. S. Rappaport, Y. Xing, H. Yan, J. Koka, R. Wang, and D. Yu, "Millimeter wave wireless communications: New results for rural connectivity," in *Proceedings of the 5th Workshop on All Things Cellular in conjunction with ACM MobiCom*, Oct. 2016.

(37) T. S. Rappaport, **S. Sun**, and M. Shafi, "5G channel model with improved accuracy and efficiency in mmWave bands," *IEEE 5G Tech Focus*, vol. 1, no. 1, Mar. 2017.

(38) **S. Sun**, H. Yan, G. R. MacCartney, and T. S. Rappaport, "Millimeter wave small-scale spatial statistics in an urban microcell scenario," in *Proceedings of the IEEE International Conference on Communications (ICC)*, Paris, France, 2017, pp. 1-7.

(39) G. R. MacCartney, H. Yan, **S. Sun**, and T. S. Rappaport, "A flexible wideband millimeter-wave channel sounder with local area and NLOS to LOS transi-

tion measurements," in *Proceedings of the IEEE International Conference on Communications (ICC)*, Paris, France, 2017, pp. 1-7.

(40) J. Lota, **S. Sun**, T. S. Rappaport, and A. Demosthenous, "5G uniform linear arrays with beamforming and spatial multiplexing at 28, 37, 64, and 71 GHz for outdoor urban communication: A two-level approach," *IEEE Transactions on Vehicular Technology*, vol. 66, no. 11, pp. 9972-9985, Nov. 2017.

(41) T. S. Rappaport, G. R. MacCartney, **S. Sun**, H. Yan, and S. Deng, "Small-scale, local area, and transitional millimeter wave propagation for 5G communications," *IEEE Transactions on Antennas and Propagation*, vol. 65, no. 12, pp. 6474-6490, Dec. 2017.

Furthermore, I have contributed to the following deliverables and white papers:

(42) **S. Sun** and T. S. Rappaport, "Antenna diversity combining and beamforming at millimeter wave frequencies," NYU WIRELESS Technical Report, TR 2014-002, Jun. 2014.

(43) G. R. MacCartney, S. Deng, **S. Sun**, and T. S. Rappaport, "Indoor office wideband millimeter-wave propagation measurements and channel models at 28 GHz and 73 GHz for ultra-dense 5G wireless networks," NYU WIRELESS Technical Report, TR 2015-002, Oct. 2015.

(44) H. Yan, G. R. MacCartney, **S. Sun**, and T. S. Rappaport, "5G millimeter-wave channel model alliance measurement parameter, scenario parameter, and measured path loss data list," NYU WIRELESS Technical Report, TR 2016-002, Sep. 2016.

(45) Aalto University, AT&T, BUPT, CMCC, Ericsson, Huawei, Intel, KT Corporation, Nokia, NTT DOCOMO, **New York University**, Qualcomm, Samsung, University of Bristol, and University of Southern California, 5G channel model for bands up to 100 GHz, Oct. 21, 2016.

(46) **S. Sun**, "NYUSIM user manual (v1.0-v1.6)," New York University and NYU WIRELESS, Jul. 2016 - Dec. 2017.

Chapter 2

Background

In order to properly design and deploy 5G wireless systems, accurate channel models are needed. Channel models describe and model how wireless channel parameters behave in a given scenario, and help analyze link-level and system-level performance, thus playing an important role in wireless system design. A proper channel model should be able to faithfully reproduce the channel parameters obtained in real-world measurements and accurately predict channel performance. As the mmWave frequency band is expected to be exploited in 5G due to its tremendous amount of raw bandwidths, knowledge and modeling for mmWave channels are in huge need, which can be gained via field measurements.

2.1 MmWave Propagation Measurements Conducted by NYU WIRELESS

In order to build realistic channel models, channel measurements are needed to learn the channel and to study channel parameter statistics. NYU WIRELESS has

conducted extensive propagation measurements at multiple mmWave frequencies in various scenarios, such as urban microcell (UMi), urban macrocell (UMa), rural macrocell (RMa), and indoor office, from 2012 to 2017 [2, 54, 58, 59]. In what follows, several measurement campaigns with over one Terabytes of raw data used over 2012-2016 for developing the NYUSIM channel model [51] are described.

2.1.1 28 GHz Propagation Measurements in UMi Scenario

The 28 GHz propagation measurements were conducted in summer 2012 in downtown Manhattan around NYUs main campus, with a maximum RF transmit power of 30.1 dBm over an 800 MHz first null-to-null RF bandwidth, yielding a maximum measurable dynamic range of 178 dB [2, 54]. Measurements were performed for a typical base station-to-mobile (access) scenario with the transmitter (TX) antenna on relatively low rooftops and the receiver (RX) antenna located at a mobile height (1.5 m) around common city blocks typical of a dense urban environment. Narrowbeam TX and RX antennas were used, each with 24.5 dBi boresight gain and 10.9° and 8.6° half-power beamwidths (HPBWs) in azimuth and elevation planes, respectively. The narrowbeam outdoor-to-outdoor measurements in Manhattan consisted of over 10,000 recorded PDPs using three TX locations and 27 RX locations that were visited repeatedly for each TX location, providing for a total of 74 TX-RX location combinations. For each TX-RX location combination, the RX antenna was swept in 10° increments (approximately the antenna HPBW) in the azimuth plane for three different RX antenna elevation pointing angles and three different TX azimuth angles, all with a fixed TX downtilt elevation of 10°, where a PDP was acquired at each distinct azimuth pointing increment at the RX. One TX antenna sweep was conducted as well, resulting in 10 total azimuth sweeps for each TX-RX

combination. T-R separation distances ranged from31 m to 425 m, but PDPs were not measurable beyond 200 m. Fig. 2.1 illustrates the TX and RX hardware and measurement locations used in the 28 GHz campaign. More detailed information on the measurement procedure and results are provided in [2, 54].

2.1.2 73 GHz Propagation Measurements in UMi Scenario

The 73 GHz outdoor propagation measurements were conducted in downtown Manhattan around the NYU campus in summer 2013, with a maximum RF transmit power of 14.6 dBm over an 800 MHz first null-to-null RF bandwidth, yielding a maximum measurable dynamic range of 181 dB. The measurements consisted of five TX locations and 27 RX locations with a few of them repeated for more than one TX location, for both base station-to-mobile and backhaul-to-backhaul scenarios. RX antenna heights of 2 m and 4.06 m were used to emulate base station-to-mobile access and wireless backhaul scenarios, respectively [54]. Four TX sites were 7 m above ground and one was 17 m. PDPs were recorded using rotatable 27 dBi gain antennas at the TX and RX to capture azimuthal sweeps in 8° (approximately the antenna HPBW) increments using many RX antenna elevation angles for different fixed TX antenna azimuth and elevation angles. Azimuthal TX sweeps were also performed with the RX antenna fixed in the azimuth and elevation planes. Up to ten RX azimuthal sweeps and up to two TX azimuthal sweeps were conducted for each TX-RX location combination for both mobile and backhaul measurement scenarios. Fig. 2.2 displays the TX and RX hardware and measurement locations used in the 73 GHz UMi campaign. More information on the measurement procedure and results is detailed in [54].

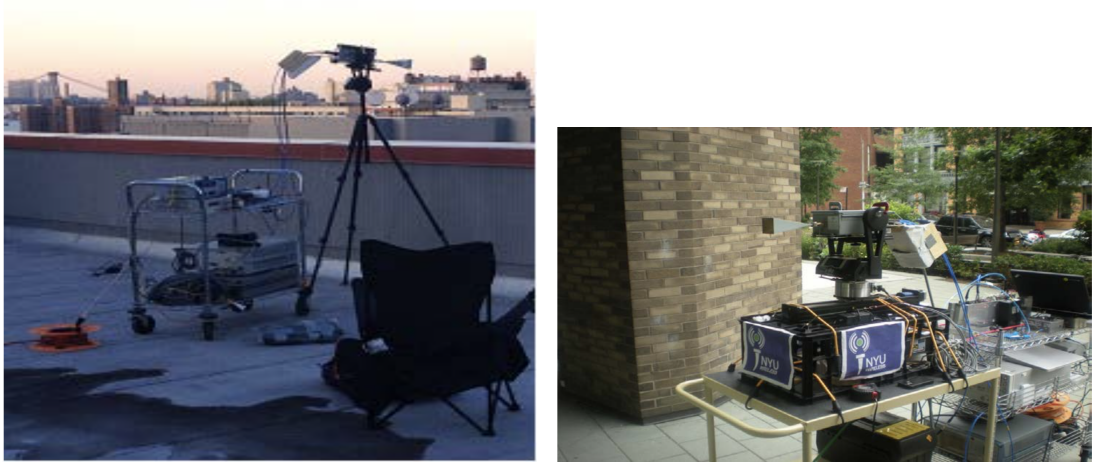

(a) (b)

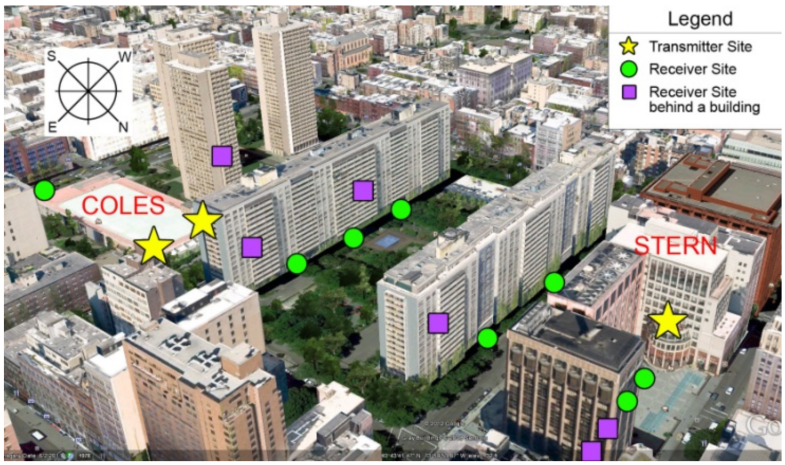

(c)

Figure 2.1: (a) Transmitter, (b) receiver, and (c) measurement locations used in the 28 GHz propagation measurements in New York City in 2012 [2].

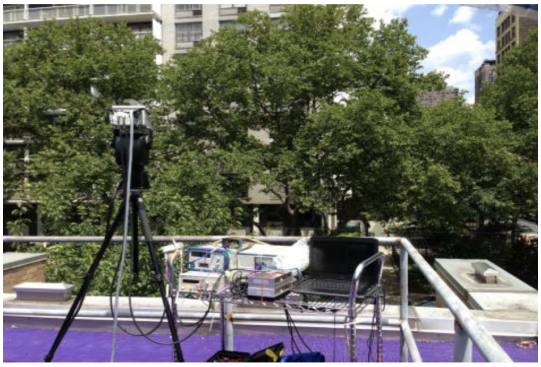

(a)

(b)

(c)

Figure 2.2: (a) Transmitter, (b) receiver, and (c) measurement locations used in the 73 GHz propagation measurements in New York City in 2013 [54].

2.1.3 73 GHz Propagation Measurements in RMa Scenario

The 73 GHz RMa measurements were carried out in Riner and Christiansburg, Virginia, rural towns in southwest Virginia in summer 2016. The TX was positioned on a porch at Professor Rappaports mountain home at a height of 110 m above the surrounding terrain [58, 59]. A narrowband continuous wave (CW) signal was transmitted with a maximum RF power of 14.7 dBm (29 mW) using a rotatable 7° azimuth and elevation HPBW horn antenna with 27 dBi of gain. An identical rotatable antenna with 27 dBi of gain and 7° azimuth and elevation HPBW was used at the RX to capture the RF signal, providing a maximum measurable path loss of 190 dB. The RMa measurements were made over a two-day period of clear weather using a receiver measurement van, with the receiving antenna fixed on a tripod outside of the van at an average height between 1.6 m and 2 m above the ground along country roads and streets near rural homes and businesses [58, 59]. Measurements were made at 14 LOS and 17 NLOS locations where a measurable signal was detected. The 2D T-R separation distance for LOS locations ranged from 33 m to 10.8 km, and from 3.4 km to 10.6 km for NLOS locations [58, 59]. Remarkably, *signals can be detected with a T-R separation distance of over 10 km even in NLOS environments*. Fig. 2.3 shows the TX and RX locations and surrounding areas in the 73 GHz RMa campaign. More information on measurement procedure and results can be found in [58, 59].

Extensive indoor measurements were also made during 2013-2016 [60, 61, 62, 63], but this technical report focuses on the outdoor UMi, UMa, and RMa scenerios since these are of greatest interest to wireless carriers who will bid on spectrum and deploy 5G networks.

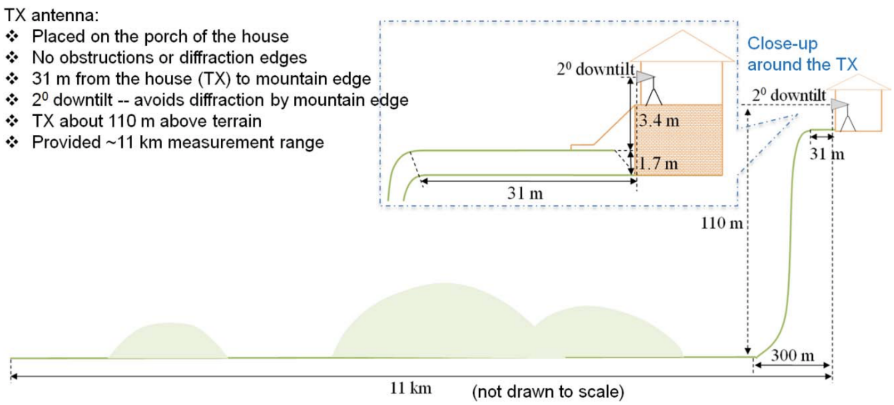

(a)

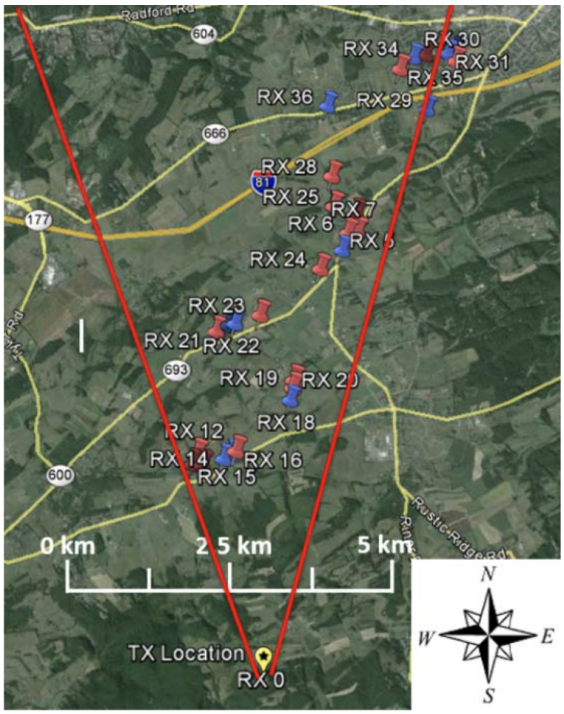

(b)

Figure 2.3: (a) Sketch of the TX location on the porch of the mountain home, and surrounding areas in the 73 GHz RMa measurements in 2016. (b) Map of TX and RX locations in the 73 GHz RMa measurements in 2016. The yellow star represents the TX, red pins indicate NLOS locations, and blue pins indicate LOS locations [58, 59].

2.2 Channel Model Basics

A radio channel is the medium linking the TX and the RX. Various objects, such as glass windows, concrete buildings, plants, moving cars, etc., exist in the real environments, thus the radio waves may be reflected, scattered or diffracted, arriving at the RX with different paths [64, 65], and transmitted signal experiences dramatic variation when going through the radio channel. The received signal is thereby the sum of multiple radio waves with different phases and delays. Fig 2.4 illustrates an example wireless channel with a base station, a user, and obstructions (buildings and a bus), where the transmitted signal is decomposed into several clusters (defined jointly in the space and time domains) as defined in the 3GPP channel model [66], or, spatial lobes as defined in the NYUSIM channel model [51] (NYUSIM also defines time clusters, where a time cluster could contain rays in different spatial lobes, and a spatial lobe could also contain rays in different time clusters [52]), and subpaths/rays within clusters (3GPP)/spatial lobes (NYUSIM), stemming from LOS propagation, reflection, scattering, and diffraction.

The signal variation is categorized into large-scale and small-scale fading [64, 65, 67]. Large-scale fading describes the average channel gain over a distance of tens to a few hundred of wavelengths, and is important for coverage prediction and interference analysis of a radio system. Shadow fading, which belongs to large-scale fading and is caused by large terrain features between the BS and mobile station (MS), is generally modeled as a Gaussian variable in dB. Small-scale fading describes the signal variation over a short distance scale [62, 68, 69, 70], e.g., fractions of wavelengths. For instance, measurement results in [62] showed that the small-scale spatial fading was very small over a 35.31-cm ($\sim$ 87 wavelengths) linear track at 73 GHz with a 1 GHz bandwidth, with at most -4 dB to +2 dB

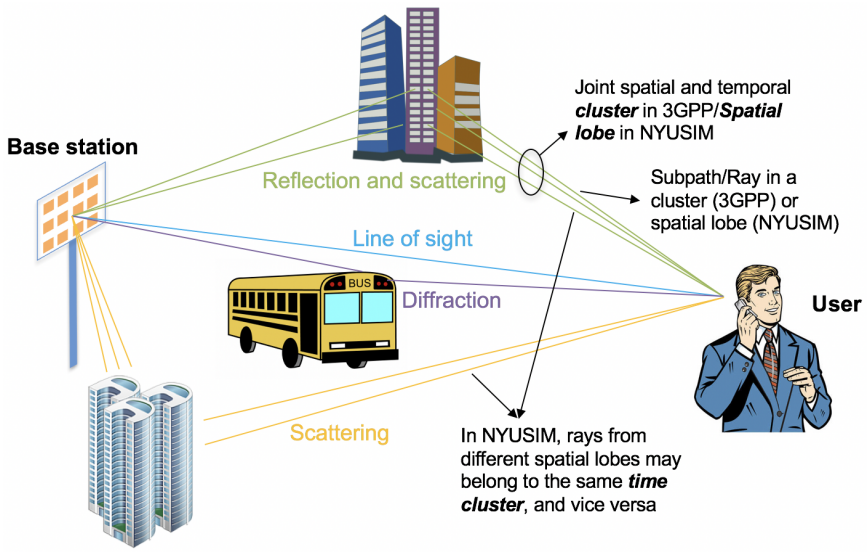

Figure 2.4: An example wireless channel with a base station, a user, and obstructions (buildings and a bus), where the transmitted signal is decomposed into several clusters (defined jointly in the space and time domains) as defined in the 3GPP channel model [66], or, spatial lobes as defined in the NYUSIM channel model [51] (NYUSIM also defines time clusters, where a time cluster could contain rays in different spatial lobes, and a spatial lobe could also contain rays in different time clusters [52]), and subpaths/rays within clusters (3GPP)/spatial lobes (NYUSIM), stemming from LOS propagation, reflection, scattering, and diffraction.

fading depth relative to the mean for an omnidirectional antenna, while the fading depth for a directional RX antenna depends on the RX orientation in relation to the environment and the TX [62]. Small-scale fading determines the performance of air interface technologies. In the delay domain, root-mean-square (RMS) delay spread is defined as the standard deviation in propagation time between multipath components (MPCs), and large delay spread often induces strong inter-symbol interference. RMS angular spread is defined as the standard deviation in the angles between MPCs. It is found from the published literature [2, 52, 71, 72, 73] that similar modeling philosophy can also be used for mmWave frequencies, as introduced below.

2.2.1 Path Loss and Large-Scale Fading

Path loss is the reduction in power of a radio wave as it propagates through the channel, which is defined as [67, 74]:

$$\mathrm{PL[dB]} = 10\log_{10}\frac{P_{\mathrm{T}}}{P_{\mathrm{R}}}, \tag{2.1}$$

where P_{T} and P_{R} are the transmitted and received power, respectively. In free space, the received power is a function of distance and wavelength/frequency, also known as Friis' law [64, 67]:

$$P_{\mathrm{R}}(d,\lambda) = P_{\mathrm{T}}G_{\mathrm{T}}G_{\mathrm{R}}\left(\frac{\lambda}{4\pi d}\right)^2, \tag{2.2}$$

where G_{T} and G_{R} are the antenna gains at the TX and RX, respectively, λ is the wavelength, d_{3D} is the spatial distance between the TX and RX. However, in real

environments, there are many dielectric and conducting obstacles and path loss is more severe than in free space, thus a lot of effort has been devoted to field measurements and path loss modeling. Several empirical path loss models have been widely used for frequencies below 6 GHz, including the Hata model for 2G systems [**?**], ITU-R M. 1225 for 3G [75], and ITU-R M. 2135 for 4G [76], etc. Similarly, for mmWave, numerous field measurements [54, 58, 59, 77, 78, 79, 80, 81] have been carried out in the 28, 38, 60, 73, and 80 GHz bands. Two main types of path loss models for mmWave channels, along with their corresponding shadow fading values, have been proposed and used by researchers and standards bodies [50, 82], i.e., the ABG model and the CI model, which are detailed in Section 6.1.2.

2.2.2 Small-Scale Fading

Small-scale fading is involved in the channel impulse response (CIR). Considering a narrowband flat fading channel, the CIR can be described as:

$$h(t,\tau) = V + g(t,\tau), \tag{2.3}$$

where V is a complex and deterministic component, which exists in the LOS case with a strong and dominant path between the TX and RX. If assuming the multiple received radio waves are wide-sense stationary uncorrelated scattering (WSSUS), $g(t,\tau)$ is typically a complex zero-mean Gaussian random variable with its envelope obeying the Rayleigh distribution. However, if there is a fixed LOS component, the phase and quadrature components of the CIR are not zero-mean variables. For such a composite channel, the amplitude obeys the Ricean distribution [83]. The Ricean factor (also named K-factor) is the power ratio of the LOS component to

that of the other components, e.g., scattered and diffracted components, and it indicates the severity of fading. When the K-factor decreases to zero, the amplitude of the fading channel becomes the Rayleigh distribution. As the channel bandwidth increases, the RX can resolve multiple paths according to their delays and the CIR will change to:

$$h(t,\tau) = V\delta(\tau - \tau_0) + \sum_{i=1}^{N} g_i(t)\delta(\tau - \tau_i), \tag{2.4}$$

where $g_i(t)$ is a complex Gaussian variable with the excess delay τ_i, $\delta(\cdot)$ is the Dirac function and N is the number of resolvable delay bins. This tapped delay line (TDL) model can describe the channel variation in delay dispersion. However, as the channel bandwidth increases from 5 MHz to 20 MHz, even to 100 MHz, the delay resolution is also enhanced significantly and more multipaths can be expected below 6 GHz. This makes the TDL model extremely complex and increases computational complexity. In [84], a novel CIR model, known as the Saleh and Valenzuela (SV) model, was proposed based upon the analysis of indoor measurements. In this model, the MPCs are assumed to arrive in clusters, where the clusters and components within a cluster form a Poisson arrival process with different rates. Then the CIR is given by:

$$h(t,\tau) = \sum_{n=0}^{N}\sum_{m=0}^{M} a_{n,m}(t,\tau)\delta(\tau - \tau_{n,m}), \tag{2.5}$$

where N denotes the number of clusters, M is the number of MPCs in a cluster, $a_{n,m}$ is the complex amplitude of the mth MPC within the nth cluster, and $\tau_{n,m}$ is the delay of the mth MPC in the nth cluster. Clusters are also defined and used in 3GPP/ITU/WINNER models, e.g., the spatial channel model (SCM). Furthermore, in the SCM, directions of MPCs and antenna patterns are considered, and it describes not only delay dispersion, but also angular dispersion, which consists of a

sum of contributions from the MPCs [85]. For the nth cluster, the impulse response can be written as follows:

$$h_n(t,\tau,\phi_{tx},\phi_{rx}) = \sum_{m=1}^{M} a_{n,m} F_{rx}(\phi_{n,m,rx}) F_{tx}(\phi_{n,m,tx}) \delta(\tau - \tau_{n,m}) \delta(\phi - \phi_{n,m,rx}) \delta(\phi - \phi_{n,m,tx}) \tag{2.6}$$

where $a_{n,m}$ is the complex amplitude of the mth MPC within the nth cluster, F_{tx} and F_{rx} are the antenna patterns at the TX and RX, respectively, $\phi_{n,m,rx}$ and $\phi_{n,m,tx}$ are the angle of arrival (AoA) and angle of departure (AoD) of this MPC, respectively. For a LOS scenario, the impulse response consists of two parts, a deterministic component, i.e., the LOS path, and a random component (often composed of scattered components). The impulse response is expressed as:

$$\begin{aligned} h_n(t,\tau,\phi_{rx},\phi_{tx}) =& \sqrt{\frac{1}{K+1}} h_n(t,\tau,\phi_{rx},\phi_{tx}) + \delta(n-1)\sqrt{\frac{K}{1+K}} a_{\mathrm{LOS}} F_{tx}(\phi_{\mathrm{LOS}}) F_{rx}(\phi_{\mathrm{LOS}}) \\ & \times \exp(j2\pi\lambda^{-1}(\mathrm{vec}r_{rx,\mathrm{LOS}} \cdot \mathrm{vec}d_{rx})) \exp(j2\pi\lambda^{-1}(\mathrm{vec}r_{tx,\mathrm{LOS}} \cdot \mathrm{vec}d_{tx})) \end{aligned} \tag{2.7}$$

where K is the K-factor, $\mathrm{vec}r_{rx,\mathrm{LOS}}$ denotes the spherical unit vector corresponding to the LOS angle at the RX, $\mathrm{vec}r_{tx,\mathrm{LOS}}$ denotes the spherical unit vector corresponding to the LOS angle at the TX, $\mathrm{vec}d_{rx}$ and $\mathrm{vec}d_{tx}$ represent the location vectors of the RX and TX antenna elements, respectively. Variables with subscript LOS represent the parameters of the LOS path. This model assumes that the LOS path appears in the first cluster.

The Geometry-based Stochastic Channel Model (GSCM) is another modeling method (used in the COST modeling framework)[85], in which the geometric position of scatterers is determined by a probability density function and ray tracing

is used to determine the actual double-directional impulse response. Furthermore, large-scale parameters (e.g., path loss, shadow fading, K-factor, angular spread (AS) and delay spread (DS)) and small-scale parameters (e.g., delays, cluster powers, cross polarization ratios (XPRs), arrival and departure angles) are proposed to describe the GSCM.

For 3D MIMO systems with N_{T} TX antennas and N_{R} RX antennas, the channel between the uth RX antenna and the sth TX antenna is characterized by a complex coefficient $h_{u,s}(\tau)$ in (2.8) [86], where (n, m) stands for the mth subpath/ray in the nth cluster, $P_{n,m}$ represents the normalized received power of subpath/ray m in cluster n such that $\sum_n \sum_m P_{n,m} = 1$, $F_{rx,u,\theta}$ and $F_{rx,u,\phi}$ are the field patterns of RX antenna u in the direction of the spherical basis vectors $\hat{\theta}$ and $\hat{\phi}$ respectively, $\theta_{n,m}$ and $\phi_{n,m}$ denote the elevation and azimuth angles for subpth/ray m in cluster n, respectively, $F_{tx,s,\theta}$ and $F_{tx,s,\phi}$ are the filed patterns of TX antenna s in the direction of the spherical basis vectors $\hat{\theta}$ and $\hat{\phi}$, respectively, $\kappa_{n,m}$ is the cross-polarization power ratio in linear scale, $\Phi_{n,m}^{\theta\theta}, \Phi_{n,m}^{\theta\phi}, \Phi_{n,m}^{\phi\theta}, \Phi_{n,m}^{\phi\phi}$ are random initial phases for subpath/ray m in cluster n for four different polarization combinations $(\theta\theta, \theta\phi, \phi\theta, \phi\phi)$, $[\exp(j\frac{2\pi}{\lambda_0}(\mathbf{W}_{tx}\mathbf{r}_{tx}(\theta_{n,m,ZoD}, \phi_{n,m,AoD})))]_s$ and $[\exp(j\frac{2\pi}{\lambda_0}(\mathbf{W}_{rx}\mathbf{r}_{rx}(\theta_{n,m,ZoA}, \phi_{n,m,AoA})))]_u$ are the TX and RX array response vectors evaluated at the TX antenna s and the RX antenna u, respectively, $\mathbf{W}_{tx}$ and $\mathbf{W}_{rx}$ denote location matrices of the TX and RX antennas in 3D Cartesian coordinates, $\mathbf{r}_{tx}(\theta_{n,m,ZoD}, \phi_{n,m,AoD})$ and $\mathbf{r}_{rx}(\theta_{n,m,ZoA}, \phi_{n,m,AoA})$ are the angular spherical unit vectors of the TX and RX corresponding to subpath/ray m in cluster n, respectively, λ_0 denotes the wavelength, and $\upsilon_{n,m}$ in the Doppler frequency. If polarization is not considered, the 2×2 polarization matrix $\begin{bmatrix} \exp(j\Phi_{n,m}^{\theta\theta}) & \sqrt{\kappa_{n,m}^{-1}\exp(j\Phi_{n,m}^{\theta\phi})} \\ \sqrt{\kappa_{n,m}^{-1}\exp(j\Phi_{n,m}^{\phi\theta})} & \exp(j\Phi_{n,m}^{\phi\phi}) \end{bmatrix}$

$$
\begin{aligned}
h_{u,s}(\tau) = & \sum_{n=1}^{N}\sum_{m=1}^{M}\sqrt{P_{n,m}}\begin{bmatrix} F_{rx,u,\theta}(\theta_{n,m,ZoA},\phi_{n,m,AoA}) \\ F_{rx,u,\phi}(\theta_{n,m,ZoA},\phi_{n,m,AoA}) \end{bmatrix}^{T} \\
& \times \begin{bmatrix} \exp(j\Phi_{n,m}^{\theta\theta}) & \sqrt{\kappa_{n,m}^{-1}\exp(j\Phi_{n,m}^{\theta\phi})} \\ \sqrt{\kappa_{n,m}^{-1}\exp(j\Phi_{n,m}^{\phi\theta})} & \exp(j\Phi_{n,m}^{\phi\phi}) \end{bmatrix} \begin{bmatrix} F_{tx,u,\theta}(\theta_{n,m,ZoD},\phi_{n,m,AoD}) \\ F_{tx,u,\phi}(\theta_{n,m,ZoD},\phi_{n,m,AoD}) \end{bmatrix} \\
& \times \left[\exp(j\frac{2\pi}{\lambda_0}(\mathbf{W}_{rx}\mathbf{r}_{rx}(\theta_{n,m,ZoA},\phi_{n,m,AoA})))\right]_u \\
& \times \left[(\exp(j\frac{2\pi}{\lambda_0}(\mathbf{W}_{tx}\mathbf{r}_{tx}(\theta_{n,m,ZoD},\phi_{n,m,AoD}))))^H\right]_s \delta(\tau-\tau_{n,m})
\end{aligned}
\tag{2.8}
$$

is replaced by $\exp(j\Phi_{n,m})$ and only vertically polarized filed patterns are applied. In the 3GPP model [66], the number of clusters and the number of subpaths/rays per cluster are fixed for a given scenario, whereas both numbers are statistical and variable in certain regions in NYUSIM. For the 3GPP LOS channel model, $h_{u,s}(\tau)$ is obtained by adding a LOS coefficient to the non-line-of-sight (NLOS) CIR and scaling both terms according to the Ricean K-factor [66]. In NYUSIM, the LOS channel matrix is calculated in the same manner as the NLOS case but with different parameters derived from measured data, both of which can be expressed by (2.8) [52].

The channel impulse response matrix $\mathcal{H}(\tau)$ is then given by:

$$
\boldsymbol{\mathcal{H}}(\tau) = \begin{bmatrix} h_{1,1}(\tau) & h_{1,2}(\tau) & \dots & h_{1,N_{\mathrm{T}}}(\tau) \\ h_{2,1}(\tau) & h_{2,2}(\tau) & \dots & h_{2,N_{\mathrm{T}}}(\tau) \\ \vdots & \vdots & \ddots & \vdots \\ h_{N_{\mathrm{R}},1}(\tau) & h_{N_{\mathrm{R}},2}(\tau) & \dots & h_{N_{\mathrm{R}},N_{\mathrm{T}}}(\tau) \end{bmatrix}
$$

Let $p(\tau)$ denote a pulse-shaping function for T_{S}-spaced signaling evaluated at τ

seconds [87], then the delay-d_{s} channel matrix, $\boldsymbol{\mathcal{H}}(d_{\mathrm{s}})$, is formulated as [87]:

$$\boldsymbol{\mathcal{H}}(d_{\mathrm{s}}) = \boldsymbol{\mathcal{H}}(\tau)p(d_{\mathrm{s}}T_{\mathrm{S}} - \tau_{n,m}) \tag{2.9}$$

Assuming OFDM modulation which is used in 4G systems, where the RF bandwidth is divided into K OFDM narrowband (e.g., 15 kHz for 4G LTE, but likely 75 GHz for 5G pre-trial [6]) sub-carriers stacked in a wide band, the frequency-domain channel response at sub-carrier k_f ($k_f = 0, ..., K_f - 1$) can be obtained from the impulse response $\boldsymbol{\mathcal{H}}(d_{\mathrm{s}})$ as follows [87]:

$$\mathbf{H}(k_{\mathrm{f}}) = \sum_{d_{\mathrm{s}}=0}^{D_{\mathrm{s}}-1} \boldsymbol{\mathcal{H}}(d_{\mathrm{s}})e^{-j2\pi d_{\mathrm{s}}k_{\mathrm{f}}/K_{\mathrm{f}}} \tag{2.10}$$

where $\mathbf{H}(k_{\mathrm{f}})$ is the matrix frequency response at sub-carrier k_{f}, D_{s} denotes the number of delay bins, and $\boldsymbol{\mathcal{H}}(d_{\mathrm{s}})$ represents the channel matrix impulse response at delay d_s. Eq. (2.10) indicates that for a narrowband channel with a single carrier frequency f, the frequency-domain channel response matrix is equivalent to [87]:

$$\mathbf{H}(f) = \sum_{d_s=0}^{D_s-1} \boldsymbol{\mathcal{H}}(d_s) \tag{2.11}$$

In what follows, $\mathbf{H}(f)$ will be denoted as $\mathbf{H}$ for simplicity. As 5G MIMO systems will likely employ OFDM modulations similar to 4G systems but with larger sub-carrier spacings [6], this technical report will focus on OFDM-like modulations with narrowband (e.g., 15 kHz for 4G LTE and 75 kHz for 5G pre-trial [6]) flat-fading sub-carriers. Note that the maximum omnidirectional RMS delay spread in mmWave channels is on the order of 250 ns [52], such that the coherence bandwidth is roughly $1/(250\text{ ns}) = 4$ MHz [67], hence RF bandwidths smaller than 4 MHz can

be considered as flat-fading. This narrowband flat-fading assumption is also used in most of the literature works to be demonstrated later in this chapter.

For mmWave channels, special changes in channel model are needed to describe the new characteristics, e.g., frequency dependency, varying cluster numbers and high path loss. For example, new models have to consider the high path loss and high penetration loss in mmWave propagation. The differences between mmWave models and microwave models are discussed below in detail.

2.3 MmWave and Microwave Model Differences

Due to the increase in frequency, radio waves with high frequency have different propagation characteristics compared to microwave [64]. For example, mmWaves can not efficiently penetrate and diffract around obstacles, e.g., cars, buildings and people. This results in less diffracting MPCs and high path loss. The following subsections focus on several channel properties in mmWave bands and discuss new requirements for channel models.

2.3.1 Frequency Dependence

MmWave channels have high free space path loss in the first meter of propagation due to its frequency dependence [50], to be shown by Eq. (4.2). Furthermore, frequency dependence on other channel parameters, e.g., delay spread and angular spread, also need further investigation. In 3GPP TR 38.901 Release 14 [66], both delay spread and angular spread are modeled as a function of frequency for the channels (except for the rural macro (RMa) scenarios) above 6 GHz.

2.3.2 Attenuation and Blockage

During propagation, mmWaves may be partially or totally absorbed by an absorbing medium, which results in additional loss. Thus, rain attenuation and atmospheric attenuation [88, 89, 90, 91] should be considered in mmWave systems, although this is not a concerned problem in microwave systems. Additionally, mmWave systems are much more sensitive to blockage by obstacles. For example, the path loss increases with the propagation distance. In [92], it was found that outdoor tinted glass had a penetration loss of 40.1 dB at 28 GHz, and three interior walls of an office building had a penetration loss of 45.1 dB, with a distance of 11.39 m between the TX and RX. Table 6.5 shows the penetration loss of different materials. If stationary or moving objects stand between the TX and RX, channel characteristics will be dramatically changed when the signal is blocked, especially for mmWave channels [93]. The shadowing caused by these objects is important for the link budget and the time variance of the channel. Furthermore, such dynamic blocking is perhaps important to capture in evaluations of technologies, e.g., beam-finding and beam-tracking capabilities.

2.3.3 Channel Sparsity

It is usually claimed that mmWave channels are sparse in the angle and delay domains [2, 71]. For example, in [52], only up to five spatial lobes are found in dense-urban NLOS environments, and the delay/angle spreading within each cluster is relatively small. However, more experimental verifications of this are needed. Nonetheless, a lower bound on the channel sparsity can still be established based on existing measurements, and in many environments the percentage of delay/angle

bins with significant energy is rather low while it is higher at centimeter-wave frequencies.

2.3.4 Large Bandwidth and Large Antenna Array

To meet the demand of future mobile data growth [94], bandwidths on the order of 1 GHz are needed. In mmWave bands, there are large bandwidths available (see Table 1.1). On the other hand, smaller wavelengths make large antenna arrays feasible [95]. Thus, the channel model should consider high resolution in both delay and angular domains. In order to model this effect, the offset angles and relative delay within a cluster should be modeled as variable rather than constant. Various types of antenna arrays, such as the uniform linear array (ULA), uniform rectangle array (URA), and uniform cylinder array (UCA), are being considered. In [96], lens antenna arrays were proposed to enable mmWave MIMO communications. Besides, compared to uniform planar arrays (UPAs), lens antenna arrays can significantly reduce the signal processing complexity and RF chain cost without performance degradation.

2.3.5 Spatial Consistency

Spatial consistency is identified as an important feature for 5G channel models [97]. The spatial consistency of a channel means that the channel evolves smoothly without discontinuities when the TX and/or RX moves or turns. It also means that channel characteristics in closely located users are highly correlated. Spatial consistency covers various aspects, e.g., large-scale parameters and small-scale parameters of delays, AoAs and AoDs, outdoor/indoor state, and LOS/NLOS state. In [66], a spatial consistency procedure is used for both cluster-specific and

ray-specific random variables to be spatially consistent. For example, cluster delays $\tau_n = \tau_{max} X_n$, where τ_{max} is the maximum delay $(2 \cdot 10^{\mu_{lgDS}+\sigma_{lgDS}})$, X_n is a spatially uniform random variable within (0,1), μ_{lgDS} and σ_{lgDS} are the mean value and standard deviation of RMS DS (see Tables 6.7 and 6.8), respectively.

2.3.6 Stationarity Regions

The study of channel stationarity plays an important role in channel modeling and estimation, since stationarity has to be assumed in order to obtain accurate estimates and reproduce channel parameters. Measurements at 2 GHz to 30 GHz have indicated that the spatial stationarity regions of mmWave bands (less than 0.09 m or so) are much smaller than those at microwave frequencies (around 0.6 m) for an allowance of similarity level of 0.6 [98]. Furthermore, recent field measurements have shown very sharp spatial decorrelation over small distance movements of just a few tens of wavelengths at mmWave frequencies [62], yet it is noteworthy that the orientation of directional antennas with respect to the surrounding environment can impact the stationarity and correlation distances, as demonstrated in [62]. Additionally, the average received power of wideband 73 GHz signals can change by 25 dB as the mobile RX transitioned around a building corner from NLOS to LOS in a UMi scenario [62]. Therefore, stationarity regions need to be carefully characterized in 5G channel modeling that incorporates mmWave bands.

2.3.7 Random Cluster Numbers

In the existing channel model for microwave bands, the number of clusters is a constant [76]. For the mmWave bands, this assumption may not be reasonable. According to recent literature, cluster/time-cluster numbers are small and random,

and are well-modeled by a Poisson distribution [52, 71]. In [99], the mean cluster number is 12 while it is less than 4 in [71] (Note that the definition of cluster is different in these two references). By making the cluster numbers random, some channel properties, e.g., capacity, will change correspondingly.

2.4 Review of Channel Models and Simulators

The construction and implementation of channel models are becoming increasingly important for wireless communication system design, and computer-aided design tools such as channel simulators are essential for performance evaluation of communications systems and for simulating network deployments, before moving forward with new technologies.

There are several channel simulators that have been developed and used by previous researchers [100, 101, 102, 103, 104, 105, 106]. For instance, Smith [107] built simulation software for indoor and outdoor propagation channels by making use of the two-ray Rayleigh fading channel model developed by Clarke [108]. Fraunhofer Heinrich Hertz Institute developed a 3-D multi-cell channel model that can accurately predict the performance for an urban macrocell setup with commercial high-gain antennas, upon which a channel simulator has been built that supports features such as time evolution, scenario transitions, and so on [101]. A channel simulator for indoor scenarios was developed for machine-to-machine applications [102]. Rappaport and Seidel developed a measurement-based statistical indoor channel model named SIRCIM (Simulation of Indoor Radio Channel Impulse Response Models) for the early development of WiFi [103] and the corresponding simulation software to generate channel impulse responses (CIRs) for indoor channels

operating from 10 MHz to 60 GHz. A similar open-source RF propagation simulator is SMRCIM (Simulation of Mobile Radio Channel Impulse Response Models), that was useful for simulating outdoor channels [104, 105]. Another software simulation program, called BERSIM [106], developed by Fung *et al.*, was able to simulate mobile radio communication links and calculate average bit error rate (BER) and bit-by-bit error patterns, that was useful for evaluating link quality in real time without requiring any radio frequency hardware. More detailed descriptions and comparisons of several popular channels models are provided below.

2.4.1 SIRCIM Channel Model and Simulator

The SIRCIM model, which is a statistical radio channel impulse response model, was developed based on propagation measurements in indoor factory and open plan office scenarios at 1.3 GHz [103] in both LOS and obstructed (OBS) topographies. The model can describe the distribution of the number of multipath components in a particular multipath delay profile, the distribution of the number of multipath components received within a local area, the probability of receiving each multipath component at a particular excess delay, the distributions of the amplitudes, phases, and time delays of multipath components received within a local area, and the probability of receiving a multipath component at small scale locations. The computer simulator SIRCIM, which is built based upon the aforementioned channel impulse response model, is able to recreate multipath power delay profiles (PDPs) and continuous-wave (CW) fading profiles that are representative of measured results. SIRCIM allows the prediction of arriving signals at a receiver from one (or many) transmitters by performing convolutions of transmitted signals with simulated channels.

2.4.2 SMRCIM Channel Model and Simulator

The SMRCIM channel model and simulator are aimed for outdoor environments including urban microcell (UMi) and suburban scenarios [104], which can generate realistic channels based on extensive measured data. The software package SMRCIM belongs to Wireless Valley Communications, Inc. SMRCIM accurately models various types of multipath, including flat-fading, small delay spreads, and very large delay spreads, which are usually encountered in an urban cellular scenario, and it also models the spatial correlation in small-aperture two-element arrays [104]. SMRCIM has been utilized to generate empirically derived random multipath channel for examining the performance of various techniques in CDMA systems [109].

2.4.3 QuaDRiGa Channel Model and Simulator

QuaDRiGa is developed at the Fraunhofer Heinrich Hertz Institute to enable the modeling of MIMO radio channels for specific network configurations, such as indoor, satellite or heterogeneous configurations. The QuaDRiGa channel model is geometry-based stochastic channel model, which collects features created in SCM(e) and WINNER channel models along with novel modeling approaches which provide features to enable quasi-deterministic multi-link tracking of users (receiver) movements in changing environments. It supports 3D propagation, 3D antenna patterns, time evolving channel traces, scenario transitions and variable terminal speeds. In the QuaDRiGa channel model, it is assumed that the base stations are fixed, the mobile terminals are moving, and scattering clusters are fixed as well and the time evolution of the radio channel is deterministic. QuaDRiGa also supports massive MIMO modeling enabled through a new multi-bounce scattering

approach and spherical wave propagation. It will be continuously extended with features required by 5G and frequencies beyond 6 GHz. The QuaDRiGa channel model is supported by data from extensive channel measurement campaigns at 10/28/43/60/82 GHz performed by the same group.

2.4.4 COST 2100 Channel Model

The COST 2100 channel model [110] is a geometry-based stochastic channel model for MIMO systems that is built on the framework of the earlier COST 259 and 273 models [111], which covers aspects such as multi-user, multi-cellular, and cooperative operation in MIMO systems. The most distinguishing feature of the COST 2100 channel model lies in that it is a cluster-based model which is not constrained by large-scale parameters (LSPs), and the environment is described independent of the mobile station location. Specifically, the COST 2100 channel model defines a large number of clusters with consistent stochastic parameters throughout the simulation environment according to the base station location, as well as the mobile station location, and determining the scattering from the visible clusters at each channel instance, and synthesizes the LSPs based on the cluster scattering. There are two key modeling concepts: *visibility region* and *cluster* [110]. A visibility region denotes a circular region given a fixed size in the simulation area, which determines the visibility of only one cluster. When the mobile station enters a visibility region, the related cluster smoothly increases its visibility. A cluster is represented by an ellipsoid in space as viewed from the base station and from the mobile station, which is characterized with specific positions and orientations toward the base station and mobile station [110].

2.4.5 METIS Channel Models

The METIS channel models consist of a map-based model, a stochastic model, and a hybrid model as a combination of both [112]. The map-based model is based on ray tracing using a simplified 3D geometric description of the propagation environment and thus inherently accounts for major propagation mechanisms such as diffraction, specular reflection, diffuse scattering, blocking, etc. Channel realizations are generated with an implementation of the map-based model and are compared to the measurement results in some selected scenarios by analysing propagation parameter statistics [112]. The stochastic model extends the geometry based stochastic channel model (GSCM), which has been further developed from WINNER/3GPP, in order to provide multi-dimensional shadowing maps with low complexity, mmWave parameters, direct sampling of the power angular spectrum, and frequency dependent path loss models [112]. The hybrid model provides a flexible and scalable channel modelling framework that tries to ibalance between the simulation complexity and realism. The METIS channel models are intended for the frequency range from sub-1 GHz to 86 GHz and beyond, bandwidths greater than 500 MHz, massive MIMO, extremely large arrays even beyond stationarity interval, direct device-to-device (D2D), machine-to-machine (M2M) and vehicular-to-vehicular (V2V) communications, spatial consistency between topologies and between users (e.g., birth-death process and/or visibility regions for clusters).

2.4.6 MiWEBA Channel Model

The MiWEBA channel model is a quasi-deterministic channel model aimed for millimeter-wave outdoor mobile access links of small cell base stations with a

typical cell radius of several hundred meters [113]. The MiWEBA channel model is developed based on a measurement campaign conducted at 60 GHz with an RF bandwidth of 250 MHz on a plaza in downtown Berlin, Germany. The quasi-deterministic channel model is a combination of a geometry-based method for a limited number of multipath components and a stochastic approach, and builds on the representation of the mmWave channel impulse response comprised of a few quasi-deterministic strong rays, a number of relatively weak random rays originating from the static surfaces reflections, and flashing rays originating from moving cars, buses, and other dynamic objects reflections [113]. The key benefit of the quasi-deterministic modeling approach compared to pure statistical models is its inherent support for spatial consistency, since it takes into account the positions of the transmitter and receiver. In the MiWEBA channel model, the propagation loss is calculated by the Friis equation, taking additional losses from the oxygen absorption into consideration. The parameters of reflected rays are calculated based upon the Fresnel equations, plus additional losses due to surface roughness [113]. The quasi-deterministic modeling approach requires a precise description of the scenario, thus it is only applicable to the specific scenario investigated and cannot be extended to other scenarios.

2.4.7 WINNER II Channel Model

The WINNER family is a set of geometry-based stochastic channel models. The channel parameters are determined stochastically, based on statistical distributions extracted from channel measurements. The WINNER II channel model is applicable for link-level and system-level simulations of local area, metropolitan area, and wide area wireless communication systems [114]. The channel model is antenna

independent, i.e., different antenna configurations and different element patterns can be inserted. The channel parameters are determined stochastically, based on statistical distributions extracted from channel measurement. Channel realizations are generated by summing contributions of rays with specific channel parameters like delay, power, angle-of-arrival and angle-of-departure. The channel model is applicable to any wireless system operating in 2 - 6 GHz frequency range with up to 100 MHz RF bandwidth. As the WINNER II channel model is devised for cellular communication between a fixed base station and a mobile user terminal, it is not adequate for situations where both link ends can be at arbitrary locations, or even ultra-dense deployment, where closely located base stations see partly the same environment. Another known defect of the WINNER approach is the lack of support for spherical waves and consistent modeling of closely located users. In particular, it yields poor realism for cases that need high spatial resolution such as massive MIMO and pencil beamforming.

2.4.8 ITU-R IMT-Advanced Channel Model

The ITU working party 5D has recently been developing a recommendation on the framework and objectives of the future development of IMT for 2020 and beyond. The ITU-R IMT-Advanced channel model is a geometry-based stochastic channel model [115], which is known as a double directional channel model. The modeling methodologies of the ITU-R IMT-Advanced channel model are similar to those in the 3GPP channel model to be described in the following subsection.

2.4.9 3GPP Channel Model

The 3GPP channel model is also a geometry-based stochastic spatial channel model developed based on the 2D channel models from ITU and WINNER II, and has been extended to 3D, which is also inspired by the extension from 2D to 3D channel model published as part of WINNERII/WINNER+ [116]. The channel model is suitable for link-level and system-level simulations to estimate realistic channels between a base station, and one or more UEs, that account for empirical correlations between large-scale parameters. The large-scale parameters denote the omnidirectional RMS delay spread, the azimuth spread, the shadow fading, and the Rician K-factor (for LOS channels), and were shown to exhibit significant correlation for a given base-to-mobile link. It is assumed that each multipath component can be represented by a planar wavefront, characterized by small-scale parameters such as path delays, powers, AoAs, and AoDs, extracted from measurement-based statistical distributions. In the 3GPP channel model, a *cluster* is defined as a group of multipath components traveling close in both the temporal and spatial domains, and a *ray* is defined as a multipath component within a cluster. A joint delay-angle clustering approach is adopted in the 3GPP channel model, such that a group of traveling multipaths must depart and arrive from a unique AoD-AoA angle combination centered around a mean propagation delay. The 3GPP TR 38.901 Release 14 channel model [66] is targeted for carrier frequency range from 0.5 GHz to 100 GHz and large channel bandwidths (up to 10% of the carrier frequency), and takes into account mmWave propagation aspects such as blocking and atmosphere attenuation. The channel model is also aimed to accommodate user terminal mobility with mobile speeds up to 500 km/h, and develop a methodology considering that model extensions to D2D and V2V may be

developed in future work. One of the most prominent blemish of the 3GPP channel model is the unrealistically large number of clusters, which might be proper to model sub-6 GHz channels, but is not suitable for modeling mmWave channels that exhibit sparsity [52, 54, 117].

2.4.10 Statistical Spatial Channel Model by NYU

NYU WIRELESS conducted mmWave measurements from 2012 through 2017 [2, 54, 58, 59], having acquired a total of over 1 Terabytes of data, at frequencies from 28 to 73 GHz in various outdoor environments in UMi, UMa, and RMa environments. as presented in Section 2.1. A 3D SSCM [52] has been developed based upon the measured data, which is comprised of similar modeling steps to the 3GPP channel model [66] such as LOS probability model, large-scale path loss model, large-scale parameters, and small-scale parameters, but with different modeling approaches and/or parameters in each step. For instance, for the large-scale path loss model, the CI model is utilized that has solid physical basis and provides lower computational complexity, higher prediction accuracy and higher parameter stability than the ABG model, as demonstrated in [50] and Chapter 4 of this technical report. For multipath clustering, the time-cluster-spatial-lobe (TCSL) clustering approach is proposed that extends the existing ultra-high frequency (UHF) 3GPP model through the additional model parameters of directional RMS lobe angular spreads for spatial lobes [52].

In the SSCM, TCs are composed of multipath components traveling close in time, and arriving from potentially different directions in a short propagation time window. SLs denote primary directions of departure (or arrival) where energy arrives over several hundred nanoseconds [52]. Per the definitions given above,

a TC contains multipath components traveling close in time, but may arrive from different SL angular directions, such that the temporal and spatial statistics are decoupled and can be recovered separately. Similarly, an SL may contain many multipath components arriving (or departing) in a space (angular cluster) but with different time delays. This distinguishing feature is obtained from real-world propagation measurements [2] which have shown that *multipath components belonging to the same TC can arrive at distinct spatial pointing angles and that energy arriving or departing in a particular pointing direction can span hundreds or thousands of nanoseconds in propagation delay, detectable due to high-gain steerable directional antennas*. The TCSL clustering scheme models the directionality of mmWave channels via separate TCs that have time-delay statistics, and via SLs that represent the strongest directions of multipath arrival and departure [52]. The TCSL framework is physically based (e.g., it uses a fixed inter-cluster void interval to represent the minimum propagation time between possible obstructions causing reflection, scattering, or diffraction), and is derived from field observations based on about 1 Terabytes of measured data over many years, and can be used to extract TC and SL statistics for any measurement or ray-tracing data sets [52]. Fig. 2.5 illustrates an omnidirectional PDP, where there are four multipath taps which are grouped into two time clusters with exponentially decaying amplitudes. The four multipath taps are then grouped into two AOA spatial lobes, as shown in Fig. 2.6.

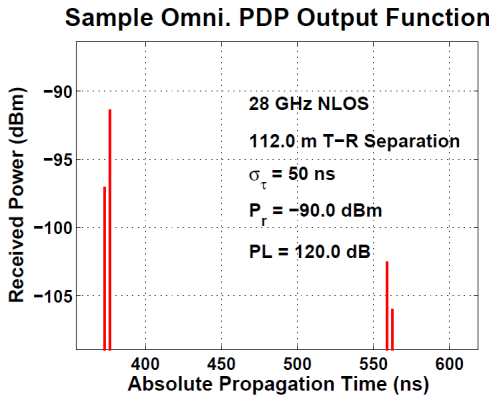

Figure 2.5: Example of an omnidirectional PDP with four multipath taps [52].

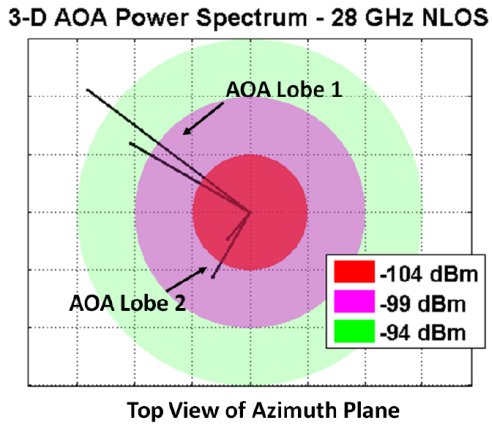

Figure 2.6: Example of an AOA power spectrum with four multipath taps [52].

2.5 Review of Channel Estimation Based on Compressed Sensing

Channel modeling is an important and fundamental step towards wireless system design, after which communication infrastructures will be built and various signal transmission and reception techniques will be utilized at both communication link ends, in which the knowledge of actual channels plays a key role in the design of signal processing strategies. Channel state information (CSI) is needed to design precoding and combining procedures at transmitters and receivers, and it can be obtained through channel estimation. Conventional MIMO channel estimation methods may not be applicable in mmWave systems because of the substantially greater number of antennas, hence new channel estimation methods are required [118]. Due to the sparsity feature of mmWave channels observed in [2, 52], which means majority of the resolvable delay/angular bins do not contain MPCs with sufficient electromagnetic energy caused by a small number of spatial lobes [52, 119], compressed sensing (CS) techniques [120] can be leveraged to effectively estimate mmWave channels [121, 122, 123]. Adaptive CS, as a branch of CS, yields better performance at low signal-to-noise ratios (SNRs) compared to standard CS techniques, and low SNRs are typical for mmWave systems before implementing beamforming gain [119]. Adaptive CS algorithms for mmWave antenna arrays were derived in [119] to estimate channel parameters for both single-path and multipath scenarios, and it was shown that the proposed channel estimation approaches could achieve comparable precoding gains compared with exhaustive training algorithms. Additionally, Destino *et al.* proposed an adaptive-least absolute shrinkage and selection operator (A-LASSO) algorithm to estimate

sparse massive MIMO channels [124]. In [125], reweighted l_1 minimization was employed to realize sparsity enhancement based on basis pursuit denoising. The authors of [126] demonstrated a CS-based channel estimation algorithm for mmWave massive MIMO channels in ultra-dense networks, in conjunction with non-orthogonal pilots transmitted by small-cell base stations.

A channel estimation algorithm was proposed in [127] for a frequency-division duplexing (FDD) multi-user (MU) massive MIMO system using the structured compressed sensing theory, which took advantage of the common sparsity and private sparsity architecture of the channel matrix in an MU massive MIMO system. A structured joint subspace matching pursuit (SJSMP) algorithm was proposed to estimate channels jointly with limited pilot at the base station [127]. The authors of [128] employed the subspace pursuit, orthogonal matching pursuit (OMP), and compressed sampling matching pursuit (CoSaMP) techniques in conjunction with minimum mean square error (MMSE) and least mean square (LMS) approaches to estimate the channel coefficients for a MIMO-OFDM (orthogonal frequency-division multiplexing) system. Simulation results showed that the proposed method was able to reduce the normalized mean square error versus SNR significantly when compared with the existing subspace pursuit, OMP, and CoSaMP combined with the least square method, and that CoSaMP combined with LMS provided better performance than the subspace pursuit and OMP with LMS with less computational complexity [128].

Marzi *et al.* investigated a compressive structure to estimate and track sparse spatial channels in the downlink in mmWave picocellular networks at 60 GHz [129], where compressive beacons were sent with pseudo-random phase settings at the base station antenna array, and compressively processed using pseudo-random phase

settings at the mobile array, which is compatible with coarse phase-only control and RF beamforming, and allows scaling to a large number of antenna elements independent of channel reciprocity [129].

In [130], a CS-based adaptive channel estimation and feedback scheme was proposed for FDD-based massive MIMO systems, which adapts non-orthogonal pilot design to reliably estimate and feed back the downlink CSI with reduced overhead using the spatially channel sparsity. Moreover, a distributed sparsity adaptive matching pursuit was proposed for jointly estimating the channels for multiple sub-carriers [130], which was able to acquire the high-dimensional CSI from a small number of non-orthogonal pilots.

Invoking the CS techniques, the authors of [131] devised a novel channel covariance estimation scheme for analog/digital hybrid architecture for time-division duplexing (TDD) mmWave single-user (SU) MIMO systems, where the mobile station has a single antenna, and the covariance was directly estimated via a one-step approach without the need to estimate the channel explicitly. Both the sparsity of mmWave channels and the Hermitian property of covariance matrices were utilized, and a time-varying analog combining matrix at the receiver was employed to effectively extend the number of measurements [131].

Low-resolution ADCs can significantly reduce the power consumption in mmWave systems, thus they are of special interest in mmWave MIMO research [132, 133, 134]. In [132], channel estimation algorithms were developed for mmWave MIMO systems with one-bit ADCs and all digital combining utilized at the receiver, in which the estimation problem was formulated as a one-bit CS problem. A modified expectation-maximization scheme was proposed which exploits the sparsity and exhibits better performance compared with the conventional expectation-maximization approach.

Furthermore, a second algorithm named generalized approximate message passing (GAMP) was applied to solve the optimization problem [132], which is computationally efficient and can reduce the mean squared error in the low and moderate SNR ranges that are typical in mmWave systems before carrying out beamforming. One limitation of the algorithm in [132] is the assumption that each element in the virtual channel obeys i.i.d. Bernoulii Gaussian distribution, otherwise there will be "leakage" such that each path is not associated with a single entry in the virtual channel. Besides, each path has an angular spread hence probably correspond to several adjacent elements [132]. The above issues may be solved by making the virtual channel sparse through a windowing scheme [132, 135].

In order to reduce power consumption in mmWave MIMO systems, hybrid beamforming architectures have been widely considered that will be detailed in Section 2.6, as well as low-resolution ADCs. To this end, a channel estimation method was proposed in [133] for such type of structures, where hybrid beamforming architectures were used at both the transmitter and receiver, and low-resolution ADCs that coarsely quantize the in-phase and quadrature components with q ($q \leq 3$) quantization bits were adopted at the receiver, which was called the mix hybrid-low resolution MIMO architecture [133]. In such a system, the received signal suffers from two compression stages: (i) the analog processing and the reduced number of RF chains, and (ii) signal quantization by the low-resolution ADCs. Accordingly, the authors of [133] proposed a compressive channel estimator which exploits the sparsity of mmWave channels to compensate for the information loss intrinsic to the aforementioned structure. A modified expectation-maximization algorithm was proposed that combines both MMSE estimation of the receieved signal before quantization and the OMP to recover the sparse channel vector

iteratively. Simulation results show that utilizing no more than three quantization bits does not reduce the mean square error substantially [133].

Huang *et al.* proposed a joint channel estimation and beamforming strategy for broadband mmWave cellular systems in [136], in which the sparse mmWave channel was estimated utilizing a low-complexity CS-based estimation algorithm. The computational complexity of the proposed algorithm was reduced by avoiding matrix inverse and singular value decomposition but using multiplication operations. Considering practical hardware constraints for mmWave structures, finite phase control with limited quantization bits for analog beamforming was applied. Simulation results show that the proposed strategy leads to only 2 dB to 3 dB loss compared to the perfect CSI case [136].

A low-rank spatial channel estimation scheme was proposed in [137] for mmWave MIMO systems, where the long-term receive-side spatial channel covariance matrix was estimated from a series of power measurements conducted in different angular directions. The maximum likelihood estimation scheme was employed to estimate the covariance matrix, which reduces to a non-negative matrix completion problem [137]. Thanks to the sparse/low-rank nature of mmWave channels with respect to the number of antenna elements, the non-negative feature of the covariance matrix significantly reduces the number of measurements. Specifically, a simple iterative soft thresholding algorithm (ISTA) approach was adopted to estimate the covariance matrix, following which a second algorithm that provides further improvements by exploiting the directional nature of the covariance using a component-wise gradient descent was proposed [137]. Simulation results unravel that the proposed algorithms converge relatively fast and can provide good channel estimates with significantly less number of measurements than unknowns. The

authors of [137] presented channel estimation methods for analog beamforming and hybrid beamforming, yet there is an increasing interest in fully digital architectures, especially using low-resolution ADCs. Covariance estimation in low-resolution digital channels would require different strategies in [137] and would be an interesting research topic for future work.

In [138], an asymmetric channel estimation method combining an exhaustive beam training at the receiver for AoAs and a CS-based scheme for the transmit beam training for AoDs was proposed for MU-MIMO mmWave systems, which makes use of the asymmetric number of antenna elements at the base station and mobile stations. In the proposed channel estimation strategy, the best receive beam was first found using an exhaustive search since the overhead for exhaustive receive beam search is affordable due to a small number of antenna elements at the user in general [138]. Then a CS-based scheme was employed to train the base station beam while the receive beam was fixed as selected in the first stage. Simulation results show that by performing beamforming at the receiver side while CS is applied at the transmitter side, the proposed algorithm yields better estimation performance compared to the conventional CS-based approach in the low SNR regime [138].

As a modified algorithm to the single-path estimation technique presented in [119], an enhanced version of the single-path estimation algorithm was proposed in [139], which utilized the property of the diagonally dominant matrix, rather than the received signal strength as in [119], as the criterion to detect the single path. The disadvantage of the received signal strength-based algorithm in [119] is that the received signal is usually submerged in the noise before conducting the beamforming, which indicates that the selected maximum power is not always associated with the desired signal [139]. Simulation results show that the proposed

modification enhances the single-path channel estimation performance in terms of the spectral efficiency [139]. However, the achievable spectral efficiency yielded by the proposed algorithm still has a large gap compared to the perfect channel knowledge case. One major limitation of the introduced method is that it only applies to single-path channels, not multipath channels.

In [140], a pilot design was proposed to facilitate fast LASSO-based sparse channel estimation that exploits the inherent delay- and angle-domain sparsity of mmWave channels, where aperture shaping was used to ensure a sparse virtual-domain MIMO channel representation [141]. It was shown by the numerical results that the proposed pilot-aided designs can approximate the spectral efficiency rendered by the perfect-CSI capacity-optimal system [140]. The strategy presented in [140] can be extended to continuous aperture phased (CAP) MIMO systems and digital beamforming using one-bit ADCs.

Based on the Least Square Estimation (LSE) and Sparse Message Passing (SMP) algorithm, the authors of [142] proposed a channel estimation strategy that leverages the intrinsic sparse feature of mmWave channels. The SMP was employed to detect the exact location of non-zero entries of the channel vector, and the LSE was utilized to estimate its value at each iteration. Furthermore, the authors analyzed the Cramer-Rao Lower Bound (CRLB) of the proposed algorithm. An intermediate virtual channel representation was used in [142] due to its ability to capture the essence of physical modeling and to render simple geometric interpretation of the scattering environment [141, 142]. Numerical simulations reveal that the proposed algorithm yields better performance compared to the traditional LSE estimator and existing sparse estimators such as the LASSO approach. Moreover, only four iterations were needed to achieve its CRLB [142].

Nevertheless, the presented algorithm has a high computational complexity owning to matrix inversion operations in coarse and fine estimation stages. Another aspect to improve is to relax the assumption that the number of non-zero entries in the virtual channel vector is exactly equal to the number of paths [142].

2.6 Review of Beamforming for mmWave MIMO Systems

The use of mmWave bands opens up the possibility of using large-scale antenna arrays where hundreds of (if not more) antennas are used. The antenna elements can be arranged in a linear array or a full-dimensional (i.e., with both elevation and azimuth angle resolution capabilities) array. These multi-element antenna arrays will provide spatial multiplexing gain but it is not necessary that an array type in one morphology is best for another. For example, some areas may require elevation beamforming (narrow beams in the elevation) and may need more antennas along the zenith axis as compared to other areas where beamforming in the azimuth may require more antennas in the azimuth. Antenna architectures are also influenced by the horizontal and vertical angle spreads in a multipath channel. The antennas likely to be used are active antennas i.e. the power amplifiers, and bulk of the signal processing hardware are at the backplane of the antennas. Therefore, the number of antenna elements (dependent upon channel model) will also have an impact on power consumption, energy efficiency, hardware complexity, etc [143].

Beamforming is a signal processing technique that focuses the signal onto desired directions by adjusting the phases and/or amplitudes for each antenna element [144]. It is necessary to conduct beamforming, especially in mmWave channels that gen-

erally experience high free space path loss in the first meter, so as to provide beamforming gain which can improve coverage and support multiple users. Three types of beamforming have been proposed and studied in the literature: analog beamforming [145], digital beamforming, and analog/digital hybrid beamforming [117, 118, 119, 146, 147, 148, 149, 150, 151, 152], as depicted in Fig. 2.7. For analog beamforming, a single RF chain is connected to all antenna elements. *The main drawback of analog beamforming is the huge power consumption of analog phase shifters.* For digital beamforming, multiple data streams are transmitted, and the number of data streams cannot exceed the smaller of the number of TX and RX antenna elements. Stream separation is done via precoding techniques such as zero-forcing (ZF) and regularized ZF (RZF) [153]. The spectral efficiency achieved by digital beamforming is the highest among the three beamforming structures, where the optimal precoder and decoder consist of the first N_{S} columns of $\mathbf{V}$ and $\mathbf{U}$, respectively, with N_{S} denoting the number of data streams, $\mathbf{V}$ and $\mathbf{U}$ representing unitary matrices derived from the channel's singular value decomposition (SVD), i.e., $\mathbf{H} = \mathbf{U}\mathbf{\Sigma}\mathbf{V}^H$. *Digital beamforming, however, requires a complete RF chain behind each antenna element, which entails high complexity and cost when the antenna number is large.* HBF, as illustrated in Fig. 2.7(c), is realized via low-dimensional digital baseband processing combined with analog RF processing usually enable by phase shifters. *In HBF, the number of RF chains is often much less than the number of TX/RX antenna elements, which is especially reasonable for mmWave channels as the channel is sparse hence a small number of RF chains can already exploit the limited number of spatial lobes, so that HBF spectrum efficiency approaches digital spectrum efficiency* [117]. Fig. 2.8 illustrates the beam patterns generated by a 256-element uniform rectangular array in an example channel realization with

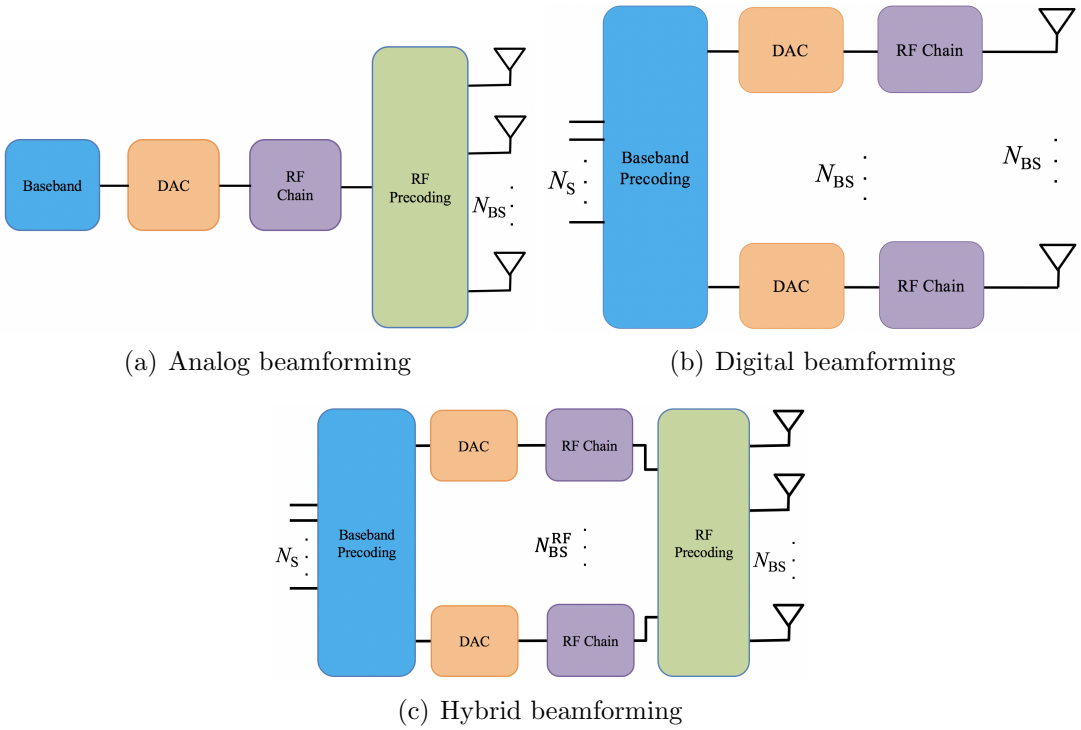

(a) Analog beamforming (b) Digital beamforming

(c) Hybrid beamforming

Figure 2.7: Block diagrams of beamforming architectures at a BS for a downlink transmission, where structures (a), (b), and (c) represent the analog beamforming, digital beamforming, and hybrid beamforming structures, respectively. N_{BS}, N_{S}, and $N_{\mathrm{RF,BS}}$ denote the numebr of BS antenna elements, the number of data streams, and the number of BS RF chains, respectively.

the NYUSIM channel model [51] using the (a) analog beam steering vector in the channel's dominant physical direction, (b) optimal digital precoding vector, and (c) hybrid precoding vector with four RF chains produced using Algorithms 1 in [117]. *The hybrid precoding results in beam patterns that closely resemble the patterns generated by optimal digital precoding, and this beam pattern similarity will ultimately lead to similar spectral efficiency* [117].

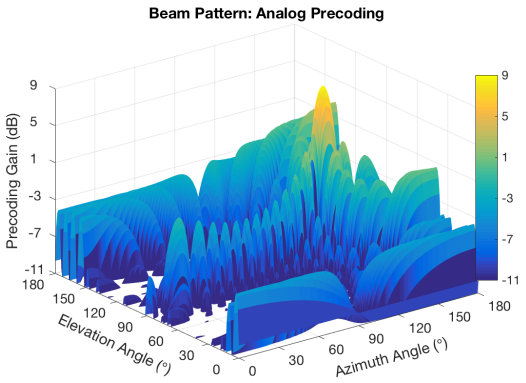

(a) Analog Precoding

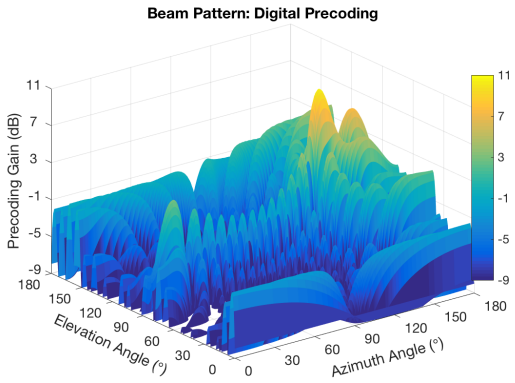

(b) Digital Precoding

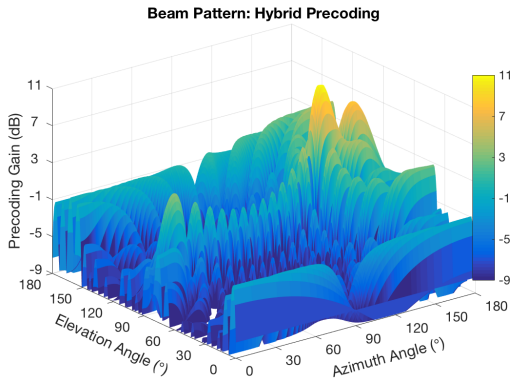

(c) Hybrid Precoding

Figure 2.8: Beam pattern generated by a 256-element uniform rectangular array in an example channel realization with the NYUSIM channel model [51] using the (a) analog beam steering vector in the channel's dominant physical direction, (b) optimal digital precoding vector, and (c) hybrid precoding vector with four RF chains produced using Algorithms 1 in [117]. *The hybrid precoding results in beam patterns that closely resemble the patterns generated by optimal digital precoding, and this beam pattern similarity will ultimately lead to similar spectral efficiency* [117].

2.6.1 Multi-User Digital Beamforming

The optimal downlink digital precoding method that achieves the capacity in MIMO broadcast channels is known to be dirty paper coding (DPC) [154], a multi-user precoding scheme whose fundamental approach is to cancel out interference via precoding at the transmitter using perfect CSI and complete knowledge of the signals to be sent. DPC, however, is a nonlinear precoding strategy and is difficult to implement in practice due to high computational complexity. As an alternative, linear precoding approaches have lower computational burden and can sometimes yield near-optimal performance [155].

2.6.1.1 Single-Antenna Users

In this scenario, a mobile UE has only one antenna element. There are several popular linear digital signal processing techniques used in MIMO systems: matched filtering (MF) transmission/reception (also known as maximum ratio transmission (MRT) transmission and/or maximum ratio combining (MRC), or conjugate beamforming), ZF [156], RZF [156], and signal-to-leakage-plus-noise ratio (SLNR)-based beamforming scheme [157].

MF aims to maximize the signal power on each stream transmitted to or from the terminals, without taking into account the effects of multi-user interference. This is realized by multiplying the transmitted/received signals by the conjugate channel responses. MF operates poorly in interference-limited scenarios since it neglects inter-user interference. In contrast to MF, ZF aims to null the inter-user interference by projecting each data stream onto the orthogonal complement of the inter-user interference. Mathematically, the ZF matrix is the pseudo-inverse of the composite instantaneous small-scale fading channel matrix. One disadvantage of ZF

is that it ignores the effect of additive Gaussian noise, thus yields poor performance under noise-limited conditions. As an enhanced version of ZF, RZF considers both interference and additive Gaussian noise, which can overcome noise inflation in the low SNR regime [156]. The precoding matrix $\mathbf{F}$ for three signal processing schemes introduced above can be mathematically expressed as:

$$\mathbf{F} = \begin{cases} \mathbf{H}^H, \text{ for MF} \\ \mathbf{H}^H(\mathbf{H}\mathbf{H}^H)^{-1}, \text{ for ZF} \\ \mathbf{H}^H(\mathbf{H}\mathbf{H}^H + \xi N_0 \mathbf{I})^{-1}, \text{ for RZF} \end{cases} \tag{2.12}$$

where $\mathbf{H}$ denotes the downlink channel matrix, ξ is a regularization factor in RZF, and N_0 represents the noise variance. When $\xi \to \infty$, RZF becomes equivalent to MF; when $\xi = 0$, RZF reverts to ZF. Note that the baseband matrices using MF, ZF, and RZF all have dimensionality constraints, as indicated by (2.12). Namely, if the dimension of $\mathbf{H}$ is $N_{\mathrm{R}} \times N_{\mathrm{T}}$, then the dimension of $\mathbf{F}$ is constrained to be $N_{\mathrm{T}} \times N_{\mathrm{R}}$. This dimensionality requirement, however, may not be satisfied in reality, especially in HBF, due to the constraint of the number of RF chains and/or data streams. Nevertheless, *SLNR-based processing does not have the dimensionality constraint and is hence more flexible*, and more details about SLNR-based beamforming approach is provided in Chapter 8.

2.6.1.2 Multi-Antenna Users

When each user is equipped with multiple antennas, a popular precoding method is block diagonalization (BD) [158], which eliminates inter-user interference and can be thought of as a generalization of channel inversion for circumstances with multiple

antennas per user. BD also has dimensionality constraints and is only applicable to situations where the number of transmit antennas is no smaller than the total number of receive antennas. Furthermore, BD requires the independence of the matrices between the transmitter and individual receivers, and user-grouping has to be performed if two or more users have highly correlated channels [159]. SLNR-based precoding is another processing strategy when there are multiple antennas per user [157], and has no dimensionality or matrix independence constraints.

2.6.2 Analog Beamforming

Analog beamforming relies on the RF domain processing and is usually implemented using phase shifters which induces constant modulus constraints on the elements of the RF beamformer [117]. Analog beamforming can also be implemented with analog switches [147, 160], which often requires antenna element selection.

2.6.3 Multi-Cell Signal Processing

Multi-cell networks suffer both intra- and inter-cell interference, which can be mitigated via proper beamforming approaches including inter-cell base station cooperation/coordination. The 3GPP completed a study on coordinated multipoint (CoMP) techniques for both downlink and uplink for the Long Term Evolution (LTE)-Advanced system in 2013 [161]. Four CoMP scenarios are considered in [161]: (1) Homogeneous network with intra-site CoMP; (2) Homogeneous network with high transmit power remote radio heads (RRHs); (3) Heterogeneous network with low power RRHs within the macrocell coverage where the transmission/reception points created by the RRHs have different cell IDs as the macrocell; (4) Heterogeneous network with low power RRHs within the macrocell coverage where the

transmission/reception points created by the RRHs have the same cell IDs as the macrocell. Each CoMP scheme may be categorized into two types: joint processing and coordinated scheduling/beamforming, where joint processing includes joint transmission and dynamic point selection (DPS)/muting. The different CoMP strategies in [161] entail different levels of complexity and requirements with respect to CSI feedback and CSI sharing ,which are detailed below in increasing order of complexity and requirements.

2.6.3.1 Coordinated Scheduling/Beamforming

In coordinated scheduling/beamforming, data for a UE is only available at and transmitted from one transmission point (TP) using its own beamforming approach in the CoMP cooperating set (downlink data transmission is done from that TP) for a time-frequency resource, but user scheduling/beamforming decisions are made with coordination among TPs. Coordinated scheduling/beamforming necessitates CSI feedback from multiple TPs. Inter-TP phase information is not required. It is possible to configure multiple CSI feedback instances [161].

2.6.3.2 Dynamic Point Selection/Muting

In DPS/muting, data is available simultaneously at multiple TPs but is transmitted from only one TP in a time-frequency resource, and the transmitting/muting TP may change from one subframe to another. DPS requires similar CSI feedback as coordinated scheduling/beamforming in the sense that no inter-TP phase information is required, although some additional channel quality indicator (CQI) report targeting other TPs may be needed. Similarly to the other schemes, optimizations to existing CSI reporting procedures are not precluded. DPS may require UE

recommendation on selected TP(s) [161].

2.6.3.3 Joint transmission

In joint transmission, data for a UE is available at multiple TPs and is simultaneously transmitted from multiple TPs to a single UE or multiple UEs in a time-frequency resource. Additional information such as inter-TP amplitude information, which is a new specification aspect, may be needed. Similar to coordinated scheduling/beamforming, enhancements or modifications to the existing CSI reporting procedures are not precluded [161].

Additionally, hybrid joint processing and coordinated scheduling/beamforming may be possible, where data for a UE may be available only in a subset of TPs in the CoMP cooperating set for a time-frequency resource, but user scheduling/beamforming decisions are made with coordination among TPs corresponding to the CoMP cooperating set [161].

2.6.4 Hybrid Beamforming

There are several possible antenna array architectures for hybrid beamforming that can be used in both CoMP and non-CoMP systems. Based on the mapping from RF chains to antenna elements, which determines the number of phase shifters needed, the hybrid precoding transceiver architectures can be categorized into the fully-connected and partially-connected architectures [117, 148], as illustrated in Fig. 2.9. The former architecture enjoys full beamforming gain for each RF chain with a natural combination between RF chains and antenna elements, i.e., each RF chain is connected to all antennas. On the other hand, sacrificing some beamforming gain, the partially-connected structure significantly reduces the hardware implementation

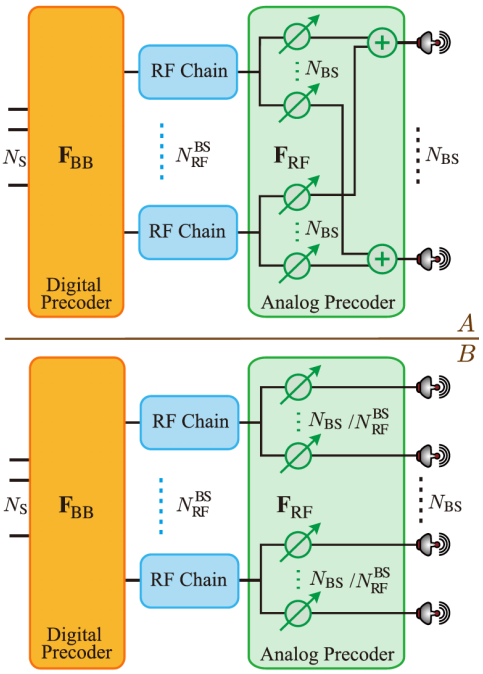

Figure 2.9: Example block diagrams of hybrid beamforming structure at BS for a downlink transmission (from [162]), where the top and bottom figures illustrate the fully-connected and partially-connected architectures, respectively.

complexity by connecting each RF chain only with part of the antennas [148].

2.6.5 Hybrid Beamforming for mmWave SU-MIMO Systems

By exploiting the spatial structure of mmWave channels, Ayach *et al.* proposed a hybrid precoding and combining approach by formulating the precoding/combining problem as a sparse reconstruction problem [117] due to the small number of spatial lobes in mmWave channels. According to the point that maximizing the spectral efficiency of mmWave systems can be approximated by minimizing the Euclidean distance between hybrid precoders and the fully digital precoder, standard basis pursuit (whose performance can be improved by using continuous basis pursuit [55],

as detailed in Chapter 7) based algorithms were proposed to approximate optimal unconstrained precoders and combiners such that they could be implemented in low-cost RF hardware. The authors in [117] focused on a fully-connected hybrid beamforming architecture, where each RF chain was connected to every antenna element in the transmit or receive array, and had a set of dedicated phase shifters. Since the RF precoding/combining matrix is implemented using analog phase shifters, all elements in the matrix have equal norm. Antenna array response vectors were utilized as the columns in the RF precoding/combining matrices, since the array response vectors form a finite spanning set for the channels row space, and they also satisfy the equal norm requirement on each element in the RF precoding/combining matrix. Iterative algorithms were therefore devised based on the above observations and the digital precoding/combining matrix was obtained via the least squares method subject to a transmit power constraint (for the digital precoding matrix). Numerical results show that the proposed spatially sparse processing can approach the spectral efficiency achieved by fully digital precoding and combining.

Hybrid precoding for the partially-connected antenna array structure has been considered in [151, 163], in which the complex capacity optimization problem is decomposed into a series of sub-problems that are easier to deal with by considering each antenna sub-array one by one. The successive interference cancellation (SIC) method is adopted to optimize the achievable capacity of each sub-array, which is implemented in an iterative manner favorable for parallelization. It is shown that the computational complexity is comparable with conventional analog precoding scheme, and that the proposed algorithm can provide near-optimal capacity performance especially when the number of antenna elements in each sub-array is small

(e.g.,4) [151, 163]. The proposed hybrid precoding scheme in [151, 163] is based on the based on the assumption that the digital precoding matrix is diagonal, which means that the digital precoder only allocates power to different data streams, and the number of RF chains should be equal to that of the data streams.

The authors of [148] proposed hybrid beamforming algorithms for both fully-connected and partially-connected antenna array architectures, based on the alternating minimization concept. The hybrid precoder design is treated as a matrix factorization problem. for the fully-connected antenna array structure, an alternating minimization (AltMin) algorithm based on manifold optimization is proposed to approach the performance of the fully digital precoder. To reduce the complexity of the aforementioned algorithm, another approach is proposed by enforcing an orthogonal constraint on the digital precoder. Moreover, for the partially-connected antenna array structure, an AltMin algorithm is also developed with the help of semidefinite relaxation. For practical implementation, the proposed AltMin algorithms are further extended to the broadband setting with OFDM modulation [148]. Simulation results demonstrate that the hybrid precoders with the fully-connected architecture can approach the performance of the fully digital precoder when the number of RF chains is slightly larger than the number of data streams, and that the hybrid precoders for the partially-connected structure provide considerable gains over analog beamforming, and it is recommendable to utilize a relatively large number of RF chains, in order to enhance both spectral and energy efficiency [148].

A near-optimal closed-form solution for fully-connected and partially-connected OFDM-based hybrid precoding is developed in [164] for frequency-selective wideband mmWave MIMO systems. Fully digital receivers are assumed. The developed solution yields the same spectral efficiency as the unconstrained fully-digital method

when the number of channel paths is smaller than the number of RF chains. Furthermore, a criterion is proposed for constructing the optimal sub-arrays that maximize a proxy of the system spectral efficiency, namely, the best partitioning/grouping of the antenna elements over the RF chains [164]. Based on the above criterion, the authors proposed a dynamic structure and a greedy algorithm which adapt the sub-array architecture per the long-term channel statistics. Simulation results show that the designed hybrid precoding method approximates the spectral efficiencies of the fully-digital scheme for both fully-connected and fixed sub-array structures. In addition, the dynamic sub-array approach is shown to be superior to any fix sub-array architecture [164].

In [165], a hybrid architecture was proposed for multi-stream for large-scale SU-MIMO beamforming systems operating at mmWave bands, where Hadamard RF codebook with low-bit (e.g., 1-bit or 2-bit) resolution phase shifters were employed, in contrast to conventional RF codebook designs available in the literature that require over 7-bit resolution to obtain identical performance with the proposed approach. Simulation results reveal that the spectral efficiency performance of the proposed hybrid structure with low-resolution phase shifters approaches the unconstrained singular-value-decomposition (SVD)-based precoding method [165].

A low-complexity frequency selective hybrid precoding scheme was presented in [87] based on GramSchmidt orthogonalization for a SU-MIMO wideband mmWave system with a limited feedback channel between the transmitter and receiver. As a first step, the RF precoders were taken from a quantized codebook, then the optimal hybrid precoder design was derived which maximizes the achievable mutual information under total power and unitary power constraints. Second, a limited feedback frequency selective hybrid precoding system was explored where both

the baseband and RF precoders are taken from quantized codebooks, for which efficient hybrid analog and digital precoding codebooks were developed. At last, a greedy hybrid precoding algorithm based on Gram-Schmidt orthogonalization for limited feedback frequency selective mmWave systems was proposed, which was shown to achieve a similar performance with a low complexity compared with the optimal hybrid precoding design that requires an exhaustive search over the RF and baseband codebooks. For future work, it would be interesting to investigate efficient hybrid precoding codebooks for wideband multi-user millimeter wave systems [87].

2.6.6 Hybrid Beamforming for mmWave MU-MIMO Systems

In [166], a joint spatial division and multiplexing (JSDM) algorithm [167] was utilized for mmWave MU-MIMO channels operating in the FDD mode. Realistic propagation channels were considered where there exists partial overlap of the angular spectra from different users caused by the presence of common scatterers. The problem of user grouping was formulated for two distinct objectives: (i) maximizing spatial multiplexing, and (ii) maximizing total received power in a graph-theoretic framework. Given the computational complexity of the problems, sub-optimum greedy algorithms were proposed as efficient solutions [166]. It is worth noting that JSDM necessitates hybrid beamforming at the base station, where pre-beamforming may be implemented in the analog RF domain, while the MU-MIMO precoding stage is implemented by baseband processing [166, 167]. Pre-beamforming can null the common multipath components so as to create linearly independent user groups, which can be served simultaneously on the same transmission source. Baseband digital precoding can allocate the user groups on

orthogonal transmission resources. Two algorithms were proposed for user grouping and pre-beamforming, where the first algorithm selects users filling many angular directions and serves fewer users with higher beamforming gain, while the second algorithm maximizes the number of users with at least one mutually non-overlapping set of directions hence tending to serve more users with lower beamforming gain [166]. Various numerical results using the realistic 28 GHz measurement data [2, 54, 168] demonstrate that JSDM with proper user selection is a promising strategy for downlink mmWave MU-MIMO channels, especially considering the fact that the JSDM approach achieves remarkable spatial multiplexing while requiring only the knowledge of the channels second-order statistics (covariance), such that feedback of instantaneous CSI at the transmitter is not required [166].

Alkhateeb *et al.* [122] developed a low-complexity hybrid precoding for downlink MU-MIMO mmWave systems, leveraging the sparse nature of the channel and the large number of deployed antennas. In particular, hybrid precoders at the transmitter and analog combiners at multiple receivers which induce a small training and feedback overhead are considered in [122], where the base station communicates with each mobile station through only one stream, and the number of base station RF chains is no smaller than the number of mobile stations. The hybrid precoding and analog combining scheme consists of two stages: (i) the base station and each user design the RF beamforming and combining vectors to maximize the desired signal power for the user with the other users interference neglected; (ii) the base station designs its zero-forcing digital precoder based on the quantized channels. The proposed algorithm was analyzed in two special cases: when the channels are single-path, and when the number of transmit and receive antennas are very large, which are relevant for mmWave systems. Simulation results show that the hybrid

precoding gain is not very sensitive to RF angles quantization, but it is vital to have a good quantization for the digital precoding layer to maintain a reasonable precoding gain over analog only approaches.

The authors in [169] proposed a novel hybrid precoding structure for multi-user OFDM mmWave systems, where two groups of phase shifters were combined to map the signals from RF chains to antennas and an effective AltMin hybrid precoding algorithm was devised. A major algorithmic innovation in [169] is a LASSO formulation for the analog precoder, which yields computationally efficient algorithms. It was revealed that implementing twice the number of phase shifters in the analog precoder is advantageous from the respects of both performance and complexity, and that inter-user interference is a major problem to tackle with besides the fully digital precoder approximation. Therefore, it is beneficial to cascade a digital baseband precoder that specializes in canceling the inter-user interference [169].

ZF-based hybrid beamforming methods for MU-MIMO mmWave systems were analyzed in [170], where the base station equipped with a large antenna array communicated with several single-antenna users. At the base station, the columns of the RF beamforming matrix was chosen from the antenna array response vectors, which was similar to the approach in [117], and the baseband digital precoding matrix was obtained via the zero-forcing scheme. Furthermore, to mitigate the noise enhancement effect induced by the zero-forcing technique, another type of baseband digital precoding matrix was calculated through the RZF approach. In addition, the authors of [170] also proposed a limited feedback protocol for mmWave channels and a robust RZF-based hybrid beamforming scheme for the MU-MIMO system. The limitation of the method proposed in [170] is that no beamforming/combining

processing can be performed at the receiver side and only one data stream per user can be transmitted since only a single antenna is available therein.

In [171], a coordinated hybrid beamforming approach that supports multi-stream transmission for each user was proposed for downlink MU massive MIMO mmWave systems. First, an RF beamforming technique based on the Generalized Low Rank Approximation of Matrices (GLRAM) approach was proposed, then an efficient modified GLRAM algorithm was developed. The proposed scheme only requires the information of the composite channel, instead of the complete physical channel matrix which is assumed to be known in the existing literature. It makes use of the coordination between the base station and users to achieve a maximal array gain and has no dimensionality constraint. The multiplexing gain is then exploited by applying the BD technique. Simulation results show that the proposed scheme approaches the fully digital BD solution [171].

Kwon *et al.* proposed a joint scheduling and hybrid beamforming downlink system with partial side information for mmWave broadcast channels [172]. The achievable sum rate upper bound and the scaling law of the asymptotic sum rate were derived, where the sum rate upper bound demonstrates the trade-off between the multiplexing gain and the MU diversity gain dependent on the number of RF chains. The base station is equipped with several RF chains and schedules a subset of users and corresponding beams for each transmission according to the signal-to-interference-plus-noise ratio (SINR) feedback. It is worth noting that the proposed hybrid system is even superior to the digital zero-forcing beamforming system in the low SNR realm typical in mmWave channels, since the proposed approach utilizes the degrees of freedom of the transmit antenna elements only for SNR gain but not for interference cancellation in sparse mmWave channels [172].

It has been demonstrated in [173] that the hybrid beamforming structure can realize any fully digital beamformer exactly regardless of the number of antenna elements, on the condition that the number of RF chains is twice the total number of data streams. For cases where fewer number of RF chains are available, the authors investigated the hybrid beamforming design problem for both the transmission scenario of a point-to-point MIMO system and a downlink multi-user multiple-input single-output (MU-MISO) system where the base station has a large-scale antenna array but each user is equipped with only one antenna. For each scenario, a heuristic hybrid beamforming design was proposed that achieves a performance close to the performance of the fully digital beamforming baseline. Finally, the proposed algorithms are modified for the more practical setting in which only finite resolution phase shifters are available. Numerical simulations show that hybrid beamforming can achieve spectral efficiency close to that of the fully digital solution with the number of RF chains approximately equal to the number of data streams, and that the proposed schemes are effective even using phase shifters with very low resolution. One key assumption in [173] is the availability of prefect CSI at the base station, which rarely occurs practically. For imperfect CSI scenario, one approach to the design of the hybrid beamformers is to first design the RF beamformers assuming perfect CSI, and then to design the digital beamformers employing robust beamforming schemes to deal with imperfect CSI [173, 174].

In [175], an adaptive single-cell MU-MIMO hybrid precoding algorithm was proposed, which iteratively designs the precoders/combiners leveraging the reciprocity of TDD mmWave systems. The combiners were designed based on the MMSE criterion and dependent on second-order statistics of the channel. Compressed measurements taking advantage of the sparsity of mmWave channels were

utilized to estimate the covariance of the received signal at the antenna array in an online manner, mitigating the training overhead and complexity. The proposed scheme avoids the explicit estimation of the channel matrix corresponding to each user, which is hard to acquire caused by the dimensionality reduction owning to the hybrid beamforming structure and the short coherence time of the mmWave channel [175]. Simulation results show that the proposed method can approach the sum spectral efficiencies of that achieved by block diagonalization One disadvantage of the proposed algorithm in [175] is that the convergence is not theoretically guaranteed.

The authors of [95] investigated optimal designs of hybrid beamforming architectures, with a focus on an N (the number of transceivers) by M (the number of active antennas per transceiver) hybrid beamforming structure. Moreover, they also studied the energy efficiency and spectrum efficiency of the $N \times M$ beamforming architecture, including their relationship at the green point (i.e., the point with the highest energy efficiency) on the energy efficiency-spectrum efficiency curve, the impact of the number of transceivers N on the energy efficiency performance for a given spectrum efficiency, and the effect of N on the green point energy efficiency. In addition, a reference signal design for the hybrid beamforming architecture is presented, which achieves better channel estimation performance than the method purely based on analog beamforming. The main feature of the design based on hybrid beamforming in [95] is the same analog beamforming on each transceiver, on top of which digital beamforming is designed to maximize the gain in a certain direction around the main beam direction of the analog beamforming.

Lin *et al.* presented low-complexity energy-efficient hybrid precoding and low-resolution ADCs for downlink MU-MIMO mmWave systems [176], and proposed

a transmission strategy comprising beamspace MIMO communications and beam selection. In the hybrid precoding structure, analog beamforming was based upon Butler matrix that multiplexes data onto orthogonal spatial beams, while digital precoding was designed using MMSE to cancel inter-user interference. Then a beam selection algorithm was created to determine a subset of beams to optimize system energy efficiency based on the limited feedback information from users. Low-resolution ADCs were employed at the user side. Power consumption per transmission data bit was minimized by adaptively selecting the best RF chain configuration [176]. Simulation results show that the proposed beam selection strategy outperforms the conventional approach based upon received signal strength, and that one-bit ADCs result in moderate degradation in the BER performance and severe degradation in the sum rate when utilizing the quadrature phase-shift keying (QPSK) signaling [176].

2.7 Beamforming in Multi-Cell MIMO Systems

For multi-cell wireless systems, a crucial aspect is to combat inter-cell interference (ICI), especially for dense networks which are envisioned attractive for mmWave frequency bands. Multi-cell cooperation is an efficient technique to mitigate ICI [177]. In the most aggressive form of multi-cell cooperation, the CSI and the data of users are fully shared among base stations via high-speed backhaul links. These base stations then act as a single distributed multi-antenna transmitter that serves multiple users through beamforming, commonly referred to as cooperative beamforming or network MIMO. Although network MIMO can completely eliminate the ICI within the base stations coverage area and even exploit the ICI link, it

requires substantial signaling overhead, synchronization, and backhaul capacity for CSI and data sharing and joint transmission [178]. In practice, however, backhaul will be bandwidth-limited due to the prohibitive costs involved in establishing high-capacity links. This restricts the amount of information that can be exchanged among base stations, which in turn determines the level of cooperation and the performance gains obtained.

In a less complex form of multi-cell cooperation, commonly referred to as *coordinated beamforming* in 3GPP LTE Advanced, only the CSI of users, but not user data, is shared among the base stations to enable joint beamforming design, whereas the data of each user is transmitted by a single BS. Without the need for data sharing, coordinated beamforming has considerably reduced signaling requirements compared to network MIMO. Fig. 2.10 illustrates an example scenario of multi-cell MU-MIMO systems, where there are three adjacent cells each with one base station and three users. Also depicted in the figure is an example of how both intended signal and interference arrive at a user, where the green solid line denotes the intended signal, and the red dash lines represent the inter-cell interference caused by base stations in adjacent cells. Coordinated beamforming algorithms can be implemented to null or mitigate the inter-cell interference.

In [179], distributed MU-MIMO was considered where several access points are connected to a central server and operate as a large distributed multi-antenna access point. This ensures that all transmitted signal power serves the purpose of data transmission, rather than creating interference. The authors proposed a strategy called AirSync which offers timing and phase synchronization to enable distributed MU-MIMO, and implemented AirSync as a digital circuit in the field programmable gate array (FPGA) of the Wireless Open-Access Research Platform

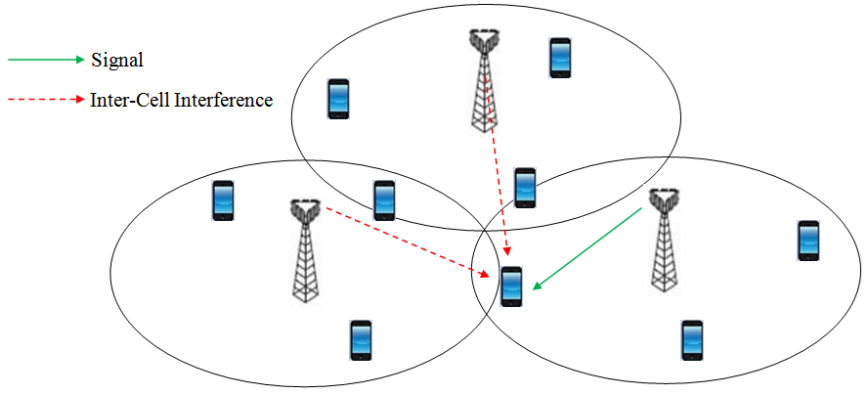

Figure 2.10: An example scenario of multi-cell MU-MIMO systems, where there are three adjacent cells each with one base station and three users. Also illustrated in the figure is an example of how both intended signal and interference arrive at a user, where the green solid line denotes the intended signal, and the red dash lines represent the inter-cell interference caused by base stations in adjacent cells.

(WARP) radio platform [179]. It was demonstrated that AirSync was able to realize the full distributed MU-MIMO multiplexing gain.

Michaloliakos *et al.* investigated joint user-beam selection for hybrid beamforming in asynchronously coordinated multi-cell networks [180], which is similar to user selection schemes in the context of MU-MIMO and aims to maximize a utility function of the users' rates. Two additional novel algorithms for establishing formal performance bounds were proposed. The first algorithm was a greedy solution of an associated maximum weight independent set problem with cardinality constraints, while the second was a greedy solution of an associated maximum cardinality problem over a set of feasible links. Numerical results revealed that the hybrid beamforming architecture coupled with the proposed user-beam selection algorithms achieved users rates which are up to 10 times higher than those achieved by current uncoordinated deployments [180].

An adaptive multi-cell 3D beamforming strategy was demonstrated in [178], where the setting is a cellular network with multiple multi-antenna base stations

and single-antenna users, imperfect CSI, and directional antennas each with a vertically adjustable beam. The effect of the elevation angle of the base station antenna pattern on the performance of the considered network was explored, when employing either a conventional single-cell transmission or a fully cooperative multi-cell transmission [178]. The major innovation is to divide the coverage area into two disjoint vertical regions and adapt the multi-cell cooperation approach at the base stations when serving each region. A fair scheduler is used to share the time slots between the vertical regions. Simulation results show that the proposed technique can achieve performance comparable with that of a fully cooperative transmission but with significantly lower complexity and signaling requirements [178].

In [181], a SLNR-based cascaded precoding algorithm was proposed to suppress interference in downlink CoMP transmission system. In a CoMP system, cells are divided into some cooperation clusters, and base stations in the same cluster can serve the original cell edge UEs cooperatively to enhance the cell edge spectral efficiency and system throughput. It is worth noting that co-channel interference denotes the interference at a desired user that is caused by all other users, while leakage refers to the interference caused by the signal intended for a desired user on the remaining users [157], namely, leakage measures how much signal power leaks into the other users. The proposed precoding scheme possesses two stages and deals with the inter-cell and inner-cell interference step by step. In the first stage, interferences from different cells are aligned to the orthogonal space of receiving matrix of the expected cell to mitigate interference to the expected cell. In the second stage, SLNR precoding is employed to suppress the interferences among users within the same cell [181]. Numerical results show that the proposed strategy can improve the system capacity while reducing the BER.

Chapter 3

Synthesizing Omnidirectional Received Power and Path Loss from Directional Measurements

3.1 Introduction

At mmWave frequencies, the increase in free space path loss resulting from the order of magnitude increase in carrier frequency is conveniently overcome by using high-gain directional antennas at the base station and/or mobile handset [182], providing sufficient gain to complete mmWave links over 200 m or so, as shown in [2] and [183]. MmWave propagation measurements are vital for accurately characterizing channels and creating statistical channel models, necessary for proper design of wireless radio-systems and realistic protocols. While electrically-steerable adaptive antennas will be used in 5G mmWave transceivers [2, 23, 40, 184, 185], technologies with such antennas are not yet commercially available at most mmWave

frequencies. In the mean-time, many researchers are using mechanically rotatable horn antennas to capture channel characteristics at a wide range of mmWave frequencies [2, 183, 186, 187]. NYU WIRELESS measurements used rotatable horns, and a method was needed to take the directional measurements in order to synthesize omnidirectional models for use in comparing results in various standard bodies, which historically have only used omnidirectional models since omnidirectional antennas were used at both TX and RX in the conventional UHF/microwave bands in 4G and prior systems.

To generate omnidirectional path loss models where arbitrary antenna patterns can be implemented for specific applications, a valid procedure is required to recover omnidirectional path loss models from directional measurements, where the TX and RX antennas are typically rotated over many azimuth and elevation angle combinations to emulate omnidirectional antennas. Omnidirectional path loss models at 28 GHz and 73 GHz were extracted from directional measurements [188] by summing up the received powers (in milli-Watts (mW)) at each and every measured non-overlapping TX and RX antenna pointing angle combination. The omnidirectional path loss was calculated by subtracting the summed received power from the transmit power, with the TX and RX antenna gains removed [49, 168]:

$$\mathrm{PL}_{i,j}[\mathrm{dB}] = P_{\mathrm{t}_{i,j}}[\mathrm{dBm}] - 10\log_{10}(\sum_{n}\sum_{m}\sum_{l}\sum_{k} P_{\mathrm{r}_{i,j}}(\phi_k, \theta_l, \varphi_m, \vartheta_n)[\mathrm{mW}]) \quad (3.1)$$

where $\mathrm{PL}_{i,j}$, $P_{\mathrm{t}_{i,j}}$, $P_{\mathrm{r}_{i,j}}$ denote the omnidirectional path loss, omnidirectional transmit power, and received power for an AoD and AoA combination (with the antenna gains removed) from the i^{th} TX to the j^{th} RX, respectively. $\phi, \theta, \varphi, \vartheta$ are the azimuth AoA, elevation AoA, azimuth AoD, and elevation AoD, respectively. This

chapter validates the method used in [188] for recovering omnidirectional received power and path loss.

3.2 Measurement Procedure

In the summers of 2012 and 2013, two outdoor propagation measurement campaigns were conducted at 28 GHz and 73 GHz, respectively, in downtown Manhattan, New York, using similar 400 Megachips-per-second (Mcps) spread spectrum sliding correlator channel sounders and directional steerable horn antennas at both the TX and RX to investigate mmWave channel characteristics in a dense UMi environment [2, 183, 189]. In the 28 GHz measurements, three TX locations and 27 RX locations were selected to conduct the measurements. Two types of horn antennas were employed: a 24.5 dBi-gain narrowbeam horn antenna with 10.9° and 8.6° half-power beamwidths (HPBWs) in the azimuth and elevation planes, respectively, and a 15 dBi-gain widebeam horn antenna with 28.8° and 30° HPBWs in the azimuth and elevation planes, respectively. The narrowbeam antenna was always utilized at the TX locations, and five of the RX locations used both the narrowbeam and widebeam antennas, including two LOS and three NLOS locations. For each TX-RX location combination (except the two LOS RX locations), the RX antenna was swept over the entire azimuth plane sequentially in increments of one HPBW at elevation angles of 0° and ±20° about the horizon, so as to measure contiguous angular snapshots of the channel impulse response over the entire 360° azimuth plane, while the TX antenna remained at a fixed azimuth and elevation angle.

In the 73 GHz measurements, there were five TX locations and 27 RX locations

with antenna heights of 2 m (mobile scenario) and 4.06 m (backhaul scenario), yielding a total of 36 TX-RX location combinations for the mobile (access) scenario and 38 combinations for the backhaul scenario. A pair of 27 dBi-gain rotatable directional horn antennas with a HPBW of 7° in both azimuth and elevation planes was employed at the TX and RX. For each TX-RX location combination, TX and RX antenna azimuth sweeps were performed in steps of 8° or 10° at various elevation angles. Additional measurement procedures and hardware specifications can be found in [2, 183, 189].

3.3 Power Synthesizing Theory

The method for synthesizing omnidirectional received power introduced in Section I is now theoretically validated step-by-step. First, assuming omnidirectional antennas are used at both the TX and RX, if N MPCs arrive at the RX, then the received signal $r(t)$ can be expressed as [67]:

$$r(t) = \sum_{n=1}^{N} a_n e^{j\Phi_n} \delta(t - \tau_n) \tag{3.2}$$

where a_n, Φ_n, and τ_n are the amplitude, phase, and propagation time delay of the n^{th} MPC, respectively. The received power is:

$$P_{tot} = \int_0^{\tau_{max}} |r(t)|^2 dt = \int_0^{\tau_{max}} \sum_{i=1}^{N} \sum_{k=1}^{N} a_i a_k e^{j(\Phi_i - \Phi_k)} \delta(t - \tau_i)\delta(t - \tau_k) dt \tag{3.3}$$

The time delay τ differs for each MPC, hence the double sum in (3.3) is zero for

$k \neq i$. Thus, the received power can be simplified to:

$$P_{tot} = \int_0^{\tau_{max}} \left\{ \sum_{i=1}^{N} {a_i}^2 \delta^2(t - \tau_i) \right\} dt = \sum_{i=1}^{N} {a_i}^2 \tag{3.4}$$

Next, suppose directional antennas are used at the same TX and RX locations with antenna gains G_T and G_R in linear units, respectively. For one AoD and AoA combination, a subset of MPCs shown in (3.2) will arrive at the RX. Assuming M MPCs reach the RX for an AoD and AoA combination, where the value of M is dependent on the AoD and AoA combination, then the received signal (r_D) for the specific AoD and AoA combination is:

$$r_D(t) = G_T \sum_{m=1}^{M} G_R \cdot a_m e^{j\Phi_m} \delta(t - \tau_m) \tag{3.5}$$

Note that each MPC in (3.5) corresponds to an MPC in (3.2). Using the same approach derived in (3.4) from (3.2), the received power for an AoD and AoA combination is:

$$P_D = G_T G_R \sum_{l=1}^{M} {a_l}^2 \tag{3.6}$$

By performing an exhausive antenna sweep over all possible AoD and AoA combinations without spatial overlap, i.e., individual measurements are separated by one HPBW in both the azimuth and elevation planes, the sum of received power over all unique AoD and AoA combinations yields:

$$\sum P_D = G_T G_R \sum_{l=1}^{N} {a_l}^2 \tag{3.7}$$

which is equivalent to the omnidirectional received power in (3.4) after removing

the antenna gains. Therefore, the sum of received powers from non-overlapping angles in the azimuth and elevation planes from directional antenna measurements results in the omnidirectional received power, after removing antenna gains.

The method for synthesizing omnidirectional received power can also be validated by considering antenna radiation patterns. The far-field radiation pattern of a horn antenna can be approximated by [190]:

$$f(\phi,\theta) = G\left[\text{sinc}^2\left(\text{a}\cdot\sin(\phi)\right)\cos^2(\phi)\right]\cdot\left[\text{sinc}^2\left(\text{b}\cdot\sin(\theta)\right)\cos^2(\theta)\right] \tag{3.8}$$

where ϕ and θ represent the azimuth and elevation angles with respect to (w.r.t.) the antenna boresight, respectively, $f(\phi,\theta)$ denotes the radiation power density at the azimuth angle ϕ and elevation angle θ, G represents the boresight gain of the antenna, and a and b are functions of the azimuth (AZ) and elevation (EL) HPBWs of the horn antenna, respectively, i.e.,

$$\text{sinc}^2\left(\text{a}\cdot\sin(\frac{\text{HPBW}_{\text{AZ}}}{2})\right)\cos^2\left(\frac{\text{HPBW}_{\text{AZ}}}{2}\right) = \frac{1}{2} \tag{3.9}$$

$$\text{sinc}^2\left(\text{b}\cdot\sin(\frac{\text{HPBW}_{\text{EL}}}{2})\right)\cos^2\left(\frac{\text{HPBW}_{\text{EL}}}{2}\right) = \frac{1}{2} \tag{3.10}$$

For instance, if the azimuth HPBW of a horn antenna is 10° (i.e., 0.17 radians), then $a = 5.06$. Fig. 3.1 displays the normalized antenna azimuth radiation pattern for a horn antenna with an azimuth HPBW of 10° at an elevation angle of 0° and at azimuth angles of 0°, 10°, and -10° w.r.t. the boresight angle, and the normalized equivalent widebeam antenna pattern by overlapping the narrowbeam antenna patterns at the three adjacent azimuth angles. It is clear from Fig. 3.1 that the HPBW in the equivalent antenna pattern is 30°, i.e., three times the 10° HPBW.

Further, the maximum gain in the normalized equivalent pattern is about 0 dB and remains constant over the range of -10° to 10°, indicating that if aggregating the radiation patterns at antenna pointing angles over the entire azimuth plane, i.e., from 0° to 360°, the resultant antenna gain will become constant and equal to the boresight gain of the directional horn antenna over the entire azimuth plane, with the same outcome true for the elevation plane. The normalized three-dimensional (3D) patterns of a single antenna and the aggregated nine antennas are illustrated in Fig. 3.2, where the antenna is assumed to have an azimuth HPBW of 10° and an elevation HPBW of 8°, with the normalized equivalent pattern obtained by overlapping the patterns at all the angle combinations of 0°, 10°, and -10° in the azimuth plane and 0°, 8°, and -8° in the elevation plane. It is evident that in the single antenna pattern, the maximum gain is concentrated only on the boresight angle, while in the synthesized pattern the maximum gain remains almost constant over the entire 20°×16° angular region. Although the antenna patterns in the simulations are canonical, they are nearly identical to the actual measured patterns of the antennas used during the measurements. Therefore, the synthesized directional antenna pattern over the entire 4π steradian sphere after removing the antenna gain will approximate the pattern of an omnidirectional antenna, indicating that it is appropriate to acquire the omnidirectional received power by summing up the powers from directional antennas in all possible non-overlapping directions, with antenna gains removed.

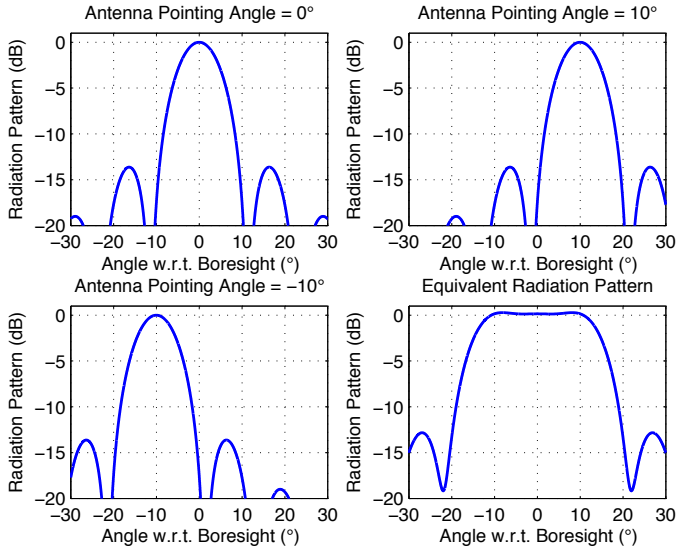

Figure 3.1: Normalized antenna pattern in the azimuth plane for a horn antenna with an azimuth HPBW of 10° at azimuth pointing angles of 0°, 10°, and -10° with respect to the boresight angle, and the normalized equivalent radiation pattern by overlapping the patterns at these three adjacent angles [49].

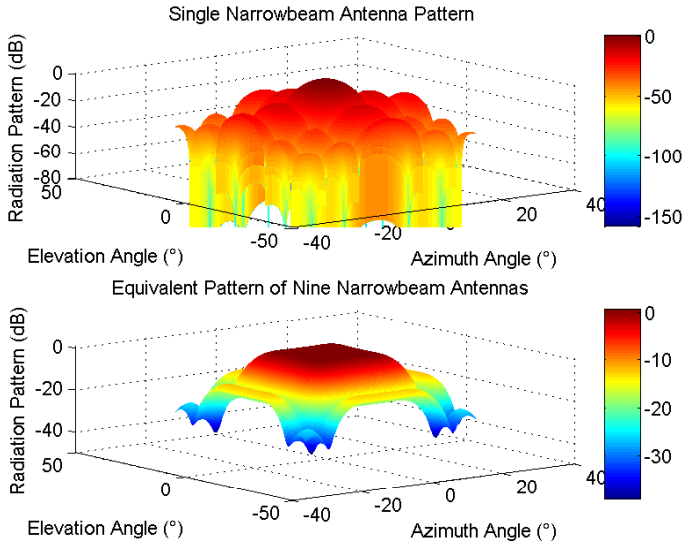

Figure 3.2: Normalized antenna pattern in both the azimuth and elevation planes for a horn antenna with an azimuth HPBW of 10° and an elevation HPBW of 8°, pointing at the boresight angle, and the normalized equivalent pattern by overlapping the patterns at all the angle combinations of 0°, 10°, and -10° in the azimuth plane and 0°, 8°, and -8° in the elevation plane [49].

3.4 Power Synthesizing Procedure and Empirical Results

3.4.1 28 GHz Measurement Data

This subsection is aimed to validate the method for synthesizing the omnidirectional received power by comparing the measured power obtained from two different directional horn antennas using the 28 GHz measurements [2] and showing that *the corresponding synthesized omnidirectional powers are independent of antenna beamwidth*. A pointing angle measured with a 30° HPBW widebeam antenna was selected, and then discretized the measured angle into nine smaller 10° angles. The power measured with the widebeam antenna is then compared to the sum of the powers obtained at the nine smaller angles using the narrowbeam antenna. Note that the 28 GHz measurements considered fixed elevation angles of 0°, and ±20°, as opposed to ±10°. The unavailable ±10° elevation angles is therefore substituted with the available ±20° elevation angles.

Three NLOS RX locations, i.e., RX 14, RX 16, and RX 19 from measurements in New York City [2] were selected to compare the received powers obtained from widebeam and narrowbeam antennas. The measured data sets were chosen such that the TX antennas were pointed in the same azimuth and elevation pointing directions for both narrowbeam and widebeam antenna azimuth sweeps. The RX elevation angle for the azimuth sweep using the widebeam antenna was 0°, and the elevations for the narrowbeam antenna sweeps were 0°, -20°, and 20°. Ideally, adjacent azimuth planes should be separated by one elevation HPBW, but due to lack of measured data in the ±10° elevation angles, the ±20° elevation angles were

examined instead. Table I details the parameters of the selected measurements, where the azimuth angles are w.r.t. the true north bearing direction, and the elevation angles are w.r.t. the horizon where positive angles denote angles above the horizon.

For fair comparison, 9.5 dB was added to the received power found using the widebeam antenna as shown in Table 3.1, which is the difference in the boresight gain of the narrowbeam and widebeam antennas, to compensate for the smaller antenna gain of the widebeam antenna, so that the only difference between the two types of antennas is the antenna beamwidth. Note that three consecutive 10.9° HPBW antennas are equivalent to a single $10.9° \times 3 = 32.7°$ HPBW antenna in the azimuth plane, but since a 32.7° azimuth HPBW antenna was not available, an antenna with 28.8° (close to 32.7°) HPBW in the azimuth plane was used. Also, the elevation angle increment is not perfectly one HPBW as explained before. Therefore, a slight difference would be expected in the powers using nine aggregated narrowbeam antennas as compared to a single widebeam antenna. By using Eq. (3.8) and integrating over the corresponding HPBWs, it is expected that the received power using a single widebeam (28.8°/30° azimuth/elevation HPBW) antenna would be around 3.8 times (i.e., 5.8 dB greater than) that of a single narrowbeam (10.9°/8.6° azimuth/elevation HPBW) antenna given the same boresight gain.

As shown in Table 3.1, the effective received power by summing up the received powers from nine narrowbeam antennas agrees well with the power obtained by one widebeam antenna. For example, when the widebeam antenna is pointed at an azimuth angle of 242° at RX 19, the effective received power using the widebeam antenna was -68.7 dBm, while the effective synthesized received power from the three narrowbeam angles was -67.0 dBm, only 1.7 dB higher. Furthermore, the

effective received powers over the entire azimuth plane(s) using the widebeam and narrowbeam antennas match relatively well at each of the three RX locations, with a maximum difference of 2.9 dB.

Fig. 3.3 is a scatter plot of the 28 GHz effective directional path loss using the widebeam and narrowbeam antennas at the three RX locations, using the 1 m close-in free space reference distance path loss model [188]. The discrete widebeam path loss is obtained using a single widebeam antenna, and the discrete narrowbeam path loss is synthesized from nine narrowbeam antennas. The "all" widebeam path loss corresponds to the effective path loss over the entire azimuth plane at a 0° elevation angle, while the "all" narrowbeam path loss is synthesized from three azimuth planes at elevation angles of 0° and ±20°. The plot clearly shows that the path loss exponents (PLEs) are both 3.9 for the discrete angle case, and 3.7 for the entire azimuth plane(s) using widebeam and narrowbeam antennas, i.e., the PLEs corresponding to different antenna beamwidths in each comparison pair agree very well with each other.

3.4.2 73 GHz Measurement Data

In the 28 GHz measurements, the measured elevation angles were fixed to 0° and ±20° about the horizon, and the ±10° elevation angles were not considered. In the measurements at 73 GHz [183], however, power delay profiles (PDPs) were acquired at elevation angles separated by 5° or 8° (close to the 7° HPBW). Therefore, some insight can be gained in the distribution of received power over elevation angles separated by about one HPBW using the 73 GHz measurement data.

Table 3.2 lists the percentage of the received power corresponding to the strongest azimuth plane, as compared to that corresponding to the strongest azimuth plane

Table 3.1: Measurement parameters and comparison of received power and path loss using narrowbeam and widebeam antennas at the receiver. The TX location is the Kaufman building on NYU's Manhattan campus (KAU), the AoD elevation is -10°, and the AoA elevation is 0° for the widebeam antenna, and 0° and ±20° for the narrowbeam antenna. W and N denote widebeam and narrowbeam antennas, respectively. ΔP_r is the difference in received power using widebeam and narrowbeam antennas [49].

RX ID	**T-R Separation (m)**	**AoD Azimuth (°)**	**AoA Azimuth (°)**		**Effective P_r (dBm)**		**Effective PL (dB)**		**ΔP_r (dB)**
			W	N	W	N	W	N	
RX 14	82	140	32	22, 32, 42	-55.9	-62.0	135.0	141.1	6.1
			62	52, 62, 72	-60.9	-56.1	140.0	135.2	-4.8
RX 16	97	140	92	82, 92, 102	-62.9	-65.1	142.0	144.2	2.2
RX 19	175	175	212	202, 212, 222	-63.9	-63.4	143.0	142.5	-0.5
			242	232, 242, 252	-68.7	-67.0	147.8	146.1	-1.7
RX 14	82	140	All Azimuth Angles		-54.7	-52.3	133.8	131.4	-2.4
RX 16	97	140	All Azimuth Angles		-61.3	-64.2	140.4	143.3	2.9
RX 19	175	175	All Azimuth Angles		-61.7	-61.3	140.8	140.4	-0.4

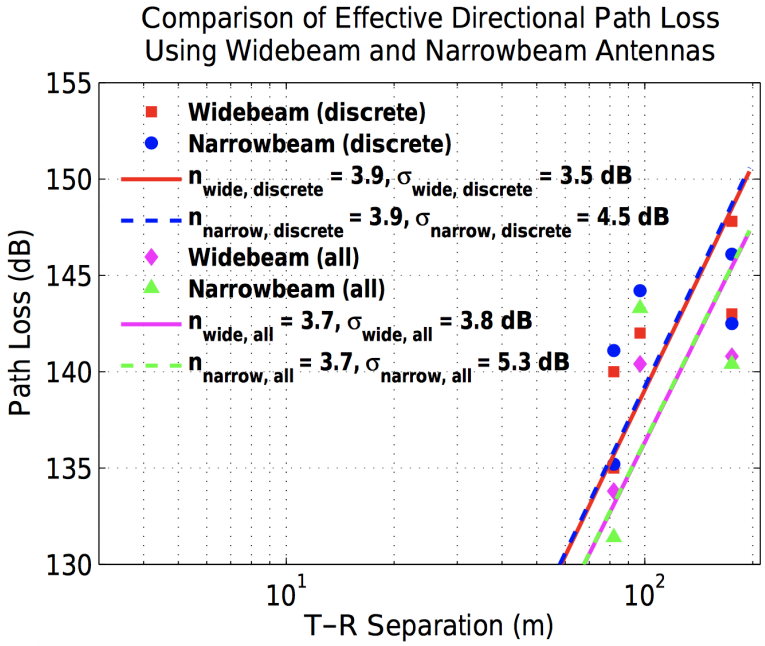

Figure 3.3: Comparison of 28 GHz NLOS effective directional path loss using the widebeam (28.8°/30° azimuth/elevation HPBW) and narrowbeam (10.9°/8.6° azimuth/elevation HPBW) antennas at three RX locations. The discrete widebeam path loss is obtained using a single widebeam antenna, and the discrete narrowbeam path loss is synthesized from nine narrowbeam antennas. The "all" path loss corresponds to the effective path loss over the entire azimuth plane(s) [49].

plus the two azimuth planes adjacent to it. The adjacent azimuth planes at the RX were separated by 5° or 8°, close to one HPBW of the antenna. It can be observed from Table 3.2 that the received power over the strongest azimuth plane accounts for the majority (over 70%) of the total received power at the strongest plus adjacent azimuth planes, with a highest ratio of 95%. Note that the adjacent azimuth planes are mostly separated by only 5° (less than one HPBW of the antenna), if the elevation angle increment increases to one HPBW, namely 7°, even higher contribution is expected from the strongest azimuth plane, i.e., the percentage of the received power over the strongest azimuth plane will be even larger. Therefore, it is sufficient to consider the power at the strongest azimuth plane alone when comparing the received powers using widebeam and narrowbeam antennas.

3.5 Concluding Remarks

This chapter presented the validation for synthesizing the omnidirectional received power and path loss from measured data using directional horn antennas by summing the received powers from each and every measured antenna pointing angle, including both theoretical analyses and measured results. It was shown that the received power using nine narrowbeam antennas agrees relatively well with that using a single widebeam antenna (where the azimuth and elevation HPBWs of the widebeam antenna are about three times those of the narrowbeam antenna), and *using directional antennas with different beamwidths yields almost identical received power and path loss synthesized over the whole azimuth plane(s).* Besides, the 73 GHz measurement data showed that when considering the total received power

Table 3.2: Ratio of the received power over the strongest azimuth plane to that corresponding to the strongest azimuth plane plus the two adjacent azimuth planes in the 73 GHz measurements in New York City [49, 183].

TX Height (m)	**RX Height (m)**	**T-R Separation (m)**	**Elevation Step (°)**	**Received Power Ratio**
7	2	128	5	72.9%
7	2	139	5	76.0%
7	2	182	5	71.9%
7	2	190	5	74.5%
7	4.06	27	5	72.0%
7	4.06	40	8	73.9%
7	4.06	74	5	72.1%
7	4.06	107	5	83.1%
7	4.06	128	5	75.3%
7	4.06	145	5	73.8%
7	4.06	182	5	73.2%
17	2	129	5	91.7%
17	2	129	5	76.7%
17	2	168	5	81.0%
17	4.06	118	5	73.9%
17	4.06	118	5	74.4%
17	4.06	127	5	91.2%
17	4.06	129	5	95.0%
17	4.06	129	5	72.8%
17	4.06	181	5	79.6%

over the strongest azimuth plane and the two adjacent azimuth planes, 72% to 95% of the received power came from the strongest azimuth plane, thus it is reasonable to consider the power at the strongest azimuth plane alone when comparing the received powers with different antenna beamwidths [49].

Chapter 4

Prediction Accuracy, Sensitivity, and Parameter Stability of Path Loss Models

This chapter investigates three large-scale path loss models that may be used over the microwave and mmWave frequency bands: the ABG model, the CI model, and the CIF model. The ABG model is shown to be a simple extension of the AB model currently used in 3GPP, where a frequency-dependent floating optimization parameter is added to the AB model. *The CI and CIF models are simpler in form (require fewer parameters) and offer better parameter stability and accuracy through the use of a physically based close-in reference distance that replaces the floating model parameters of the ABG model.* In this chapter, systematic comparisons between the parameters, shadow fading standard deviations, and prediction performance of these three models in the UMa, UMi street canyon (SC), indoor hotspot (InH) office, and InH shopping mall scenarios are provided,

using eight sets of measurement data from NYU, two sets from The University of Texas at Austin (UT Austin), eight sets from Nokia/AalborgUniversity (AAU), and 12 sets from Qualcomm [2, 50, 54].

4.1 Large-Scale Propagation Path Loss Models

The ABG, CI, and CIF path loss models are multi-frequency statistical (i.e., stochastic) models that describe large-scale propagation path loss over distance at all relevant frequencies in a certain scenario [61, 79]. It will be noted that the CI and CIF models have a very similar form compared to the existing 3GPP path loss model (i.e., the floating-intercept, or alpha-beta (AB) model) [191], where one merely needs to substitute the floating constant (which has been shown to vary substantially across different measurements, frequencies and scenarios [82, 192]) with a free-space constant that is a function of frequency based on a 1 m standard free space reference distance. As shown subsequently, this subtle change provides a frequency-dependent term while yielding greater prediction accuracy and better parameter stability when using the models outside of the range of the measured data set from which the models are developed.

Testing the efficacy of a path loss model outside of the range for which measurements are originally collected and used to solve for model parameters is a critical, but often ignored, test. Testing model accuracy and parameter stability is needed since engineers will inevitably require propagation models for new applications, distances, or scenarios not originally contemplated in the original experiments used to build the path loss model. For future 5G wireless system level and link layer analysis and simulation in new spectrum bands, where new types of directional

antennas, umbrella cells, repeater architectures, and new regulations and network topologies are used [168], it is critical to know that a chosen model can be used in new scenarios while still exhibiting parameter stability, accuracy, and usefulness beyond the limited original number of field measurements. This chapter offers such sensitivity and analysis when comparing the three candidate 5G stochastic path loss models.

The equation for the ABG model is given by [193]:

$$\begin{aligned} \mathrm{PL}^{\mathrm{ABG}}(f,d)[\mathrm{dB}] =& 10\alpha\log_{10}\left(\frac{d}{1\ m}\right) + \beta + 10\gamma\log_{10}\left(\frac{f}{1\ GHz}\right) + \chi_{\sigma}^{\mathrm{ABG}}, \\ & \text{where } d \geq\ 1 \text{ m} \end{aligned} \tag{4.1}$$

where $\mathrm{PL}^{\mathrm{ABG}}(f,d)$ denotes the path loss in dB over frequency and distance, α and γ are coefficients showing the dependence of path loss on distance and frequency, respectively, β is an optimized offset value for path loss in dB, d is the 3D TX-RX (T-R) separation distance in meters, f is the carrier frequency in GHz, and $\chi_{\sigma}^{\mathrm{ABG}}$ is a zero-mean Gaussian random variable with a standard deviation σ in dB describing large-scale signal fluctuations (i.e., shadowing) about the mean path loss over distance and frequency. Note that the ABG model has three model parameters for determining mean path loss over distance and frequency, as well as the shadowing standard deviation (a total of four parameters). When used at a single frequency, the ABG model reverts to the existing 3GPP floating-intercept/AB model with three parameters with γ set to 0 or 2 [54, 114, 194]. The ABG model parameters α, β, γ, and σ are obtained from measured data using the closed-form solutions that minimize the shadow fading (SF) standard deviation.

The equation for the CI model is given by (4.2) [67]:

$$\mathrm{PL}^{\mathrm{CI}}(f,d)[\mathrm{dB}] = \mathrm{FSPL}(f,d_0)[\mathrm{dB}] + 10n\log_{10}(d/d_0) + \chi_{\sigma}^{\mathrm{CI}}, \text{ where } d \geq d_0 \quad (4.2)$$

where f is also in GHz (for both the CI and CIF models), d_0 is the close-in free space reference distance, n denotes the PLE, and $\chi_{\sigma}^{\mathrm{CI}}$ is a zero-mean Gaussian random variable with a standard deviation σ in dB. Whereas the ABG model requires four parameters, the CI model only requires one parameter, the PLE, to determine the mean path loss with distance and frequency, and uses a total of two parameters (the PLE n and $\chi_{\sigma}^{\mathrm{CI}}$). A useful property of (4.2) is that $10n$ describes path loss in dB in terms of decades of distances beginning at d_0 (making it very easy to compute power over distance in one's mind when d_0 is set to 1 m [54, 79, 192]). In (4.2), d is the 3D T-R separation distance, and $\mathrm{FSPL}(f,d_0)$ denotes the free space path loss (FSPL) in dB at a T-R separation distance of $d_0 = 1$ m at the carrier frequency f:

$$\mathrm{FSPL}(f, 1\text{ m})[\mathrm{dB}] = 20\log_{10}\left(\frac{4\pi f \times 10^9}{c}\right) = 32.4 + 20\log_{10}\left(\frac{f}{1\text{ GHz}}\right) \quad (4.3)$$

where c is the speed of light. Note that the CI model inherently has an intrinsic frequency dependency of path loss already embedded within the FSPL term. The PLE model parameter in (4.2) is obtained by first removing the FSPL given by (4.3) from the path loss on the left side of (4.2) for all measured data points across all frequencies, and then calculating the single PLE jointly for multiple frequencies, as detailed in the Appendix and [54]. The CI model in (4.2) can be written in the

3GPP form as [193]:

$$\begin{aligned}\mathrm{PL}^{\mathrm{CI}}(f,d)[\mathrm{dB}] =& \mathrm{FSPL}(f,1\text{ m})[\mathrm{dB}] + 10n\log_{10}(d/1\text{ m}) + \chi_{\sigma}^{\mathrm{CI}} \\ =& 10n\log_{10}\left(\frac{d}{1\text{ m}}\right) + 32.4 + 20\log_{10}\left(\frac{f}{1\text{ GHz}}\right) + \chi_{\sigma}^{\mathrm{CI}},\ \text{where } d \geq 1\text{ m}\end{aligned}$$

The choice of $d_0 = 1$ m as the close-in free space reference distance is shown here to provide excellent parameter stability and model accuracy for outdoor UMi and UMa, and indoor channels across a vast range of microwave and mmWave frequencies, and creates a standardized modeling approach. While the choice of a close-in reference distance of 1 m may be in the near-field of large antenna arrays, the error caused by this in practical wireless system design is negligible, and is more realistic than the ABG model, as shown subsequently and in [54].

A recent path loss model also suitable for multi-frequency modeling follows as a more general form of the CI model, and is called the CIF model, given by Eq. (4.4) when $d_0 = 1$ m [50, 61]:

$$\begin{aligned}\mathrm{PL}^{\mathrm{CIF}}(f,d)[\mathrm{dB}] =& \mathrm{FSPL}(f,1\text{ m})[\mathrm{dB}] + 10n\left(1 + b\left(\frac{f-f_0}{f_0}\right)\right)\log_{10}(d) + \chi_{\sigma}^{\mathrm{CIF}}, \\ =& 10n\left(1 + b\left(\frac{f-f_0}{f_0}\right)\right)\log_{10}(d) + 32.4 + 20\log_{10}\left(\frac{f}{1\text{ GHz}}\right) + \chi_{\sigma}^{\mathrm{CIF}}, \\ & \text{where } d \geq 1\text{ m}\end{aligned} \tag{4.4}$$

where n denotes the distance dependence of path loss (similar to the PLE in the CI model), and b is a model parameter that captures the amount of linear frequency dependence of path loss about the weighted average of all frequencies considered in the model. The parameter f_0 is the average frequency calculated by (4.5) that is

an input parameter computed from the measurement set used to form the model, and serves as the balancing point for the linear frequency dependence of the PLE:

$$f_0 = \frac{\sum_{k=1}^{K} f_k N_k}{\sum_{k=1}^{K} N_k} \tag{4.5}$$

where K is the number of unique frequencies, N_k is the number of path loss data points corresponding to the k^{th} frequency f_k, and χ_σ^{CIF} in (4.4) is a zero-mean Gaussian random variable with a standard deviation σ in dB that describes large-scale shadowing. Note that the calculated f_0 is rounded to the nearest integer in GHz in this work. The CIF model reverts to the CI model for the single frequency case (when f_0 is equal to the single frequency f) or when $b = 0$ (i.e., when there is no frequency dependence on path loss, besides that which occurs in the first meter of free space propagation). As shown subsequently, UMa channels modeled by CIF have a value of b very close to zero, indicating that almost all of the frequency-dependent effects are incorporated in the first meter of free space propagation [54, 61].

The CI and CIF models provide a close-in free space anchor point which assures that the path loss model (regardless of transmit power) always has a physical tie and continuous relationship to the transmitted power over distance, whereas the AB and ABG models use a floating constant based on a fit to the data, without consideration for the close-in free space propagation that always occurs in practice near an antenna out in the open (this implies that particular measured path loss values could greatly impact and skew the ABG path loss model parameters, since there is not a physical anchor to assure that close-in free space transmission occurs in the first meter of propagation from the TX antenna). *The CI and CIF*

models are therefore based on fundamental principles of wireless propagation, dating back to Friis and Bullington, where the PLE parameter offers insight into path loss based on the environment, having a PLE value of 2 in free space (as shown by Friis) and a value of 4 for the asymptotic two-ray ground bounce propagation model (as shown by Bullington) [67]. Previous UHF (Ultra-High Frequency) and microwave models used a close-in reference distance of 1 km or 100 m since BS towers were tall without any nearby obstructions, and inter-site distances were on the order of many kilometers for those frequency bands [67, 195]. d_0 = 1 m is used in 5G path loss models since coverage distances will be shorter at higher frequencies. Furthermore, with future small cells, BSs are likely to be mounted closer to obstructions [2, 54]. The CI and CIF d_0 =1 m reference distance is a suggested standard that ties the true transmitted power or path loss to a convenient close-in distance, as suggested in [54]. Standardizing to a reference distance of 1 m makes comparisons of measurements and models simple, and provides a standard definition for the PLE, while enabling intuition and rapid computation of path loss. Now this chapter shows with measured data that the 1 m reference is very effective for large-scale path loss modeling across a vast range of frequencies.

As discussed in [54], emerging mmWave mobile systems will have very few users within a few meters of the BS antenna (in fact, no users are likely to be in the near field, since transmitters will be mounted on a lamppost or ceiling), and users in the near field will have strong signals or will be power-controlled compared to typical users much farther from the transmitter such that any path loss error in the near field (between 1 m and the Fraunhofer distance) will be very minor, and so much smaller than the dynamic range of signals experienced by users in a commercial system.

Table 4.1: Parameters in the CI and CI-opt path loss models in UMa and UMi scenarios. Freq. Range denotes frequency range. # of Data Points represents the number of data points after distance binning and path loss thresholding. Dist. Range denotes distance range, CI-opt represents the CI model with an optimized free space reference distance d_0. Δ_σ denotes the difference in the SF standard deviation between the CI and CI-opt models [50].

Sce.	Env.	Freq. Range (GHz)	# of Data Points	Dist. Range (m)	Model	PLE	$d_0(m)$	σ (dB)	Δ_σ (dB)
UMa	LOS	2	253	60-564	CI-opt	2.1	6.2	1.7	0.0
					CI	2.0	1	1.7	
		10	253	60-564	CI-opt	2.0	0.1	3.1	0.0
					CI	2.0	1	3.1	
		18	253	60-564	CI-opt	2.1	14.7	2.0	0.0
					CI	2.0	1	2.0	
		28	253	60-564	CI-opt	2.0	50.0	2.3	0.0
					CI	2.0	1	2.3	
		38	20	70-930	CI-opt	1.7	32.9	3.4	0.1
					CI	1.9	1	3.5	
		2-38	1032	60-930	CI-opt	2.0	0.1	2.4	0.0
					CI	2.0	1	2.4	
	NLOS	2	583	74-1238	CI-opt	3.3	10.0	3.2	0.3
					CI	2.8	1	3.5	
		10	581	74-1238	CI-opt	3.4	4.3	4.0	0.1
					CI	3.1	1	4.1	

Table 4.1: Parameters in the CI and CI-opt path loss models in UMa and UMi scenarios. Freq. Range denotes frequency range. # of Data Points represents the number of data points after distance binning and path loss thresholding. Dist. Range denotes distance range, CI-opt represents the CI model with an optimized free space reference distance d_0. Δ_σ denotes the difference in the SF standard deviation between the CI and CI-opt models [50].

Sce.	Env.	Freq. Range (GHz)	# of Data Points	Dist. Range (m)	Model	PLE	$d_0(m)$	σ (dB)	Δ_σ (dB)
UMa	NLOS	18	468	78-1032	CI-opt	3.2	2.2	4.4	0.1
					CI	3.0	1	4.5	
		28	225	78-634	CI-opt	2.6	0.5	4.9	0.0
					CI	2.7	1	4.9	
		38	12	60-376	CI-opt	2.5	0.1	10.3	0.2
					CI	2.7	1	10.5	
		2-38	1869	60-1238	CI-opt	3.4	8.1	5.6	0.1
					CI	2.9	1	5.7	
UMi SC	LOS	28	4	31-54	CI-opt	3.8	34.2	2.4	0.8
					CI	2.1	1	3.2	
		73	6	27-54	CI-opt	-0.7	46.6	3.9	1.2
					CI	2.1	1	5.1	
		28, 73	10	27-54	CI-opt	0.8	50.0	4.3	0.1
					CI	2.1	1	4.4	
	NLOS	2.9	18	109-235	CI-opt	3.5	8.2	2.9	0.0
					CI	2.9	1	2.9	

Table 4.1: Parameters in the CI and CI-opt path loss models in UMa and UMi scenarios. Freq. Range denotes frequency range. # of Data Points represents the number of data points after distance binning and path loss thresholding. Dist. Range denotes distance range, CI-opt represents the CI model with an optimized free space reference distance d_0. Δ_σ denotes the difference in the SF standard deviation between the CI and CI-opt models [50].

Sce.	Env.	Freq. Range (GHz)	# of Data Points	Dist. Range (m)	Model	PLE	$d_0(m)$	σ (dB)	Δ_σ (dB)
UMi SC	NLOS	28	18	61-186	CI-opt	3.3	0.7	8.6	0.0
					CI	3.4	1	8.6	
		29	16	109-235	CI-opt	3.6	5.0	4.9	0.0
					CI	3.1	1	4.9	
		73	30	48-190	CI-opt	2.9	0.1	7.4	0.0
					CI	3.4	1	7.4	
		2.9-73	82	48-235	CI-opt	2.8	0.1	7.8	0.2
					CI	3.2	1	8.0	

Table 4.2: Parameters in the CI and CI-opt path loss models in the InH scenario. Freq. Range denotes frequency range. # of Data Points represents the number of data points after distance binning and path loss thresholding. Dist. Range denotes distance range, CI-opt represents the CI model with an optimized free space reference distance d_0. Δ_σ denotes the difference in the SF standard deviation between the CI and CI-opt models [50].

Sce.	Env.	Freq. Range (GHz)	# of Data Points	Dist. Range (m)	Model	PLE	$d_0(m)$	σ (dB)	Δ_σ (dB)
InH Office	LOS	2.9	12	5-49	CI-opt	1.8	0.1	5.0	0.2
					CI	1.6	1	5.2	
		28	6	4-21	CI-opt	1.1	1.1	1.2	0.0
					CI	1.1	1	1.2	
		29	12	5-49	CI-opt	1.5	0.9	4.5	0.0
					CI	1.5	1	4.5	
		73	6	4-21	CI-opt	0.4	3.7	1.2	1.8
					CI	1.3	1	3.0	
		2.9-73	36	4-49	CI-opt	1.7	0.1	4.6	0.0
					CI	1.5	1	4.6	
	NLOS	2.9	30	5-67	CI-opt	3.9	4.6	5.9	0.6
					CI	3.1	1	6.5	
		28	17	4-46	CI-opt	3.3	4.4	8.8	0.3
					CI	2.7	1	9.1	
		29	29	5-67	CI-opt	4.4	4.7	6.4	0.8
					CI	3.3	1	7.2	

Table 4.2: Parameters in the CI and CI-opt path loss models in the InH scenario. Freq. Range denotes frequency range. # of Data Points represents the number of data points after distance binning and path loss thresholding. Dist. Range denotes distance range, CI-opt represents the CI model with an optimized free space reference distance d_0. Δ_σ denotes the difference in the SF standard deviation between the CI and CI-opt models [50].

Sce.	Env.	Freq. Range (GHz)	# of Data Points	Dist. Range (m)	Model	PLE	$d_0(m)$	σ (dB)	Δ_σ (dB)
InH Office	NLOS	73	15	4-42	CI-opt	2.8	0.5	9.1	0.1
					CI	3.0	1	9.2	
		2.9-73	91	4-67	CI-opt	3.9	3.9	7.9	0.4
					CI	3.1	1	8.3	
InH SM	LOS	2.9	14	19-149	CI-opt	1.9	0.1	3.2	0.0
					CI	1.9	1	3.2	
		29	14	19-149	CI-opt	1.8	7.6	3.1	0.0
					CI	1.9	1	3.1	
		61	14	19-149	CI-opt	1.6	50	3.4	0.0
					CI	2.0	1	3.4	
		2.9-61	42	19-149	CI-opt	1.9	7.0	3.4	0.0
					CI	1.9	1	3.4	
	NLOS	2.9	26	24-229	CI-opt	2.1	0.1	4.8	0.0
					CI	2.2	1	4.8	
		29	26	24-229	CI-opt	2.2	0.1	4.2	0.0
					CI	2.3	1	4.2	

Table 4.2: Parameters in the CI and CI-opt path loss models in the InH scenario. Freq. Range denotes frequency range. # of Data Points represents the number of data points after distance binning and path loss thresholding. Dist. Range denotes distance range, CI-opt represents the CI model with an optimized free space reference distance d_0. Δ_σ denotes the difference in the SF standard deviation between the CI and CI-opt models [50].

Sce.	Env.	Freq. Range (GHz)	# of Data Points	Dist. Range (m)	Model	PLE	$d_0(m)$	σ (dB)	Δ_σ (dB)
InH SM	NLOS	61	26	24-229	CI-opt	2.3	0.1	4.5	0.0
					CI	2.5	1	4.5	
		2.9-61	78	24-229	CI-opt	2.2	0.1	4.8	0.0
					CI	2.3	1	4.8	

One may argue that a close-in reference distance other than 1 m may be a better approach to maximize model accuracy of the CI model [196, 197]. The research group which the author of this technical report belong to, in fact, originally used d_0 values greater than 1 m in past research in order to ensure the model would only be used in the far field of directional antennas [2, 198, 199], but they later found a 1 m reference was more suitable for use as a standard, due to the fact that there was very little difference in standard deviation when using a 1 m reference distance (i.e., model error was not significantly different when using a different value of d_0 [54]), and given the fact that very few or any users will be within the first few meters of the transmitter antenna.

To compare the performance of the CI model between using a 1 m free space reference distance and an optimized or empirically determined free space reference distance d_0, as proposed in [196, 197], the 30 measurement data sets from

Nokia/AAU, UT, NYU, and Qualcomm were used to compare model parameters and standard deviations. Tables 4.1 and 4.2 list the model parameters in the 1 m CI model as compared to the CI model with an optimized d_0 (CI-opt) at various frequencies ranging from 2 GHz to 73 GHz for the UMa, UMi, and InH scenarios in both LOS and NLOS environments, where the PLE and d_0 for CI-opt were jointly optimized via the MMSE method demonstrated in the Appendix (to preclude unreasonable d_0 values caused by the sparsity of some data sets, the range of d_0 was set to between 0.1 m and 50 m). All of the scattered path loss data samples were locally averaged over 2 m distance bins (other binning values can also be explored, and little difference was found in results using 2, 5, or 10 m local average bins), in order to remove the small-scale fading effects and to reduce the difference in the number of data points across measurement campaigns. In addition, all path loss values weaker than FSPL at 1 m plus 100 dB were not considered for analysis, based on the reasonable assumption that there would be fewer weaker measurements at higher frequencies due to the greater path loss in the first meter, so a frequency-dependent signal threshold was implemented to ensure that the measured data sets would slightly emphasize more measurements at the higher frequencies, resulting in a relatively comparable number of points for the different frequencies from various measurement campaigns. The results of this chapter were not heavily influenced by the binning or frequency-dependent thresholding, but these approaches were found to yield comparable coverage distances over the multiple frequencies based on the particular antennas and transmit powers used.

As shown in Tables 4.1 and 4.2, for both outdoor and indoor scenarios, the SF between using $d_0 = 1$ m and an optimized d_0 differs by no more than 0.3 dB in most cases (more than an order of magnitude smaller than the standard deviation).

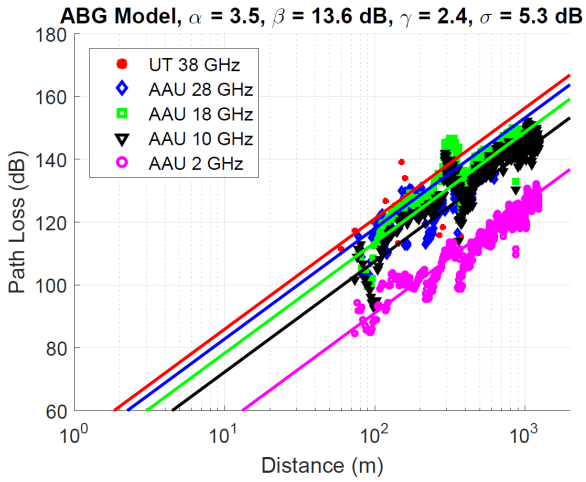

Figure 4.1: ABG path loss model in the UMa scenario across different frequencies and distances in the NLOS environment. Model parameters using all of the displayed data are given at the top of the graph [50].

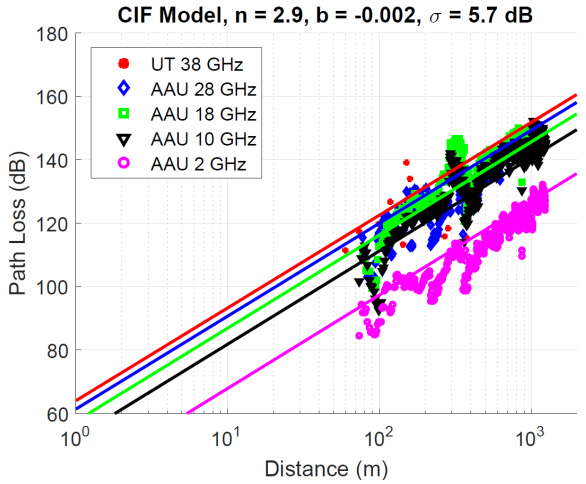

Figure 4.2: CIF path loss model in the UMa scenario across different frequencies and distances in the NLOS environment. Model parameters using all of the displayed data are given at the top of the graph [50].

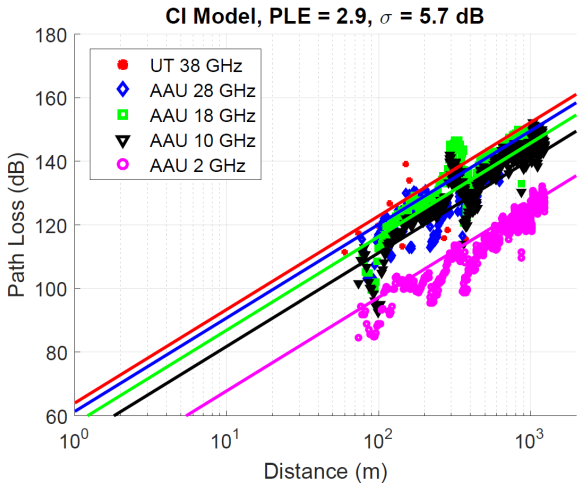

Figure 4.3: CI path loss model in the UMa scenario across different frequencies and distances in the NLOS environment. Model parameters using all of the displayed data are given at the top of the graph [50].

Note that the only significant differences in error between the $d_0 = 1$ m and the optimized d_0 value occur when there are very few measurement points, and the PLE in CI-opt generally has a physically unreasonable value in these rare cases (e.g., the PLE is less than 1, indicating much less loss than a metal waveguide; or the PLE is negative, indicating decrease of path loss with distance; or the PLE is unreasonably high). The majority of the measurement sets, the 1 m free space reference distance model χ_σ is always within 0.1 dB of the optimized d_0 model, illustrating virtually no difference in standard deviation between the two approaches. Therefore, the 1 m CI model provides sufficiently accurate fitting results compared to the CI-opt model, and requires only one model parameter (PLE) to be optimized by the adoption of a 1 m standard close-in free space reference distance, while the CI-opt model requires two model parameters (PLE and d_0) for modeling the mean path loss over distance, and sometimes yields unrealistic PLEs and reference distances. For the remainder of this technical report, the CI model (4.2) is assumed to use $d_0 = 1$ m,

as suggested in [54].

The ABG (4.1), CI (4.2) and CIF (4.4) models with $d_0 = 1$ m are a function of both distance and frequency, where the CI and CIF models have frequency dependence expressed primarily by the frequency-dependent FSPL term (4.3) in the first meter of free space propagation. While the ABG model offers some physical basis in the α term, being based on a 1 m reference distance similar to the n term in (4.2) and (4.4), it departs from physics when introducing both an offset β (which is an optimization parameter that is not physically based), and a frequency weighting term γ that has no proven physical basis, although recent measurements show that the path loss increases with frequency across the mmWave band in the indoor office scenario [200] (both the β and γ parameters are used for curve fitting, as was done in the WINNER floating-intercept (AB) model) [54, 114, 194]. It is noteworthy that the ABG model is identical to the CI model if equating α in the ABG model in (4.1) with the PLE n in the CI model in (4.2), γ in (4.1) with the free space PLE of 2, and β in (4.1) with $20log_{10}(4\pi \times 10^9/c)$ in (4.3).

Using the three path loss models described above, and the 30 measurement data sets over a wide range of microwave and mmWave frequencies (2 to 73 GHz) and distances (4 to 1238 m), the path loss model parameters were computed for the three models. The PLE in the CI model, the n and b in the CIF model, and the α, β, and γ parameters in the ABG model were all calculated via the MMSE fit on all of the path loss data from all measured frequencies and distances for a given scenario (UMa, UMi, or InH), using closed-form solutions that minimize the SF standard deviation, as detailed in the Appendix. In order to focus solely on the comparison of propagation models, LOS and NLOS measurements were separated, and the probabilities of LOS or NLOS were not included, although such probability

models as described in [54, 71, 191, 201, 202, 203] may exploit the results of this work.

Figs. 4.1 - 4.3 show scatter plots of all the data sets optimized for the ABG, CIF, and CI models in the UMa scenario in the NLOS environment, respectively. Table 4.3 summarizes the path loss parameters in the ABG, CI, and CIF models for the UMa, UMi, and InH scenarios in both LOS and NLOS environments. As shown in Table 4.3, the CI and CIF models each provide a PLE of 2.0, 2.1, 1.5, and 1.9 in the LOS environment for the UMa, UMi SC, InH office and InH shopping mall (SM) scenarios, respectively, which agrees well with a free space PLE of 2 in UMa, UMi SC, and InH SM settings, or models the waveguiding effects in the InH office scenario, respectively. Although the CI and CIF models yield slightly higher SF standard deviation than the ABG model in most cases, this increased standard deviation is usually a fraction of a dB and is within standard measurement error arising from frequency and temperature drift, connector and cable flex variations, and calibration errors in an actual measurement campaign. Notably, these errors are often an order of magnitude less than the corresponding actual SF standard deviations in all three models. It is noteworthy that the CIF model even renders lower SF standard deviations than the ABG model for the LOS InH office and NLOS InH SM scenarios, indicating the greater accuracy of CIF compared to ABG in these settings, even though the CIF model has fewer optimization parameters. Furthermore, for the UMa and LOS UMi SC scenarios, the CI and CIF models always yield identical PLEs and standard deviations for the same data set, and the b parameter in the CIF model is virtually zero. For the NLOS UMi SC, and InH SM scenarios, b in the CIF model is slightly positive, implying that path loss increases with frequency beyond the first meter of free space propagation.

Table 4.3: Parameters in the ABG, CI, and CIF path loss models in UMa, UMi, and InH scenarios (Sce.) in both LOS and NLOS environments (Env.). Freq. Range denotes frequency range, and Dist. Range denotes distance range. # of Data Points represents the number of data points after distance binning and path loss thresholding. Δ_σ denotes the difference in the SF standard deviation between the CI or CIF model and the ABG model [50].

Sce.	Env.	Freq. Range (GHz)	# of Data Points	Dist. Range (m)	Model	α (ABG) or PLE (CI) or n (CIF)	β (ABG) (dB)	γ (ABG) or b (CIF)	σ (dB)	Δ_σ (dB)
UMa	LOS	2-38	1032	60-930	ABG	1.9	35.8	1.9	2.4	-
					CI	2.0	-	-	2.4	0.0
					CIF	2.0	-	-0.014	2.4	0.0
	NLOS	2-38	1869	61-1238	ABG	3.5	13.6	2.4	5.3	-
					CI	2.9	-	-	5.7	0.4
					CIF	2.9	-	-0.002	5.7	0.4
UMi SC	LOS	28, 73	10	27-54	ABG	1.1	46.8	2.1	4.3	-
					CI	2.1	-	-	4.4	0.1
					CIF	2.1	-	0.003	4.4	0.1
	NLOS	2.9-73	82	48-235	ABG	2.8	31.4	2.7	6.8	-
					CI	3.2	-	-	8.0	1.2
					CIF	3.2	-	0.076	7.1	0.3
InH Office	LOS	2.9-73	36	4-49	ABG	1.6	32.9	1.8	4.5	-
					CI	1.5	-	-	4.6	0.1
					CIF	1.5	-	-0.102	4.4	-0.1
	NLOS	2.9-73	91	4-67	ABG	3.9	19.0	2.1	7.9	-
					CI	3.1	-	-	8.3	0.4
					CIF	3.1	-	-0.001	8.3	0.4
InH SM	LOS	2.9-61	42	19-149	ABG	1.9	31.2	2.2	3.3	-
					CI	1.9	-	-	3.4	0.1
					CIF	1.9	-	0.042	3.3	0.0
	NLOS	2.9-61	78	24-229	ABG	2.0	34.4	2.3	4.6	-
					CI	2.3	-	-	4.8	0.2
					CIF	2.3	-	0.054	4.5	-0.1

Table 4.4: Parameters in the AB/ABG and CI (i.e., CIF when $b = 0$) path loss models in the UMa and UMi scenarios (Sce.) in the NLOS environment (Env.) for different frequency (Freq.) and distance (Dist.) ranges. # of Data Points represents the number of data points after distance binning and path loss thresholding [50].

Sce.	Env.	Freq./Freq. Range (GHz)	# of Data Points	Dist. Range (m)	n^{CI}	α^{ABG}	β^{ABG} (dB)	γ^{ABG}	σ^{CI} (dB)	σ^{ABG} (dB)	$\sigma^{CI} - \sigma^{ABG}$ (dB)
UMa	NLOS	2	583	74-1238	2.8	3.3	19.6	2	3.5	3.2	0.3
		18	468	78-1032	3.0	3.2	28.5	2	4.5	4.4	0.1
		28	225	78-634	2.7	2.6	34.0	2	4.9	4.9	0.0
		38	12	60-376	2.7	1.0	69.3	2	10.5	9.6	0.9
		2-38	1869	60-1238	2.9	3.5	13.6	2.4	5.7	5.3	0.4
UMi SC	NLOS	2.9	18	109-235	2.9	3.5	18.9	2	2.9	2.9	0.0
		28	18	61-186	3.4	3.3	34.1	2	8.6	8.6	0.0
		29	16	109-235	3.1	3.6	21.3	2	4.9	4.9	0.0
		73	30	48-190	3.4	2.9	42.6	2	7.4	7.4	0.0
		2.9-73	82	48-235	3.2	2.8	31.4	2.7	8.0	6.8	1.2

Table 4.4 lists the model parameters in the ABG and CI models at different frequencies in the NLOS environment for the UMa and UMi scenarios, with the last line for each scenario showing the parameters for the multi-frequency model. Note that for single frequencies, γ in the ABG model is set to 2, thus reverting to the AB model used in 3GPP and WINNER II channel models [114, 191, 202], and the CIF model reverts to the CI model. Fig. 4.4 illustrates a useful example of the CI and ABG models as compared to ideal free space path loss at 28 GHz for the UMa NLOS environment, using the parameters for 2 - 38 GHz in Table 4.4. Fig. 4.4 is useful since it shows how any one of the three path loss models might be used at a particular single frequency in wireless system design, after the multi-frequency model had been developed using a wide range of data over a vast range of frequencies (in this case, the four measurement data sets for the UMa scenario listed in Table 4.4).

A few key observations can be obtained from these figures and Table 4.4. First, the α and β parameters in the AB model can vary as widely as 2.3 and 49.7 dB across frequencies, respectively, as shown in Table 4.4. The large variation of α and β in the AB model was also observed in [54]. Second, the PLE n in the CI model varies only marginally for the single frequency case, with a largest variation of merely 0.5 for all the scenarios. The SF standard deviations for the CI and ABG models differ by only a fraction of a dB over all frequencies and distances in most cases, and the difference is less than an order of magnitude of the SF for either model, making the models virtually identical in accuracy over frequency and distance. There is a case for UMi where the ABG model has 1.2 dB lower SF standard deviation than the CI model, but there are only 82 data points in this case, and recent working using a much larger data set showed only 0.4 dB difference

(8.2 dB for CI and 7.8 dB for ABG) for the UMi SC NLOS scenario [204], and this difference is more than an order of magnitude smaller than either standard deviation.

As shown in Fig. 4.4, the parameters derived from 2 to 38 GHz for the UMa NLOS environment, when applied at 28 GHz, indicate that the ABG NLOS model underestimates path loss to be *much less than free space* when very close to the transmitter (a nonsensical result!) and predicts much less path loss than CI NLOS out to $\sim$ 30 m. Perhaps more importantly, the floating-intercept ABG model overestimates path loss (i.e., underestimates interference) at greater distances compared with the CI model at far distances [54]. These results are clearly seen by comparing the path loss vs. distance end-points in Figs. 4.1, 4.3 and 4.4. The CI model is thus more conservative when analyzing interference-limited systems at larger distances and more realistic when modeling NLOS signal strengths at close-in distances.

From the above analysis, the CI model provides more stability and intrinsic accuracy at distance end-points using fewer parameters (i.e., PLE and $\chi_{\sigma}^{\mathrm{CI}}$) across wide ranges of frequencies with only a fraction of a decibel higher SF standard deviation in most cases when compared to the four-parameter ABG model. The CI model is anchored to FSPL in the first meter, and gives intuitive meaning through the PLE parameter, since $10n$ mathematically describes the path loss in dB with respect to a decade increase of distance beginning at 1 m, making it very easy to compute power or path loss over distance [50]. Only a very subtle change of a single constant is needed to the AB/ABG model to implement the simpler CI/CIF model, i.e., replacing the floating intercept parameter with a FSPL term that is physically based and is inherently a function of frequency. While Tables 4.3 and 4.4 show

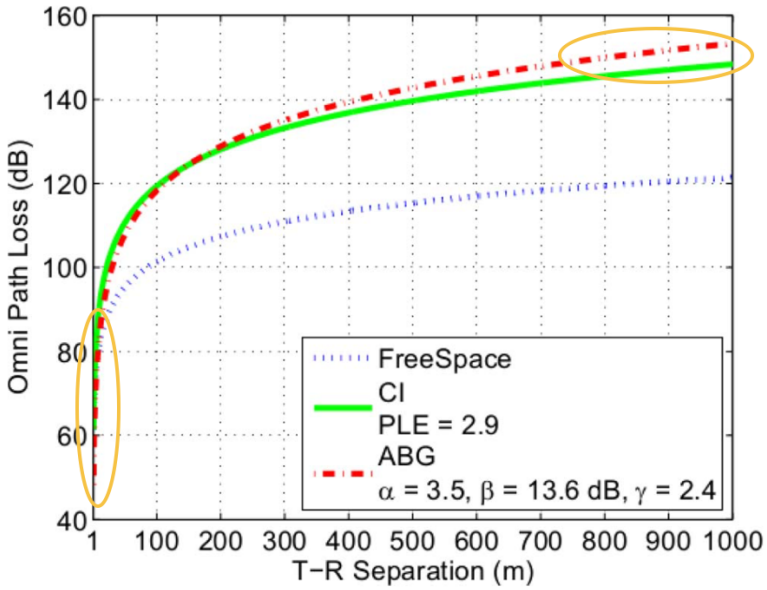

Figure 4.4: Example comparison of free space, CI and ABG path loss models at 28 GHz for the UMa NLOS environment using the parameters derived with measurements from 2 - 38 GHz in Table 4.3. Note how the ABG model estimates 5 dB less signal power (i.e., 5 dB less out-of-cell interference) at 1 km and more signal power when close to the transmitter as compared to CI [50], as highlighted by the orange circles.

how the ABG, CI, and CIF models all provide comparable curve fitting standard deviations over a wide frequency range, the CI and CIF models offer superior accuracy and reliability when subject to extensive sensitivity analyses.

4.2 Prediction and Sensitivity Performance

This section investigates the prediction accuracy and sensitivity of the three path loss models, i.e., ABG, CI and CIF. Because of the vast number of experimental data points provided by the authors, it was possible to test the efficacy of the path loss models in situations where they are used outside of the particular frequencies, locations, or distances. Prediction performance and model sensitivity were tested by creating path loss models using a subset of the measurements (to obtain the optimized model parameters) and then testing those resulting models against the other subset of measurements (which were outside of the data sets used to generate the original model parameters). This test is needed to establish whether engineers could use the models with confidence in new scenarios or distances or frequencies different than what were used to form the original models. If future systems use more transmit power or have greater range than the measurement systems used to derive the model parameters, or are to be used at different frequencies than what were measured to produce the models, a sensitivity analysis such as this is critical for comparing and selecting path loss models.

The measured data from all experiments for the UMa, UMi SC, and InH office scenarios shown in Table 4.3 are split into two sets [50]: a measurement set and a prediction set, where the term *measurement set* refers to the set of measured data used to compute the optimum (i.e., minimum SF standard deviation) parameters

of the path loss model, and the term *prediction set* refers to a different set of measured data that is scattered about the distance-dependent mean path loss model constructed from the measurement set. For a specific path loss model (e.g., ABG, CI, or CIF), the SF standard deviation is calculated using the measured data in the prediction set as distributed about the distance-dependent mean path loss model constructed from the measurement set. As the measurement set varies with distance, frequency, or city, as explained below, the optimized model parameters computed from the measurement set, as well as the SF standard deviation for the prediction set (i.e., the prediction error), also change. Therefore, two types of comparisons are simultaneously performed as the measurement set varies: first, the SF standard deviation for the prediction set about the model formed from the measurement set is computed and compared for each of the three path loss models in order to compare the accuracy for each model under identical measurement set conditions; second, the optimized model parameters from the measurement set are determined and compared between the three path loss models, to determine the sensitivity and stability of the model parameters over different sets of measurement data. Only the NLOS data are used in this prediction performance and sensitivity study, since NLOS environments offer greater variability, higher SF standard deviation, and are most likely to produce errors in 5G analysis and simulation.

4.2.1 Prediction in Distance

In this subsection, the total data set of each of the UMa, UMi SC, and InH office NLOS data of Table 4.3 is used and broken up into a measurement set and a prediction set based on distance. The prediction set was kept fixed in this investigation and the measurement sets were varied over distance, where the

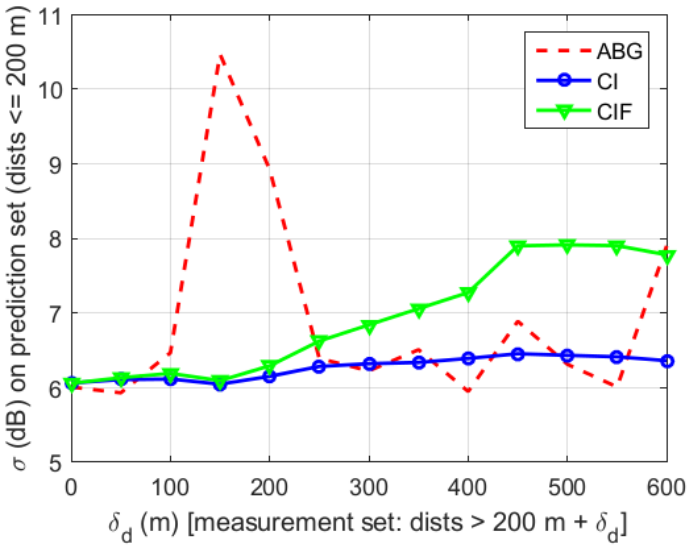

Figure 4.5: Shadow fading standard deviation of the ABG, CI, and CIF path loss models for prediction in distance when the prediction set is close to the transmitter in the UMa scenario [50].

optimum model parameters (corresponding to the minimum SF standard deviation) were computed for each specific measurement set. The measurement sets included measured data at distances which kept getting further away from the prediction set.

The first investigation of this experiment is for the case when the prediction set contains measurement points that are closer to the TX (base station) than the measurement set. In this case, the prediction set is all the measured data with distances smaller than or equal to $d_{max} = 200$ m, and the measurement sets varied to include all distances greater than $d_{max} + \delta_d$ ($\delta_d \geqslant 0$). Fig. 4.5 and Fig. 4.6 show the prediction errors and parameter variations of the ABG, CI, and CIF models for prediction in distance in the UMa scenario. As can be seen in Fig. 4.5, the prediction error of the CIF model generally increases with the increase of the distance between the two data sets. However, remarkably, the CI path loss model

has a constant SF standard deviation for the prediction set, regardless of how far away the measurement set gets [50]. On the other hand, the SF standard deviation of the ABG model over the prediction set varies substantially as δ_d increases. For the CI model, the largest difference in the standard deviation of the scattered data in the prediction set, around the optimized model derived from the measurement set, is only 0.4 dB across the entire range of δ_d (from 0 to 600 m), and about 2 dB for the CIF model, while the standard deviation of the ABG model reaches as high as 10.5 dB when $\delta_d = 150$ m, and varies by 4.5 dB across the entire range of δ_d. This shows how erratic and sensitive the ABG model is to the particular data used to create the model parameters, and illustrates the heightened sensitivity for certain situations when using the ABG model — no such problems exist for the CI or CIF model [50]. The parameter stability of the PLE in the CI model and the n and b values in the CIF model is much better than the parameters of the ABG model when varying the distance between the two sets, as seen in Fig. 4.6. In particular, the α of the ABG model can vary a lot (3.2 to 4.6), which could have significant effects in system-level simulations, as the level of signal strength or interference greatly depends on the value of α (i.e., the distance-related parameter). In addition, the β of the ABG model can vary by 39.5 dB [50].

For the UMi scenario, the prediction set uses T-R separation distances smaller than or equal to 50 m, and the distance is larger than 50 m for the measurement set; for the InH office scenario, the prediction set corresponds to T-R separation distances smaller than or equal to 15 m, and the measurement set contains data with distances larger than 15 m, considering the generally shorter T-R separations compared to outdoor cases. The prediction results for the UMi SC scenario are illustrated in Figs. 4.7 and 4.8, while Figs. 4.9 and 4.10 display the prediction

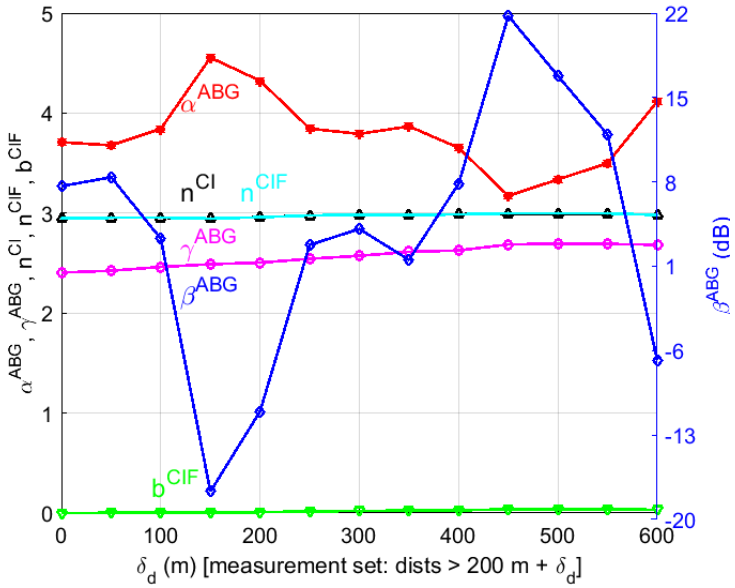

Figure 4.6: Parameters of the ABG, CI, and CIF path loss models for prediction in distance when the prediction set is close to the transmitter in the UMa scenario. Note that the scale for β (dB) in the ABG model is to the right [50].

performance for the InH office scenario [50]. As shown by Figs. 4.7 to 4.10, the prediction error of the ABG model fluctuates significantly and rises dramatically as the measurement set gets further away from the prediction set, and may become incredibly high, e.g., over 20 dB. On the other hand, the CI and CIF models yield low (at most 8.2 dB) and very stable prediction errors across the entire range of δ_d for both UMi and InH scenarios, which implies that the CI and CIF models are both more accurate than the ABG model under varying data sets, and are not sensitive to the data set used to generate the model parameters. Similar to the UMa case, the model parameters in the CI and CIF models exhibit little variation, while the α and β in the ABG model vary significantly over the investigated range of δ_d [50].

The second investigation of this experiment is for the case that the measurement

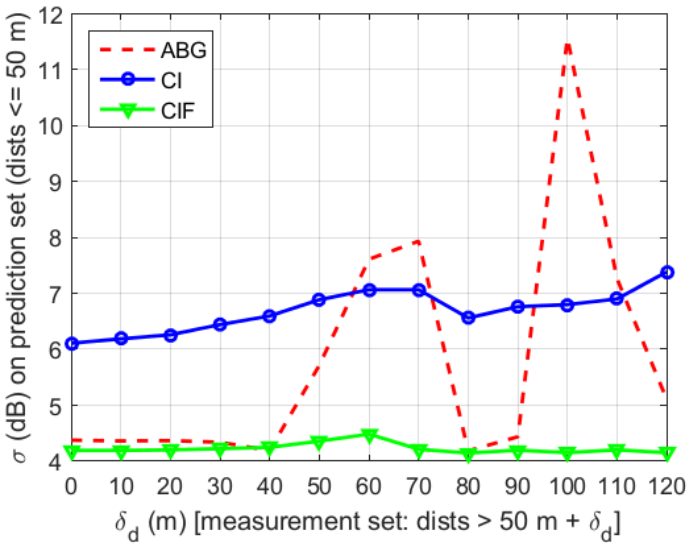

Figure 4.7: Shadow fading standard deviation of the ABG, CI, and CIF path loss models for prediction in distance when the prediction set is close to the transmitter in the UMi SC scenario [50].

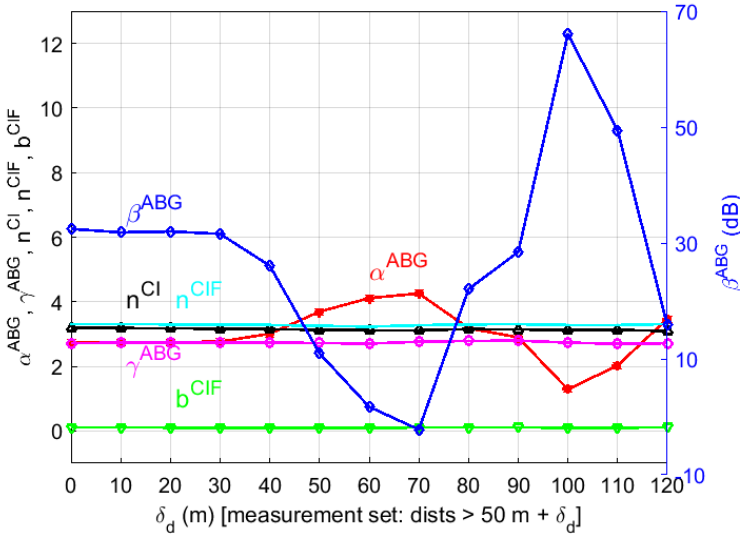

Figure 4.8: Parameters of the ABG, CI, and CIF path loss models for prediction in distance when the prediction set is close to the transmitter in the UMi SC scenario. Note that the scale for β (dB) in the ABG model is to the right [50].

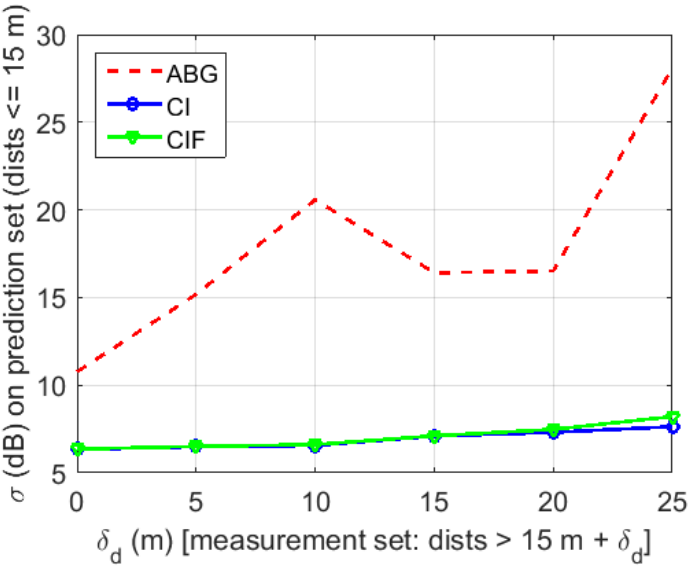

Figure 4.9: Shadow fading standard deviation of the ABG, CI, and CIF path loss models for prediction in distance when the prediction set is close to the transmitter in the InH office scenario [50].

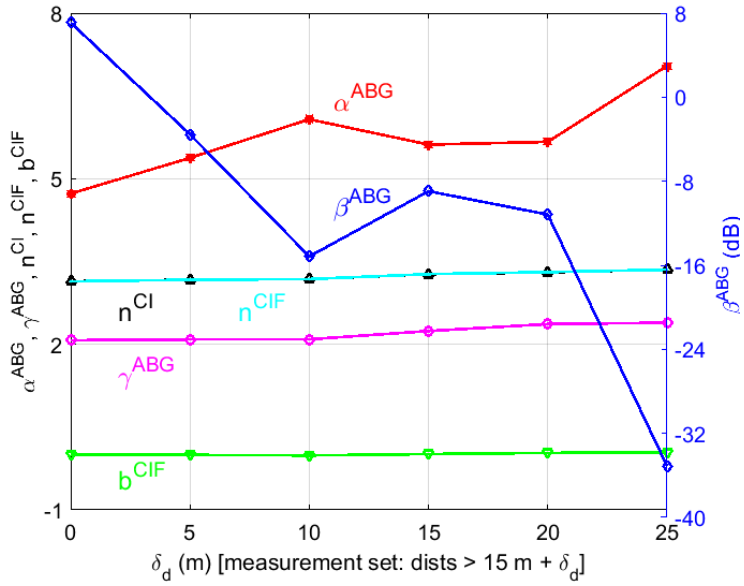

Figure 4.10: Parameters of the ABG, CI, and CIF path loss models for prediction in distance when the prediction set is close to the transmitter in the InH office scenario. Note that the scale for β (dB) in the ABG model is to the right [50].

set contains measured data closer to the TX (base station) than the prediction set [50]. In this case, the prediction set contains all UMa measurements with distances larger than or equal to $d_{min} = 600$ m, and the measurement set varies with all distances smaller than $d_{min} - \delta_d$ ($\delta_d \geqslant 0$). The results for this case in the UMa scenario are shown in Fig. 4.11 and Fig. 4.12 for the SF standard deviation on the prediction set and the parameters of the path loss models, respectively, both as a function of δ_d. As shown by Fig. 4.11, the prediction errors of both the CI and CIF path loss models vary very little as the distance between the measurement set and prediction set increases, while the prediction error of the ABG model on the prediction set exhibits significant variation as δ_d increases. Notice that the prediction errors of both the CI and CIF models vary by up to only 1.4 dB across the entire range of δ_d (from 0 to 400 m); in contrast, the prediction error of the ABG model can be as large as 16.1 dB and the maximum difference in prediction error reaches 12.5 dB across the entire range of δ_d. Moreover, the stabilities of the modeling parameters in the CI and CIF models are much better compared to those of the ABG model when varying the distance between the two sets, as illustrated by Fig. 4.12, where the α and β of the ABG model vary by 2.2 and 46.6 dB, respectively. This, again, shows the great sensitivity and inaccuracy (gross errors) of the ABG model to the particular data used to create the model parameters and the remarkable accuracy and robustness of the CI/CIF models to various measurement sets [50].

4.2.2 Prediction in Frequency

In this section, the prediction set contains the data for a given frequency and the measurement set corresponds to all the other frequencies. For example, the

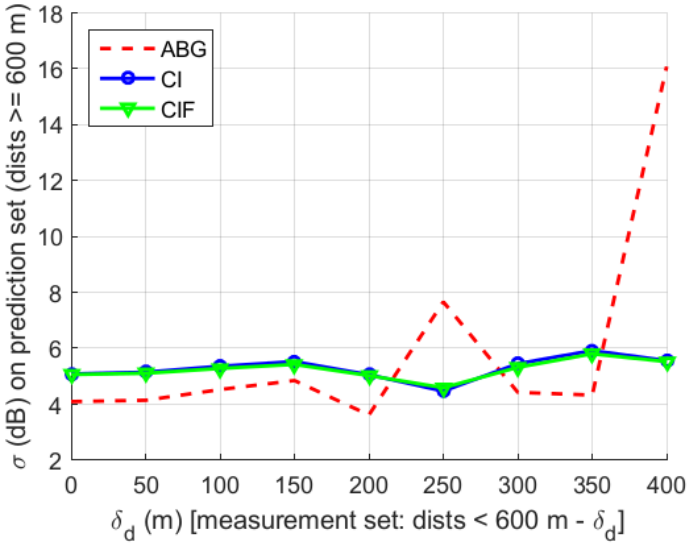

Figure 4.11: Shadow fading standard deviation of the ABG, CI, and CIF path loss models for prediction in distance when the measurement set is close to the transmitter in the UMa scenario [50].

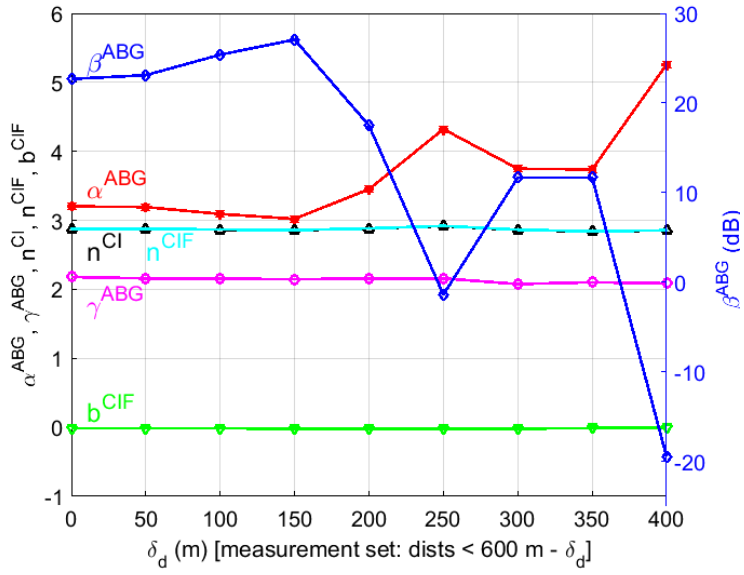

Figure 4.12: Parameters of the ABG, CI, and CIF path loss models for prediction in distance when the measurement set is close to the transmitter in the UMa scenario. Note that the scale for β (dB) in the ABG model is to the right [50].

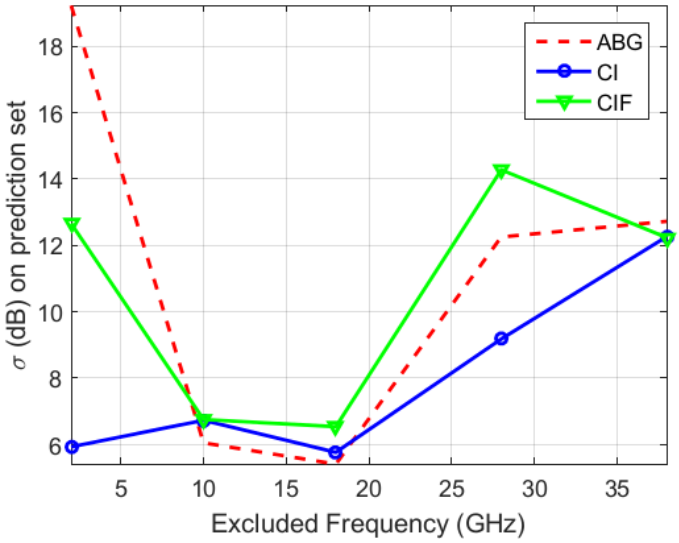

Figure 4.13: Shadow fading standard deviation for the ABG, CI, and CIF path loss models for prediction in frequency in the UMa scenario. The measurement set is for all frequencies except the excluded one shown on the x axis which is the prediction set [50].

prediction set could be all data at 2 GHz and the measurement set the data for all the other frequencies (10, 18, 28, and 38 GHz) for the UMa scenario.

Fig. 4.13 depicts the RMS error for the three path loss models on the prediction and measurement sets for the frequency shown on the x axis (where the frequency on the x axis comprises all data in the prediction set). It can be observed from Fig. 4.13 that although all the three models yield varying prediction errors across the entire frequency range, the variation is the largest for the ABG model. The prediction error of the ABG model is much greater (about 19 dB) at lower frequencies where legacy 4G systems will work, showing the liability of the ABG model for simultaneous use in lower frequency and mmWave systems. The CI model shows the most robust and accurate prediction over all frequencies. The parameters of the three path loss models for prediction in frequency are shown in Fig. 4.14. It is obvious from

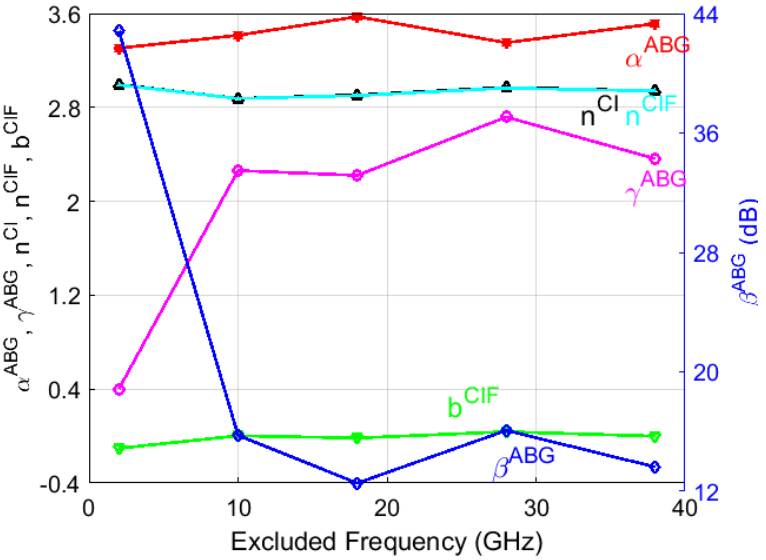

Figure 4.14: Parameters of the ABG, CI, and CIF path loss models for prediction in frequency in the UMa scenario. The measurement set is for all frequencies except the excluded one shown on the x axis which is the prediction set. Note that the scale for β (dB) in the ABG model is to the right [50].

Fig. 4.14 that the parameters in the CI and CIF models vary much less across frequencies as compared to the parameters in the ABG model, demonstrating the liability of the ABG model in terms of the sensitivity analysis of specific frequencies and measurements used in the data sets [50].

4.2.3 Prediction Across Environments

Fig. 4.13 and Fig. 4.14 also show the prediction performance of the three path loss models across environments, when considering an arbitrary single frequency, e.g., focusing on the results associated with 38 GHz. The 2, 10, 18, and 28 GHz data were measured in the Aalborg UMa environment, while the 38 GHz data were obtained from the Austin UMa environment, hence prediction results at 38 GHz actually show how the three path loss models behave when using the Aalborg data

to predict the Austin data. As seen in Fig. 4.13, the prediction errors for the CI and CIF models at 38 GHz are slightly smaller than the ABG model, indicating that all three models yield comparable prediction performance when applied in different cities [50].

These results, as well as those in [82], show superior prediction ability and robust sensitivity of the CI path loss model for outdoor scenarios, and the virtue of the CIF model for indoor settings in the large majority of cases. This advantage is especially useful for 5G mmWave standardization where an accurate, trustworthy model must be developed without the benefit of a complete set of measurements across all frequencies and all environments, especially given the fact that future spectrum may be allocated in bands different from what was originally measured [50].

4.3 Concluding Remarks

This chapter has provided a comparison of three large-scale propagation path loss models, i.e., the ABG (four parameters), CI (two parameters), and CIF (three parameters) models, over the microwave and mmWave frequency bands using 30 sets of measurement data from 2 GHz to 73 GHz for UMa, UMi, and InH scenarios [50].

First, comparisons were made between the 1-m CI model and the CI model with an optimized reference distance d_0 (CI-opt). Results show that the two-parameter 1-m CI model provides virtually identical accuracy as compared to the three-parameter CI-opt model, and the CI-opt model can sometimes yield unrealistic PLEs. The data prove that a 1-m free-space reference distance, rather than an optimized d_0, is justified for the CI model [50].

Work here showed that the ABG, CI and CIF models are all very comparable

in prediction accuracy when large data sets exist, even though the ABG model requires more model parameters and lacks a physical basis for its floating intercept value. By contrast, the CI and CIF models are physically tied to the transmitter power via the utilization of a 1-m close-in free-space reference distance that has inherent frequency dependency over the entire microwave and mmWave bands. This allows for comparable accuracy but greater parameter stability using fewer model parameters, and for easy "in your head" computation of mean path loss at all distances, by virtue of just a single model parameter (PLE or n) for the CI model (where $10n$ is the path loss in dB per decade of distance beyond 1 m) and two model parameters (n and b) for the CIF model. No change in mathematical form, and the change of just a single constant is all that is needed to change the existing 3GPP floating-intercept (AB/ABG) path loss model to the simpler and more stable CI/CIF models which provide virtually identical accuracy compared to the four-parameter ABG model over a vast range of frequencies — from today's cellular to future mmWave bands. This chapter showed that the AB and ABG models have parameter values that vary greatly across different frequency and distance ranges, while reducing the SF standard deviation by only a fraction of a dB in most cases compared to the physically-based CI and CIF models that use fewer model parameters. The single greatest difference between standard deviations for all three models over all scenarios was found to be 1.2 dB for the UMi scenario, where only 82 data points were available. However, a recent study with a much richer data set [204] showed only 0.4 dB difference between the ABG and CI models in UMi [50].

This chapter showed, by way of example at 28 GHz, that the ABG NLOS model has inherent inaccuracy at both small (< 30 m) and large (several hundred

meters) distances, and predicts *less than free space* loss when close to the TX while underestimating interference at large distances when used at an arbitrary frequency as compared to CI. Hence, the ABG model will lead to overly optimistic capacity simulations. Especially for future small cell deployments, where dozens of neighboring BSs could produce interference, the simulation results would be vastly different between the ABG and CI/CIF models [50].

A key contribution of this chapter was a sensitivity analysis that showed the CI and CIF models are superior to the ABG model in both stability performance and prediction accuracy (i.e., SF standard deviation) over a vast frequency range, when using the model to predict path loss at different distances and frequencies relative to the set of data from which the parameters of the path loss models were originally determined. Thus, for unexpected scenarios or for situations where a path loss model may be used at different distances or frequencies than the measurements used to create the original model, the sensitivity analysis in this chapter shows the CI and CIF models are more robust, accurate, and reliable as compared to the ABG model [50].

Finally, the CI model was shown to be most suitable for outdoor environments because of its accuracy, simplicity, and superior sensitivity performance due to its physical close-in free space reference point, given the fact that measured path loss exhibits little dependence on frequency in outdoor environments beyond the first meter of free space propagation (captured in the FSPL term). On the other hand, the CIF model is well suited for indoor environments, since it provides a smaller standard deviation than the ABG model in many cases even with fewer model parameters, and has superior accuracy when scrutinized with the sensitivity analysis [50].

Chapter 5

5G Channel Simulator — NYUSIM

5.1 NYUSIM Overview

NYU WIRELESS conducted mmWave measurements from 2012 through 2017, having acquired a total of over 1 Terabytes of data, at frequencies from 28 to 73 GHz in various outdoor environments in UMi, UMa, and RMa environments. The measurements and analysis done in [2, 48, 49, 50, 51, 52, 54, 59, 61, 205, 206, 207, 208] led to this NYUSIM channel simulator.

NYUSIM performs drop-based Monte Carlo simulation to generate a CIR at each drop (i.e., user location) assuming no user mobility. Channels for different user locations are assumed to be independent, justified by small correlation distances (up to about 10 centimeters) found in measurements [62]. NYUSIM provides an accurate rendering of actual CIRs in both time and space, as well as realistic signal levels that were measured, and may be utilized to support realistic physical layer

and link layer simulations such as those conducted in [48, 106, 209, 210]. The models and simulation approach in NYUSIM involves the research of more than a dozen graduate and undergraduate students, and as of late 2017, over 10,000 downloads of NYUSIM have been recorded. NYUSIM is applicable for a wide range of carrier frequencies from 500 MHz to 100 GHz, and RF bandwidths from 0 (continuous wave (CW)) to 800 MHz.

It is worth noting that *in the 3GPP TR 38.901 Release 14 channel model for frequencies above 6 GHz [66], the number of clusters is unrealistically large. For example, in the UMi street canyon scenario, the number of clusters in the LOS environment is as high as 12, and 19 in the NLOS environment, which is not supported by the real-world measurements at mmWave bands* [2, 52, 54, 205]. In contrast, *in the SSCM implemented in NYUSIM [52], the number of time clusters ranges from 1 to 6, and the mean number of spatial lobes is about 2 and is upper-bounded by 5, which are obtained from field observations and are much smaller than those in the 3GPP channel model* [48, 51, 66, 208]. The impractical number of clusters in the 3GPP channel model is likely to result in a higher rank of mmWave channels, unrealistic eigen-channel distributions, and thereby inaccurate spectral efficiency prediction for 5G mmWave channels [48, 208].

5.2 Channel Model Implemented in NYUSIM

The broadband SSCM [52] developed by NYU WIRELESS is used in NYUSIM with some important extensions such as including MIMO antenna arrays, adding atmospheric attenuation into path loss, adding more propagation scenarios, generating directional PDPs using accurate directional antenna patterns, etc., to extend

the SSCM to the NYUSIM channel model and a standalone channel simulation software [51]. The SSCM is introduced in [52] and Section 2.4.10 of this technical report and key extensions are detailed below.

5.3 Extensions of SSCM to NYUSIM

5.3.1 Path Loss Model and Additional Propagation Scenarios

The CI path loss model with a 1 m anchor point, with an extra attenuation term due to various atmospheric attenuation factors [211], is employed in NYUSIM, which is expressed as [50, 54, 168]:

$$\begin{aligned} \mathrm{PL}^{\mathrm{CI}}(f,d)[\mathrm{dB}] =& \mathrm{FSPL}(f,d_0)[\mathrm{dB}] + 10n\log_{10}\left(\frac{d}{d_0}\right) + \mathrm{AT}[\mathrm{dB}] + \chi_{\sigma}^{\mathrm{CI}}, \\ & \text{where } d \geq d_0 \text{ m} \end{aligned} \tag{5.1}$$

where d_0 denotes the free space reference distance in meters, which is set to 1 m in the NYUSIM channel model [50]. Users can change d_0 to some value other than 1 m in NYUSIM_MainCode.m, but d_0 should not exceed 5 m to guarantee free space propagation within d_0. AT is the attenuation term induced by the atmosphere, which is characterized by:

$$\mathrm{AT}[\mathrm{dB}] = \alpha[\mathrm{dB/m}] \times d[\mathrm{m}] \tag{5.2}$$

where α is the attenuation factor in dB/m for the frequency range of 1 GHz to 100 GHz, which includes the collective attenuation effects of dry air (including oxygen),

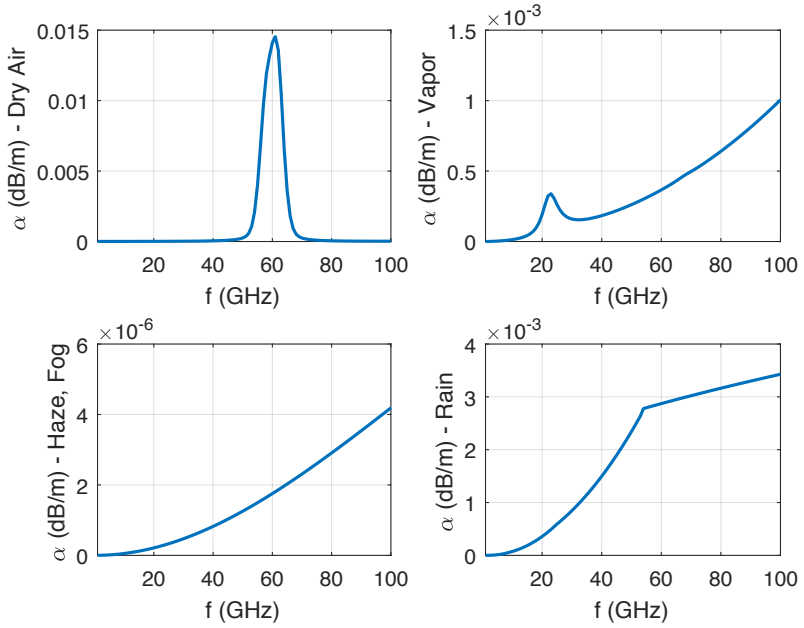

Figure 5.1: Propagation attenuation due to dry air, vapor, haze, and rain at mmWave frequencies, with a barometric pressure of 1013.25 mbar, a relative humidity of 80%, a temperature of 20°C, and a rain rate of 5 mm/hr [211].

water vapor, rain, and haze [211]. d is the 3D T-R separation distance as in (5.1).

Fig. 5.1 illustrates example propagation attenuation values due to dry air, vapor, haze, and rain at mmWave frequencies from 1 GHz to 100 GHz, with a barometric pressure of 1013.25 mbar, a relative humidity of 80%, a temperature of 20°C, and a rain rate of 5 mm/hr, while the collective attenuation effects of these four main natural absorbers are displayed in Fig. 5.2. These results were obtained and reproduced from five reported controlled experiments on atmospheric attenuation [211].

The SSCM is applicable to the UMi scenario, while in NYUSIM, the scenario is extended to UMa and RMa with different PLEs and/or TCSL statistics as compared to the UMi scenario. In the latest version (Version 1.6) of NYUSIM, the PLE and shadow fading standard deviations for UMi, UMa, and RMa scenarios are displayed

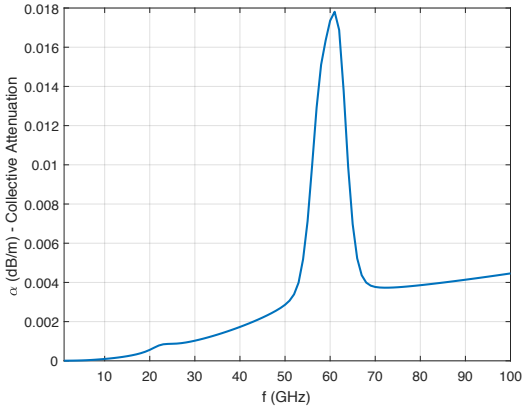

Figure 5.2: Collective attenuation effects of dry air, vapor, haze, and rain at mmWave frequencies, with a barometric pressure of 1013.25 mbar, a relative humidity of 80%, a temperature of 20°C, and a rain rate of 5 mm/hr [211].

in Table 5.1. The CI path loss model is employed for UMi and UMa scenarios, while for the RMa scenario, the CIH model (CI model with a height-dependent PLE) is adopted, as given by Eqs. (21) and (22) in [59]. The RMa PLE values in Table 5.1 are for a base station height of 35 m. Note that although the channel parameters for the UMi scenario are also used for the UMa and RMa (except for the path loss model parameters) scenarios in NYUSIM, users can adjust the UMa and RMa channel parameters in the source code according to their own needs. Furthermore, for the RMa scenario, the number of TCs and the number of SLs are both set to one, and the maximum number of MPCs is set to two, based on our RMa mmWave field measurements [59]. The BS height is only used for RMa in the CIH path loss model but not other scenarios.

5.3.2 MIMO Antenna Arrays at Both TX and RX

In NYUSIM, antenna arrays, such as uniform linear arrays (ULAs) and uniform rectangular arrays (URAs), are allowed to be equipped at both the BS and UE.

The entries in the MIMO channel matrix **H** are obtained by extending the omnidirectional CIR over the antenna array manifold at the TX and/or RX using Eqs. (2.8)- (2.11). Assuming the RX is equipped with a ULA with eight antenna elements with half-wavelength spacing at a carrier frequency of 28 GHz, Fig. 5.3 illustrates the downlink received PDPs at each RX antenna element (i.e., small-scale PDPs) for various RF bandwidths, i.e., 800 MHz, 100 MHz, and 0 MHz (CW), generated using NYUSIM. Due to the high temporal resolution at an 800 MHz RF bandwidth, the magnitude of small-scale MPCs remain almost constant over several wavelengths (see Fig. 5.3(a)). When the RF bandwidth decreases, however, a delay bin may contain a number of unresolvable MPCs whose phases and magnitudes add up in a vectorial manner, thus the overall magnitude of a delay bin usually vary over a small-scale local area, as shown in Figs. 5.3(b) and 5.3(c).

5.3.3 Directional PDPs with Accurate Directional Antenna Patterns

5G mmWave systems are expected to use antenna arrays with directional radiation patterns, thus directional PDPs are of great importance and research interest. To generate directional PDPs at arbitrary TX-RX pointing angle combination for

Table 5.1: PLEs and shadow fading standard deviations for different scenarios in NYUSIM [50]. The RMa PLEs are for a base station height of 35 m [59].

Scenario		PLE	Shadow Fading Standard Deviation (dB)
UMi	LOS	2	4.0
	NLOS	3.2	7.0
UMa	LOS	2	4.0
	NLOS	2.9	7.0
RMa	LOS	2.31	1.7
	NLOS	3.07	6.7

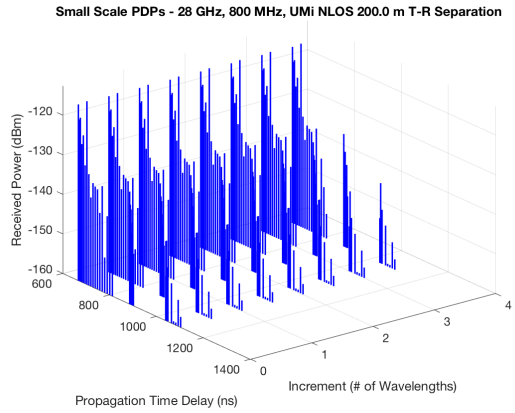

(a) 800 MHz RF Bandwidth

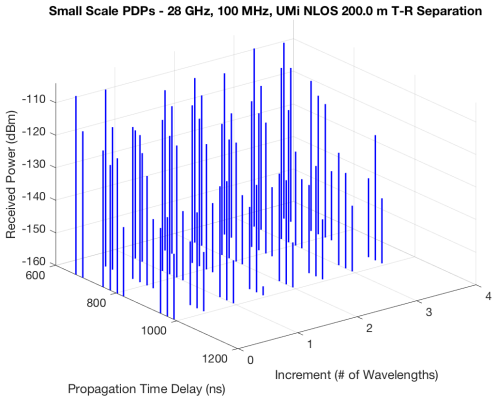

(b) 100 MHz RF Bandwidth

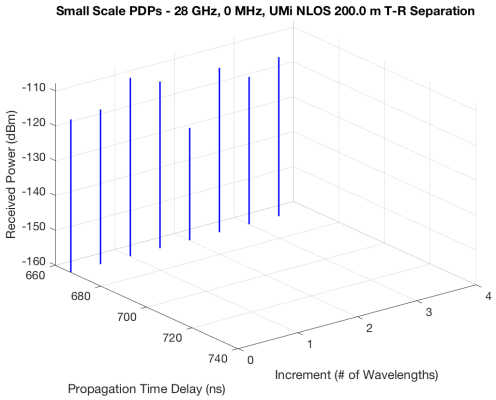

(c) Continuous Wave

Figure 5.3: Small-scale PDPs at each RX antenna element with half-wavelength spacing for (a) 800 MHz, (b) 100 MHz, and (c) 0 MHz RF bandwidth.

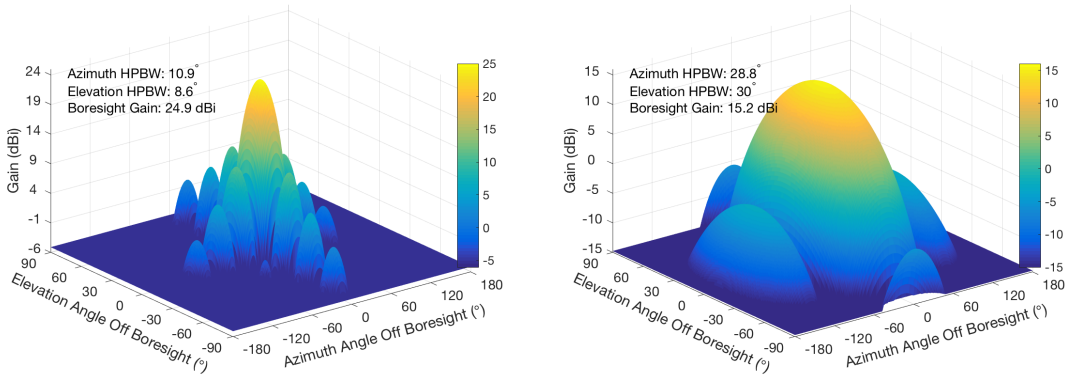

(a) (b)

Figure 5.4: Example antenna radiation patterns based on (5.3).

user-defined azimuth and elevation antenna HPBWs based on the omnidirectional PDPs produced by NYUSIM, the MPC power levels are weighted by a desired antenna pattern, such that the MPCs closest to a desired direction are amplified, while those farthest away are set to 30 dB down relative to the strongest MPC [66]. In NYUSIM, an antenna pattern emulating the horn antenna pattern used in the mmWave field measurements [2, 54] is used and is approximated as follows:

$$G(\phi,\theta) = \max\Big(G_0 \mathrm{sinc}^2\big(\mathrm{a}\cdot\sin(\phi)\big)\cos^2(\phi)\mathrm{sinc}^2\big(\mathrm{b}\cdot\sin(\theta)\big)\cos^2(\theta), \frac{\mathrm{G}_0}{1000}\Big)$$
$$\text{where } G_0 = \frac{41253\eta}{\phi_{3\mathrm{dB}}\theta_{3\mathrm{dB}}},\ \eta = 0.7,\ \mathrm{sinc}^2\left(\mathrm{a}\cdot\sin\left(\frac{\phi_{3\mathrm{dB}}}{2}\right)\right)\cos^2\left(\frac{\phi_{3\mathrm{dB}}}{2}\right) = \frac{1}{2},$$
$$\mathrm{sinc}^2\left(\mathrm{b}\cdot\sin\left(\frac{\theta_{3\mathrm{dB}}}{2}\right)\right)\cos^2\left(\frac{\theta_{3\mathrm{dB}}}{2}\right) = \frac{1}{2}. \tag{5.3}$$

where the term $\frac{G_0}{1000}$ is set according to the side-lobe level defined in the 3GPP channel model [66]. The corresponding example radiation patterns are illustrated in Fig. 5.4, which *match the gains and patterns of the horn antennas used in field measurements* [2].

5.3.4 Range Extension

Extensive mmWave propagation measurements conducted by NYU WIRELESS have shown that in dense urban environments, mmWave signals can cover around 200 m cell radius even under NLOS conditions [2, 54, 168], and is likely to reach 500 m in lightly populated urban and suburban areas. Furthermore, recent RMa propagation measurements at 73 GHz demonstrated over 10 km coverage range in clear weather [59]. To make NYUSIM cater for more users and wider applications, the maximum allowable T-R separation distance is extended from 500 m to 1 km in NYUSIM v1.6, by removing all the lower bounds on received power (including cluster power, subpath power, and lobe power), or equivalently, upper bounds on path loss, assuming there exits such a virtual receiver that can detect very low received power.

For LOS environments, calculated path loss beyond 500 m is still accurate using the NYUSIM path loss models (e.g., CI and CIH [50, 59]) since they are applicable to over 10 km distances. For NLOS environments, however, the NLOS path loss models employed in NYUSIM may not be accurate for distances larger than 500 m since they were developed for ranges within 500 m [50], thus caution should be given when setting the distance beyond 500 m for UMi or UMa NLOS scenarios. The dynamic range for multipath components in the extended range is extended to 220 dB from the default value of 190 dB used for distances no larger than 500 m.

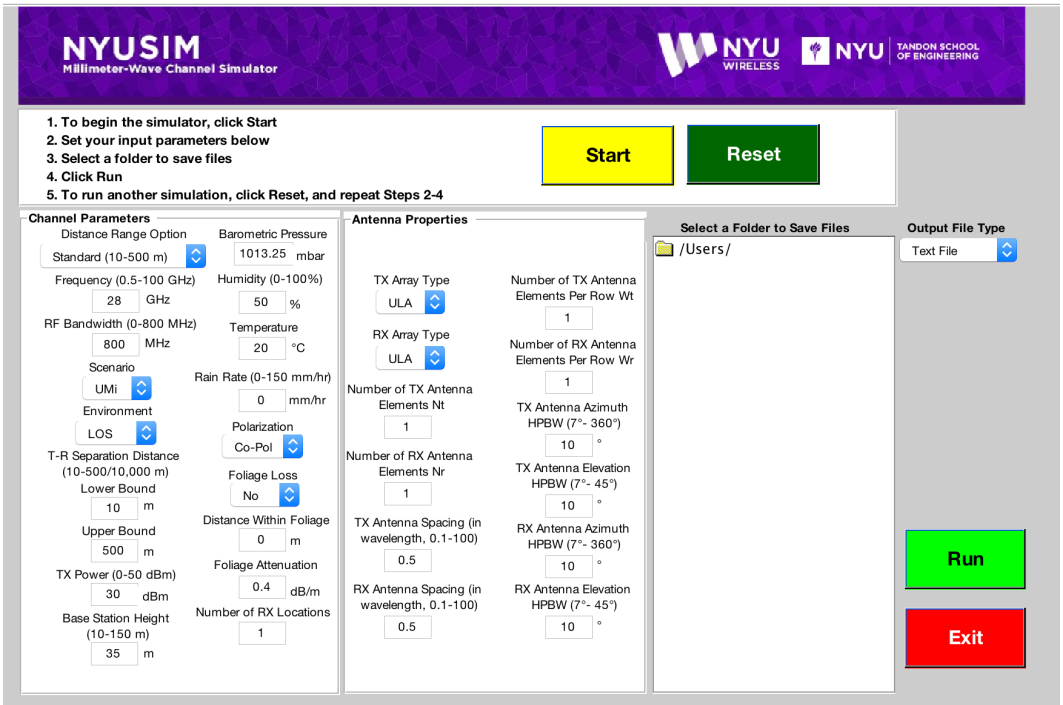

Figure 5.5: GUI of NYUSIM.

5.4 Graphical User Interface and Simulator Basics

Fig. 5.5 shows the graphical user interface (GUI) of NYUSIM. The simulator performs Monte Carlo simulations, generating certain numbers of samples of CIRs at specific T-R separation distances, where the number of samples and the range of T-R separation distances are to be specified by users, as explained in the following subsection. It takes about 22 minutes to generate and save 100 CIRs and all the output files (five .png files, seven sets of .txt files and seven .mat files for each CIR simulation run as detailed in Section 2.2) on a PC server with two processors (2.40 GHz and 2.39 GHz) and 96.0 GB RAM.

5.4.1 Input Parameters

There are 30 input parameters to the channel simulator, which are grouped into two main categories: *Channel Parameters* and *Antenna Properties*, as shown on the GUI in Fig. 5.5. The panel *Channel Parameters* contains 18 fundamental input parameters about the propagation channel, as listed and explained below:

1. Distance Range Option: a selectable parameter denoting the distance range. Two options, "Standard (10-500 m)", and "Extended (10-10,000 m)", are applicable. The default setting is "Standard (10-500 m)". For the distance range no larger than 500 m, the dynamic range (i.e., largest possible path loss) is set to 190 dB in NYUSIM based on field measurement results [2, 50, 54], while for the distance range beyond 500 m, the dynamic range is set to 220 dB.

2. Frequency (GHz): an editable parameter denoting the carrier frequency in GHz. The default value is 28 (GHz), and it can be varied from 0.5 to 100 (GHz) with at most one decimal point.

3. RF Bandwidth (MHz): an editable parameter denoting the RF bandwidth of the transmitted signal in MHz. The default value is 800 MHz, and it can be varied from 0 to 800 MHz. As the simulator was developed from real-world measurements obtained with an RF bandwidth of 800 MHz, it can only scale down from 800 MHz.

4. Scenario: a selectable parameter denoting the scenario. Three options, "UMi", "UMa", and "RMa", are applicable. The channel parameters for the UMi scenario are also used for the UMa and RMa scenarios in this simulator,

except that the RMa scenario has its own path loss model parameters. The default option is "UMi".

5. Environment: a selectable parameter denoting the environment, either LOS or NLOS. The default setting is LOS.

6. Lower Bound of T-R Separation Distance (m): an editable parameter denoting the smallest distance between the TX and RX in meters with at most one decimal place. The default value is 10 m, and it can be varied from 10 m to 500 m for the standard range (verified by extensive measurements by NYU), and 10 m to 10 km for the extended range, but no more than the upper bound of the T-R separation distance.

7. Upper Bound of T-R Separation Distance (m): an editable parameter denoting the largest distance between the TX and RX in meters with at most one decimal place. The default value is 500 m, and it can be varied from 10 m to 500 m for the standard range (verified by extensive measurements by NYU), and 10 m to 10 km for the extended range, but no less than the lower bound of the T-R separation distance.

8. TX Power (dBm): an editable parameter denoting the transmit power in dBm. The default value is 30 (dBm), and can be set to any value ranging from 0 to 50 (dBm).

9. Base Station Height (m): an editable parameter denoting the base station height in m. The default value is 35 (m) [66], and can be set to any value ranging from 10 to 150 (m) [59]. This base station height is only applicable to RMa modeling and is ignored for other scenarios.

10. Barometric Pressure: an editable parameter denoting the barometric pressure in mbar used in evaluating propagation path loss induced by dry air. The default and typical value is 1013.25 mbar (millibar) (i.e., nominal for sea level), and may range from 10^{-5} to 1013.25 (mbar) [211].

11. Humidity: an editable parameter denoting the relative humidity in percentage used in evaluating propagation path loss induced by vapor. The default value is 50 (%), and can be set to any number between 0 and 100 (%).

12. Temperature: an editable parameter denoting the temperature in degrees Celsius used in evaluating propagation path loss induced by haze/fog. The default and typical value is 20 (°C), and may range from -100 to 50 (°C) [211].

13. Rain Rate: an editable parameter denoting the rain rate in mm/hr used in evaluating propagation path loss induced by rain. The default value is 0 (mm/hr), and the typical range is 0 to 150 (mm/hr) [2].

14. Polarization: a selectable parameter denoting the polarization relation between the TX and RX antennas or antenna arrays. The default setting is Co-Pol (co-polarization), and can be changed to X-Pol (cross-polarization). The cross-polarization discrimination (XPD) can vary from 5 dB to 27 dB [212, 213, 214], depending on the frequency and environment. In this simulator, for Co-Pol, no extra loss will be added to the path loss, while an extra 25 dB loss will be added to the path loss for X-Pol due to polarization mismatch based on the measurement results in [214]. For more detailed background, please refer to [214].

15. Foliage Loss: a selectable parameter indicating whether or not foliage loss

will be considered in the simulation. The default setting is No (which implies foliage loss will not be considered), and can be changed to Yes (which means foliage loss will be considered).

16. Distance Within Foliage: an editable parameter representing the distance in meters that the transmitted signal travels within foliage. The default value is 0, and can be set to any non-negative number no larger than the lower bound of the T-R separation distance.

17. Foliage Attenuation: an editable parameter denoting the propagation loss induced by foliage in dB/m. The default value is 0.4 (dB/m) based on the measurement results in [214], and can be set to any value between 0 and 10 (dB/m). For more detailed background, please refer to [214].

18. Number of RX Locations: an editable parameter denoting the number of RX locations. It can be any positive integer number. The default value is 1, and can be set to any integer from 1 to 10,000.

The panel *Antenna Properties* contains 12 input parameters related to the TX and RX antenna arrays, as listed and explained below:

1. TX Array Type: a selectable parameter denoting the TX antenna array type. The default setting is ULA, and can be changed to URA.

2. RX Array Type: a selectable parameter denoting the RX antenna array type. The default setting is ULA, and can be changed to URA.

3. Number of TX Antenna Elements N_t: an editable parameter denoting the total number of TX antenna elements in the array. The default value is 1, and can be set to any integer from 1 to 128.

4. Number of RX Antenna Elements N_r: an editable parameter denoting the total number of RX antenna elements in the array. The default value is 1, and can be set to any integer from 1 to 64.

5. TX Antenna Spacing (in wavelength): an editable parameter denoting the spacing between adjacent TX antennas in the array in terms of the carrier wavelength. The default value is 0.5, and can be set to any positive number with up to one decimal place from 0.1 to 100. Note that larger antenna spacing leads to lower spatial correlation hence higher achievable rate [210]. Also, no antenna mutual coupling considered for simplicity, likely to result in more optimistic achievable rate for closely-spaced (e.g., less than 0.5 wavelength spacing) antennas [14].

6. RX Antenna Spacing (in wavelength): an editable parameter denoting the spacing between adjacent RX antennas in the array in terms of the carrier wavelength. The default value is 0.5, and can be set to any positive number with up to one decimal place from 0.1 to 100.

7. Number of TX Antenna Elements Per Row W_t: an editable parameter denoting the number of TX antennas in one dimension when the TX Array Type is ULA or URA, which should divide the number of TX antenna elements. The default value is 1.

8. Number of RX Antenna Elements Per Row W_r: an editable parameter denoting the number of RX antennas in one dimension when the RX Array Type is ULA or URA, which should divide the number of RX antenna elements. The default value is 1.

9. TX Antenna Azimuth HPBW (degrees): an editable parameter denoting the azimuth HPBW of the TX antenna (array) in degrees. The default value is 10°, and can be set to any value from 7° to 360° (since the smallest azimuth HPBW of the antennas used in the measurements for the simulator was 7°).

10. TX Antenna Elevation HPBW (degrees): an editable parameter denoting the elevation HPBW of the TX antenna (array) in degrees. The default value is 10°, and can be set to any value from 7° to 45° (since the smallest elevation HPBW of the antennas used in the measurements for the simulator was 7°).

11. RX Antenna Azimuth HPBW (degrees): an editable parameter denoting the azimuth HPBW of the RX antenna (array) in degrees. The default value is 10°, and can be set to any value from 7° to 360°.

12. RX Antenna Elevation HPBW (degrees): an editable parameter denoting the elevation HPBW of the RX antenna (array) in degrees. The default value is 10°, and can be set to any value from 7° to 45°.

It is worth noting that the HPBWs are only used for generating directional PDPs per users' requests. The HPBW in the input parameters is for the entire antenna array, instead of for each antenna element, when the number of antenna elements is more than one at the TX and/or RX. Conventionally, the HPBW of an antenna array is a function of the number of antenna elements and the antenna spacing, but in this simulator these three parameters (i.e., the HPBW, number of antenna elements, and antenna spacing) can be independently specified by the user, since there may be a wide range of beamforming approaches (e.g., digital, analog, hybrid), in all of which different individual antenna element types (e.g., patch antennas, vertical antennas, horns) may be used. To make the simulator as

general as possible, the number of individual antenna elements is specified (without specifying the gain or combining losses thereof) and the total array HPBW. Note that the antenna pattern and implementation details are only very loosely defined to specify the gain in the particular pointing (maximum gain) direction.

Since some antenna elements may have more gain or loss depending on the specific array type (e.g., ULA); that is, someone may choose to fabricate their individual array with more individual antenna element gain than another person will, and losses vary with fabrication process (e.g., on chip antenna elements have more loss when a lens is not used than if a lens is used). Instead of dealing with the myriad antenna fab and connection details needed to make an array — there are numerous variables — the total HPBW and the number of elements are allowed to be specified, without specifying the individual antenna element gain. For example, assuming there are four elements in an antenna array, where each element has 6 dB gain because they are patch or Yagi/directional or horn antennas for each element, then this array can have the same overall HPBW as a 16 element array with unity gain dipole or vertical elements.

Without specifying the specific antenna elements and their interconnected characteristics, only the HPBW is specified while the beam pattern is left undefined. Consequently, one has the freedom to implement an antenna pattern of their choice for system simulations, which may include interference from signals outside of the main gain direction. Besides the antenna pattern in (5.3), below are some other heuristic approaches of constructing one's own antenna pattern based on the specified HPBW, where the antenna gains in the following equations are all relative to an isotropic antenna.

- The antenna pattern employed in [52] has the following form:

$$G(\phi,\theta) = \max(G_0 e^{-\alpha\phi^2-\beta\theta^2}, \frac{G_0}{100}),\ \text{where } \alpha = \frac{4\ln(2)}{\phi_{3dB}^2},\ \beta = \frac{4\ln(2)}{\theta_{3dB}^2},\ G_0 = \frac{41253\eta}{\phi_{3dB}\theta_{3dB}} \tag{5.4}$$

  where $(\phi,\ \theta)$ denote the azimuth and elevation angle offsets from the boresight direction in degrees, G_0 is the maximum directive gain (boresight gain) in linear units, $(\phi_{3dB},\ \theta_{3dB})$ represent the azimuth and elevation HPBWs in degrees, $(\alpha,\ \beta)$ are parameters that depend on the HPBW values, and $\eta = 0.7$ is a typical average antenna efficiency.

- The radiation pattern of a sectored cell site antenna was employed in [215], where the azimuthal radiation pattern is modeled as a cardioid given by [215]

$$r(\theta) = \alpha[1 + \sin(\theta + \frac{\pi}{2})] \tag{5.5}$$

  where r is the gain of the antenna at azimuth angle θ from its maximum lobe and is a scaling factor. The elevation radiation pattern is an ellipse with the base station at a focus point [215]:

$$\frac{x^2}{a^2} + \frac{y^2}{b^2} = 1 \tag{5.6}$$

- A sectored antenna pattern model was introduced in [216], where constant directivity gains are assumed for the main lobe and the side lobe.

5.4.2 Output Folder Selection

To the right of the above two category panels (*channel parameters* and *antenna properties*) on the GUI, there is an option named "Select a Folder to Save Files". This option allows users to select a folder to save the output files (e.g., figures, data files) from the simulator. The default path is the disk that contains the current running folder. Users can select a folder inside the default path by clicking on the desired paths/folders.

5.4.3 Output File Type Selection

To the right of the folder selection option on the GUI, there is an option named "Output File Type". This option allows users to select a file type for the output data files from the simulator. The default type is *Text File*, and can be switched to *MAT File*, and *Both Text and MAT File*.

5.4.4 Operation of the GUI

Five basic steps, as shown on the top left panel on the GUI, need to be executed to run the channel simulator:

1. To begin (reset) the simulator, click Start (Reset)
2. Set your input parameters below
3. Select a folder to save files
4. Click Run
5. To run another simulation, click Reset, and repeat Steps 2-4

The meanings of these steps are detailed as follows. When opening the GUI for the first time, users shall click on the yellow button "Start" to initiate the simulator and enable the input of the GUI. Next, users can set and/or select the 30 input parameters according to their own needs; the simulator will execute the default values for each parameter if there is no input from the user. Then, users shall select a folder to save all the output files by clicking on the desired paths/folders under the option "Select a Folder to Save Files". Finally, users shall click on the light green button "Run" to run the simulations. While the simulator is running, a progress bar will pop up at the bottom left of the GUI, which informs users of the progress of the simulations. After the simulation is complete, the progress bar will disappear automatically, and the five figures generated from the first simulation run will pop up on the screen. To initiate another set of simulation runs (e.g., with different input parameter values), users shall click on the dark green button "Reset", after which all the input parameters from the previous simulation run will be set as the default input values. The simulator can be closed at any time by clicking the red button "Exit" on the bottom right of the GUI.

If the input parameter exceeds the predefined range shown on the NYUSIM GUI or is not reasonable/logical, an error message will pop up to let the user either reset the parameter on GUI or modify the NYUSIM source code without using the GUI to meet users' own needs. For example, if the input number of TX antenna elements per row W_t is larger than the input number of TX antenna elements N_t, a corresponding error message will pop up. Users shall click "OK" on the error bar, then click the dark green button "Reset" on the GUI to reset the input parameter, and the following steps are identical to those described above.

5.5 Output Files

5.5.1 Output Figures

For each simulation run, five figures will be generated and stored that are based on the particular results of the simulation that is being run, and an additional figure of path loss scatter plot will be generated and stored after N ($N \geq 1$) continuous simulation runs with the same input parameters are complete. Note that the T-R separation distance is not an input parameter, but, instead, the lower bound and upper bound of the T-R separation distance are input parameters, such that the actual T-R separation distance will vary automatically among different simulation runs. Regardless of the number of simulation runs (RX locations), the five figures generated from the first simulation run, as well as the last figure generated for N ($N \geq 1$) continuous simulation runs with the same input parameters, will pop up on the screen for visual purposes. The contents of those figures are as follows:

- 3D AoD power spectrum, as illustrated in Fig. 5.6.
- 3D AoA power spectrum, as shown in Fig. 5.7.
- A sample omnidirectional PDP, as displayed in Fig. 5.8. Some fundamental information such as the frequency, environment, T-R separation distance, RMS delay spread, omnidirectional received power, omnidirectional path loss, and PLE [2, 54] is displayed on the PDP plot. The red solid line on the PDP denotes the noise threshold (i.e., the minimum received power of each resolvable multipath component) determined by the transmit power, dynamic range of the measurement system (180 dB), and a 10 dB SNR, i.e., the threshold equals the transmit power in logarithmic scale minus 170 dB.

- A sample directional PDP with strongest power, where directional antenna gain patterns are implemented at the TX and/or RX, as depicted in Fig. 5.9. This figure is generated by allowing users to implement arbitrary directional antenna patterns (gains and HPBWs) in an omnidirectional PDP, since directional antennas/antenna arrays will be utilized at the TX and/or the RX in a realistic mmWave communication system to provide gains to compensate for the higher free space path loss at mmWave frequencies. To obtain the directional PDP with the strongest received power, NYUSIM searches for the best pointing angle out of all possible pointing angles, using the specified antenna details (i.e., azimuth and elevation HPBWs of TX and RX antennas) after first generating the omnidirectional PDP, such that the pointing angle of the TX and RX are found that gives the strongest received power. The TX/RX antenna gain pattern is calculated by NYUSIM using Eq. (5.4) by employing the azimuth and elevation HPBWs of TX and RX antennas specified by the user on the GUI. This feature makes the channel simulator more valuable as it shows how a PDP will look like in a channel with directional antennas/antenna arrays used at the communication link end. On the directional PDP figure, relevant channel and antenna parameters, such as the frequency, environment, T-R separation distance, directional RMS delay spread, directional received power, directional path loss, directional PLE, and TX and RX antenna HPBWs and gains, are also displayed, where the directional path loss equals the transmit power plus TX and RX antenna gains, minus the directional received power [49, 54, 61].

- A series of PDPs over each receive antenna element obtained using Eq. (3) of [87], as shown in Fig. 5.10, where the antenna array type, number of

antenna elements, and antenna element spacing are specified on the GUI by the user.

- A path loss scatter plot entitled "PathLossPlot" generated after N ($N \geq 1$) continuous simulation runs with the same input parameters, as illustrated in Fig. 5.11. This figure shows omnidirectional path loss and directional path loss values for over the entire distance range generated from the N ($N \geq 1$) continuous simulation runs, along with the fitted PLE and shadow fading standard deviation using the MMSE method [50, 61]. In the legend of the figure "PathLossPlot", n denotes the PLE, σ is the shadow fading standard deviation, "omni" denotes omnidirectional, "dir" represents directional, and "dir-best" means the direction with the strongest received power. For producing the directional path loss at each RX location, NYUSIM searches for all possible pointing angles in increments of the azimuth and elevation HPBWs of the TX/RX antenna specified by the user on the GUI after first generating the omnidirectional PDP. The TX/RX antenna gain pattern is calculated by NYUSIM using Eq. (5.4) based on the azimuth and elevation HPBWs of TX and RX antennas specified by the user on the GUI. The directional path loss is equal to the transmit power plus the TX and RX antenna gains, minus the directional received power [2, 54, 217, 218]. For generating Fig. 5.11, the antenna azimuth and elevation HPBWs are set to 10.9° and 8.6°, respectively, at both the TX and the RX, to match the antenna HPBWs used in the 28 GHz measurements [2, 54]. The simulated PLE and shadow fading standard deviation values agree well with the measured results presented in Table V and Table VIII of [54]. Directional path loss and directional PLE will always be larger (i.e., a directional channel is more lossy) than the omnidirectional

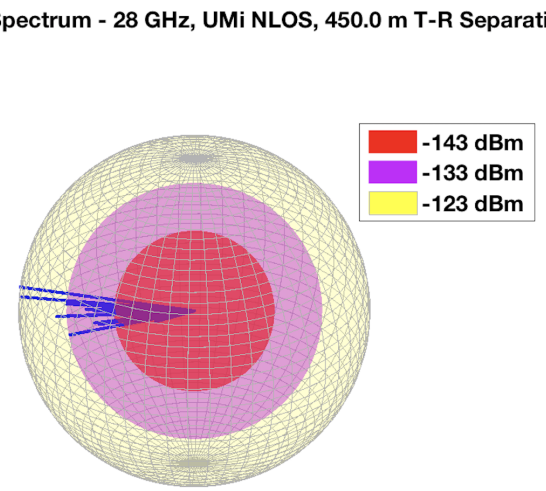

Figure 5.6: Example of a 3D AOD power spectrum generated from NYUSIM. Top view of azimuth plane.

case, because the directional antenna will spatially filter out many multipath components due to its directional pattern, such that the RX receives fewer multipath components hence less energy, thereby the directional path loss is higher after removing the antenna gain effect from the received power [54, 61].

If the generated path loss in a simulation run exceeds the corresponding dynamic range, i.e., if there are no detectable multipath components, then it will be shown on the output figures that "No Detectable Multipath Components above the Threshold of XXX dBm", where the threshold value equals the transmit power in dBm minus the dynamic range in dB for that simulation run, such as -190 dBm. Note that no path loss data points will be shown on the path loss scatter plot as long as there are no detectable multipath components in the omnidirectional PDP, regardless of the directional PDP. Users may modify this in "NYUSIM_MainCode.m" per their own needs.

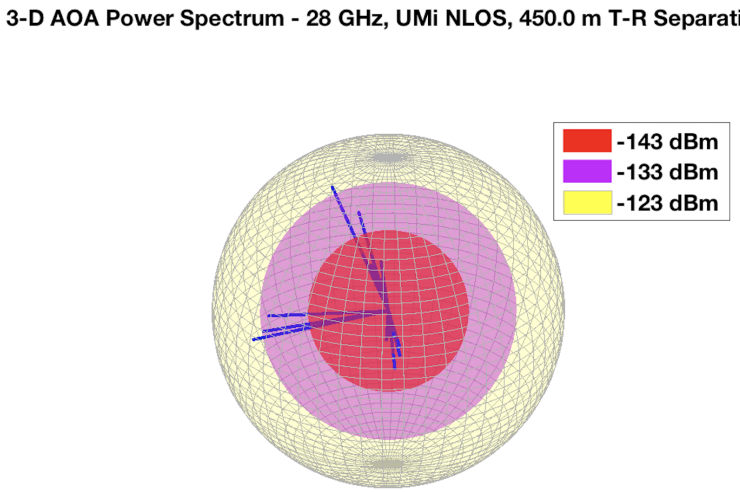

Figure 5.7: Example of a 3D AOA power spectrum generated from NYUSIM. Top view of azimuth plane.

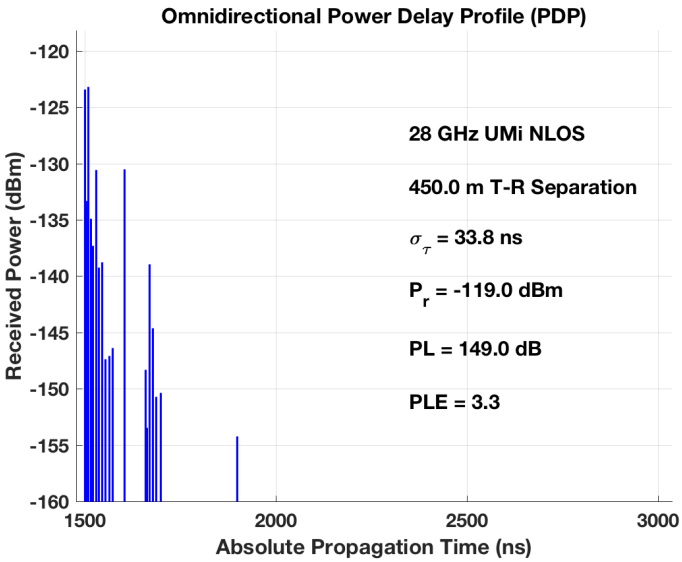

Figure 5.8: Example of an omnidirectional PDP generated from NYUSIM.

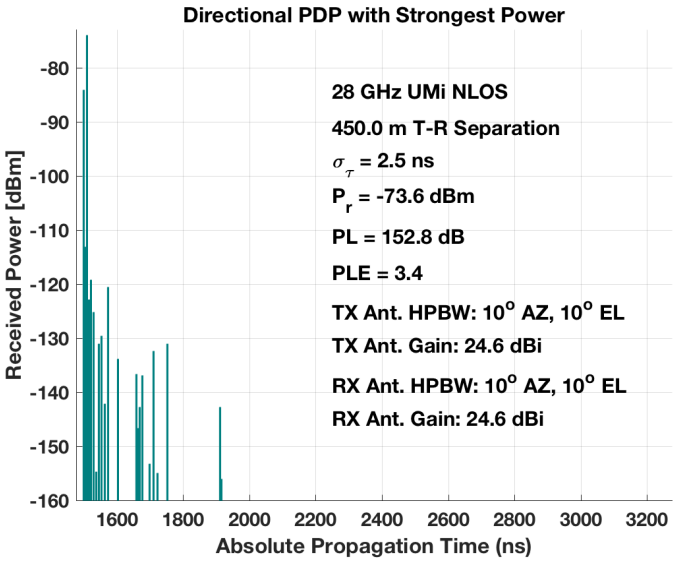

Figure 5.9: Example of an directional PDP with the strongest received power generated from NYUSIM. "Ant." denotes antenna.

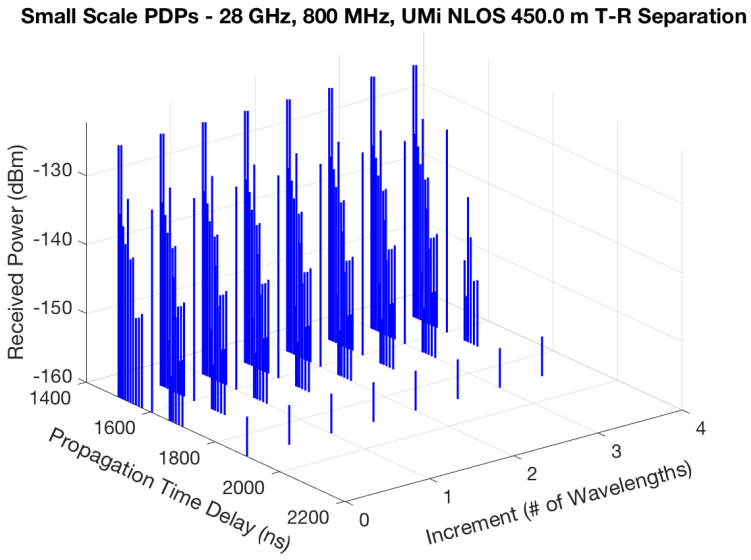

Figure 5.10: Example of the PDPs over different receive antenna elements generated from NYUSIM.

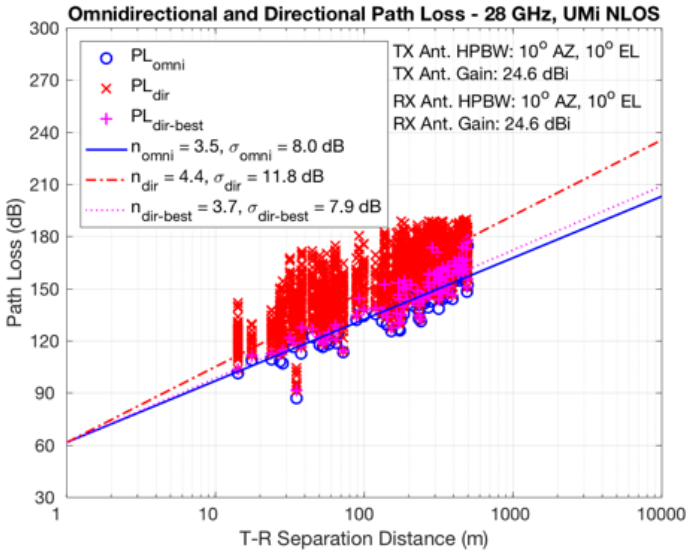

Figure 5.11: Example of a scatter plot showing the omnidirectional and directional path loss values generated from NYUSIM with 100 simulation runs for the 28 GHz UMi LOS scenario.n denotes the pass loss exponent (PLE), σ is the shadow fading standard deviation, "omni" denotes omnidirectional, "dir" represents directional, "dir-best" means the direction with the strongest received power, "Ant." denotes antenna, "AZ" and "EL" stand for azimuth and elevation, respectively.

5.5.2 Output Data Files

For each simulation run, five sets of .txt files and five corresponding .mat files are generated, namely, "AODLobePowerSpectrum$n$_Lobe$x$.txt", "AODLobePowerSpectrum$n$.mat", "AOALobePowerSpectrum$n$_Lobe$x$.txt", "AOALobePowerSpectrum$n$.mat", "OmniPDPn.txt", "OmniPDPn.mat", "DirectionalPDPn.txt", "DirectionalPDPn.mat", "SmallScalePDPn.txt", and "SmallScalePDPn.mat", where n denotes the n^{th} RX location (i.e., n^{th} simulation run), and x represents the x^{th} spatial lobe. After N ($N \geq 1$) continuous simulation runs with the same input parameters are complete, another three .txt files and three corresponding .mat files are produced, i.e., "BasicParameters.txt", "BasicParameters.mat", "OmniPDPInfo.txt", "OmniPDPInfo.mat", "DirPDPInfo.txt", and "DirPDPInfo.mat".

Each text file "AODLobePowerSpectrum$n$_Lobe$x$" is associated with the output figure of 3D AoD power spectrum, and contains five parameters (columns) of each resolvable multipath component in an AoD spatial lobe, which are listed and explained below.

1. pathDelay (ns): an array containing the absolute propagation time delays of all resolvable multipath components in nanoseconds (ns).

2. pathPower (mWatts): an array containing the received powers of all resolvable multipath components in mWatts.

3. pathPhase (rad): an array containing the phases of all resolvable multipath components in radians.

4. AOD (degree): an array containing the azimuth AoDs of all resolvable multipath components in degrees.

5. ZOD (degree): an array containing the zenith angles of departure (ZoDs) of all resolvable multipath components in degrees.

Note that inside the corresponding .mat file "AODLobePowerSpectrum$n$" is a structure containing the lobe matrices, each of which is composed of five columns as described above. Each text file "AOALobePowerSpectrum$n$_Lobe$x$" is associated with the output figure of 3D AoA power spectrum, and contains five parameters (columns) of each resolvable multipath component in an AoA spatial lobe, which are listed and explained below.

1. pathDelay (ns): an array containing the absolute propagation time delays of all resolvable multipath components in nanoseconds (ns).

2. pathPower (mWatts): an array containing the received powers of all resolvable multipath components in mWatts.

3. pathPhase (rad): an array containing the phases of all resolvable multipath components in radians.

4. AOA (degree): an array containing the azimuth AoAs of all resolvable multipath components in degrees.

5. ZOA (degree): an array containing the zenith angles of arrival (ZoAs) of all resolvable multipath components in degrees.

Note that inside the corresponding .mat file "AOALobePowerSpectrum$n$" is a structure containing the lobe matrices, each of which is composed of five columns as described above. Each .txt and .mat file "OmniPDPn" is associated with the output figure of omnidirectional PDP, and contains two columns: the first column denotes the propagation time delay in nanoseconds, and the second column

represents the received power in dBm. Each .txt and .mat file "DirectionalPDPn" is associated with the output figure of omnidirectional PDP with directional antenna gain patterns implemented, and contains two columns: the first column denotes the propagation time delay in nanoseconds, and the second column represents the received power in dBm. Each .txt and .mat file "SmallScalePDPn" is associated with the output figure of the series of omnidirectional PDPs over RX antenna elements, and contains three columns: the first column denotes the receiver antenna separation in terms of number of wavelengths, the second column is the propagation time delay in nanoseconds, and the third column represents the received power in dBm. Note that the noise power is set to -150 dBm for visual purpose. The text file "BasicParameters.txt" and the .mat file "BasicParameters.mat" subsume all the input parameter values as shown on the GUI when running the simulation.

The text file "OmniPDPInfo.txt" and the .mat file "OmniPDPInfo.mat" contain five columns where each column represents a key parameter for each of the N omnidirectional PDPs from N continuous simulation runs. The parameters are listed and explained below.

1. T-R Separation Distance (m)
2. Received Power (dBm): omnidirectional received power in dBm
3. Path Loss (dB): omnidirectional path loss in dB
4. RMS Delay Spread (ns): omnidirectional RMS delay spread in nanosecond (ns)
5. Ricean K-factor (dB): ratio of the strongest power of the multipath component (the first arriving multipath component in LOS) to the sum of powers of the

other multipath components [205], converted from linear to the dB scale.

The text file "DirPDPInfo.txt" and the .mat file "DirPDPInfo.mat" contain 11 columns where each column represents a key parameter for each of the directional PDPs from N continuous simulation runs, where the same kind of parameters from each simulation run are cascaded in the same column. The parameters are listed and explained below.

1. Simulation run number
2. T-R Separation Distance (m)
3. Time Delay (ns): absolute propagation time delay of each resolvable multipath component in ns
4. Received Power (dBm): received power of each resolvable multipath component in dBm without antenna gains
5. Phase (rad): phase of each resolvable multipath component in radians
6. Azimuth AoD (degree): azimuth AoD of each resolvable multipath component in degrees
7. Elevation AoD (degree): elevation AoD of each resolvable multipath component in degrees
8. Azimuth AoA (degree): azimuth AoA of each resolvable multipath component in degrees
9. Elevation AoA (degree): elevation AoA of each resolvable multipath component in degrees

10. Path Loss (dB): directional path loss obtained by aligning the TX/RX antenna boresight on the AoD/AoA of each resolvable multipath component. The directional path loss equal the transmit power plus the TX/RX antenna boresight gains, minus directional received power.

11. RMS Delay Spread (ns): directional RMS delay spread in ns for each directional PDP

5.6 Applications of NYUSIM

The output figure and data files generated from NYUSIM can be used in various ways based on users' needs, e.g., to simulate channel impulse responses for mmWave systems, to investigate MIMO performance, etc.

5.6.1 MIMO Channel Condition Number

First, an example of how to obtain the condition number of a MIMO channel by making use of the output data files "BasicParameters.mat" and "DirPDPInfo.mat" is shown, assuming OFDM modulation is utilized.

The condition number is defined as the ratio of the largest to smallest singular value in the singular value decomposition of a matrix, and is a metric to characterize the quality of MIMO channels in the context of wireless communications [16, 168, 219, 220]. The condition number will be high (e.g., over 20 dB) if the minimum singular value is close to zero, and will be 0 dB if singular values are equal. Physically, a small condition number value (e.g., below 20 dB) indicates good orthogonality of different sub-channels (a sub-channel usually has a distinct spatial direction), and the channel gains are comparable in different spatial directions. The rank of a

matrix is the dimension of the vector space generated (or spanned) by its columns (or rows) [221], and it determines how many data streams can be multiplexed over the channel in the context of MIMO communications [24, 219, 222]. The condition number is related to the rank of a matrix: a low condition number usually corresponds to a high rank and vice versa; the matrix has full rank (the highest rank) when the condition number is equal or close to 0 dB (the lowest theoretical condition number).

Let's look at the condition number of a MIMO channel matrix for a single narrowband sub-carrier in an OFDM system. The output data files "BasicParameters.mat" and "DirPDPInfo.mat" contain paramount parameters of each resolvable multipath component, which will be useful in generating the MIMO channel coefficient for an OFDM sub-carrier. Take ULAs at both the transmitter and receiver for example, the equation for generating such a channel coefficient is provided below, which is adapted from Eq.(2) in [166]:

$$h_{m,k}(f) = \sum_{p} \alpha_{m,k,p} e^{j\Phi_{m,k,p}} e^{-j2\pi f \tau_{m,k,p}} e^{-j2\pi d_T m \sin(\phi_{m,k,p})} e^{-j2\pi d_R k \sin(\varphi_{m,k,p})} \tag{5.7}$$

where $h_{m,k}(f)$ denotes the MIMO channel coefficient between the m^{th} transmit antenna and the k^{th} receive antenna for the sub-carrier f, p represents the p^{th} resolvable multipath component, α is the amplitude of the channel gain, Φ denotes the phase of the multipath component, τ represents the time delay, d_T and d_R are the antenna element spacing at the transmitter and receiver, respectively, while ϕ and φ denote the azimuth angle of departure and angle of arrival, respectively. All of the above parameters can be extracted from the files "BasicParameters.mat" and "DirPDPInfo.mat". For each sub-carrier f in a MIMO-OFDM system, there exists

an $N_t \times N_r$ channel matrix H whose elements are $h_{m,k}(f)$, where $m = 1, ..., N_t$ and $k = 1, ..., N_r$. The condition number of H can be obtained consequently.

Using the above mentioned approach, and the input parameters on the NYUSIM GUI with the following values:

- Frequency: 28 GHz
- RF bandwidth: 800 MHz
- Scenario: UMi
- Environment: LOS
- Lower Bound of T-R Separation Distance: 100 m
- Upper Bound of T-R Separation Distance: 100 m
- TX Power: 30 dBm
- Base Station Height: 35 m
- Barometric Pressure: 1013.25 mbar
- Humidity: 50%
- Temperature: 20°C
- Rain Rate: 0 mm/hr
- Polarization: Co-Pol
- Foliage Loss: No
- Number of RX Locations: 100

- TX Array Type: ULA
- RX Array Type: ULA
- Number of TX Antenna Elements N_t: 2
- Number of RX Antenna Elements N_r: 2
- TX Antenna Spacing: 0.5 wavelength
- RX Antenna Spacing: 0.5 wavelength
- Number of TX Antenna Elements Per Row W_t: 2
- Number of RX Antenna Elements Per Row W_r: 2
- TX Antenna Azimuth HPBW: 10°
- TX Antenna Elevation HPBW: 10°
- RX Antenna Azimuth HPBW: 10°
- RX Antenna Elevation HPBW: 10°

and assuming the frequency interval between adjacent sub-carriers is 500 kHz, which corresponds to 800 MHz/500 kHz = 1600 sub-carriers, 100 simulation runs (i.e., set the number of RX locations to 100) are performed to emulate 100 random MIMO channel realizations with the input parameters described above. Then the following changes are made to the four input parameters below with all the other input parameter values remaining the same:

- Number of TX Antenna Elements N_t: 3
- Number of RX Antenna Elements N_r: 3

- Number of TX Antenna Elements Per Row W_t: 3
- Number of RX Antenna Elements Per Row W_r: 3

Fig. 5.12 illustrates the empirical CDF of the condition number of channel matrices for OFDM sub-carriers with the above two sets of input parameters in one of the 100 simulation runs. The empirical CDF of the corresponding rank of the channel matrices are plotted in Fig. 5.13, where the rank here is defined as the number of singular values of the channel matrix that are larger than $\sigma_m/1000$, where σ_m is the maximum singular value of the channel matrix. By this definition of rank, the singular values that are 30 dB smaller than the maximum singular value are essentially ignored, which is physically reasonable since the singular value is a measure of the channel gain along its corresponding singular vector and it makes little sense to consider the direction with an extremely small channel gain. It is apparent from Fig. 5.12 that the condition numbers of the individual OFDM sub-carriers for a 3×3 MIMO channel is about 18 dB larger compared to the 2×2 case on average, and the relatively large condition number of the 3×3 channel matrix may stem from the fact that the matrix is rank deficient, as evident from Fig. 5.13, in which about 96% of the channel matrices have a rank of 2 instead of 3 (full rank).

Based on the results from the 100 random simulation runs, it is found that the average median value of the condition numbers of the channel matrices for individual sub-carriers over the 100 simulation runs is around 13 dB (i.e., the difference in dB between the largest and smallest singular value of the channel matrix is 13 dB), and the average matrix rank is 2. When the numbers of TX and RX antenna elements are both changed to 3, the average median value of the

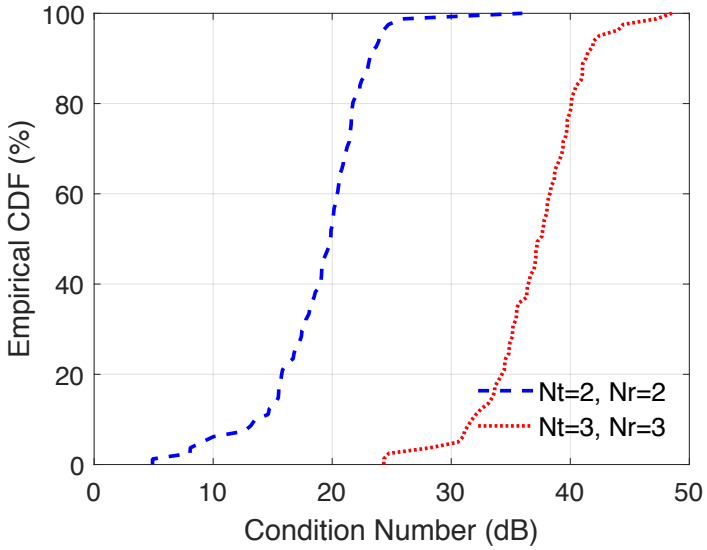

Figure 5.12: Empirical CDF of the condition number of channel matrices for OFDM sub-carriers with different transmit and receive antenna elements N_t and N_r for MIMO-OFDM channels in one simulation run.

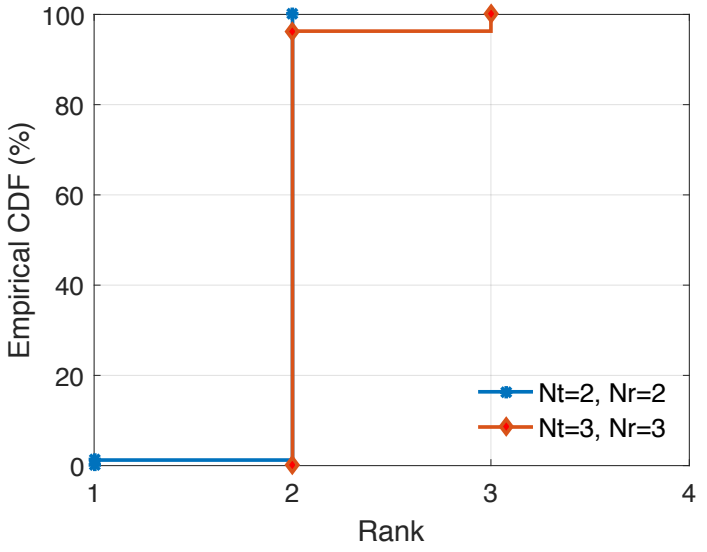

Figure 5.13: Empirical CDF of the rank of channel matrices for OFDM sub-carriers with different transmit and receive antenna elements N_t and N_r for MIMO-OFDM channels in one simulation run.

condition number increase to 31 dB, with a mean rank of roughly 2, indicating that two spatial streams can be sent simultaneously using the spatial multiplexing technique in this case.

The MATLAB code for extracting channel coefficients based on Eq. (5.7), generating the channel matrix for each sub-carrier frequency, and calculating the condition number and rank in the example above is contained in the package named "Application Example Code" available on the NYUSIM downloading website.

5.6.2 MIMO Channel Spectral Efficiency

Chapters 6 and 8 will demonstrate MIMO channel spectral efficiencies obtained using NYUSIM, and will compare with the results obtained using the 3GPP channel model.

5.7 Concluding Remarks

This chapter presented the development of an open-source channel software simulator, NYUSIM, developed from extensive broadband propagation measurements at mmWave frequencies. NYUSIM recreates wideband PDPs/CIRs and channel statistics for a variety of carrier frequencies, RF bandwidths, antenna beamwidths, environment scenarios, and atmospheric conditions, and is equipped with a GUI that makes the simulator more user-friendly. Over 10,000 downloads have already been logged by major corporations and universities worldwide. Simulated results from NYUSIM match well with the measured data. NYUSIM can be employed to perform various other types of analysis and is useful for 5G communication system development and deployment.

Chapter 6

Investigation and Comparison of 3GPP and NYUSIM Channel Models for Impact on System Performance

As shown in Chapters 2 and 5, the extensive measurements in NYC showed there are major difference in the temporal and spatial statistics used by 3GPP and those found in the field by NYU WIRELESS. Hence, it is important to quantify how different channel models would impact the analysis or simulation of wireless systems for 5G networks. This chapter provides a summary of the key parameters of the 3GPP TR 38.901 Release 14 [66] and NYUSIM [51] channel models, examples of methodologies/simulations/calculations on how to apply the channel models to evaluate 5G mmWave channel performance, and demonstration of the wide-ranging results produced. The most remarking results are as follows:

- In the case of cell range prediction, the different large-scale path loss models and shadow fading values in the 3GPP and NYUSIM channel models lead to a noticeable difference on the cell range evaluation given a certain cell-edge SNR.

- In terms of the eigenvalue properties of the channel, one model predicts significantly more dominant eigen modes than the other. This implies that the spatial degrees of freedom predicted by both channel models are quite different, hence resulting in different numbers of available spatial streams to be multiplexed.

- In terms of spectrum efficiency, the performance of a single-cell single-user is a base case. Which channel model predicts higher spectral efficiency depends on the number of transmitted data streams, and NYUSIM predicts a much higher occurrence of peak rates than the 3GPP model when the number of data streams is small (e.g., no more than four).

- Extending the single-cell case to a multi-cell multi-user case, a new HBF algorithm is proposed. It will be shown that the median values of per-user spectrum efficiency is roughly half for the 3GPP model relative to the NYUSIM model when there are a relatively small number of RF chains at each BS.

6.1 Recommended Parameter Values

6.1.1 LOS Probability Model

LOS probability denotes the probability that a given user terminal (UT) or UE is in a LOS condition with respect to the BS. LOS probability models in 3GPP [66] and NYUSIM [51, 223] channel models for UMi and UMa scenarios are summarized in Tables 6.1 and 6.2, respectively. More information is detailed below.

6.1.1.1 LOS Probability Model in the 3GPP Channel Model

The LOS probability models for various scenarios in 3GPP are provided in Table 7.4.2-1 in [66]. The LOS probability model is a function of the two-dimensional (2D) T-R separation distance, and sometimes a function of the TX and RX heights. It is inherited and modified from the previous LOS probability model derived for sub-6 GHz bands by 3GPP [225].

6.1.1.2 LOS Probability Model in NYUSIM

The NYUSIM LOS probability model has a similar form to the one in the 3GPP channel model, but with the entire formula (i.e., the second equation in Table 7.4.2-1 in [66]) squared and the parameter values updated based statistical modeling from a high resolution ray-tracing approach now described. For a given TX location in Manhattan, a circle was discretized in 100 evenly-spaced points on the circumference around the TX location and overlaid on an aerial building map. For each position along the circle external to a building or obstruction, ray-tracing was used to draw a line from the RX to the TX. If that line to the TX penetrated through at least one building, the corresponding initial position at radius R on the circle was

Table 6.1: LOS probability models in the UMi scenario [47, 66, 224].

	LOS probability models	**Parameters**
3GPP	**Outdoor users:** $P_{\text{LOS}}(d_{\text{2D}}) = \min(d_1/d_{\text{2D}}, 1)(1 - \exp(-d_{\text{2D}}/d_2)) + \exp(-d_{\text{2D}}/d_2)$ **Indoor users:** Use $d_{\text{2D-out}}$ in the formula above instead of d_{2D}	$d_1 = 18$ m $d_2 = 36$ m
NYUSIM (squared) model	**Outdoor users:** $P_{\text{LOS}}(d_{\text{2D}}) = (\min(d_1/d_{\text{2D}}, 1)(1 - \exp(-d_{\text{2D}}/d_2)) + \exp(-d_{\text{2D}}/d_2))^2$	$d_1 = 22$ m $d_2 = 100$ m

Table 6.2: LOS probability models for the UMa scenario [47, 66, 224].

	LOS probability models	**Parameters**
3GPP	**Outdoor users:** $P_{\text{LOS}} = \begin{cases} 1, & d_{\text{2D}} \leq 18 \text{ m} \\ \left[\frac{d_1}{d_{\text{2D}}} + \exp\left(-\frac{d_{\text{2D}}}{d_2}\right)\left(1 - \frac{d_1}{d_{\text{2D}}}\right)\right]\left(1 + C'(h_{\text{UT}})\frac{5}{4}\left(\frac{d_{\text{2D}}}{100}\right)^3 \exp\left(-\frac{d_{\text{2D}}}{150}\right)\right), & 18 \text{ m} < d_{\text{2D}} \end{cases}$ where, $C'(h_{\text{UT}}) = \begin{cases} 0, & h_{\text{UT}} \leq 13 \text{ m} \\ \left(\frac{h_{\text{UT}}-13}{10}\right)^{1.5}, & 13 \text{ m} \leq h_{\text{UT}} \leq 23 \text{ m} \end{cases}$ **Indoor users:** Use $d_{\text{2D-out}}$ in the formula above instead of d_{2D}	$d_1 = 18$ m $d_2 = 63$ m
NYUSIM (squared) model	**Outdoor users:** $P_{\text{LOS}} = \begin{cases} 1, & d_{\text{2D}} \leq 20 \text{ m} \\ \left(\left[\frac{d_1}{d_{\text{2D}}} + \exp\left(-\frac{d_{\text{2D}}}{d_2}\right)\left(1 - \frac{d_1}{d_{\text{2D}}}\right)\right]\left(1 + C'(h_{\text{UT}})\frac{5}{4}\left(\frac{d_{\text{2D}}}{100}\right)^3 \exp\left(-\frac{d_{\text{2D}}}{150}\right)\right)\right)^2, & 20 \text{ m} < d_{\text{2D}} \end{cases}$	$d_1 = 20$ m $d_2 = 160$ m

denoted as an NLOS position, otherwise it was denoted as a LOS position. This was repeated for all positions along the circle circumference, and the ratio of the number of LOS positions to the total number of positions along the circle provided the LOS probability. This was performed over radii ranging from 10 m to 200 m, in increments of 1 m [52], and for four TX locations.

Fig. 6.1 illustrates the LOS probability models in the 3GPP and NYUSIM channel models in UMi and UMa scenarios for a UE height of 1.5 m. As shown by Fig. 6.1, the 3GPP LOS probability model has clearly a non-zero tail at large distances (several hundred meters), which is not likely to be true in urban environments where numerous tall buildings exist, while NYUSIM shows essentially zero probability at large distances in urban areas which is different from the 3GPP model. On the other hand, for T-R separation distances smaller than about 120 m (for UMi) or 160 m (for UMa), NYUSIM predicts a larger LOS probability compared to 3GPP. Through 1000 random channel simulation runs for the UMi street canyon scenario over distances from 10 m to about 300 m (where cell size was based on the condition that 95% of the area within a cell has an SNR $\geq$ 5 dB, detailed in Section V-B), the simulated LOS probability is 9.1% and 17.2% using 3GPP and NYUSIM models, respectively. The difference in the LOS probability impacts spectral efficiency, since LOS facilitates stronger mmWave propagation (i.e., larger SNR) compared to the NLOS condition due to more severe diffraction loss at mmWave frequencies than at sub-6 GHz.

6.1.2 Large-Scale Path Loss Model

For a communication link with TX power P_T, the received power P_R [dBm] = P_T [dBm] + G_T [dB] + G_R [dB] - PL [dB] [168], where G_T and G_R are the TX

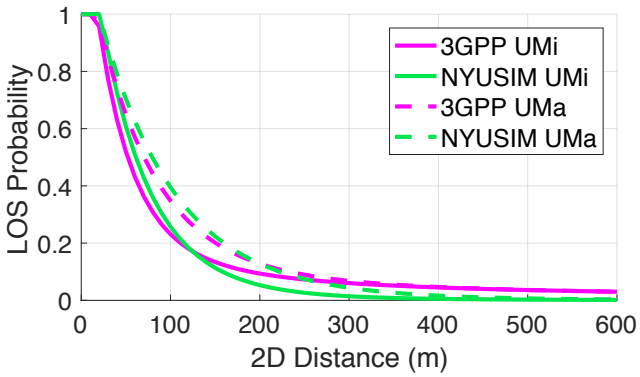

Figure 6.1: Comparison of LOS probability models in the 3GPP channel model [66] and NYUSIM [51] in UMi and UMa scenarios for a UE height of 1.5 m.

and RX antenna gain corresponding to F_{tx} and F_{rx} in Eq. (2.6) at a specific angle, respectively, and PL denotes the large-scale path loss. Large-scale path loss models in 3GPP and NYUSIM are listed and compared in Table 6.3 and Table 6.4. for the UMi and UMa scenarios, respectively.

6.1.2.1 Large-Scale Path Loss Model in the 3GPP Channel Model

It is clear from Table 6.3 that in the UMi street canyon LOS scenario, the CI path loss model is utilized for d_{3D} smaller than the breakpoint distance d_{BP}. After the breakpoint distance, a new term involving the BS and UE heights is added to the CI model, where the BS height is set to 10 m, and the UE height ranges from 1.5 m to 22.5 m. In the UMi street canyon NLOS scenario, the ABG path loss model is adopted with a term accounting for the UE height added to it, while the CI model is listed as an optional path loss model. Similar situations exist in the UMa scenario, except that the BS height is changed to 25 m.

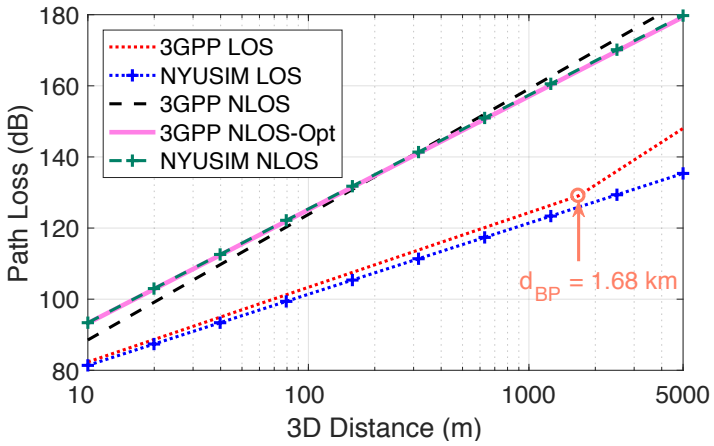

Figure 6.2: Path loss models in the 3GPP channel model and NYUSIM in UMi LOS and NLOS scenarios for a BS height of 10 m and a UE height of 1.5 m. "Opt" denotes the optional NLOS CI path loss model in the 3GPP channel model.

6.1.2.2 Large-Scale Path Loss Model in NYUSIM

In both UMi and UMa scenarios, the single-slope CI model is employed in NYUSIM, since breakpoints were never observed in outdoor measurements in Manhattan or Austin.

Fig. 6.2 illustrates the path loss models in the 3GPP channel model and NYUSIM in UMi LOS and NLOS scenarios for a BS height of 10 m and a UE height of 1.5 m. Fig. 6.2 shows that for the UMi LOS scenario, the 3GPP ABG model predicts larger path loss as compared to the NYUSIM CI model, and there exists an extremely large breakpoint distance of 1.68 km which well exceeds typical UMi cell sizes hence reverting the double-slope model to a single-slope model. For the NLOS environment, the 3GPP ABG model predicts less mean path loss for T-R separation distances smaller than 296 m when compared with the NYUSIM CI model. On the other hand, the 3GPP optional NLOS CI model matches the NYUSIM NLOS CI model very well.

Table 6.3: Path loss models in the UMi scenario [47, 52, 66].

	PL is in dB, f_c is in GHz, $d_{\mathbf{2D}}$ and $d_{\mathbf{3D}}$ are in meters	**Shadow fading std [dB]**	**Applicability range and Parameters**
	3GPP [66]		
3GPP UMi LOS	$\mathrm{PL} = \begin{cases} 32.4 + 21\log_{10}(d_{3D}) + 20\log_{10}(f_c), & 10 \text{ m} \le d_{2D} \le d'_{BP} \\ 32.4 + 40\log_{10}(d_{3D}) + 20\log_{10}(f_c) - 9.5\log_{10}((d'_{BP})^2 & \\ +(h_{BS} - h_{UT})^2), & d'_{BP} \le d_{2D} \le 5000 \text{ m} \end{cases}$ where d'_{BP} is specified in the note below.	$\sigma_{SF} = 4$	$0.5 \le f_c \le 100$ GHz $h_{BS} = 10$ m $1.5 \text{ m} \le h_{UT} \le 22.5$ m
3GPP UMi NLOS	$\mathrm{PL} = \max(\mathrm{PL}_{UMi-LOS}, \mathrm{PL}'_{UMi-NLOS})$ $\mathrm{PL}'_{UMi-NLOS} = 35.3\log_{10}(d_{3D}) + 22.4 + 21.3\log_{10}(f_c) - 0.3(h_{UT} - 1.5)$ **Optional: CI model with 1 m reference distance** $\mathrm{PL} = 32.4 + 20\log_{10}(f_c) + 31.9\log_{10}(d_{3D})$	$\sigma_{SF} = 7.82$ $\sigma_{SF} = 8.2$	$0.5 \le f_c \le 100$ GHz $10 \text{ m} \le d_{2D} \le 5000$ m $h_{BS} = 10$ m $1.5 \text{ m} \le h_{UT} \le 22.5$ m
	NYUSIM [51, 52]		
NYUSIM UMi LOS	**CI model with 1 m reference distance:** $\mathrm{PL} = 32.4 + 20\log_{10}(d_{3D}) + 20\log_{10}(f_c)$	$\sigma_{SF} = 4.0$	$0.5 \le f_c \le 100$ GHz
NYUSIM UMi NLOS	**CI model with 1 m reference distance:** $\mathrm{PL} = 32.4 + 32\log_{10}(d_{3D}) + 20\log_{10}(f_c)$	$\sigma_{SF} = 7.0$	$0.5 \le f_c \le 100$ GHz

Note : PL is path loss. All distances or heights are in meters and frequency related values are in GHz, unless it is stated otherwise. $h'_{BP} = 4h'_{BS}h'_{UT}f_c/c$, where f_c is the center frequency in Hz, h'_{BS} and h'_{UT} are the effective antenna heights at the BS and the UT, respectively. In UMi scenario the effective antenna heights are computed as follows: $h'_{BS} = h_{BS} - 1.0$ m, $h'_{UT} = h_{UT} - 1.0$ m, where h_{BS} and h_{UT} are the actual antenna heights, and the effective environment height is assumed to be equal to 1.0 m. In UMa scenario the effective antenna heights are computed as follows: $h'_{BS} = h_{BS} - h_E$, $h'_{UT} = h_{UT} - h_E$, where h_{BS} and h_{UT} are the actual antenna heights, and the effective environment height h_E is a function of the link between a BS and a UT. In the event that the link is determined to be LOS, $h_E = 1$ m with a probability equal to $1/(1 + C(d_{2D}, h_{UT}))$ (see Page 26 of [66]).

Table 6.4: Path loss models in the UMa scenario [47, 52, 66].

	PL is in dB, f_c is in GHz, $d_{\mathbf{2D}}$ and $d_{\mathbf{3D}}$ are in meters	**Shadow fading std [dB]**	**Applicability range and Parameters**
3GPP [66]			
3GPP UMa LOS	$\text{PL} = \begin{cases} 28.0 + 22\log_{10}(d_{\text{3D}}) + 20\log_{10}(f_c), \ 10 \text{ m} \leq d_{\text{2D}} \leq d'_{\text{BP}} \\ 28.0 + 40\log_{10}(d_{\text{3D}}) + 20\log_{10}(f_c) - 9\log_{10}((d'_{\text{BP}})^2 \\ +(h_{\text{BS}} - h_{\text{UT}})^2), \ d'_{\text{BP}} \leq d_{\text{2D}} \leq 5000 \text{ m} \end{cases}$ where d'_{BP} is specified in Table 6.3.	$\sigma_{\text{SF}} = 4$	$0.5 \leq f_c \leq 100$ GHz $h_{\text{BS}} = 25$ m $1.5 \text{ m} \leq h_{\text{UT}} \leq 22.5$ m
3GPP UMa NLOS	$\text{PL} = \max\left(\text{PL}_{\text{UMa-LOS}}, \text{PL}'_{\text{UMa-NLOS}}\right)$ $\text{PL}'_{\text{UMa-NLOS}} = 13.54 + 39.08\log_{10}(d_{\text{3D}}) + 20\log_{10}(f_c)$ $-0.6(h_{\text{UT}} - 1.5)$ **Optional: CI model with 1 m reference distance** $\text{PL} = 32.4 + 20\log_{10}(f_c) + 30\log_{10}(d_{\text{3D}})$	$\sigma_{\text{SF}} = 6$ $\sigma_{\text{SF}} = 7.8$	$0.5 \leq f_c \leq 100$ GHz $10 \text{ m} \leq d_{\text{2D}} \leq 5000$ m $h_{\text{BS}} = 25$ m $1.5 \text{ m} \leq h_{\text{UT}} \leq 22.5$ m
NYUSIM [52]			
NYUSIM UMa LOS	**CI model with 1 m reference distance:** $\text{PL} = 32.4 + 20\log_{10}(d_{3D}) + 20\log_{10}(f_c)$	$\sigma_{SF} = 4.0$	$0.5 \leq f_c \leq 100$ GHz
NYUSIM UMa NLOS	**CI model with 1 m reference distance:** $\text{PL} = 32.4 + 29\log_{10}(d_{3D}) + 20\log_{10}(f_c)$	$\sigma_{SF} = 7.0$	$0.5 \leq f_c \leq 100$ GHz

6.1.3 Outdoor-to-Indoor (O2I) Penetration Loss Model

6.1.3.1 O2I Penetration Loss Model in the 3GPP Channel Model

In the 3GPP channel model, the overall path loss (especially for indoor users) mainly consists of three parts: outdoor path loss, O2I penetration loss, and indoor path loss, which can be modeled as [66]:

$$\text{PL [dB]} = \text{PL}_b + \text{PL}_{tw} + \text{PL}_{in} + N(0, \sigma_P^2) \tag{6.1}$$

where PL_b is the basic outdoor path loss, PL_{tw} is the building penetration loss through the external wall, PL_{in} is the indoor loss which depends on the depth into the building, and σ_P is the standard deviation for the penetration loss. The building penetration loss PL_{tw} has the following form:

$$\text{PL}_{tw} \text{ [dB]} = \text{PL}_{npi} - 10\log_{10} \sum_{i=1}^{N} \left(p_i \times 10^{-\frac{L_{\text{material}_i}}{10}} \right) \tag{6.2}$$

where PL_{npi} is an additional loss added to the external wall loss to account for non-perpendicular incidence, which is 5 dB in the 3GPP channel model. $L_{\text{material}_i} = a_{\text{material}_i} + b_{\text{material}_i} \cdot f_c$ is the penetration loss of material i, f_c is the frequency in GHz, p_i is the proportion of the i-th material, where $\sum p_i = 1$, and N is the number of materials. Penetration loss of several materials and the O2I penetration loss models are given in Tables 6.5 and 6.6, respectively.

Two variants of the O2I penetration model are provided: a low-loss and a high-loss model. The composition of low and high loss is a simulation parameter to be determined by channel model users, and is dependent on the use of metal-coated glass in buildings and the deployment scenarios [66]. Both low-loss and high-loss

Table 6.5: O2I penetration loss of different materials [66]

Material	**Penetration loss [dB]**
Standard multi-pane glass	$L_{\text{glass}} = 2 + 0.2f_c$
IRR glass	$L_{\text{IRRglass}} = 23 + 0.3f_c$
Concrete	$L_{\text{concrete}} = 5 + 4f_c$
Wood	$L_{\text{wood}} = 4.85 + 0.12f_c$

Table 6.6: O2I penetration loss parameters [47, 66, 226]

		Path loss through external wall: PL_{tw} **[dB]**	**Standard deviation** σ_P **[dB]**
3GPP	Low-loss model	$5 - 10\log_{10}(0.3 \cdot 10^{-L_{\text{glass}}/10} + 0.7 \cdot 10^{-L_{\text{concrete}}/10})$	4.4
	High-loss model	$5 - 10\log_{10}(0.7 \cdot 10^{-L_{\text{IRRglass}}/10} + 0.3 \cdot 10^{-L_{\text{concrete}}/10})$	6.5
NYUSIM parabolic model	Low-loss model	$10\log_{10}(5 + 0.03f_c^2)$	4.0
	High-loss model	$10\log_{10}(10 + 5f_c^2)$	6.0

models in the 3GPP channel model in Table 6.6 are applicable to UMa and UMi street canyon scenarios, whereas only the low-loss model is applicable to RMa [66].

6.1.3.2 O2I Penetration Loss Model in NYUSIM

In NYUSIM, a very succinct parabolic model with a good fit for predicting building penetration loss (BPL) of either high loss or low loss buildings was provided in [226] as:

$$\text{BPL [dB]} = 10\log_{10}(A + B \cdot f_c^2) \tag{6.3}$$

where f_c is in GHz, $A = 5$, and $B = 0.03$ for low loss buildings, and $A = 10$ and $B = 5$ for high loss buildings, as shown in Table 6.6.

6.1.4 Cluster Definition

The cluster definition and clustering algorithm may vary in different channel models [227]. This subsection introduces the cluster definition and clustering algorithm in the 3GPP and NYUSIM channel models.

6.1.4.1 Cluster Definition in the 3GPP Channel Model

In the 3GPP channel model [66], clusters are characterized by a *joint* delay-angle probability density function, such that a group of traveling MPCs must depart and arrive from a unique AoD-AoA combination centered around a mean propagation delay [52, 66]. High-resolution parameter extraction algorithms, e.g., SAGE (space-alternating generalized expectation-maximization) and KPowerMeans algorithms [228, 229] that have high computational complexity, are often employed to obtain cluster characteristics.

6.1.4.2 Cluster Definition in NYUSIM

NYUSIM uses TCSL concepts to describe multipath behavior for omnidirectional and directional CIRs [51, 52, 223], as presented in Section 2.4.10.

6.1.5 Large-Scale Parameters

6.1.5.1 Large-Scale Parameters in the 3GPP Channel Model

In the 3GPP channel model [66], LSPs mainly include DS, angular spreads (ASA, ASD, ZSA, ZSD), Ricean K-factor (K) and SF taking into account cross correlation [66]. These LSPs act as fundamental channel modeling parameters and play a key role in generating other relevant channel modeling parameters such as

small-scale parameters (SSPs). The most important LSPs and their statistics in the 3GPP channel model are provided in Table 6.7 and Table 6.8 for UMi and UMa scenarios, respectively.

6.1.5.2 Large-Scale Parameters in NYUSIM

Tables 6.7 and 6.8 show the LSPs and their statistics at various mmWave frequencies in NYUSIM [205]. In addition to the statistics of LSPs in the log scale as given in the 3GPP model, NYUSIM also provides the statistics in their regular units, such as nanoseconds for delay spread, and degrees for angular spreads, which is more intuitive [205].

6.1.6 Small-Scale Parameters

6.1.6.1 Small-Scale Parameters in the 3GPP Channel Model

SSPs in the 3GPP channel model mainly contain the following parameters: cluster excess delays, cluster powers, and cluster arrival angles and departure angles for both azimuth and elevation. Key channel modeling parameters for generating SSPs in UMi street canyon and UMa scenarios are listed in Table 6.9 and Table 6.10, respectively.

6.1.6.2 Small-Scale Parameters in NYUSIM

Since the cluster definitions in the 3GPP channel model [66] and NYUSIM [52] are discrepant, SSPs in NYUSIM are also a little different from those in the 3GPP channel model. In NYUSIM, SSPs include time cluster excess delays, time cluster powers, and mean AoD and AoA azimuth and elevation angles for each spatial lobe.

Table 6.7: Large-scale parameters in the UMi scenario for frequencies from 0.5 GHz to 100 GHz [52, 66, 205]. Note: For 3GPP UMi and frequencies below 2 GHz, use $f_c = 2$ when determining the values of the frequency-dependent LSP values [66].

	Parameter Name		LOS	NLOS
3GPP [66]	**Delay spread (DS)** lgDS= $\log_{10}$(DS [s] /1s)	μ_{lgDS}	$-0.24\log_{10}(1+f_c)-7.14$	$-0.24\log_{10}(1+f_c)-6.83$
		σ_{lgDS}	0.38	$0.16\log_{10}(1+f_c)+0.28$
	AoD spread (ASD) lgASD = $\log_{10}$(ASD [°] /1°)	μ_{lgASD}	$-0.05\log_{10}(1+f_c)+1.21$	$-0.23\log_{10}(1+f_c)+1.53$
		σ_{lgASD}	0.41	$0.11\log_{10}(1+f_c)+0.33$
	AoA spread (ASA) lgASA = $\log_{10}$(ASA [°] /1°)	μ_{lgASA}	$-0.08\log_{10}(1+f_c)+1.73$	$-0.08\log_{10}(1+f_c)+1.81$
		σ_{lgASA}	$0.014\log_{10}(1+f_c)+0.28$	$0.05\log_{10}(1+f_c)+0.3$
	ZoA spread (ZSA) lgZSA = $\log_{10}$(ZSA [°] /1°)	μ_{lgZSA}	$-0.1\log_{10}(1+f_c)+0.73$	$-0.04\log_{10}(1+f_c)+0.92$
		σ_{lgZSA}	$-0.04\log_{10}(1+f_c)+0.34$	$-0.07\log_{10}(1+f_c)+0.41$
	Shadow fading (SF) [dB]	σ_{SF}	see Table 6.3	see Table 6.3
	K-factor (K) [dB]	μ_K	9	N/A
		σ_K	5	N/A
	XPR [dB]	μ	9	8
		σ	3	3
NYUSIM [52, 205]	**Delay spread (DS)**	med [ns]	17.5	28 GHz: 29.9 73 GHz: 44.8
		μ [ns]	26.6	28 GHz: 42.1 73 GHz: 45.9
	lgDS= $\log_{10}$(DS [s] /1s)	μ	-7.71	28 GHz: -7.64 73 GHz: -7.53
		σ	0.34	28 GHz: 0.50 73 GHz: 0.51
	AoD spread (ASD)	med [°]	18.5	28 GHz: 30.9 73 GHz: 26.0
		μ [°]	32.3	28 GHz: 33.7 73 GHz: 29.0
	lgASD = $\log_{10}$(ASD [°] /1°)	μ	1.28	28 GHz: 1.38 73 GHz: 1.34
		σ	0.50	28 GHz: 0.41 73 GHz: 0.39
	AoA spread (ASA)	med [°]	50.9	28 GHz: 22.0 73 GHz: 37.1
		μ [°]	56.9	28 GHz: 22.0 73 GHz: 37.1
	lgASA = $\log_{10}$(ASA [°] /1°)	μ	1.69	28 GHz: 1.39 73 GHz: 1.50
		σ	0.27	28 GHz: 0.39 73 GHz: 0.20
	ZoA spread (ZSA)	med [°]	4.0	28 GHz: 6.1 73 GHz: 3.5
		μ [°]	4.0	28 GHz: 6.2 73 GHz: 3.8
	lgZSA = $\log_{10}$(ZSA [°] /1°)	μ	0.60	28 GHz: 0.72 73 GHz: 0.55
		σ	0.09	28 GHz: 0.30 73 GHz: 0.15
	Shadow fading (SF) [dB]	σ_{SF}	see Table 6.3	see Table 6.3
	K-factor (K) [dB]	μ_K	2.4	28 GHz: -0.4 73 GHz: 1.5
		σ_K	2.0	28 GHz: 4.3 73 GHz: 6.8
	XPR [dB]	μ	9	8
		σ	3	3

Table 6.8: Large-scale parameters in the UMa scenario for frequencies from 0.5 GHz to 100 GHz [52, 66, 205]. Note: For 3GPP UMa and frequencies below 6 GHz, use $f_c = 6$ when determining the values of the frequency-dependent LSP values [66].

	Parameter Name		LOS	NLOS
3GPP [66]	**Delay spread (DS)** lgDS= $\log_{10}$(DS [s] /1s)	μ_{lgDS}	$-0.0963\log_{10}(f_c) - 6.955$	$-0.204\log_{10}(f_c) - 6.28$
		σ_{lgDS}	0.66	0.39
	AoD spread (ASD) lgASD = $\log_{10}$(ASD [°] /1°)	μ_{lgASD}	$0.1114\log_{10}(f_c) + 1.06$	$-0.1144\log_{10}(f_c) + 1.5$
		σ_{lgASD}	0.28	0.28
	AoA spread (ASA) lgASA = $\log_{10}$(ASA [°] /1°)	μ_{lgASA}	1.81	$-0.27\log_{10}(f_c) + 2.08$
		σ_{lgASA}	0.20	0.11
	ZoA spread (ZSA) lgZSA = $\log_{10}$(ZSA [°] /1°)	μ_{lgZSA}	0.95	$-0.3236\log_{10}(f_c) + 1.512$
		σ_{lgZSA}	0.16	0.16
	Shadow fading (SF) [dB]	σ_{SF}	see Table 6.4	see Table 6.4
	K-factor (K) [dB]	μ_K	9	N/A
		σ_K	3.5	N/A
	XPR [dB]	μ	8	7
		σ	4	3
NYUSIM [52, 205]	**Delay spread (DS)**	med [ns]	17.5	28 GHz: 29.9 73 GHz: 44.8
		μ [ns]	26.6	28 GHz: 42.1 73 GHz: 45.9
	lgDS= $\log_{10}$(DS [s] /1s)	μ	-7.71	28 GHz: -7.64 73 GHz: -7.53
		σ	0.34	28 GHz: 0.50 73 GHz: 0.51
	AoD spread (ASD)	med [°]	18.5	28 GHz: 30.9 73 GHz: 26.0
		μ [°]	32.3	28 GHz: 33.7 73 GHz: 29.0
	lgASD = $\log_{10}$(ASD [°] /1°)	μ	1.28	28 GHz: 1.38 73 GHz: 1.34
		σ	0.50	28 GHz: 0.41 73 GHz: 0.39
	AoA spread (ASA)	med [°]	50.9	28 GHz: 22.0 73 GHz: 37.1
		μ [°]	56.9	28 GHz: 22.0 73 GHz: 37.1
	lgASA = $\log_{10}$(ASA [°] /1°)	μ	1.69	28 GHz: 1.39 73 GHz: 1.50
		σ	0.27	28 GHz: 0.39 73 GHz: 0.20
	ZoA spread (ZSA)	med [°]	4.0	28 GHz: 6.1 73 GHz: 3.5
		μ [°]	4.0	28 GHz: 6.2 73 GHz: 3.8
	lgZSA = $\log_{10}$(ZSA [°] /1°)	μ	0.60	28 GHz: 0.72 73 GHz: 0.55
		σ	0.09	28 GHz: 0.30 73 GHz: 0.15
	Shadow fading (SF) [dB]	σ_{SF}	see Table 6.4	see Table 6.4
	K-factor (K) [dB]	μ_K	2.4	28 GHz: -0.4 73 GHz: 1.5
		σ_K	2.0	28 GHz: 4.3 73 GHz: 6.8
	XPR [dB]	μ	8	7
		σ	4	3

Table 6.9: Key channel modeling parameters used for generating small-scale parameters in the UMi scenario for frequencies from 0.5 GHz to 100 GHz [52, 66, 205]. Note: For 3GPP UMi and frequencies below 2 GHz, use $f_c = 2$ when determining the values of the frequency-dependent LSP values [66].

	Parameter Name	LOS	NLOS
3GPP [66]	**Number of clusters**	12	19
	Number of rays per cluster	20	20
	Cluster DS [ns]	5	11
	Cluster ASD [°]	3	10
	Cluster ASA [°]	17	22
	Cluster ZSA [°]	7	7
	Per cluster shadowing std [dB]	3	3
NYUSIM [52, 205]	**Number of time clusters**	Discrete Uniform [1, 6]	
	Number of subpaths per time cluster	Discrete Uniform [1, 30]	
	Number of spatial lobes (departure)	Poisson(1.9)	Poisson(1.5)
	Number of spatial lobes (arrival)	Poisson(1.8)	Poisson(2.1)
	RMS lobe azimuth spread (departure) [°]	8.5	11.0
	RMS lobe elevation spread (departure) [°]	2.5	3.0
	RMS lobe azimuth spread (arrival) [°]	10.5	7.5
	RMS lobe elevation spread (arrival) [°]	11.5	6.0
	Per cluster shadowing std [dB]	1	3

Table 6.10: Key channel modeling parameters used for generating small-scale parameters in the UMa scenario for frequencies from 0.5 GHz to 100 GHz [52, 66, 205]. Note: For 3GPP UMa and frequencies below 6 GHz, use $f_c = 6$ when determining the values of the frequency-dependent LSP values [66].

	Parameter Name	LOS	NLOS
3GPP [66]	**Number of clusters**	12	20
	Number of rays per cluster	20	20
	Cluster DS [ns]	max(0.25, -3.4084log10(f_c)+6.5622)	max(0.25, -3.4084log10(f_c)+6.5622)
	Cluster ASD [°]	5	2
	Cluster ASA [°]	11	15
	Cluster ZSA [°]	7	7
	Per cluster shadowing std [dB]	3	3
NYUSIM [52, 205]	**Number of time clusters**	Discrete Uniform [1, 6]	
	Number of subpaths per time cluster	Discrete Uniform [1, 30]	
	Number of spatial lobes (departure)	Poisson(1.9)	Poisson(1.5)
	Number of spatial lobes (arrival)	Poisson(1.8)	Poisson(2.1)
	RMS lobe azimuth spread (departure) [°]	8.5	11.0
	RMS lobe elevation spread (departure) [°]	2.5	3.0
	RMS lobe azimuth spread (arrival) [°]	10.5	7.5
	RMS lobe elevation spread (arrival) [°]	11.5	6.0
	Per cluster shadowing std [dB]	1	3

Table 6.11: Cross-correlation coefficients in the UMi scenario for frequencies from 0.5 GHz to 100 GHz [52, 66, 205]. Note: For 3GPP UMi and frequencies below 2 GHz, use $f_c = 2$ when determining the values of the frequency-dependent LSP values [66].

	Parameter Name	LOS	NLOS
3GPP [66]	**ASD vs DS**	0.5	0
	ASA vs DS	0.8	0.4
	ASA vs SF	-0.4	-0.4
	ASD vs SF	-0.5	0
	DS vs SF	-0.4	-0.7
	ASD vs ASA	0.4	0
	ASD vs K	-0.2	N/A
	ASA vs K	-0.3	N/A
	DS vs K	-0.7	N/A
	SF vs K	0.5	N/A
	ZSD vs SF	0	0
	ZSA vs SF	0	0
	ZSD vs K	0	N/A
	ZSA vs K	0	N/A
	ZSD vs DS	0	-0.5
	ZSA vs DS	0.2	0
	ZSD vs ASD	0.5	0.5
	ZSA vs ASD	0.3	0.5
	ZSD vs ASA	0	0
	ZSA vs ASA	0	0.2
	ZSD vs ZSA	0	0
NYUSIM [52, 205]	**ASD vs DS**	0.32	28 GHz: -0.051 73 GHz: 0.021
	ASA vs DS	0.49	28 GHz: 0.153 73 GHz: 0.264
	ASA vs SF	0.54	28 GHz: -0.637 73 GHz: 0.044
	ASD vs SF	-0.04	28 GHz: 0.051 73 GHz: 0.008
	DS vs SF	0.35	28 GHz: -0.508 73 GHz: -0.187
	ASD vs ASA	0.72	28 GHz: 0.405 73 GHz: -0.257
	ASD vs K	-0.16	28 GHz: -0.217 73 GHz: 0.162
	ASA vs K	0.07	28 GHz: -0.069 73 GHz: -0.428
	DS vs K	-0.46	28 GHz: -0.133 73 GHz: -0.449
	SF vs K	-0.03	28 GHz: -0.278 73 GHz: 0.029
	ZSA vs SF	0.16	28 GHz: -0.480 73 GHz: -0.327
	ZSA vs K	-0.37	28 GHz: -0.077 73 GHz: -0.105
	ZSA vs DS	0.44	28 GHz: 0.347 73 GHz: 0.144
	ZSA vs ASD	0.95	28 GHz: 0.042 73 GHz: -0.027
	ZSA vs ASA	0.72	28 GHz: 0.323 73 GHz: 0.081

Table 6.12: Cross-correlation coefficients in the UMa scenario for frequencies from 0.5 GHz to 100 GHz [52, 66, 205]. Note: For 3GPP UMa and frequencies below 6 GHz, use $f_c = 6$ when determining the values of the frequency-dependent LSP values [66].

	Parameter Name	LOS	NLOS
3GPP [66]	**ASD vs DS**	0.4	0.4
	ASA vs DS	0.8	0.6
	ASA vs SF	-0.5	0
	ASD vs SF	-0.5	-0.6
	DS vs SF	-0.4	-0.4
	ASD vs ASA	0	0.4
	ASD vs K	0	N/A
	ASA vs K	-0.2	N/A
	DS vs K	-0.4	N/A
	SF vs K	0	N/A
	ZSD vs SF	0	0
	ZSA vs SF	-0.8	-0.4
	ZSD vs K	0	N/A
	ZSA vs K	0	N/A
	ZSD vs DS	-0.2	-0.5
	ZSA vs DS	0	0
	ZSD vs ASD	0.5	0.5
	ZSA vs ASD	0	-0.1
	ZSD vs ASA	-0.3	0
	ZSA vs ASA	0.4	0
	ZSD vs ZSA	0	0
NYUSIM [52, 205]	**ASD vs DS**	0.32	28 GHz: -0.051 73 GHz: 0.021
	ASA vs DS	0.49	28 GHz: 0.153 73 GHz: 0.264
	ASA vs SF	0.54	28 GHz: -0.637 73 GHz: 0.044
	ASD vs SF	-0.04	28 GHz: 0.051 73 GHz: 0.008
	DS vs SF	0.35	28 GHz: -0.508 73 GHz: -0.187
	ASD vs ASA	0.72	28 GHz: 0.405 73 GHz: -0.257
	ASD vs K	-0.16	28 GHz: -0.217 73 GHz: 0.162
	ASA vs K	0.07	28 GHz: -0.069 73 GHz: -0.428
	DS vs K	-0.46	28 GHz: -0.133 73 GHz: -0.449
	SF vs K	-0.03	28 GHz: -0.278 73 GHz: 0.029
	ZSA vs SF	0.16	28 GHz: -0.480 73 GHz: -0.327
	ZSA vs K	-0.37	28 GHz: -0.077 73 GHz: -0.105
	ZSA vs DS	0.44	28 GHz: 0.347 73 GHz: 0.144
	ZSA vs ASD	0.95	28 GHz: 0.042 73 GHz: -0.027
	ZSA vs ASA	0.72	28 GHz: 0.323 73 GHz: 0.081

Table 6.13: Simulation settings for comparing channel eigenvalues and spectral efficiencies between the 3GPP channel model [66] and NYUSIM [51, 223].

Parameter	Setting
Carrier Frequency	28 GHz
Transmit Power	46 dBm for all UEs in the cell
95% Cell-Edge SNR	5 dB
BS Antennas	uniform rectangular array consisting of N_{T} cross-polarized elements in the x-z plane
BS Antenna Spacing	half wavelength
BS Antenna Element Gain	8 dBi [66]
BS Antenna Element Pattern	Model 2, Page 18 in 3GPP TR 36.873 Release 12 [225]
MS Antennas	uniform rectangular array consisting of N_{R} cross-polarized elements in the x-z plane
MS Antenna Spacing	half wavelength
MS Antenna Element Gain	0 dBi
MS Antenna Element Pattern	omnidirectional
Receiver Noise Figure	10 dB

Key channel modeling parameters for generating SSPs in NYUSIM are also given by Table 6.9 and Table 6.10 in comparison with those in the 3GPP channel model for UMi and UMa scenarios, respectively.

It is worth noting from Tables 6.9 and 6.10 that the number of clusters and the number of rays per cluster in the 3GPP channel model have fixed values, whereas the number of time clusters, the number of subpaths per time cluster, and the number of spatial lobes (both departure and arrival) do not hold particular values but follow certain distributions and can vary in each channel realization. Furthermore, the numbers of clusters in the 3GPP model are much higher as compared to the measured numbers of time clusters (around 3 to 4 on average) and spatial lobes (about 2 on average) in NYUSIM. Those differences lead to a significant difference in channel sparsity predicted by the two channel models, and have a huge impact on spectral efficiency evaluation, as will be demonstrated later by simulation results.

6.1.7 Cross-Correlations

Cross-correlation coefficients between various channel modeling parameters in both 3GPP and NYUSIM are displayed in Table 6.11 and Table 6.12 for the UMi street canyon scenario and the UMa scenario, respectively.

6.1.8 Eigenvalues of $\mathbf{HH}^H$

Eigenvalues represent power gains of uncorrelated parallel sub-channels, which are directly related to spectral efficiency. The downlink $N_{\mathrm{R}} \times N_{\mathrm{T}}$ MIMO channel matrix $\mathbf{H}$ is generated using both 3GPP [66] and NYUSIM [51, 52, 205, 223] channel models, for a system operating at 28 GHz with 100 MHz RF bandwidth, and 256 BS antennas and 16 MS antennas, composing a URA in the x-z plane on each side. Simulation settings are detailed in Table 6.13. OFDM-like modulation [230, 231] is assumed. Due to the significantly large bandwidths, it is speculated that the nature of the mmWave propagation channel will be wideband (e.g., 1 GHz RF bandwidth), and this wide bandwidth is likely to be aggregated over RF channels which are 100 MHz wide and which use many OFDM sub-carriers that are each narrowband (flat-fading) in nature [48, 230]. Although the channel coefficients in $\mathbf{H}$ over the 100 MHz usually vary with carrier frequency, mean values and statistics of the eigenvalues of $\mathbf{HH}^H$ are generally frequency-independent over the 100 MHz bandwidth. To justify this, mean values of the singular values obtained by SVD of the matrix $\mathbf{H}$ averaged over 3000 random channel realizations are plotted in Fig. 6.3 against the narrowband (75 kHz RF bandwidth as envisioned for initial 5G systems [6]) sub-carriers [231] from 27.95 GHz to 28.05 GHz in increments of 10 MHz assuming OFDM-like modulation (actual OFDM modulation has much

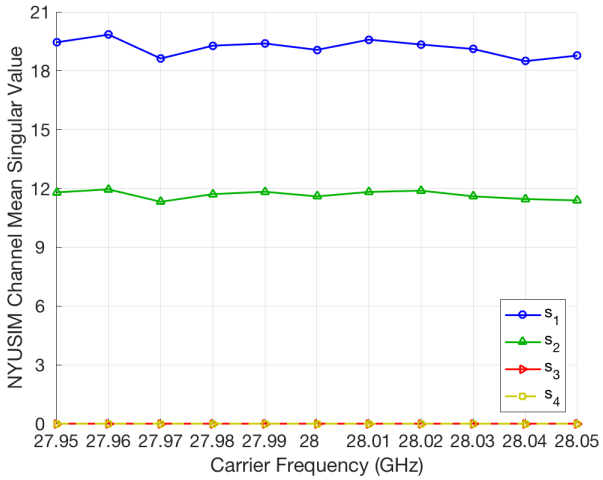

Figure 6.3: Mean values of the largest four singular values of the channel matrix $\mathbf{H}$ averaged over 3000 random channel realizations versus the narrowband (75 kHz RF bandwidth as envisioned for initial 5G systems [6]) carrier frequency from 27.95 GHz to 28.05 GHz in increments of 10 MHz assuming OFDM-like modulation (actual OFDM modulation has much smaller sub-carrier spacings, e.g. 15 kHz for 4G LTE and 75 kHz for 5G pre-trial [6]; here 10 MHz is used purely for plotting purposes). s_i denotes the mean value of the i-th largest singular value of $\mathbf{H}$.

smaller sub-carrier spacings, e.g. 15 kHz for 4G LTE and 75 kHz for 5G pre-trial [6]; here 10 MHz is used purely for plotting purposes), where the singular values of $\mathbf{H}$ are the square root of the corresponding eigenvalues of $\mathbf{HH}^H$. It is evident from Fig. 6.3 that the *mean values (statistics) of singular values vary little with carrier frequency over the 100 MHz RF bandwidth*. In other words, the narrowband flat fading will be identical in statistics at any sub-carrier in the 100 MHz RF channel bandwidth, so for simplicity, the channel impulse response from the 3GPP channel model and the NYUSIM channel model, respectively, is used and the resulting narrowband complex channel gain/channel state at the center frequency sub-carrier of 28.000 GHz is applied when investigating eigenvalues and spectral efficiency.

The eigenvalues of $\mathbf{HH}^H$ are calculated and normalized eigenvalue magnitudes

are obtained as follows:

$$\eta_i = \frac{\eta_i'}{\sum_{i=1}^{N_{\mathrm{R}}} \eta_i'} \tag{6.4}$$

where η_i denotes the ith largest normalized eigenvalue of $\mathbf{H}\mathbf{H}^H$, η_i' is the ith largest eigenvalue of $\mathbf{H}\mathbf{H}^H$, and N_{R} denotes the number of receive antennas.

Fig. 6.4 depicts the cumulative distribution functions (CDFs) of the largest four channel eigenvalues of $\mathbf{H}\mathbf{H}^H$ for both 3GPP [66] and NYUSIM [51, 52, 223] for each individual user in a single-cell three-user MIMO system in the UMi scenario. It is observed from Fig. 6.4 that the highest two eigenvalues in NYUSIM are larger than those in 3GPP, while the third and fourth eigenvalues are smaller most of the time. This indicates that NYUSIM yields only a few but strong dominant eigenmodes, whereas the 3GPP model generates more eigenmodes with weaker powers. The number of dominant eigen channels (i.e., the channel rank) in NYUSIM is statistical and can vary over the range of 1 to 5, where 5 is the maximum number of spatial lobes [52], with an average and typical value of 2 as shown by Tables 6.9 and 6.10 and over numerous simulations.

Fig. 6.5 illustrates the average normalized eigenvalue magnitude of $\mathbf{H}\mathbf{H}^H$ as a function of the eigenvalue index for both 3GPP [66] and NYUSIM [51, 52, 223] models, where the normalized eigenvalue magnitude is obtained by dividing the eigenvalue by the sum of all the eigenvalues in linear scale of a channel matrix. As shown by Fig. 6.5, the first two dominant eigen channels of 3GPP and NYUSIM channel models are roughly equal in normalized magnitude. Furthermore, all the eigenvalues of the 3GPP channel are within 25 dB of the largest eigenvalue. On the contrary, for NYUSIM, only four normalized eigenvalues are greater than -25 dB, and the non-dominant eigenvalue magnitudes decrease rapidly. This indicates the sparse feature of the mmWave channel such that the number of available spatial

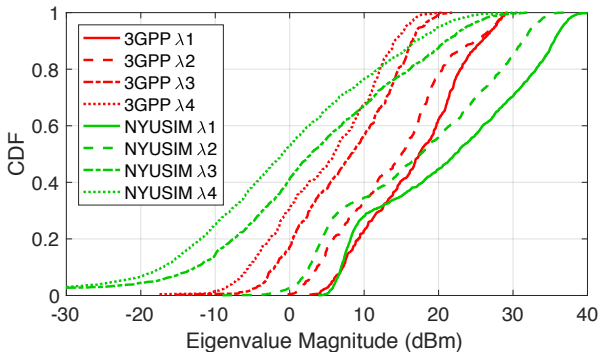

Figure 6.4: CDFs of the largest four channel eigenvalues at 28 GHz in 3GPP and NYUSIM channel models for each individual user in a single-cell three-user MIMO system in the UMi scenario. The transmit and receive antenna arrays are uniform rectangular array composed by 256 and 8 cross-polarized elements, respectively. The carrier frequency is 28 GHz with an RF bandwidth of 100 MHz and narrowband frequency-flat fading sub-carriers. Each BS antenna element has a radiation pattern as specified in Table 7.3-1 of [66] with a maximum gain of 8 dBi, and each RX antenna element possesses an omnidirectional pattern. The total transmit power is 46 dBm.

multiplexing streams is relatively limited. This is likely caused by the small number of clusters and narrow angular spreads modeled in mmWave channels by NYUSIM.

6.2 Examples and Applications

6.2.1 Mobile System Coverage and Performance Studies

This is fundamental to mobile research in the ability to design and predict coverage for different morphologies.

Let us assume a single-cell MU-MIMO system operating at 28 GHz with an RF bandwidth of 100 MHz and narrowband frequency-flat fading sub-carriers with OFDM modulation in the UMi street canyon scenario. The BS is equipped with

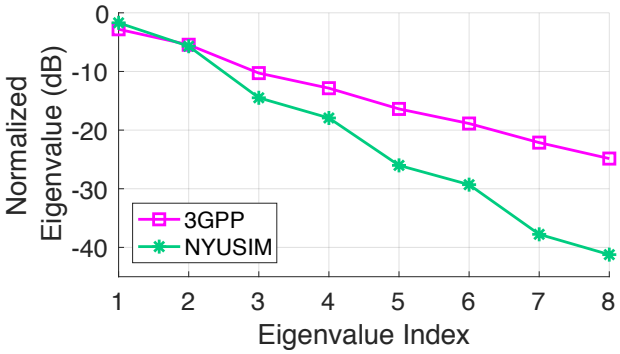

Figure 6.5: Comparison of normalized channel eigenvalues at 28 GHz in 3GPP and NYUSIM channel models for each individual user in a single-cell three-user MIMO system in the UMi street canyon scenario. The normalized eigenvalue magnitude is obtained by dividing the eigenvalue by the sum of all the eigenvalues in linear scale of a channel matrix. The transmit and receive antenna arrays are URAs composed by 256 and 8 cross-polarized elements, respectively. The transmit and receive antenna arrays are uniform rectangular array composed by 256 and 8 cross-polarized elements, respectively. The carrier frequency is 28 GHz with an RF bandwidth of 100 MHz and narrowband frequency-flat fading sub-carriers. Each BS antenna element has a radiation pattern as specified in Table 7.3-1 of [66] with a maximum gain of 8 dBi, and each RX antenna element possesses an omnidirectional pattern. The total transmit power is 46 dBm.

N_{T} cross-polarized antenna elements comprising a URA (where $N_{\mathrm{T}}/2$ elements are $+45^{\circ}$ slanted, and the other $N_{\mathrm{T}}/2$ are -45° slanted). There are three UEs in the cell, and each UE has eight cross-polarized omnidirectional antenna elements constituting a URA (where four elements are $+45^{\circ}$ slanted, and the other four are -45° slanted). Cross-polarized antenna elements are considered herein since they can effectively reduce the physical size while making use of different polarization components. Each BS antenna element has a radiation pattern as specified in Table 7.3-1 of [66] with a maximum gain of 8 dBi, and each RX antenna element possesses an omnidirectional pattern. In the simulations, it is assumed that 95% of the area in the cell has an SNR larger than or equal to 5 dB, and the upper bound of the T-R separation distance (i.e., cell radius) is calculated based on this assumption by using the following equation:

$$\mathrm{PL}(f_c, d_{\max})[\mathrm{dB}] = 10\log_{10} N_{\mathrm{T}} + \mathrm{P_T} + \mathrm{G_T} - N_0 - \mathrm{SNR}_{\text{cell-edge}} \tag{6.5}$$

where $\mathrm{P_T}$ represents the transmit power in dBm, $\mathrm{G_T}$ is the gain of each TX antenna element in dB, N_o denotes the noise power in dBm, and $\mathrm{SNR}_{\text{cell-edge}}$ is the cell-edge SNR in dB, which is 5 dB in the simulations. The most vital term in Eq. (6.5) is $\mathrm{PL}(f_c, d_{\max})$, which denotes the large-scale path loss in dB at the cell edge $d_{\max}$, and should correspond to an SNR no smaller than the cell-edge SNR 95% of the time statistically. This is realized through the shadow fading term in $\mathrm{PL}(f_c, d_{\max})$. For instance, when using the CI path loss model, $\mathrm{PL}(f_c, d_{\max})$ is expressed as:

$$\mathrm{PL}(f_c, d_{\max})[\mathrm{dB}] = 32.4 + 10n\log_{10}(d_{\max}) + 20\log_{10}(f_c) + z * \sigma_{\mathrm{SF}} \tag{6.6}$$

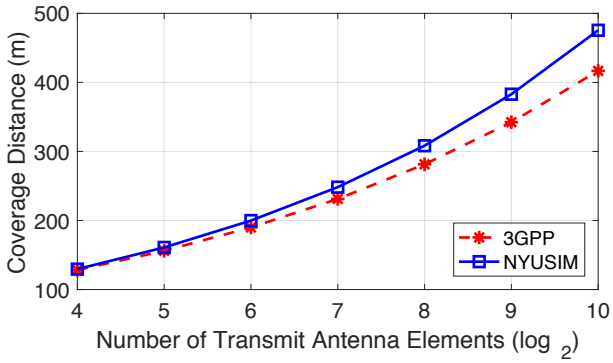

Figure 6.6: Maximum coverage distance of the BS as a function of the BS antenna elements in a single-cell three-user MIMO system operating at 28 GHz with an RF bandwidth of 100 MHz and narrowband frequency-flat fading sub-carriers in the UMi street canyon scenario, using both 3GPP and NYUSIM channel models. The BS is equipped with N_T cross-polarized antenna elements comprising a URA, and each UE has 0 dB antenna gain. Each BS antenna element has a radiation pattern as specified in Table 7.3-1 of [66] with a maximum gain of 8 dBi, and each RX antenna element possesses an omnidirectional pattern. The total transmit power is 46 dBm which is equally shared by the three users.

where σ_{SF} represents the shadow fading standard deviation in dB. Since shadow fading is a zero-mean Gaussian random variable [67, 232] hence having a probability density function (PDF), z is a constant that splits the area under the PDF into two parts such that the two parts occupy 95% and 5% of the total area under the PDF, respectively, and z is calculated to be 1.645 via the Q-function [232].

For the UMi street canyon scenario, the upper bound of the T-R separation distance, i.e., the maximum coverage distance of the BS, is calculated based on the above assumption for varying number of BS antenna elements using both 3GPP and NYUSIM channel models, where the number of BS antenna elements ranges from 16 to 1024, and the carrier frequency is 28 GHz with an RF bandwidth of 100 MHz and narrowband frequency-flat fading sub-carriers. The BS is equipped with a URA with cross-polarized antenna elements, and each UE has 0 dB antenna

gain. Each BS antenna element has a radiation pattern as specified in Table 7.3-1 of [66] with a maximum gain of 8 dBi, and each RX antenna element possesses an omnidirectional pattern. The total transmit power is 46 dBm which is equally shared by the three users in a cell. The maximum coverage distances calculated using Eqs. (6.5) and (6.6) are illustrated in Fig. 6.6, which shows that NYUSIM predicts 1.0%-14.1% greater cell radius compared to 3GPP. For example, when there are 256 BS antenna elements, the maximum coverage distance is 281.4 m and 308.3 m predicted by 3GPP and NYUSIM, respectively, where the latter is 9.6% greater than the former.

6.2.2 Simulation Results and Analysis

The HBF algorithm proposed in [117] for the fully-connected architecture is employed to investigate the spectral efficiency in a single-cell SU-MIMO mmWave system, using the simulation settings in Table 6.13 with 256 and 16 BS and UE antenna elements, respectively. The CDFs of the spectral efficiency of the single-cell SU-MIMO system are depicted in Fig. 6.7 for different numbers of RF chains and data streams using both 3GPP [66] and NYUSIM [51] channel models. The number of RF chains in the legend denotes both the transmit and receive RF chains. Fig. 6.7(a) depicts the case of one data stream, which shows that regardless of the number of RF chains, *the spectral efficiency yielded by NYUSIM is (up to 42%) larger than that generated by the 3GPP model when only one data stream is transmitted, due to the larger dominant channel eigenvalue produced by NYUSIM and is consistent with the results in [208] for the one-stream case.* Furthermore, the spectral efficiency using the HBF algorithm is closer to the digital beamforming performance utilizing NYUSIM than using the 3GPP model. More importantly,

for the 3GPP model, there is a noticeable increase in the spectral efficiency as the number of RF chains increases from 1 to 2, while the spectral efficiency increase is very trivial for NYUSIM. Fig. 6.7(b) illustrates the case of four data streams. Several observations can be drawn from Fig. 6.7(b). First, the digital beamforming spectral efficiency using NYUSIM is larger as compared to the 3GPP channel model in most cases, since the sum of the highest four channel eigenvalues in NYUSIM is greater than that in the 3GPP channel model. Second, for CDF points lower than 90%, the spectral efficiency gap between the digital beamforming and HBF is more significant for NYUSIM than for the 3GPP model, which indicates that the product of the analog and digital hybrid beamforming matrices can not be made sufficiently close to the optimal digital beamforming matrix as required in [117]. This is probably because in some channel realizations the number of MPCs produced by NYUSIM is smaller than four, such that there are not large enough antenna array response vector basis from which the analog steering directions can be selected [117]. Moreover, *for the 3GPP channel model, the spectral efficiency increases when the number of RF chains increases from 4 to 8, likely due to the fact that the number of clusters in the UMi scenario in the 3GPP channel model is 12 for LOS and 19 for NLOS, thus increasing the RF chains from 4 to 8 can make better use of the channel spatial dimensions. As a comparison, the spectral efficiency yielded by NYUSIM remains almost unchanged for 4 and 8 RF chains, since the number of spatial lobes does not exceed 5 with an average number of 2 so that increasing the number of RF chains from 4 to 8 is unlikely to provide extra multiplexing gain.* Therefore, *the 3GPP model suggests that spectral efficiency can be enhanced by increasing the number of RF chains, while NYUSIM indicates that there is no need to increase the RF chains beyond five or so as the spectral efficiency will not be improved.* The

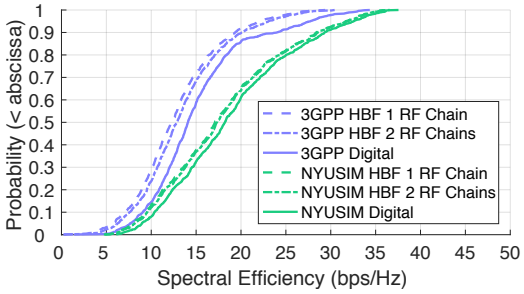

(a) One Data Stream

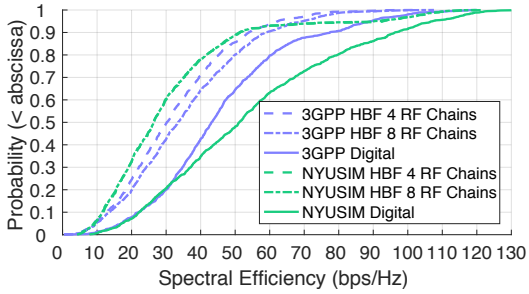

(b) Four Data Streams

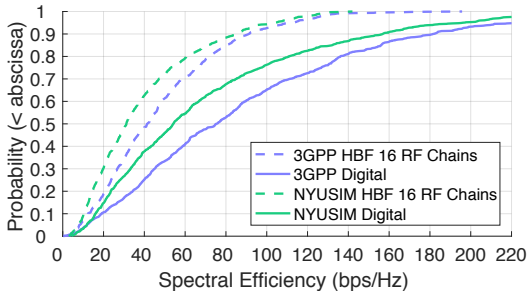

(c) 16 Data Streams

Figure 6.7: CDFs of the sum spectral efficiency of the single-cell SU-MIMO system using the HBF algorithm proposed in [117] for different numbers of RF chains using both 3GPP [66] and NYUSIM [51] channel models. The number of RF chains in the legend denotes both the transmit and receive RF chains. The number of data streams between the BS and UE is one, four, and 16 in (a), (b), and (c), respectively.

spectral efficiency CDFs corresponding to 16 data streams and 16 RF chains are displayed in Fig. 6.7(c), which reveals that the 3GPP model yields higher spectral efficiency for both HBF and digital beamforming. This is because of the increased number of data streams hence increased multipath richness that makes the 3GPP channel closer to a Rayleigh channel, thus resulting in larger spectral efficiency.

Table 6.16 shows that for the three-cell MU-MIMO using the HBF algorithm proposed in this chapter with two streams per user, NYUSIM predicts larger per-user and sum spectral efficiencies than the 3GPP channel model, probably because

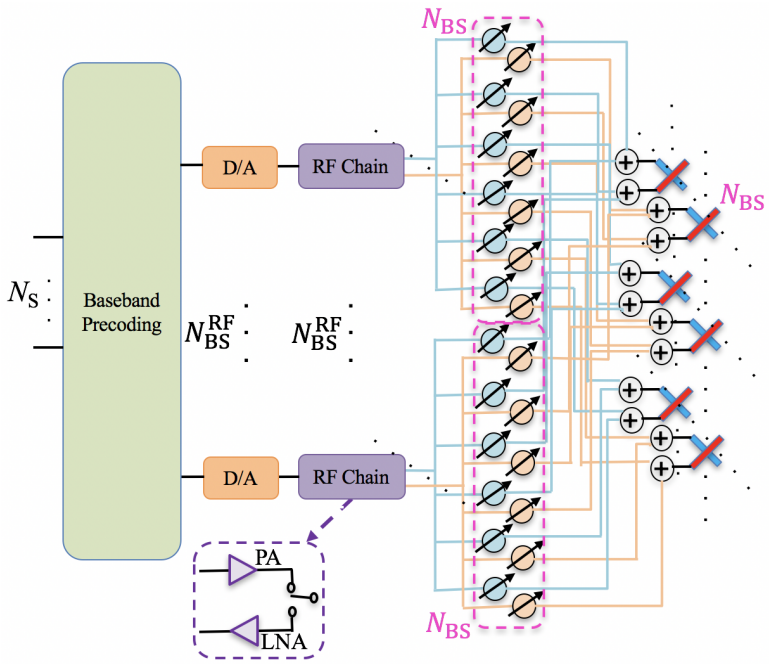

Figure 6.8: An example of the HBF architecture diagram with various hardware units at the BS (the MS side can be derived similarly), with N_{BS} antenna elements composing a URA, $N_{\mathrm{BS}}^{\mathrm{RF}}$ RF chains, and N_{S} data streams. Adding one RF chains entails the addition of one extra DAC/ADC at the BS/MS, one extra power amplifier (PA) and low-noise amplifier (LNA) at the BS/MS, as well as $N_{\mathrm{BS}}/N_{\mathrm{MS}}$ extra phase shifters at the BS/MS, which significantly increases the hardware complexity, cost, and power consumption.

Table 6.14: RF hardware needed for the 3GPP channel model [66] and NYUSIM [51, 223] to achieve the same or similar spectrum efficiency in the single-cell SU-MIMO case using the HBF algorithm proposed in [117] for the UMi scenario. The carrier frequency is 28 GHz with an RF bandwidth of 100 MHz and narrowband frequency-flat fading sub-carriers. The BS is equipped with 256 cross-polarized antenna elements comprising a URA, and each UE has 16 cross-polarized omnidirectional antenna elements constituting a URA. Each BS antenna element has a radiation pattern as specified in Table 7.3-1 of [66] with a maximum gain of 8 dBi, and each RX antenna element possesses an omnidirectional pattern. The total transmit power is 46 dBm. In the simulations, it is assumed that 95% of the area in the cell has an SNR larger than or equal to 5 dB, and the upper bound of the T-R separation distance is calculated based on this assumption.

Beam-forming Approach	**Channel Model**	**Average Spectral Efficiency (bps/Hz)**	**# of Streams**	**# of TX RF Chains**	**# of RX RF Chains**	**# of Phase Shifters at TX/RX**	**# of PAs/L-NAs at TX/RX**
Digital [117]	**3GPP**	15.1	1	256	16	256 / 16	256 / 16
	NYUSIM	19.0	1	256	16	256 / 16	256 / 16
HBF [117]	**3GPP**	12.8	1	1	1	256 / 16	1 / 1
	NYUSIM	18.0	1	1	1	256 / 16	1 / 1
	3GPP	22.8	2	6	6	1536 / 96	6 / 6
	NYUSIM	22.9	2	2	2	512 / 32	2 / 2
	3GPP	29.6	3	6	4	1536 / 64	6 / 4
	NYUSIM	29.6	3	3	3	768 / 48	3 / 3
	3GPP	35.2	4	8	4	2048 / 64	8 / 4
	NYUSIM	35.3	5	5	5	1280 / 80	5 / 5

of the stronger two dominant eigen channels per user, and the smaller AoA spread per user such that channels among different users are less correlated leading to less interference when compared to the 3GPP model. The evaluation performance of the 3GPP and NYUSIM channel models for various spatial multiplexing and beamforming scenarios is summarized in Table 6.17.

Table 6.14 compares the number of RF chains needed for both 3GPP and NYUSIM channel models to achieve the same or similar spectral efficiency using the

Table 6.15: RF hardware needed for the 3GPP channel model [66] and NYUSIM [51, 223] to achieve the same or similar spectrum efficiency in the single-cell SU-MIMO case using the HBF algorithm proposed in [117] for the UMi scenario. The carrier frequency is 28 GHz with an RF bandwidth of 100 MHz and narrowband frequency-flat fading sub-carriers. The BS is equipped with 256 cross-polarized antenna elements comprising a URA, and each UE has 16 cross-polarized omnidirectional antenna elements constituting a URA. Each BS antenna element has a radiation pattern as specified in Table 7.3-1 of [66] with a maximum gain of 8 dBi, and each RX antenna element possesses an omnidirectional pattern. The total transmit power is 46 dBm. In the simulations, it is assumed that the receive SNR is 10 dB.

Beam-forming Approach	**Channel Model**	**Average Spectral Efficiency (bps/Hz)**	**# of Streams**	**# of TX RF Chains**	**# of RX RF Chains**	**# of Phase Shifters at TX/RX**	**# of PAs/L-NAs at TX/RX**
HBF [117]	**3GPP**	9.1	2	3	2	768 / 32	3 / 2
	NYUSIM	9.1	2	2	2	512 / 32	2 / 2
	3GPP	10.0	4	10	10	2560 / 160	10 / 10
	NYUSIM	10.1	4	4	4	1024 / 64	4 / 4

HBF algorithm proposed in [117]. In Table 6.14, the spectral efficiency is averaged over all the user locations in a cell with a cell-edge SNR of 5 dB. Alternatively, the spectral efficiency can be calculated with a fixed receive SNR (i.e., 10 dB) at all user locations, which is shown in Table 6.15. Note that for HBF, adding one RF chains entails the addition of one extra DAC/ADC at the BS/MS, one extra power amplifier (PA) and low-noise amplifier (LNA) at the BS/MS, as well as $N_{\text{BS}}/N_{\text{MS}}$ extra phase shifters at the BS/MS, as shown in Fig. 6.8, which significantly increases the hardware complexity, cost, and power consumption, especially for large N_{BS} and N_{MS} that are likely to be the case in mmWave systems. It is evident from Tables 6.14 and 6.15 that *the 3GPP model necessitates more RF chains, i.e., higher hardware complexity, cost, and power consumption, to achieve comparable spectral efficiency to NYUSIM*. For instance, as shown by Table 6.14, when only one data

Table 6.16: Sum spectral efficiency in bps/Hz in multi-cell multi-user MIMO systems for both types of base station HBF architecture shown in Fig. 8.3 using 3GPP [66] and NYUSIM [51, 52] channel models. There are three cells with one base station and three users per cell, the total transmit power per cell is 46 dBm, and the number of antennas is 256 per base station and eight per user. The number of data streams per user is two, and the number of total RF chains per base station is six. The 10%, 50%, and 90% points denote the corresponding points in the CDF of the sum spectral efficiency.

	Sum Spectral Efficiency (bps/Hz)	**10% Point**	**50% Point**	**90% Point**
Structure 1 (Fig. 8.3(a))	**3GPP**	14.0	29.5	41.0
	NYUSIM	38.1	56.9	79.0
Structure 2 (Fig. 8.3(b))	**3GPP**	27.1	52.1	65.3
	NYUSIM	56.9	77.3	98.1

Table 6.17: Summary of the evaluation performance on spectral efficiency/capacity of the 3GPP channel model [66] and NYUSIM [51, 223].

Scenario	**Model Predicting Larger Capacity**
Spatial Multiplexing Based on H	**3GPP** (due to increased multipath richness in the 3GPP model)
Spatial Multiplexing Based on $\mathbf{HF}_{\mathrm{RF}}$	**3GPP** (due to increased multipath richness in the 3GPP model although $\mathbf{F}_{\mathrm{RF}}$ makes the channel correlated)
Digital Beamforming	**3GPP (with a large number of data streams) or NYUSIM (with a small number of data streams)** (shown by Fig. 6.7)
HBF for Single-Cell Single-User Single-Stream	**NYUSIM** (due to channel sparsity and larger dominant eigenvalue in the NYUSIM model and HBF processing that changes the channel properties as seen by the RX; shown by Fig. 6.7(a))
HBF for Multi-Cell Multi-User Multi-Stream	**NYUSIM** (due to channel sparsity and larger dominant eigenvalue in the NYUSIM model and HBF processing that changes the channel properties as seen by the RX; to be shown by Figs. 8.11 and 8.13 in Chapter 8)

stream is transmitted, the average spectral efficiency yielded by the 3GPP model even with the maximum possible RF chains (256 TX RF chains and 16 RX RF chains) is still smaller than the NYUSIM spectral efficiency with the minimum possible RF chains (one TX RF chain and one RX RF chain), due to the much stronger dominant eigen channel in NYUSIM as shown in Fig. 6.4. When two data streams are transmitted, the 3GPP model needs three times as many RF chains and phase shifters to yield similar spectral efficiency to that of NYUSIM. When four or more data streams are transmitted, NYUSIM can generate similar spectral efficiency with comparable or fewer total RF chains as compared to the 3GPP model, but more data streams are required since the third and latter eigen channels in NYUSIM are much weaker than those in the 3GPP model.

6.3 Concluding Remarks

This chapter provided a comprehensive comparison of two representative channel models, the 3GPP model and the NYUSIM model, and demonstrated the profound impact of the models on 5G channel performance evaluation via simulations. *Key differences between the two channel models are the LOS probability model, path loss model, and cluster/TCSL statistics, among which cluster/TCSL statistics matter most.* Analyses and simulation results show that *channel model selection has a huge influence on deployment decisions and on various metrics, such as spectrum efficiency, coverage and performance, cell radius, and hardware/signal processing requirements.*

The 3GPP and NYUSIM channel models utilize different LOS probability models, path loss models, cluster definitions, and large-scale and small-scale parameters,

etc. Particularly, *the number of clusters in the 3GPP model is over two to four times as large as the maximum number of spatial lobes in NYUSIM, leading to different channel sparsity levels in the two models.* The difference in LOS probability and path loss models gives rise to discrepant cell radius prediction results that can differ by 50 m or so for around 500 transmit antenna elements. Compared to NYUSIM, the larger cluster number (i.e., more rich multipath) in the 3GPP model results in more eigen channels and more similar powers among those eigen channels, thus is advantageous for spatial multiplexing. On the other hand, the NYUSIM channel exhibits sparsity and has fewer but stronger dominant eigenmodes, hence generating higher spectral efficiency when combined with appropriate HBF procedures. For example, for the one-stream case in a SU-MIMO system using the HBF algorithm in [117], the average spectral efficiency yielded by the 3GPP model even with the maximum possible RF chains is still smaller than the NYUSIM spectral efficiency with the minimum possible RF chains. Different channel models can lead to substantially varied predictions on diverse channel performance metrics and hardware requirements, thus it is vital to select an accurate channel model for 5G wireless system performance evaluation.

Chapter 7

Millimeter Wave MIMO Channel Estimation Based on Adaptive Compressed Sensing

CSI is necessary to design precoding and combining procedures at transmitters and receivers, and it can be obtained through channel estimation. Due to the facts that large antenna arrays will be used in mmWave systems, and that mmWave channels exhibit sparsity due to the limited number of dominant spatial lobes [51, 52, 205], conventional MIMO channel estimation methods may not be applicable in mmWave systems, hence new channel estimation methods are required [118], and CS techniques [120] can be leveraged to effectively estimate mmWave channels [121, 122]. Adaptive CS, as a branch of CS, yields better performance at low SNRs compared to standard CS techniques, and low SNRs are typical for mmWave systems before implementing beamforming gain [119]. Adaptive CS algorithms for estimating mmWave channel parameters with the presence of antenna arrays were derived

in [119] for both single-path and multipath scenarios, and it was shown that the proposed channel estimation approaches could achieve comparable precoding gains compared with exhaustive training algorithms [119]. However, in [119] and the majority of existing work, standard basis pursuit (SBP) is used to construct beamforming dictionary matrices, which renders the problem of basis mismatch so that not all AoDs and AoAs can be estimated accurately. Therefore, more advanced beamforming dictionary constructing approaches are needed to improve estimation accuracy and hence spectral efficiency.

This chapter presents an enhanced approach to the creation of beamforming dictionary matrices for mmWave MIMO channel estimation in comparison with the one introduced in [119], based on adaptive CS concepts. The main novelty of the proposed method here is the adoption of the CBP method instead of the conventional grid-based (i.e., SBP) approach to build beamforming dictionary matrices [55]. This chapter shows that the proposed dictionary can significantly improve the estimation accuracy, i.e., reduce the probability of estimation error, of AoDs and AoAs. Furthermore, built on the CBP-based dictionary, two new multipath channel estimation algorithms are proposed that have lower computational complexity compared to the one introduced in [119], while offering better estimation accuracy for various signal sparsities. NYUSIM [51, 52] was used in the simulation to investigate the performance of the proposed algorithms.

The following notations are used throughout this chapter. $\mathbb{N}$ denotes the set of natural numbers; $\text{tr}(\mathbf{X})$ and $\text{vec}(\mathbf{X})$ indicate the trace and vectorization of $\mathbf{X}$, respectively; The Hadamard, Kronecker and Khatri-Rao products between two matrices are denoted by $\circ$, $\otimes$, and $*$, respectively.

7.1 System Model

Let us consider a BS equipped with N_{BS} antennas and N_{RF} RF chains communicating with an MS with N_{MS} antennas and N_{RF} RF chains, where $N_{\mathrm{RF}} \leq N_{\mathrm{MS}} \leq N_{\mathrm{BS}}$. System interference issues, such as co-channel interference from other BSs and MSs, are intentionally not considered because of the limited interference found in directional mmWave channels [118], and also, the focus of this chapter is to quantify and compare the performance of channel estimation methods in a single link [55]. System aspects are ongoing research topics. A carrier frequency of 28 GHz with an 800 MHz RF bandwidth and narrowband frequency-flat fading sub-carriers are assumed in the simulation settings in this chapter, but the CBP method and proposed algorithms are applicable to any mmWave frequency and bandwidth. In the channel estimation stage, the BS employs M_{BS} beamforming vectors to transmit M_{BS} symbols, while the MS utilizes M_{MS} combining vectors to combine the received signal. The BS is assumed to implement analog/digital hybrid precoding with a precoding matrix $\mathbf{F} = \mathbf{F}_{\mathrm{RF}}\mathbf{F}_{\mathrm{BB}}$, where $\mathbf{F}_{\mathrm{RF}} \in \mathbb{C}^{N_{\mathrm{BS}} \times N_{\mathrm{RF}}}$ and $\mathbf{F}_{\mathrm{BB}} \in \mathbb{C}^{N_{\mathrm{RF}} \times M_{\mathrm{BS}}}$ denote the RF and baseband precoding matrices, respectively. Similarly, at the MS, the combiner $\mathbf{W}$ also consists of RF and baseband combiners represented by $\mathbf{W}_{\mathrm{RF}} \in \mathbb{C}^{N_{\mathrm{MS}} \times N_{\mathrm{RF}}}$ and $\mathbf{W}_{\mathrm{BB}} \in \mathbb{C}^{N_{\mathrm{RF}} \times M_{\mathrm{MS}}}$, respectively. The received signal at the MS is given by [55]:

$$\mathbf{Y} = \mathbf{W}^H \mathbf{H} \mathbf{F} \mathbf{S} + \mathbf{Q} \tag{7.1}$$

where $\mathbf{H} \in \mathbb{C}^{N_{\mathrm{MS}} \times N_{\mathrm{BS}}}$ denotes the channel matrix, $\mathbf{S} \in \mathbb{C}^{M_{\mathrm{BS}} \times M_{\mathrm{BS}}}$ is a diagonal matrix containing the M_{BS} transmitted symbols, and $\mathbf{Q} \in \mathbb{C}^{M_{\mathrm{MS}} \times M_{\mathrm{BS}}}$ represents the complex Gaussian noise. The design of analog/digital hybrid precoding and combining matrices have been extensively investigated [117, 148], and this topic

is deferred to future work and channel estimation is focused on in this chapter. Additionally, although CSI can also be obtained by uplink training and channel reciprocity in TDD systems, this chapter focuses on the downlink training since channel reciprocity usually does not hold for FDD systems, and even in TDD systems if there exist non-linear devices that are not self-calibrated so as to incur non-reciprocal effects.

The mmWave channel can be approximated by a geometric channel model with L scatterers due to its limited scattering feature [2, 168, 184], and the channel matrix can be written as

$$\mathbf{H} = \sqrt{\frac{N_{\mathrm{BS}} N_{\mathrm{MS}}}{L}} \sum_{l=1}^{L} \alpha_l \mathbf{a}_{\mathrm{MS}}(\varphi_l, \vartheta_l) \mathbf{a}_{\mathrm{BS}}^{H}(\phi_l, \theta_l) \tag{7.2}$$

where α_l is the complex gain of the l^{th} path between the BS and MS including the path loss, where a path refers to a cluster of multipath components traveling closely in time and/or spatial domains, $\phi_l, \varphi_l \in [0, 2\pi)$ are the azimuth AoD and AoA of the l^{th} path, $\theta_l, \vartheta_l \in [-\pi/2, \pi/2]$ are the elevation AoD and AoA. $\mathbf{a}_{\mathrm{BS}}(\phi_l, \theta_l)$ and $\mathbf{a}_{\mathrm{MS}}(\varphi_l, \vartheta_l)$ are the antenna array response vectors at the BS and MS, respectively. The NYUSIM simulator produces a wide range of sample ensembles for (7.2) and incorporates multiple antenna elements and physical arrays including ULAs [51]. Using a ULA, the array response vector can be expressed as (take the BS for example)

$$\mathbf{a}_{\mathrm{BS}}(\phi_l) = \frac{1}{\sqrt{N_{\mathrm{BS}}}} [1, e^{j\frac{2\pi}{\lambda} d cos(\phi_l)}, \cdots, e^{j(N_{\mathrm{BS}}-1)\frac{2\pi}{\lambda} d cos(\phi_l)}]^T \tag{7.3}$$

where the incident angle is defined as 0 if the beam is parallel with the array direction, λ denotes the carrier wavelength, and d is the spacing between adjacent antenna elements.

7.2 Formulation of the mmWave Channel Estimation Problem

Considering the mmWave channel matrix given by (7.2), estimating the channel is equivalent to estimating the AoD, AoA, and path gain of each path, and training precoders and combiners are necessary to conduct the channel estimation. The mmWave channel estimation can be formulated as a sparse problem due to its limited dominant paths, e.g., on average 1 to 6 time clusters and 2 to 3 spatial lobes were found from real-world measurements using a 10 dB down threshold, as presented in [52]. Therefore, some insights can be extracted from the CS theory. Assuming all transmitted symbols are equal for the estimation phase, i.e., $\mathbf{S} = \sqrt{P}\mathbf{I}_{M_{\text{BS}}}$ (P is the average power per transmission) and by vectorizing the received signal $\mathbf{Y}$ in (7.1) to $\mathbf{y}$, the received signal can be approximated with a sparse formulation as follows [119]

$$\begin{aligned}
\mathbf{y} &= \sqrt{P}\text{vec}(\mathbf{W}^H\mathbf{H}\mathbf{F}) + \text{vec}(\mathbf{Q}) \\
&= \sqrt{P}(\mathbf{F}^T \otimes \mathbf{W}^H)\text{vec}(\mathbf{H}) + \mathbf{n}_{\text{Q}} \\
&= \sqrt{P}(\mathbf{F}^T \otimes \mathbf{W}^H)(\mathbf{A}^*_{\text{BS,D}} * \mathbf{A}_{\text{MS,D}})\mathbf{z} + \mathbf{n}_{\text{Q}} \\
&= \sqrt{P}(\mathbf{F}^T\mathbf{A}^*_{\text{BS,D}} \otimes \mathbf{W}^H\mathbf{A}_{\text{MS,D}})\mathbf{z} + \mathbf{n}_{\text{Q}} \\
&= \sqrt{P}\mathbf{F}^T\mathbf{A}^*_{\text{BS,D}}\mathbf{z}_{\text{BS}} \otimes \mathbf{W}^H\mathbf{A}_{\text{MS,D}}\mathbf{z}_{\text{MS}} + \mathbf{n}_{\text{Q}}
\end{aligned} \tag{7.4}$$

where $\mathbf{A}_{\text{BS,D}}$ and $\mathbf{A}_{\text{MS,D}}$ denote the beamforming dictionary matrices at the BS and MS, respectively. $\mathbf{z}_{\text{BS}} \in \mathbb{C}^{N\times 1}$ and $\mathbf{z}_{\text{MS}} \in \mathbb{C}^{N\times 1}$ are two sparse vectors that have non-zero elements in the locations associated with the dominant paths, with N denoting the number of measurements in the channel estimation stage, and

$\mathbf{z} = \mathbf{z}_{\mathrm{BS}} * \mathbf{z}_{\mathrm{MS}}$.

A beamforming dictionary based on angle quantization was proposed in [119], where the AoDs and AoAs were assumed to be taken from a uniform grid of N points with $N \gg L$ where L denotes the number of paths, and the resulting dictionary matrix is expressed as (take the BS side for example, the MS dictionary matrix can be derived similarly)

$$\mathbf{A}_{\mathrm{BS,D}} = [\mathbf{a}_{\mathrm{BS}}(\phi_1), \cdots, \mathbf{a}_{\mathrm{BS}}(\phi_N)] \tag{7.5}$$

where $\mathbf{a}_{\mathrm{BS}}(\phi_n)$ $(n = 1, ..., N)$ denotes the BS array response vector for the grid point ϕ_n.

Given that the true continuous-domain AoDs and AoAs may lie off the center of the grid bins, the grid representation in this case will destroy the sparsity of the signal and result in the so-called basis mismatch [233]. This can be mitigated to a certain extent by finer discretization of the grid, but that may lead to higher computation time and higher mutual coherence of the sensing matrix, thus becoming less effective for sparse signal recovery [120]. There are several approaches to mitigate the basis mismatch problem. One promising approach, named CBP, is proposed in [233], where one type of CBP is implemented with first-order Taylor interpolator, which will be demonstrated shortly. Since the antenna array factor $\mathbf{a}(\phi)$ is a continuous and smooth function of ϕ, it can be approximated by linearly combining $\mathbf{a}(\phi_k)$ and the derivative of $\mathbf{a}(\phi)$ at the point ϕ_k via a first-order Taylor expansion:

$$\mathbf{a}(\phi) = \mathbf{a}(\phi_k) + (\phi - \phi_k)\frac{\partial \mathbf{a}(\phi)}{\partial \phi}\bigg|_{\phi_k} + \mathcal{O}((\phi - \phi_k)^2) \tag{7.6}$$

where $\phi_k = 2\pi(k-1)/N$ is the grid-point with minimal distance from ϕ. This

motivates a dictionary consisting of the original discretized array factors $\mathbf{a}(\phi)$ and its derivatives $\frac{\partial \mathbf{a}(\phi)}{\partial \phi}$, i.e., $\mathbf{a}(\phi)$ and $\frac{\partial \mathbf{a}(\phi)}{\partial \phi}$ can be regarded as two sets of basis for the dictionary. Therefore, the entire basis for the proposed dictionary matrix can be formulated as

$$\mathbf{B}_{\mathrm{BS}} = [\mathbf{a}_{\mathrm{BS}}(\phi_1), \cdots, \mathbf{a}_{\mathrm{BS}}(\phi_N), \mathbf{b}_{\mathrm{BS}}(\phi_1), \cdots, \mathbf{b}_{\mathrm{BS}}(\phi_N)] \tag{7.7}$$

where $\mathbf{b}_{\mathrm{BS}}(\phi_n) = \frac{\partial \mathbf{a}_{\mathrm{BS}}(\phi)}{\partial \phi}\big|_{\phi_n}$, and the corresponding interpolator is given by

$$\mathbf{t}_{\mathrm{BS}} = [\underbrace{1, \cdots, 1}_{N}, \underbrace{\Delta\phi, \cdots, \Delta\phi}_{N}] \tag{7.8}$$

where $\Delta\phi$ denotes the angle offset from the angles on the grid, and $|\Delta\phi| \leq \frac{\pi}{N}$. The proposed dictionary is hence written as

$$\tilde{\mathbf{A}}_{\mathrm{BS,D}} = \mathbf{B}_{\mathrm{BS}} * \mathbf{t}_{\mathrm{BS}} = [\mathbf{a}_{\mathrm{BS}}(\phi_1), \cdots, \ \mathbf{a}_{\mathrm{BS}}(\phi_N), \ \Delta\phi\mathbf{b}_{\mathrm{BS}}(\phi_1), \cdots, \ \Delta\phi\mathbf{b}_{\mathrm{BS}}(\phi_N)] \tag{7.9}$$

7.3 Multi-Resolution Hierarchical Codebook

The proposed hierarchical beamforming codebook is composed of S levels, where each level contains beamforming vectors with a certain beamwidth that covers certain angular regions [55]. Due to the symmetry of the antenna pattern of a ULA, if a beam covers an azimuth angle range of $[\phi_a, \phi_b]$, then it also covers $2\pi - [\phi_a, \phi_b]$. In each codebook level s, the beamforming vectors are divided into K^{s-1} subsets, each of which contains K beamforming vectors. Each of these K beamforming vectors is designed such that it has an almost equal projection on the vectors $\mathbf{a}_{\mathrm{BS}}(\bar{\phi})$, where $\bar{\phi}$ denotes the angle range covered by this beamforming vector, and

zero projection on the array response vectors corresponding to other angles. Note that there is no strict constraint on the number of sectors K at each stage, yet considering practical angle-searching time, $K = 3$ or 4 is a reasonable choice. Once the value of K is defined, the total number of estimation measurements N is $2K^S$. The value of N should be minimized while guaranteeing the successful estimation of angles, thus S should be neither too large nor too small. Through simulations, it is found that $S = 3, K = 4$ ($N = 128$) and $S = 4, K = 3$ ($N = 162$) are two sensible combinations [55].

In each codebook level s and subset k, the m^{th} column of the beamforming vector $[\mathbf{F}_{(s,k)}]_{:,m}, m = 1, ..., K$ in the codebook $\mathcal{F}$ is designed such that [55]:

$$[\mathbf{F}_{(s,k)}]_{:,m}^{H}\mathbf{a}_{\text{BS}}(\bar{\phi}_u) = \begin{cases} C, & \text{for } \bar{\phi}_u \in \oplus_{s,k,m}^{\text{BS}} \\ 0, & \text{otherwise} \end{cases}$$

$$[\mathbf{F}_{(s,k)}]_{:,m}^{H}\mathbf{b}_{\text{BS}}(\bar{\phi}_u) = 0, \forall\ \bar{\phi}_u \tag{7.10}$$

with

$$\begin{aligned} \oplus_{s,k,m}^{\text{BS}} = &\Big[\frac{\pi}{K^s}\big(K(k_s^{\text{BS}} - 1) + m_{\text{BS}} - 1\big), \frac{\pi}{K^s}(K(k_s^{\text{BS}} - 1) + m_{\text{BS}})\Big] \\ &\cup \Big[2\pi - \frac{\pi}{K^s}(K(k_s^{\text{BS}} - 1) + m_{\text{BS}}), 2\pi - \frac{\pi}{K^s}\big(K(k_s^{\text{BS}} - 1) + m_{\text{BS}} - 1\big)\Big] \end{aligned} \tag{7.11}$$

where C is a constant such that each $\mathbf{F}_{(s,k)}$ has a Frobenius norm of K. The fact that the product of $[\mathbf{F}_{(s,k)}]_{:,m}^{H}$ and $\mathbf{b}_{\text{BS}}(\bar{\phi}_u)$ is zero in (7.10) can be derived from (7.6) to (7.9). The matrix $\mathbf{F}_{(s,k)}$ hence equals the product of the pseudo-inverse of $\tilde{\mathbf{A}}_{\text{BS,D}}$ and the $(k \times K - (K-1))^{\text{th}}$ to $(k \times K)^{\text{th}}$ columns of the angle coverage matrix

$\mathbf{G}_{(s)}$ with its m^{th} column given by (7.12) [55]:

$$[\mathbf{G}_{(s)}]_{:,m} = [\underbrace{C's \text{ and } 0's}_{N}, \underbrace{0, \cdots, 0}_{N}]^T \tag{7.12}$$

where C's are in the locations $\oplus_{s,k,m}^{\text{BS}}$. The combining matrix $\mathbf{W}_{(s,k)}$ in the codebook $\mathcal{W}$ at the receiver can be designed in a similar manner. It is noteworthy that the difference between the angle coverage matrix $\mathbf{G}_{(s)}$ in [119] and the one proposed here is that the m^{th} column of the former contains only the first N rows without the last N 0's in (7.12), i.e., the former did not force $[\mathbf{F}_{(s,k)}]_{:,m}^H \mathbf{b}_{\text{BS}}(\bar{\phi}_u)$ to be zero, hence failing to alleviate the leakage incurred by angle quantization [55].

Fig. 7.1 illustrates the beam patterns of the beamforming vectors in the first codebook level of an example hierarchical codebook introduced in [119] and the hierarchical codebook proposed in this chapter with $N = 162$ and $K = 3$. Comparing the two beam patterns, *the codebook generated using the CBP-based dictionary* $\tilde{\mathbf{A}}_{\text{BS,D}}$ *in* (7.9) *produces a smoother (i.e., fewer ripples) pattern contour in contrast to that yielded by the codebook introduced in [119], namely, the beams associated with* $\tilde{\mathbf{A}}_{\text{BS,D}}$ *are able to cover the intended angle ranges more evenly* [55]. Due to the more uniform projection on the targeted angle region, the beamforming vectors generated using $\tilde{\mathbf{A}}_{\text{BS,D}}$ can mitigate the leakage induced by angle quantization, thus improving the angle estimation accuracy, as will be shown later.

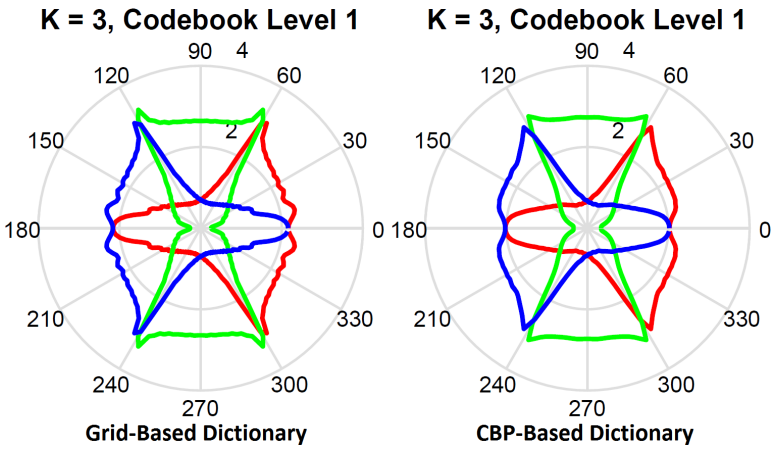

Figure 7.1: Beam patterns of the beamforming vectors in the first codebook level of an example hierarchical codebook using the grid-based and CBP-based dictionaries with $N = 162$, $K = 3$ [55].

7.4 Adaptive estimation algorithms for mmWave MIMO channels

For single-path channels, there is only one non-zero element in the vector $\mathbf{z}$ in (7.4). To effectively estimate the location of this non-zero element, and consequently the corresponding AoD, AoA, and path gain, the following algorithm, which is an improved version of Algorithm 1 in [119], is used in conjunction with the innovative CBP-based dictionary matrices [55].

Algorithm 1 operates as follows. In the initial stage, the BS uses the training precoding vectors of the first level of the codebook $\mathcal{F}$. For each of those vectors, the MS uses the measurement vectors of the first level of $\mathcal{W}$ to combine the received signal. After the precoding-measurement steps of this stage, the MS compares the power of the received signals to determine the one with the maximum received power. As each one of the precoding/measurement vectors is associated with a certain range of the quantized AoA/AoD, the operation of the first stage divides

Algorithm 1 Adaptive Estimation Algorithm for Single-Path mmWave MIMO channels [55]

Require: K, S, codebooks $\mathcal{F}$ and $\mathcal{W}$, $N = 2K^S$

Initialization: $k_1^{\mathrm{BS}} = 1$, $k_1^{\mathrm{MS}} = 1$
for $s \leq S$ **do**
  for $m_{\mathrm{BS}} \leq K$ **do**
    BS uses $[\mathbf{F}_{(s,k_s^{\mathrm{BS}})}]_{:,m_{\mathrm{BS}}}$
    for $m_{\mathrm{MS}} \leq K$ **do**
      MS uses $[\mathbf{W}_{(s,k_s^{\mathrm{MS}})}]_{:,m_{\mathrm{MS}}}$
    end for $m_{\mathrm{MS}} \leq K$
  end for $m_{\mathrm{BS}} \leq K$
end for $s \leq S$
for $s \leq S$ **do**
  $\mathbf{Y}_{(s)} = \sqrt{P_s}[\mathbf{W}_{(s,k_s^{\mathrm{MS}})}]^H \mathbf{H}[\mathbf{F}_{(s,k_s^{\mathrm{BS}})}] + \mathbf{Q}$
  $\{m_{\mathrm{BS}}^*, m_{\mathrm{MS}}^*\} = \underset{\forall m_{\mathrm{BS}}, m_{\mathrm{MS}}=1,\ldots,K}{\operatorname{argmax}} [\mathbf{Y}_{(s)} \circ \mathbf{Y}_{(s)}^*]_{m_{\mathrm{MS}}, m_{BS}}$
  $\hat{\phi}_{\mathrm{can}} \in \oplus_{s,k,m}^{\mathrm{BS}}$, $\hat{\varphi}_{\mathrm{can}} \in \oplus_{s,k,m}^{\mathrm{MS}}$ % $\oplus_{s,k,m}^{\mathrm{BS}}$ is given by Eq. (7.11), and $\oplus_{s,k,m}^{\mathrm{MS}}$ can be calculated similarly
  $k_{s+1}^{\mathrm{BS}} = K(k_s^{\mathrm{BS}} - 1) + m_{\mathrm{BS}}^*$, $k_{s+1}^{\mathrm{MS}} = K(k_s^{\mathrm{MS}} - 1) + m_{\mathrm{MS}}^*$,
end for $s \leq S$
$\mathbf{A}_{\mathrm{can,BS}} = [\mathbf{a}_{\mathrm{BS}}(\hat{\phi}_{\mathrm{can}})]$ % Antenna array matrix for the candidate AoDs
$\mathbf{A}_{\mathrm{can,MS}} = [\mathbf{a}_{\mathrm{MS}}(\hat{\varphi}_{\mathrm{can}})]$ % Antenna array matrix for the candidate AoAs
$\mathbf{Z} = \mathbf{A}_{\mathrm{can,MS}}^H \mathbf{H} \mathbf{A}_{\mathrm{can,BS}} + \mathbf{Q}$ % Received signal matrix corresponding to the candidate AoDs and AoAs
$(\hat{\phi}, \hat{\varphi}) = \arg\max\ \mathbf{Z} \circ \mathbf{Z}^*$ % Finding the optimal AoD and AoA that maximize the Hadamard product of the received signal matrix
$\hat{\alpha} = \sqrt{\mathbf{Z}_{(\hat{\phi},\hat{\varphi})} \circ \mathbf{Z}_{(\hat{\phi},\hat{\varphi})}^*}/(N_{\mathrm{BS}} * N_{\mathrm{MS}})$ % Estimated path gain magnitude associated with the estimated AoD and AoA

Ensure: $\hat{\phi}, \hat{\varphi}, \hat{\alpha}$

the entire angle range $[0,\ 2\pi)$ into K partitions, and compares the power of the sum of each of them. Hence, the selection of the strongest received signal implies the selection of the range of the quantized AoA/AoD that is highly likely to contain the single path of the channel. The output of the maximum power is then used to determine the subsets of the beamforming vectors of level $s+1$ $(1 \leq s \leq S-1)$ of $\mathcal{F}$ and $\mathcal{W}$ to be used in the next stage. Since N must be even multiples of K in order to construct the precoding and measurement codebooks, there are two possible ranges of AoD/AoA selected out after Step 15 of Algorithm 1, which are denoted as $\hat{\phi}_{\text{can}}$ and $\hat{\varphi}_{\text{can}}$. Step 16 is aimed at "filtering" out the AoD/AoA from these two ranges. The MS then feeds back the selected subset of the BS precoders to the BS to use it in the next stage, which needs only $\log_2 K$ bits.

Based on Algorithm 1 and inspired by the estimation algorithm in [119] for multipath channels (as opposed to single-path channels), two low-complexity algorithms for estimating multipath channels are established, namely Algorithms 2 and 3, and are explained below. In Algorithm 2, $\mathcal{I}^{\text{BS}}_{(i,s)}$ and $\mathcal{I}^{\text{MS}}_{(i,s)}$ contain the precoding and measurement matrix indexes of the i^{th} path in the s^{th} stage, respectively. Algorithm 2 operates as follows: A procedure similar to Algorithm 1 is utilized to detect the first strongest path. The indexes of the beamforming matrices corresponding to the previous detected l $(1 \leq l \leq L-1)$ paths are stored and used in later iterations. Note that in each stage s from the second iteration on, the contribution of the paths that have already been estimated in previous iterations are projected out one path by one path before determining the new promising AoD/AoA ranges. In the next stage $s+1$, two AoD/AoA ranges are selected for further refinement, i.e., the one selected at stage s of this iteration, and the one selected by the preceding path at stage $s+1$ of the previous iteration. The algorithm makes L outer

iterations to estimate L paths. Thanks to the sparse nature of mmWave channels, the number of dominant paths is usually limited, which means the total number of precoding-measurement steps will not be dramatically larger compared to the single-path case.

Algorithm 2 Adaptive Estimation Algorithm for Multipath mmWave MIMO channels [55]

Require: K, S, codebooks $\mathcal{F}$ and $\mathcal{W}$, $N = 2K^S$

1: **Initialization**: $\mathcal{I}^{\text{BS}}_{(:,1)} = [1, ..., 1]^T$, $\mathcal{I}^{\text{MS}}_{(:,1)} = [1, ..., 1]^T$, where $\mathcal{I}^{\text{BS}} \in \mathbb{N}^{L\times S}$, $\mathcal{I}^{\text{MS}} \in \mathbb{N}^{L\times S}$

2: Use Algorithm 1 to detect the AoD, AoA, and path gain for the first strongest path

3: Repeat Algorithm 1 for the l^{th} $(2 \leq l \leq L)$ path until Step 11 in Algorithm 1

4: For the s^{th} stage in the i^{th} $(2 \leq i \leq L)$ iteration, project out previous path contributions one path by one path

$\mathbf{Y}_{(s)} = \sqrt{P_s}[\mathbf{W}_{(s,k_s^{\text{MS}})}]^H \mathbf{H}[\mathbf{F}_{(s,k_s^{\text{BS}})}] + \mathbf{Q}$

$\mathbf{y}_{(s)} = \text{vec}(\mathbf{Y}_{(s)})$

$\mathbf{V}_{(i,s)} = \mathbf{F}^T_{(s,\mathcal{I}^{\text{BS}}_{(i,s)})}[\tilde{\mathbf{A}}_{\text{BS,D}}]^*_{:,\mathcal{I}^{\text{BS}}_{(i,s)}} \otimes \mathbf{W}^H_{(s,\mathcal{I}^{\text{MS}}_{(i,s)})}[\tilde{\mathbf{A}}_{\text{MS,D}}]_{:,\mathcal{I}^{\text{MS}}_{(i,s)}}$ % Calculating the contribution of previous paths in the form of Eq. (7.4)

$\mathbf{y}_{(s)} = \mathbf{y}_{(s)} - \mathbf{V}_{(i,s)}\mathbf{V}^{\dagger}_{(i,s)}\mathbf{y}_{(s)}$

5: Convert $\mathbf{y}_{(s)}$ to the matrix form $\mathbf{Y}_{(s)}$

6: Repeat Algorithm 1 from Step 12 to obtain the AoD, AoA, and path gain for the i^{th} strongest path until all the L paths are estimated

Ensure: AoDs, AoAs, and path gains for the L dominant paths

Algorithm 3 is similar to Algorithm 2, but with an even lower complexity. The major difference between Algorithm 3 and Algorithm 2 stems from the way of projecting out previous path contributions: Algorithm 3 does not require storing the beamforming matrix indexes, but instead, it utilizes the antenna array response vectors associated with the estimated AoDs/AoAs to subtract out the contributions of previously detected paths simultaneously. Therefore, compared with Algorithm 2, Algorithm 3 results in less computation and storage cost, and a higher estimation speed (i.e., lower latency). When compared with the multipath channel estimation

Algorithm 3 Adaptive Estimation Algorithm for Multipath mmWave MIMO channels [55]

Require: K, S, codebooks $\mathcal{F}$ and $\mathcal{W}$, $N = 2K^S$

1: **Initialization**: $\mathcal{I}^{\mathrm{BS}}_{(:,1)} = [1, ..., 1]^T$, $\mathcal{I}^{\mathrm{MS}}_{(:,1)} = [1, ..., 1]^T$, where $\mathcal{I}^{\mathrm{BS}} \in \mathbb{N}^{L \times S}$, $\mathcal{I}^{\mathrm{MS}} \in \mathbb{N}^{L \times S}$

2: Use Algorithm 1 to detect the AoD, AoA, and path gain for the first strongest path

3: Repeat Algorithm 1 for the l^{th} $(2 \leq l \leq L)$ path until Step 11 in Algorithm 1

4: For the s^{th} stage in the i^{th} $(2 \leq i \leq L)$ iteration, project out previous path contributions simultaneously

$\hat{\mathbf{A}}_{\mathrm{BS}} = [\mathbf{a}_{\mathrm{BS}}(\hat{\phi})]$, $\hat{\mathbf{A}}_{\mathrm{MS}} = [\mathbf{a}_{\mathrm{MS}}(\hat{\varphi})]$ % $\hat{\phi}$ and $\hat{\varphi}$ are the AoDs and AoAs of all the previously detected paths, respectively

$\mathbf{Y}_{(s)} = \sqrt{P_s}[\mathbf{W}_{(s,k_s^{\mathrm{MS}})}]^H \mathbf{H}[\mathbf{F}_{(s,k_s^{\mathrm{BS}})}] + \mathbf{Q}$

$\mathbf{y}_{(s)} = \mathrm{vec}(\mathbf{Y}_{(s)})$

$\mathbf{V}_{(i,s)} = [\mathbf{W}_{(s,k_s^{\mathrm{MS}})}]^H \hat{\mathbf{A}}_{\mathrm{MS}} \hat{\mathbf{A}}^H_{\mathrm{BS}} [\mathbf{F}_{(s,k_s^{\mathrm{BS}})}]$ % Calculating the contribution of previous paths in the form of Eq. (7.1)

$\mathbf{v}_{(i,s)} = \mathrm{vec}(\mathbf{V}_{(i,s)})$

$\mathbf{y}_{(s)} = \mathbf{y}_{(s)} - \mathbf{v}_{(i,s)} \mathbf{v}^{\dagger}_{(i,s)} \mathbf{y}_{(s)}$

5: Convert $\mathbf{y}_{(s)}$ to the matrix form $\mathbf{Y}_{(s)}$

6: Repeat Algorithm 1 from Step 12 to obtain the AoD, AoA, and path gain for the i^{th} strongest path until all the L paths are estimated

Ensure: AoDs, AoAs, and path gains for the L dominant paths

presented in [119], the most prominent advantages of both Algorithm 2 and Algorithm 3 are that they do not require the re-design of multi-resolution beamforming codebooks for each stage when the number of dominant paths vary, and only a single path is selected in each stage instead of L paths in [119], thus substantially reducing the calculation and memory overhead [55].

7.5 Simulation Results

In this section, the performance of the proposed CBP-based dictionary and Algorithms 1, 2, and 3 are evaluated in terms of average probability of estimation error of AoDs and AoAs, and spectral efficiency, via numerical Monte Carlo simulations. The channel matrix takes the form of (7.2), where the path powers, phases, AoDs, and AoAs are generated using NYUSIM [51]. ULAs are assumed at both the BS and MS with 64 and 32 antenna elements, respectively. All simulation results are averaged over 10,000 random channel realizations, with a carrier frequency of 28 GHz and an RF bandwidth of 800 MHz and OFDM modulation with narrowband sub-carriers. In calculating spectral efficiency, eigen-beamforming is assumed at both the transmitter (with equal power allocation) and receiver. Other beamforming techniques can also be employed, and the performance of the beamforming dictionaries and algorithms were found to be similar.

The simulated probabilities of estimation errors of AoDs and AoAs as a function of the average receive SNR, using Algorithm 1 and both grid-based and CBP-based dictionaries for single-path channels, are depicted in Fig. 7.2 for the cases of $N = 162$, $K = 3$, and $N = 128$, $K = 4$, which are found to yield the best performance via numerous trials. In Fig. 7.2, the probability of estimation error denotes the

ratio of the incorrectly estimated angles to the total number of angles estimated and is averaged over 10,000 random channel realizations. An estimation error is considered to take place when the absolute difference between the estimated angle (AoD or AoA) and the true angle is larger than $\frac{\pi}{N}$ (e.g., 1.1° when $N = 162$ and 1.4° when $N = 128$). In actual cellular systems, if the angular spread of a cluster (3GPP nomenclature) or spatial lobe (NYUSIM nomenclature) is larger than the absolute difference between the estimated AoD/AoA and the true AoD/AoA, then the estimation error will not cause significant degradation in spectral efficiency. As shown by Fig. 7.2, the CBP-based approach renders much smaller estimation errors, by up to two orders of magnitude. For the two cases considered in Fig. 7.2, the grid-based method generates huge estimation error probability that is over 80% even at an SNR of 20 dB; on the other hand, the estimation error probability of the CBP-based counterpart decreases rapidly with SNR, and is less than 0.5% for $N = 128$, $K = 4$ and a 20 dB SNR. These results imply that the CBP-based approach is able to provide much better channel estimation accuracy with a small number of measurements compared to the conventional grid-based fashion, hence is worth using in mmWave MIMO systems for sparse channel estimation and signal recovery [55].

To explicitly show the effect of estimation error on channel spectral efficiency using different beamforming dictionaries, the achievable spectral efficiency is plotted and compared as a function of the average receive SNR for both the grid-based and CBP-based dictionaries for single-path channels, as well as the spectral efficiency with perfect CSI at the transmitter, for the case of $N = 162$, $K = 3$, and $N = 128$, $K = 4$, as described in Fig. 7.3. It is assumed that the angular spread of a path (i.e., cluster (3GPP nomenclature) or spatial lobe (NYUSIM nomenclature)) is zero.

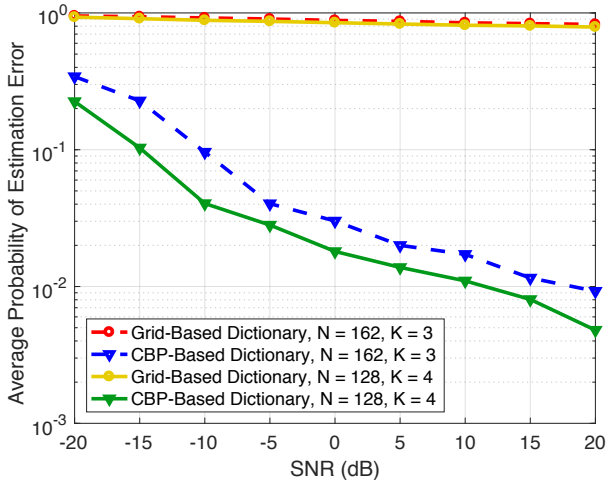

Figure 7.2: Average probability of error in estimating AoD/AoA for single-path channels, using both the grid-based dictionary and CBP-based dictionary [55].

As stated in the previous paragraph, the angular spread of a cluster or spatial lobe in actual cellular systems is larger than zero, thus the resultant spectral efficiency degradation will be smaller than in Fig. 7.3. It is evident from Fig. 7.3 that for both cases considered, the CBP-based dictionary yields much higher spectral efficiency, by about 2.7 bits/s/Hz to 13 bits/s/Hz, compared with the grid-based one over the entire SNR range of -20 dB to 20 dB. Furthermore, the CBP-based method achieves near-optimal performance over the SNRs spanning from 0 dB to 20 dB, with a gap of less than 0.7 bits/s/Hz [55].

Fig. 7.4 illustrates the average probability of error in estimating AoDs/AoAs for multipath channels with $N = 162$, $K = 3$, and $N = 128$, $K = 4$ for an average receive SNR of 20 dB, using proposed Algorithms 2 and 3 for two to six dominant paths, as well as Algorithm 2 in [119]. For the approach in [119], since all L paths have to be estimated simultaneously in a multipath channel, it does not work for $L < K$, thus no results are available for $L = 2$ when $K = 3$ or 4. The SNR denotes the ratio of the total received power from *all* paths to the noise power. As shown

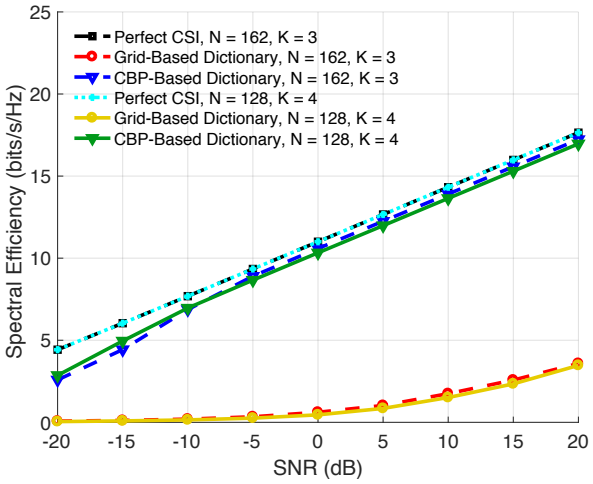

Figure 7.3: Average spectral efficiency for single-path channels for the cases of perfect CSI, grid-based dictionary and CBP-based dictionary [55].

in Fig. 7.4, both Algorithm 2 (Algo 2) and Algorithm 3 (Algo 3) produce lower estimation errors than the approach in [119] in both multipath-channel cases; for the case of $N = 128$, $K = 4$, Algorithm 3 yields the lowest estimation error, i.e., highest accuracy, and meanwhile enjoys the lowest computation expense among the three algorithms. In addition, the estimation error tends to increase more slowly and converge to a certain value as the number of dominant paths increase for all of the three algorithms [55].

The spectral efficiency performance of the three algorithms above, with $N = 162$, $K = 3$, and $L = 3$, is displayed in Fig. 7.5, which reveals the superiority of Algorithm 3 pertaining to spectral efficiency, followed by Algorithm 2, compared with the approach in [119]. For instance, at an SNR of 10 dB, Algorithms 2 and 3 yield around 5 and 8 more bits/s/Hz than the approach in [119], respectively, and the discrepancies expand as the SNR ascends. The proposed algorithms work well for single-path channels, and significantly outperforms the approach in [119] method for multipath channels, although there is still a noticeable spectral efficiency

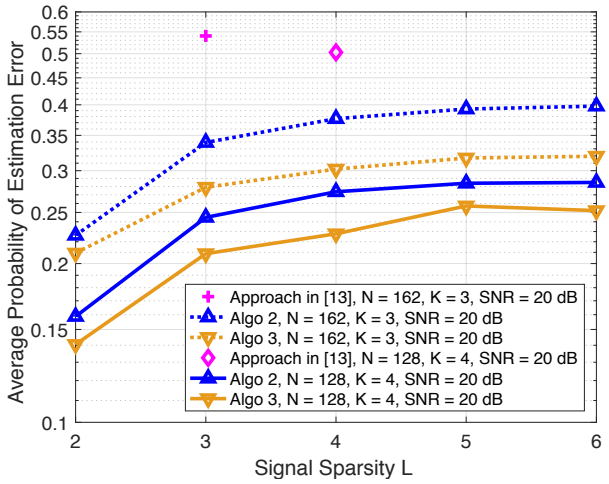

Figure 7.4: Average probability of error in estimating AoD/AoA for multipath channels using the CBP-based dictionary [55]. [13] in the figure denotes [119] in this technical report.

gap compared to the perfect CSI case, due to the non-negligible angle estimation errors shown in Fig. 7.4 [55]. Further work is needed to improve Algo 2 and Algo 3 to more effectively estimate multipath channels.

7.6 Concluding Remarks

Based on the concept of adaptive compressed sensing and by exploiting the sparsity of mmWave channels, this chapter presented an innovative approach for designing the precoding/measurement dictionary matrices, and two new low-complexity algorithms for estimating multipath channels. In contrast to the conventional grid-based method, *the principle of CBP was leveraged in devising the beamforming dictionary matrices, which had lower mutual coherence due to the first-order Taylor interpolation, and was shown to be more beneficial for sparse signal reconstruction* [55].

Simulations were performed based on the open-source 5G channel simulator

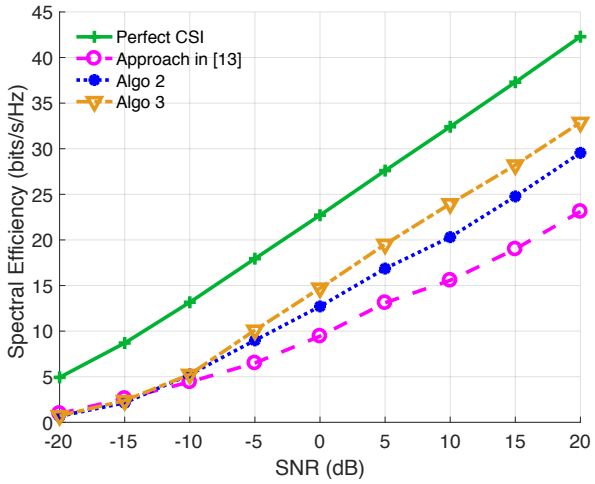

Figure 7.5: Average spectral efficiency for multipath channels with the CBP-based dictionary using the approach in [119], and Algorithms 2 and 3 proposed in this chapter, with $N = 162$, $K = 3$, and $L = 3$ [55]. [13] in the figure denotes [119] in this technical report.

NYUSIM for broadband mmWave systems. Results show that the *CBP-based dictionary renders up to over two orders of magnitude higher estimation accuracy (i.e., lower probability of estimation error) of AoDs and AoAs, and more than 12 bits/s/Hz higher spectral efficiency, with a small number of estimation measurements for single-path channels*, as opposed to the grid-based approach, as shown in Figs. 7.2 and 7.3. Moreover, the newly proposed two algorithms, Algorithm 2 and Algorithm 3, can offer better estimation and spectral efficiency performance with lower computational complexity and time consumption for multipath channels, when compared with existing algorithms, as shown in Figs. 7.4 and 7.5 [55].

Interesting extensions to this work will be to improve the multipath estimation algorithms to make them more effective, and to extend the multipath estimation algorithms to the case where the number of dominant paths is unknown, as well as to implement the proposed dictionary matrices and algorithms to other types of

antenna arrays such as 2D arrays.

Chapter 8

Multi-Cell Multi-User Multi-Stream Hybrid Beamforming

In this chapter, multi-cell multi-user multi-stream analog and digital HBF strategies for mmWave MIMO systems are investigated, which has not been studied before to my best knowledge. It is assumed that the TPs in different cells have full CSI and can exchange the CSI among each other, such that they can take actions to mitigate inter-cell interference, which corresponds to the coordinated beamforming per the definition by 3GPP [161]. We first formulate a multi-cell communication framework based upon today's conventional three-sector BS antenna configuration, where each 120° sector (i.e., cell, as defined in 3GPP parlance [161]) uses a URA with 256 antenna elements (eight rows by 16 columns by two polarization states) for each TP, similar to what is envisioned for 5G MIMO systems [230]. The spacing between adjacent co-polarized elements is $\lambda/2$ in azimuth and λ in elevation with

λ denoting the carrier wavelength (e.g., 10.7 mm at 28 GHz and 4.1 mm at 73 GHz), and the radiation pattern of each TP antenna element is given in Table 8.1, which provides a HPBW resolution of about 8° in both azimuth and elevation in the broadside direction of the URA at each TP. Note that the number of RF chains used to feed the URA dictates the number of independent RF streams that may be transmitted to all users in a cell. A number of (3 or 12 in this work) UEs, each with an eight-element (two rows by two columns by two polarization states) URA and four RF chains (for up to four streams per user), are randomly dropped in each cell over distances of 10 m to the cell radius (e.g., 50 m or 200 m). URAs are considered because they are able to form beams in both azimuth and elevation dimensions, as exploiting the zenith characteristics of the propagation channel will be essential for enhanced performance at mmWave frequencies [23]. 28 GHz carrier frequency with 100 MHz RF bandwidth and OFDM modulation with narrowband frequency-flat sub-carriers are assumed, and the calculation of the channel matrix is given by Eqs. (2.8)-(2.11) and explained by the text around them. The main contributions of this chapter are summarized as follows.

- Built on the multi-cell framework, eigenvalue distributions for channels after RF precoding in a multi-cell multi-user system with a single stream per user are investigated for both signal and interference channels, which has not been studied before. HBF based on RZF is employed at each TP. The channel matrices are generated using both the 3GPP TR 38.901 Release 14 channel model [66] and the NYUSIM channel model [51]. The eigenvalue densities are approximated with a gamma distribution. The approximation of eigenvalue densities is motivated by the fact that exact densities are extremely challenging to derive so that the best "trade-off" approach is to approximate.

- Leveraging the approximate channel eigenvalue densities of the 3GPP [66] and the NYUSIM [51] channel models, for a single-stream multi-cell system employing hybrid processing, a general methodology is given to derive tight analytical approximations of the expected per-user SINR, and expected per-cell sum spectral efficiency. Our analyses assume a bank of analog phase shifters for the analog precoding and RZF processing for digital beamforming. Due to the joint design of both analog and digital processing matrices, there is tremendous analytical complexity involved in deriving the aforementioned expressions. Hence, to the best of my knowledge, such general analysis of mmWave systems have been missing from the vast literature.

- A novel coordination-based HBF approach containing leakage-suppression and signal-maximization precoding (LSP) is proposed. Four multi-cell multi-stream downlink HBF approaches, where three use coordinated beamforming (including LSP) and one does not use any TP coordination (as a baseline), are compared in terms of spectral efficiency under various conditions (e.g., different cell radii, user numbers, and stream numbers per user). Both the 3GPP [66] and NYUSIM [51] channel models are adopted, and equal power allocations are used for each stream (i.e. no power control or water filling per stream). Numerical results demonstrate that benefits of multi-cell coordination depend on the underlying channel model and the interference levels, to be shown in Fig. 8.11.

Table 8.1: Simulation settings using the 3GPP [66] and NYUSIM [51] models.

Parameter	Setting
Carrier Frequency	28 GHz
Bandwidth	100 MHz [66]
Transmit Power Without Array Gain	35.2 dBm per UE (46 dBm for a cell with 12 UEs)
95% Cell-Edge SNR	5 dB
BS Antennas	three panels for the three TP sectors, where each panel is a uniform rectangular array consisting of 256 cross-polarized elements in the x-z plane [66]
BS Antenna Spacing	half wavelength in azimuth; one wavelength in elevation
BS Antenna Element Gain	8 dBi [66]
BS Antenna Element Pattern	Model 2, Page 18 in 3GPP TR 36.873 Release 12 [225]
UE Antennas	uniform rectangular array consisting of eight cross-polarized elements in the x-z plane [66]
UE Antenna Spacing	half wavelength in azimuth; one wavelength in elevation
UE Antenna Element Gain	0 dBi [66]
UE Antenna Element Pattern	omnidirectional [66]
Receiver Noise Figure	10 dB

8.1 Multi-Cell System Layout and Hybrid Beamforming Framework

8.1.1 Multi-Cell System Layout

We consider an mmWave system with three adjacent cells (i.e., sectors), each having one TP and multiple (e.g., 3 or 12) UEs. Only three adjacent cells are studied herein since inter-cell interference among these three cells dominate the interference due to the geographical proximity and use of mmWave frequencies, thus this case is representative of homogeneous multi-cell networks with both intra- and inter-cell interference. The four proposed HBF algorithms are applicable to general cases with more cells. Fig. 8.1 depicts an example of the three-cell layout with three users per cell. *Throughout this chapter, a carrier frequency of 28 GHz is used, with an RF bandwidth of 100 MHz, assuming OFDM modulation with narrowband*

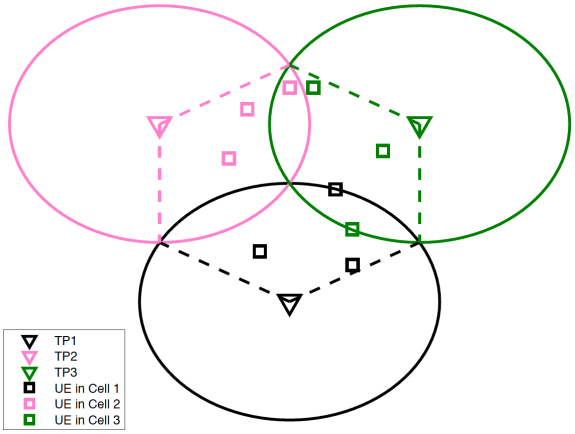

Figure 8.1: An example of the three-cell layout where there is one BS URA and three UEs per cell generated using MATLAB, where each cell is a sector with an azimuth span of 120° served by one BS URA. The radius of each cell is 300 m. The UEs in each cell are distributed uniformly and randomly with T-R separation distances ranging from 10 m to 300 m [66]. It is assumed that 95% of the area in a cell has an SNR larger than or equal to 5 dB, and the upper bound of the T-R separation distance is calculated based on this assumption and rounded to 200 m for both models for fair comparison.

frequency-flat fading sub-carriers as explained in detail in Chapter 6, reflecting current thinking for 5G spectrum allocations [20, 230, 231]. Simulation parameter are given in Table 8.1.

8.1.2 Base Station Antenna Array Configurations

A situation that is widely utilized in 5G system deployment is considered herein: the TP in each sector is equipped with a two-dimensional antenna array consisting of cross-polarized elements arranged in N_1 rows by N_2 columns by two polarizations, for a total of $2N_1N_2$ antenna elements. Two versions of array configurations have been explored by researchers [230]: a single-panel version and a four-panel version, as illustrated in Fig. 8.2 with a total of 512 elements comprising 16 rows by 16 columns by two polarizations. It is assumed in [230] that the array generates one

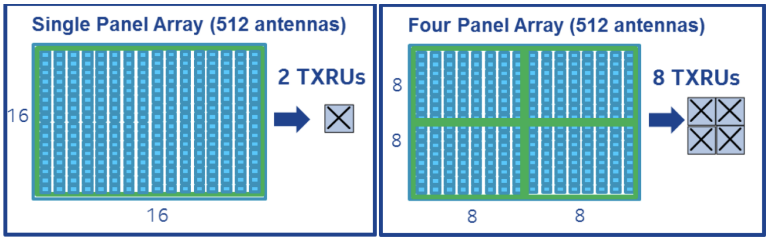

Figure 8.2: An example of hybrid antenna arrays configurations with a total of 512 elements comprising 16 rows by 16 columns by two polarizations [230]. Left: single-panel version with two transceiver ports. Right: four-panel version with eight transceiver ports.

RF beam per polarization per panel. Therefore, the single-panel array renders two RF beams, i.e., two logical ports, while the four-panel array creates eight RF beams associated with eight logical ports.

For MU-MIMO operation, the single-panel array generates multiple RF beams per polarization per panel to serve multiple users simultaneously. Whereas in the four-panel array, one RF beam is created per polarization per panel to serve a maximum of four co-scheduled users with one user per panel. The simulation results in [230] indicate that single-panel arrays can provide much higher gains in performance compared to multi-panel arrays (130% versus 50%), primarily due to the narrower RF beams with higher gains formed by the single-panel array compared to the four-panel array, since the single-panel array has more antennas than each panel in the four-panel array [230]. Therefore, this technical report focuses on the single-panel array configuration due to its superior throughput performance in MU-MIMO.

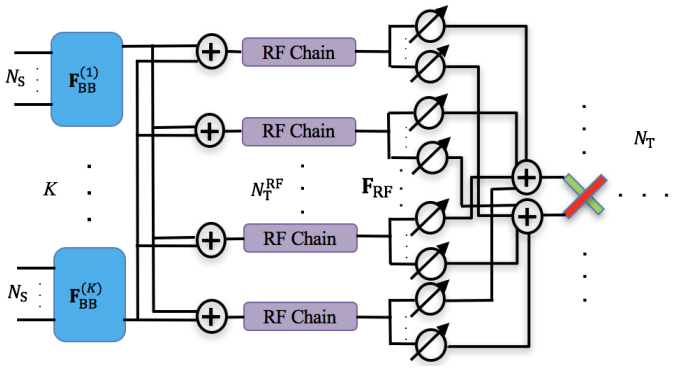

Figure 8.3: Multi-cell HBF architecture at the TP in each cell (there are three TPs in one BS, and one TP serves one cell). N_{S} denotes the number of data streams per user in each cell, K is the number of users in each cell, $N_{\mathrm{T}}^{\mathrm{RF}}$ represents the total number of RF chains at each TP, and N_{T} denotes the number of TP antenna elements in each cell, where $N_{\mathrm{S}} \leq N_{\mathrm{T}}^{\mathrm{RF}} < N_{\mathrm{T}}$. In this multi-cell single-stream work, $N_S = 1$, $K = 3$, $N_{\mathrm{T}}^{\mathrm{RF}} = 3$, and $N_{\mathrm{T}} = 256$.

8.2 Multi-Cell Multi-User Single-Stream Hybrid Beamforming

This section investigates HBF for a multi-cell MU-MIMO system where each TP communicates with each of its home-cell users via a single data stream. The HBF architecture at each TP is illustrated in Fig. 8.3, where there are K baseband digital precoding units with one for each user in the same cell, one data stream is transmitted for each home-cell user, and each baseband precoding unit is connected with $N_{\mathrm{T}}^{\mathrm{RF}}$ RF chains with $N_{\mathrm{T}}^{\mathrm{RF}} = K$. Each RF chain is connected to all of the N_{T} TP antennas through N_{T} phase shifters, thus the total number of phase shifters equals $N_{\mathrm{T}}^{\mathrm{RF}} N_{\mathrm{T}}$. Each user is assumed to be equipped with only one antenna, or an antenna array with analog beamforming only, for analytical simplicity.

As each TP communicates with each UE via a URA with N_{T} antennas, the dimension is $1 \times N_{\mathrm{T}}$ for the channel matrix $\mathbf{h}_{k,l,l}$, and $N_{\mathrm{T}} \times N_{\mathrm{T}}^{\mathrm{RF}}$ for $\mathbf{F}_{\mathrm{RF}_l}$. The

$1 \times N_{\mathrm{T}}^{\mathrm{RF}}$ effective channel $\check{\mathbf{H}}_{k,l,i}$ after RF precoding is:

$$\check{\mathbf{h}}_{k,l,i} = \mathbf{h}_{k,l,i}\mathbf{F}_{\mathrm{RF}_i} \tag{8.1}$$

where $\mathbf{F}_{\mathrm{RF}_i}$ is designed based on Algorithm 1 in [170]. The $K \times N_{\mathrm{T}}^{\mathrm{RF}}$ composite effective channel from TP i to all the K users in cell l is expressed as:

$$\check{\mathbf{H}}_{l,i} = [\check{\mathbf{h}}_{1,l,i}^{H}, \check{\mathbf{h}}_{2,l,i}^{H}, ..., \check{\mathbf{h}}_{K,l,i}^{H},]^{H} \tag{8.2}$$

where the superscript H denotes conjugate transpose. The received signal at user k in cell l can be formulated as:

$$y_{k,l} = \underbrace{\sqrt{\frac{P_{\mathrm{T}}}{\eta_l \mathrm{PL}_{k,l,l}}}\check{\mathbf{h}}_{k,l,l}\mathbf{f}_{\mathrm{BB}_{k,l}}s_{k,l}}_{\text{Desired Signal}} + \underbrace{\sum_{(m,i)\neq(k,l)}\sqrt{\frac{P_{\mathrm{T}}}{\eta_i \mathrm{PL}_{k,l,i}}}\check{\mathbf{h}}_{k,l,i}\mathbf{f}_{\mathrm{BB}_{m,i}}s_{m,i}}_{\text{Interference}} + \underbrace{n_{k,l}}_{\text{Noise}} \tag{8.3}$$

where P_{T} represents the total transmit power in Watts at each TP, $\mathrm{PL}_{k,l,i}$ denotes the large-scale distance-dependent path loss in Watts, including shadow fading, from TP i to user k in cell l. $\eta_l = ||\mathbf{F}_{\mathrm{RF}_l}\mathbf{F}_{\mathrm{BB}_l}||_F^2$ is a scaling factor to satisfy the total transmit power constraint $||\sqrt{P_{\mathrm{T}}}\mathbf{F}_{\mathrm{RF}_l}\mathbf{F}_{\mathrm{BB}_l}/\sqrt{\eta_l}||_F^2 = P_{\mathrm{T}}$, where F denotes the Frobenius norm, and $\mathbf{F}_{\mathrm{BB}_l} = [\mathbf{f}_{\mathrm{BB}_{1,l}}, ..., \mathbf{f}_{\mathrm{BB}_{K,l}}]$. $s_{k,l}$ represents the desired transmitted signal for user k in cell l with $\mathbb{E}[|s_{k,l}|^2] = 1$, and $n_{k,l} \sim \mathcal{CN}(0, N_0)$ is complex Gaussian noise with variance N_0. The SINR of user k in cell l is therefore given by:

$$\mathrm{SINR}_{k,l} = \frac{\frac{P_{\mathrm{T}}}{\eta_l \mathrm{PL}_{k,l,l}}|\check{\mathbf{h}}_{k,l,l}\mathbf{f}_{\mathrm{BB}_{k,l}}|^2}{\sum\limits_{(m,i)\neq(k,l)}\frac{P_{\mathrm{T}}}{\eta_i \mathrm{PL}_{k,l,i}}|\check{\mathbf{h}}_{k,l,i}\mathbf{f}_{\mathrm{BB}_{m,i}}|^2 + N_0} \tag{8.4}$$

The expected per-user SINR can be obtained by calculating $\mathbb{E}[\mathrm{SINR}_{k,l}]$. The exact evaluation of $\mathbb{E}[\mathrm{SINR}_{k,l}]$, however, is extremely unwieldy or even intractable. Therefore, the first-order delta method expansion can be adopted, hence the expected per-user SINR is approximated by [234]:

$$\mathbb{E}[\mathrm{SINR}_{k,l}] \approx \frac{\frac{P_{\mathrm{T}}}{\tilde{\eta}_l \mathrm{PL}_{k,l,l}} \mathbb{E}[|\check{\mathbf{h}}_{k,l,l} \mathbf{f}_{\mathrm{BB}_{k,l}}|^2]}{\sum\limits_{(m,i)\neq(k,l)} \frac{P_{\mathrm{T}}}{\tilde{\eta}_i \mathrm{PL}_{k,l,i}} \mathbb{E}[|\check{\mathbf{h}}_{k,l,i} \mathbf{f}_{\mathrm{BB}_{m,i}}|^2] + N_0} \tag{8.5}$$

where $\tilde{\eta}_l = \mathbb{E}[\eta_l]$ and $\tilde{\eta}_i = \mathbb{E}[\eta_i]$. In what follows, the expected values in the numerator and denominator of (8.5) are derived separately using approximated densities for an arbitrary eigenvalue and a joint pair of arbitrary eigenvalues of both signal and interference channels for the 3GPP and NYUSIM channel models. The approximated density for an arbitrary eigenvalue is obtained via simulations, followed by the derivation of the approximated density for a joint pair of arbitrary eigenvalues, as detailed below.

8.2.1 Channel Eigenvalue Distribution

The eigenvalue distribution for uncorrelated and correlated Wishart matrices are well known, as presented in [235, 236, 237, 238, 239]. *Eigenvalue distributions for channels after RF precoding in HBF, however, have not been investigated in the prior literature.* This is because joint processing of $\mathbf{F}_{\mathrm{RF}}$ and $\mathbf{F}_{\mathrm{BB}}$ twice alters both the magnitude and phase of the preferential channel directions, and therefore the complexity of exact expressions is very high. While the computation of exact eigenvalue densities with such complex channel models remains an open problem in multivariate statistics, accurate approximations is employed in order to facilitate the subsequent analysis. In this subsection, eigenvalue distributions of $\check{\mathbf{H}}\check{\mathbf{H}}^H$ for

the 3GPP channel model and the NYUSIM channel model are studied, where $\check{\mathbf{H}}$ denotes the effective channel matrix after TP RF precoding, i.e., $\check{\mathbf{H}} = \mathbf{H}\mathbf{F}_{\mathrm{RF}}$. Below are existing works on eigenvalue distributions and the rationale for deriving the approximated eigenvalue distributions in this technical report.

- In the simplest case of uncorrelated scattering, the entries of $\mathbf{H}$ are i.i.d. complex Gaussian random variables, widely known as Rayleigh fading, $\mathbf{H}\mathbf{H}^H$ is an uncorrelated central complex Wishart matrix, and the corresponding PDF of an arbitrary eigenvalue of $\mathbf{H}\mathbf{H}^H$ is derived in [235] via the orthogonal basis expansion of $\mathbf{H}\mathbf{H}^H$ as it is non-trivial to compute the density of each eigenvalue, even for the simplest case of Rayleigh fading.

- For the case of semi-correlated Rayleigh fading with spatial correlation at either transmit or receive end of the link, $\mathbf{H}\mathbf{H}^H$ takes the form of a correlated central complex Wishart distribution. The corresponding arbitrary eigenvalue densities are derived in [153, 236, 238, 239, 240] for various types of spatial correlation models.

- For an uncorrelated LOS channel, or an uncorrelated Ricean channel, which corresponds to the case with the Ricean factor larger than 0 and the presence of only one dominant multipath component in the two-wave with diffuse power (TWDP) distribution [241] describing small-scale, local area fading experienced by narrowband wireless receivers, $\mathbf{H}\mathbf{H}^H$ follows an uncorrelated non-central complex Wishart structure, whose eigenvalue densities were derived in [237].

- As shown in [242], LOS components pointing in certain directions can be regarded as inducing additional spatial correlation. The resultant $\mathbf{H}\mathbf{H}^H$ is a

correlated non-central complex Wishart matrix, and the arbitrary eigenvalue densities for such channels were derived in [238, 239] and extended in [242] by exploiting the above fact.

- For a NLOS channel matrix combined with RF precoding and RF combining, it is conjectured that this is akin to inducing spatial correlation at both ends of the link in the direction of the boresight of the antenna (array). The antenna elements of the array are closely located (e.g., half wavelength) hence inducing spatial correlation as well. Furthermore, with a fixed number of scattering clusters and subpaths within each cluster, the channel models can be statistically treated as an arbitrary link gain pre-multiplied by a correlated random variable dependent on the antenna array configuration and the direction-of-departure/arrival distribution. Thus, the resultant arbitrary eigenvalue density will be similar to the second point mentioned above.

Note that for the first four types of channels above, the underlying mathematical form of the arbitrary eigenvalue density is a product of exponential functions with a finite power of the arbitrary eigenvalue upper bounded by the minimum of the transmit and receive antenna dimension. *This is equivalent to the mathematical form of the density of a gamma-distributed random variable [243]. Moreover, while the exponential and chi-square distributions also exhibit the above mathematical form, they are special cases of the gamma distribution with specific shape and scale parameters. Furthermore, the gamma distribution results in the best Kolmogorov-Smirnov (KS) test statistic among all other contending distributions*[1]. Therefore, it is reasonable to use the gamma distribution to approximate the eigenvalue density

[1]The KS test is a widely used measure in communications theory to determine the accuracy of an approximate statistical distribution relative to a specific system related metric [244].

distribution. In what follows, to obtain approximated eigenvalue distributions, the PDFs of ordered eigenvalues are first plotted via simulations, and then the PDF curves are fitted with the gamma distribution by optimizing its shape and rate parameters.

It is worth mentioning that only *NLOS* mmWave channels are considered herein because it can be regarded as a starting point, since *LOS* channels will have more complicated eigenvalue distributions due to the extra channel correlation induced by LOS paths as explained above. Furthermore, NLOS mmWave channels are of greater research interest than LOS channels, as LOS propagation is always feasible and predictable, while the feasibility and performance of NLOS propagation need examination. Therefore, this work focuses on the eigenvalue densities of NLOS channels only, and the eigenvalue densities for LOS channels and LOS-NLOS mixed channels are worth future investigation.

For both the 3GPP and NYUSIM channel models, the approximated PDF of the n-th largest eigenvalue, λ_n, of $\check{\mathbf{H}}_{l,l}\check{\mathbf{H}}_{l,l}^H$ in NLOS environments is found to be:

$$f_{\lambda_n}(\lambda_n) \approx \frac{b_n^{a_n}\lambda_n^{a_n-1}e^{-b_n\lambda_n}}{\Gamma(a_n)},\ n=1,...,N \tag{8.6}$$

where a_n and b_n are the shape and rate parameters to be determined via simulations. When $K=3$, for instance, $a_n = 1+\frac{20}{30^n}$ and $b_n = \frac{3}{20}\prod_{s=1}^{n} s!$ for the 3GPP channel model, while $a_n = 1+\frac{1}{3^n}$ and $b_n = \frac{3\times 5^n}{5000}$ for NYUSIM. $\Gamma(\cdot)$ denotes the complete gamma function, and N is the smaller dimension of $\check{\mathbf{H}}_{l,l}$, which equals K for the single-stream-per-user case considered in (8.3). Based on the PDFs $f_{\lambda_n}(\lambda_n)$ of the ordered eigenvalues, the approximated PDF of an arbitrary eigenvalue of $\check{\mathbf{H}}_{l,l}\check{\mathbf{H}}_{l,l}^H$ is

derived and expressed as [236]:

$$f_{\lambda_{\text{arb}}}(\lambda_{\text{arb}}) \approx \frac{1}{K}\sum_{n=1}^{K} \frac{b_n^{a_n}\lambda_{\text{arb}}^{a_n-1}e^{-b_n\lambda_{\text{arb}}}}{\Gamma(a_n)},\ n=1,...,K \tag{8.7}$$

The approximated joint density of the ordered eigenvalues $\lambda_1 \geq ... \geq \lambda_K$ of $\check{\mathbf{H}}_{l,l}\check{\mathbf{H}}_{l,l}^H$ using the 3GPP channel model is given by [235]:

$$f_{\boldsymbol{\lambda},ordered}(\lambda_1,...,\lambda_K) = A^{-1}\prod_{n=1}^{K} f(\lambda_n)\prod_{n<j}^{K}(\lambda_n-\lambda_j)^2,\ \lambda_1 \geq ... \geq \lambda_K \geq 0 \tag{8.8}$$

where A is a normalizing factor. The unordered eigenvalues then have the density [235]:

$$f_{\boldsymbol{\lambda}}(\lambda_1,...,\lambda_K) = (K!A)^{-1}\prod_{n=1}^{K} f(\lambda_n)\prod_{n<j}^{K}(\lambda_n-\lambda_j)^2 \tag{8.9}$$

Note that $\prod_{n<j}^{K}(\lambda_n-\lambda_j)$ is the determinant of a Vandermonde matrix [235]. By applying the Gram Schmidt orthogonalization procedure to the sequence $1, \lambda, ..., \lambda^{K-1}$ in the space of real-valued functions with the orthogonality relationship:

$$\int_0^{\infty} \phi_n(\lambda)\phi_j(\lambda)\lambda^{-1}d\lambda = \delta_{nj} \tag{8.10}$$

Thus (8.9) can be transformed to:

$$f_{\lambda}(\lambda_1,...,\lambda_K) = C\sum_{\alpha,\beta}(-1)^{\text{per}(\alpha)+\text{per}(\beta)}\prod_{n}\phi_{\alpha_n}(\lambda_n)\phi_{\beta_n}(\lambda_n)\lambda_n^{-1} \tag{8.11}$$

where the sum is over all possible permutations α, β of $\{1,...,K\}$, and per$(\cdot)$ denotes

the sign of the permutation. Integrating the right hand side of (8.11) over $\lambda_2, ..., \lambda_K$ results in:

$$\begin{aligned} f(\lambda_1) =& C \sum_{\alpha,\beta} (-1)^{\text{per}(\alpha)+\text{per}(\beta)} \phi_{\alpha_1}(\lambda_1)\phi_{\beta_1}(\lambda_1)\lambda_1^{-1} \prod_{n\geq 2} \delta_{\alpha_n\beta_n} \\ =& C(K-1)! \sum_{n=1}^{K} \big(\phi_n(\lambda_1)\big)^2 \lambda_1^{-1} = \frac{(K-1)!}{K!} \sum_{n=1}^{K} \big(\phi_n(\lambda_1)\big)^2 \lambda_1^{-1} \\ =& \frac{1}{K} \sum_{n=1}^{K} \big(\phi_n(\lambda_1)\big)^2 \lambda_1^{-1} \end{aligned} \tag{8.12}$$

where the third equality follows from the fact that $\big(\phi_n(\lambda_1)\big)^2\lambda_1^{-1}$ integrates to unity and hence C must equal $1/K!$. Comparing (8.12) with (8.7), it is observed that

$$\phi_n(\lambda) = \sqrt{\frac{b_n^{a_n}\lambda^{a_n}e^{-b_n\lambda}}{\Gamma(a_n)}} \tag{8.13}$$

Integrating the right hand side of (8.11) over $\lambda_3, ..., \lambda_K$ gives rise to the joint density in (8.15):

$$\begin{aligned} f(\lambda_1,\lambda_2) =& C \sum_{\alpha,\beta} (-1)^{\text{per}(\alpha)+\text{per}(\beta)} \phi_{\alpha_1}(\lambda_1)\phi_{\beta_1}(\lambda_1)\lambda_1^{-1}\phi_{\alpha_2}(\lambda_2)\phi_{\beta_2}(\lambda_2)\lambda_2^{-1} \prod_{n\geq 3} \delta_{\alpha_n\beta_n} \\ =& \frac{(K-2)!}{K!} \sum_{n=1}^{K} \sum_{\substack{q=1 \\ q\neq n}}^{K} (\lambda_1\lambda_2)^{-1} \Big[\big(\phi_n(\lambda_1)\big)^2 \big(\phi_q(\lambda_2)\big)^2 - \phi_n(\lambda_1)\phi_q(\lambda_1)\phi_q(\lambda_2)\phi_n(\lambda_2) \Big] \\ =& \frac{1}{K(K-1)} \sum_{n=1}^{K} \sum_{\substack{q=1 \\ q\neq n}}^{K} (\lambda_1\lambda_2)^{-1} \Big[\big(\phi_n(\lambda_1)\big)^2 \big(\phi_q(\lambda_2)\big)^2 - \phi_n(\lambda_1)\phi_q(\lambda_1)\phi_n(\lambda_2)\phi_q(\lambda_2) \Big] \end{aligned} \tag{8.14}$$

where $\phi_n(\lambda)$ is given by (8.13). The approximated joint density of two arbitrary

unordered eigenvalues of $\check{\mathbf{H}}_{l,l}\check{\mathbf{H}}_{l,l}^H$ is given by:

$$f_{\lambda,\text{unord}}(\lambda_1,\lambda_2) \approx \frac{1}{K(K-1)} \sum_{n=1}^{K} \sum_{\substack{q=1 \\ q\neq n}}^{K} (\lambda_1\lambda_2)^{-1} \Big[\big(\phi_n(\lambda_1)\big)^2 \big(\phi_q(\lambda_2)\big)^2 - \phi_n(\lambda_1)\phi_q(\lambda_1)\phi_n(\lambda_2)\phi_q(\lambda_2) \Big] \tag{8.15}$$

where $\phi_n(\lambda)$ is given by (8.13). The approximated PDF for the n-th largest eigenvalue of $\check{\mathbf{H}}_{l,i}^H\check{\mathbf{H}}_{l,i}$ (or equivalently $\check{\mathbf{H}}_{l,i}\check{\mathbf{H}}_{l,i}^H$) ($i \neq l$), where $\check{\mathbf{H}}_{l,i}$ represents the effective other-cell interference (OCI) channel, is found to be:

$$f_{\sigma_n}(\sigma_n) \approx \frac{d_n^{c_n}\sigma_n^{c_n-1}e^{-d_n\sigma_n}}{\Gamma(c_n)}, \ n = 1, ..., K \tag{8.16}$$

where $c_n = 1 + \frac{20}{100^n}$ and $d_n = \frac{10^{n-1}}{4}$ for the 3GPP model, and $c_n = 1 + \frac{1}{30^n}$ and $d_n = 6^{n-3}$ for NYUSIM, when $K = 3$. Note that there is variation with the coefficients in (8.6) and (8.16) for the 3GPP and NYUSIM models. One reason for this variation is the way the underlying channel impulse responses are generated from the 3GPP and NYUSIM models that results in very different eigenvalues, which will be shown later in Figs. 8.4, 8.5, and 6.4. The approximated PDF for an arbitrary eigenvalue of $\check{\mathbf{H}}_{l,i}^H\check{\mathbf{H}}_{l,i}$ is given by [236]:

$$f_{\sigma_{\text{arb}}}(\sigma_{\text{arb}}) \approx \frac{1}{K} \sum_{n=1}^{K} \frac{d_n^{c_n}\sigma_{\text{arb}}^{c_n-1}e^{-d_n\sigma_{\text{arb}}}}{\Gamma(c_n)}, \ n = 1, ..., K \tag{8.17}$$

Figs. 8.4 and 8.5 illustrate the PDFs of an arbitrary (unordered) eigenvalue of $\check{\mathbf{H}}\check{\mathbf{H}}^H$ for both desired signal and interference channels generated by the 3GPP and NYUSIM channel models, which show that the analytical expressions given by (8.7) and (8.17) match the simulated PDFs very well.

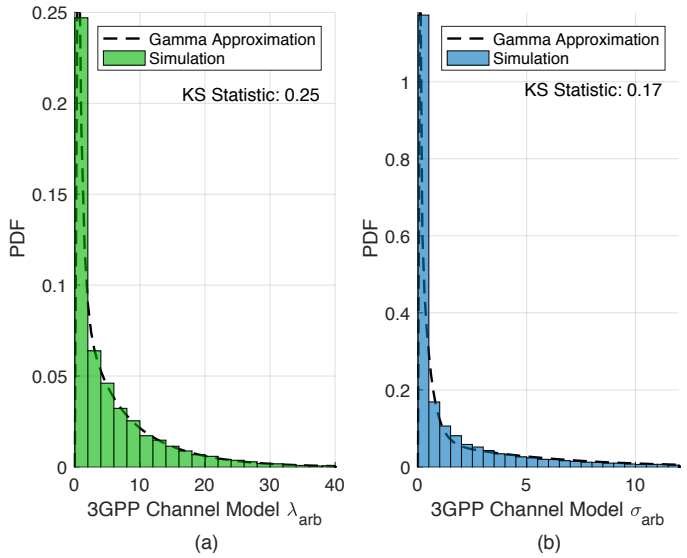

Figure 8.4: Probability density distribution of an arbitrary eigenvalue of $\check{\mathbf{H}}\check{\mathbf{H}}^H$ for the 3GPP channel model for three users per cell, where $\check{\mathbf{H}}$ denotes the effective channel matrix after transmit RF precoding, i.e., $\check{\mathbf{H}} = \mathbf{H}\mathbf{F}_{\mathrm{RF}}$. (a) is for desired signal channels, while (b) is for interference channels.

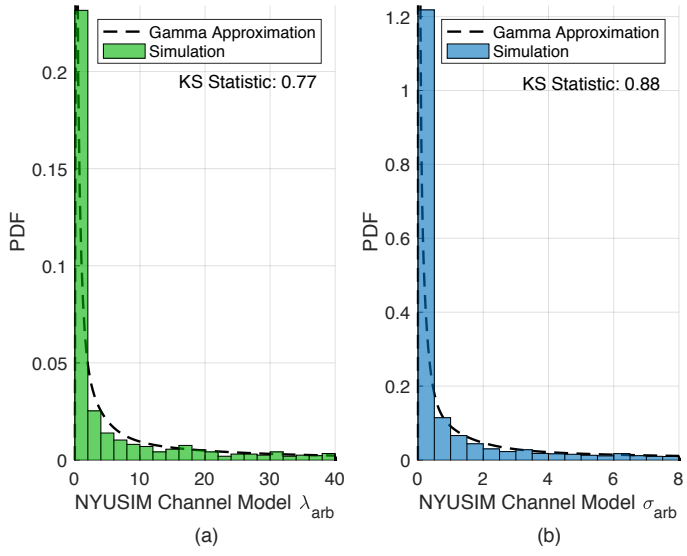

Figure 8.5: Probability density distribution of an arbitrary eigenvalue of $\check{\mathbf{H}}\check{\mathbf{H}}^H$ for the NYUSIM channel model for three users per cell, where $\check{\mathbf{H}}$ denotes the effective channel matrix after transmit RF precoding, i.e., $\check{\mathbf{H}} = \mathbf{H}\mathbf{F}_{\mathrm{RF}}$. (a) is for desired signal channels, while (b) is for interference channels.

8.2.2 Integrals and Special Functions

In this chapter, the following integrals and special functions are often used when computing expected signal power and expected interference power in the subsequent analysis. Let

$$J_{m,n}(\xi) = \int_0^\infty \frac{\lambda^{m+a-1} e^{-b\lambda}}{(\lambda+\xi)^n} d\lambda, \text{ where } m, n \in \mathbb{N}, \ a, b > 0 \tag{8.18}$$

which can be solved by a change of variable $\lambda = x - \xi$ to obtain

$$J_{m,n}(\xi) = \int_\xi^\infty \frac{(x-\xi)^{m+a-1} e^{-b(x-\xi)}}{x^n} dx = \int_\xi^\infty (x-\xi)^{m+a-1} \frac{e^{-bx}}{x^n} e^{b\xi} dx \tag{8.19}$$

Applying the Taylor series expansion to $(x-\xi)^{m+a-1}$ at 0 yields

$$(x-\xi)^{m+a-1} \approx \sum_{s=0}^{\lfloor m+a-1 \rfloor} \frac{\Gamma(m+a)}{s!\Gamma(m+a-s)} (-\xi)^{m+a-s} x^s \tag{8.20}$$

Therefore, (8.19) can be recast as

$$\begin{aligned} J_{m,n}(\xi) &\approx \int_\xi^\infty \underbrace{\sum_{s=0}^{\lfloor m+a-1 \rfloor} \frac{\Gamma(m+a)}{s!\Gamma(m+a-s)} (-\xi)^{m+a-s} x^s}_{(x-\xi)^{m+a-1}} \frac{e^{-bx}}{x^n} e^{b\xi} dx \\ &= \sum_{s=0}^{\lfloor m+a-1 \rfloor} \frac{\Gamma(m+a)}{s!\Gamma(m+a-s)} (-\xi)^{m+a-s} e^{b\xi} \underbrace{\int_\xi^\infty x^{s-n} e^{-bx} dx}_{h(n,\xi)} \end{aligned} \tag{8.21}$$

For the purpose of this chapter, two special cases of $h(n,\xi)$ are of interest, $n = 1$ and $n = 2$, which will be frequently encountered in the following analysis. These are given by (8.22), where $E_1(\cdot)$ denotes the exponential integral and $\tilde{\Gamma}(\cdot,\cdot)$ is the

$$h(1,\xi)=\int_{\xi}^{\infty}x^{s-1}e^{-bx}dx\overset{\text{let }\omega=bx}{=\!=\!=}\frac{1}{b^{s}}\int_{b\xi}^{\infty}\omega^{s-1}e^{-\omega}d\omega=\begin{cases}E_1(b\xi) & \text{if} \quad s=0\\ \frac{1}{b^{s}}\tilde{\Gamma}(s,b\xi) & \text{if} \quad s\geq 1\end{cases}$$

and

$$h(2,\xi)=\int_{\xi}^{\infty}x^{s-2}e^{-bx}dx\overset{\text{let }\omega=bx}{=\!=\!=}\frac{1}{b^{s-1}}\int_{b\xi}^{\infty}\omega^{s-2}e^{-\omega}d\omega=\begin{cases}-bE_1(b\xi)+\frac{e^{-b\xi}}{\xi} & \text{if} \quad s=0\\ E_1(b\xi) & \text{if} \quad s=1\\ \frac{1}{b^{s-1}}\tilde{\Gamma}(s-1,b\xi) & \text{if} \quad s\geq 2\end{cases} \tag{8.22}$$

---

upper incomplete gamma function.

8.2.3 Expected Per-User Signal Power

Throughout this chapter, 28 GHz carrier frequency with 100 MHz RF bandwidth and narrowband OFDM sub-carriers are assumed; no power control or water filling is assumed. The expected per-user signal power in (8.5) is:

$$\delta_{k,l}=\frac{P_{\mathrm{T}}}{\tilde{\eta}_l \mathrm{PL}_{k,l,l}}\mathbb{E}[|\check{\mathbf{h}}_{k,l,l}\mathbf{f}_{\mathrm{BB}_{k,l}}|^2] \tag{8.23}$$

When RZF precoding is employed at baseband, the un-normalized RZF precoding vector for user k in cell l, $\mathbf{f}_{\mathrm{BB}_{k,l}}$, is the k-th column of the $N_{\mathrm{T}}^{\mathrm{RF}}\times K$ matrix $\mathbf{F}_{\mathrm{BB}_l}$, such that

$$\mathbf{F}_{\mathrm{BB}_l}=\check{\mathbf{H}}_{l,l}^{H}(\check{\mathbf{H}}_{l,l}\check{\mathbf{H}}_{l,l}^{H}+\xi_l\mathbf{I}_K)^{-1} \tag{8.24}$$

The constant $\xi_l>0$ represents the regularization parameter specific to TP l. In

this work, ξ_l is set to the following value based on [156, 170]:

$$\xi_l = \frac{KN_0}{P_{\mathrm{T}}} \tag{8.25}$$

An eigenvalue decomposition leads to $\check{\mathbf{H}}_{l,l}\check{\mathbf{H}}_{l,l}^H = \mathbf{U}\mathbf{\Lambda}\mathbf{U}^H$[2]. The entries in $\mathbf{U}$ have an isotropic distribution for NLOS conditions. For LOS conditions where there is a dominant specular component, $\mathbf{U}$ is not isotropic, but the averaging over the random AoDs/AoAs in the array steering vectors makes $\mathbf{U}$ retain its isotropicity. Therefore, the expected value in (8.23) over the isotropicity of $\mathbf{U}$ can be expressed as [153, 156, 242]:

$$\varrho_{k,l} = \mathbb{E}[|\check{\mathbf{h}}_{k,l,l}\mathbf{f}_{\mathrm{BB}_{k,l}}|^2] = \mathbb{E}\left[\left(\sum_{a=1}^{K}\frac{\lambda_a}{\lambda_a+\xi_l}|u_{l,a}|^2\right)^2\right] \tag{8.26}$$

The expression in (8.26) can be further averaged over the entries of $\mathbf{U}$ and can be reformulated as [153, 156]:

$$\varrho_{k,l} = \frac{1}{K(K+1)}\left\{\mathbb{E}_\lambda\left[\left(\sum_{a=1}^{K}\frac{\lambda_a}{\lambda_a+\xi_l}\right)^2\right] + \mathbb{E}_\lambda\left[\sum_{a=1}^{K}\left(\frac{\lambda_a}{\lambda_a+\xi_l}\right)^2\right]\right\} \tag{8.27}$$

where $\mathbb{E}_\lambda[\cdot]$ represents the expectation over the eigenvalues of $\check{\mathbf{H}}_{l,l}\check{\mathbf{H}}_{l,l}^H$. Now the expected values in (8.27) for 3GPP and NYUSIM channel models will be calculated using the approximated PDFs of eigenvalues derived above. For the first expectation

[2]To facilitate the analytical study later on, an SVD or an economy-size SVD is first performed such that $\check{\mathbf{H}}_{l,l} = \mathbf{U}\mathbf{\Lambda}^{1/2}\mathbf{V}^H$, which leads to $\check{\mathbf{H}}_{l,l}\check{\mathbf{H}}_{l,l}^H = \mathbf{U}\mathbf{\Lambda}^{1/2}\mathbf{V}^H\mathbf{V}\mathbf{\Lambda}^{1/2}\mathbf{U}^H = \mathbf{U}\mathbf{\Lambda}\mathbf{U}^H$.

term in (8.27), it can be recognized that

$$\mathbb{E}_\lambda\left[\left(\sum_{k=1}^{K}\frac{\lambda_k}{\lambda_k+\xi_l}\right)^2\right]=\mathbb{E}_\lambda\left[\sum_{k=1}^{K}\left(\frac{\lambda_k}{\lambda_k+\xi_l}\right)^2\right]+\mathbb{E}_\lambda\left[\sum_{a=1}^{K}\sum_{\substack{b=1\\b\neq a}}^{K}\left(\frac{\lambda_a}{\lambda_a+\xi_l}\right)\left(\frac{\lambda_b}{\lambda_b+\xi_l}\right)\right] \tag{8.28}$$

We begin by evaluating the first term on the right-hand side of (8.28), yielding

$$s_l=\mathbb{E}_\lambda\left[\sum_{k=1}^{K}\left(\frac{\lambda_k}{\lambda_k+\xi_l}\right)^2\right]=K\left[\int_0^\infty\frac{\lambda^2}{(\lambda+\xi_l)^2}f_{\lambda_{\text{arb}}}(\lambda)d\lambda\right]=\sum_{n=1}^{K}\int_0^\infty\frac{\lambda^2}{(\lambda+\xi_l)^2}f_{\lambda_n}(\lambda)d\lambda \tag{8.29}$$

where $f_{\lambda_n}(\cdot)$ denotes the approximated PDF for the n-th largest eigenvalue as expressed in (8.6). s_l in (8.29) can be solved using the special functions in (8.21) and (8.22) with $m=n=2$. By utilizing the joint density of two arbitrary eigenvalues in (8.15), the second term on the right-hand side of (8.28) can be

written as:

$$\begin{aligned}
\epsilon_l =& \mathbb{E}_\lambda \left[\sum_{a=1}^{K} \sum_{\substack{b=1 \\ b\neq a}}^{K} \left(\frac{\lambda_a}{\lambda_a + \xi_l} \right) \left(\frac{\lambda_b}{\lambda_b + \xi_l} \right) \right] \\
=& K(K-1) \int_0^\infty \int_0^\infty \left(\frac{\lambda_a}{\lambda_a + \xi_l} \right) \left(\frac{\lambda_b}{\lambda_b + \xi_l} \right) f_{\lambda,\text{unord}}(\lambda_a, \lambda_b) d\lambda_b d\lambda_a \\
=& \sum_{n=1}^{K} \sum_{\substack{q=1 \\ q\neq n}}^{K} \int_0^\infty \int_0^\infty \left(\frac{\lambda_a}{\lambda_a + \xi_l} \right) \left(\frac{\lambda_b}{\lambda_b + \xi_l} \right) (\lambda_a \lambda_b)^{-1} \Big[\big(\phi_n(\lambda_a)\big)^2 \big(\phi_q(\lambda_b)\big)^2 \\
& - \phi_n(\lambda_a)\phi_q(\lambda_a)\phi_n(\lambda_b)\phi_q(\lambda_b) \Big] d\lambda_b d\lambda_a \\
=& \sum_{n=1}^{K} \sum_{\substack{q=1 \\ q\neq n}}^{K} \left\{ \left[\int_0^\infty \left(\frac{\lambda_a}{\lambda_a + \xi_l} \right) \big(\phi_n(\lambda_a)\big)^2 \lambda_a^{-1} d\lambda_a \right]^2 - \left[\int_0^\infty \left(\frac{\lambda_a}{\lambda_a + \xi_l} \right) \phi_n(\lambda_a)\phi_q(\lambda_a)\lambda_a^{-1} d\lambda_a \right]^2 \right\} \\
=& \sum_{n=1}^{K} \sum_{\substack{q=1 \\ q\neq n}}^{K} \left\{ \left[\int_0^\infty \left(\frac{\lambda_a}{\lambda_a + \xi_l} \right) f_{\lambda_n}(\lambda_a) d\lambda_a \right]^2 - \left[\int_0^\infty \left(\frac{\lambda_a}{\lambda_a + \xi_l} \right) \phi_n(\lambda_a)\phi_q(\lambda_a)\lambda_a^{-1} d\lambda_a \right]^2 \right\}
\end{aligned} \tag{8.30}$$

which can be solved using the special functions in (8.21) and (8.22) with $m = n = 1$. The second expectation in (8.27) equals:

$$p_l = \mathbb{E}_\lambda \left[\sum_{k=1}^{K} \left(\frac{\lambda_k}{\lambda_k + \xi_l} \right)^2 \right] = s_l \tag{8.31}$$

Therefore, combining (8.29), (8.30) and (8.31), the expected signal power in (8.23) is given by:

$$\delta_{k,l} = \left(\frac{P_\text{T}}{\tilde{\eta}_l \text{PL}_{k,l,l}} \right) \left[\frac{2s_l + \epsilon_l}{K(K+1)} \right] \tag{8.32}$$

in which [170]

$$\tilde{\eta}_l = \mathbb{E}[||\mathbf{F}_{\mathrm{RF}_l}\mathbf{F}_{\mathrm{BB}_l}||_F^2] \approx \mathbb{E}_\lambda\left[\sum_{k=1}^{K}\frac{\lambda_k}{(\lambda_k+\xi_l)^2}\right] = K\int_0^\infty \frac{\lambda}{(\lambda+\xi_l)^2} f_{\lambda_{\mathrm{arb}}}(\lambda)d\lambda \quad (8.33)$$

where the approximation stems from the fact that the array response vectors of $\mathbf{F}_{\mathrm{RF}_l}$ become orthogonal to each other as $N_{\mathrm{T}} \to \infty$, such that $\mathbf{F}_{\mathrm{RF}_l}^H\mathbf{F}_{\mathrm{RF}_l} = \mathbf{I}_{N_{\mathrm{T}}^{\mathrm{RF}}}$ (see (21) in [170]). $\tilde{\eta}_l$ in (8.33) can be solved using the special functions in (8.21) and (8.22) with $m = 1$ and $n = 2$, yet an alternative approach can also be used to compute $\tilde{\eta}_l$ as explained below. Numerous numerical results reveal that the eigenvalues of $\check{\mathbf{H}}_{l,l}\check{\mathbf{H}}_{l,l}^H$ are at least three orders of magnitude larger than ξ_l, thus $\frac{\lambda}{(\lambda+\xi_l)^2} \approx \frac{\lambda}{\lambda^2} = \frac{1}{\lambda}$. Consequently, (8.33) can be approximated as:

$$\begin{aligned}
\tilde{\eta}_l &= K\int_0^\infty \frac{\lambda}{(\lambda+\xi_l)^2} f_{\lambda_{\mathrm{arb}}}(\lambda)d\lambda \\
&\approx K\int_{\lambda_{\min}}^\infty \frac{1}{\lambda} f_{\lambda_{\mathrm{arb}}}(\lambda)d\lambda = \sum_{n=1}^{K}\int_{\lambda_{\min}}^\infty \frac{b_n^{a_n}\lambda^{a_n-2}e^{-b_n\lambda}}{\Gamma(a_n)}d\lambda \\
&= \sum_{n=1}^{K}\left(\frac{b_n}{\Gamma(a_n)}\Upsilon\Big(a_n-1, b_n\lambda_{\min}\Big)\right)
\end{aligned} \quad (8.34)$$

where $\lambda_{\min} = \min(\lambda_{\mathrm{arb}})$, and $\Upsilon\Big(a_n-1, b_n\lambda_{\min}\Big)$ is defined in (8.35). Plugging (8.34) back into (8.32), the expected per-user signal power $\delta_{k,l}$ is solved and will be used in (8.50) to calculate the expected per-user SINR.

$$\Upsilon\Big(a_n-1,b_n\lambda_{\min}\Big)=\begin{cases}\tilde{\Gamma}\big(a_n-1,b_n\lambda_{\min}\big) & \text{if} \quad a_n>1\\ E_1(b_n\lambda_{\min}) & \text{if} \quad a_n=1\\ -\frac{(b_n\lambda_{\min})^{a_n-1}e^{-b_n\lambda_{\min}}}{a_n-1}+\frac{1}{a_n-1}\tilde{\Gamma}\Big(a_n,b_n\lambda_{\min}\Big) & \text{if} \quad 0<a_n<1\end{cases} \tag{8.35}$$

8.2.4 Expected Per-User Interference Power

The expected interference power at the kth user in cell l in (8.5) is given by:

$$\begin{aligned}\varsigma_{k,l}&=\sum_{(m,i)\neq(k,l)}\frac{P_{\mathrm{T}}}{\tilde{\eta}_i\mathrm{PL}_{k,l,i}}\mathbb{E}[|\check{\mathbf{h}}_{k,l,i}\mathbf{f}_{\mathrm{BB}_{m,i}}|^2]\\&=\underbrace{\frac{P_{\mathrm{T}}}{\tilde{\eta}_l\mathrm{PL}_{k,l,l}}\sum_{\substack{m=1\\m\neq k}}^{K}\mathbb{E}[|\check{\mathbf{h}}_{k,l,l}\mathbf{f}_{\mathrm{BB}_{m,l}}|^2]}_{\text{Intra-Cell Interference}}+\underbrace{\sum_{\substack{i=1\\i\neq l}}^{L}\frac{P_{\mathrm{T}}}{\tilde{\eta}_i\mathrm{PL}_{k,l,i}}\sum_{m=1}^{K}\mathbb{E}[|\check{\mathbf{h}}_{k,l,i}\mathbf{f}_{\mathrm{BB}_{m,i}}|^2]}_{\text{Inter-Cell Interference}}\end{aligned} \tag{8.36}$$

The first term on the right-hand side of (8.36) denotes the inter-user interference (IUI) within the same cell, and can be evaluated as the difference between the total (signal plus intra-cell interference) power from TP l and the desired signal power at user k in cell l [234]. The expected total power from TP l to user k in cell l is given by:

$$\gamma_{k,l}=\mathbb{E}[||\check{\mathbf{h}}_{k,l,l}\mathbf{F}_{\mathrm{BB}_l}||^2]=\mathbb{E}\bigg[\sum_{a=1}^{K}\frac{|u_{k,a}|^2\lambda_a^2}{(\lambda_a+\xi_l)^2}\bigg]=\frac{1}{K}\mathbb{E}_{\lambda}\bigg[\sum_{a=1}^{K}\frac{\lambda_a^2}{(\lambda_a+\xi_l)^2}\bigg]=\frac{s_l}{K} \tag{8.37}$$

where s_l is given by (8.29). Consequently, the intra-cell interference in (8.36) can

be expressed as:

$$\begin{aligned}\varsigma_{k,l_{\mathrm{IUI}}} =&\frac{P_{\mathrm{T}}}{\tilde{\eta}_l \mathrm{PL}_{k,l,l}} \sum_{\substack{m=1 \\ m\neq k}}^{K} \mathbb{E}[|\check{\mathbf{h}}_{k,l,l}\mathbf{f}_{\mathrm{BB}_{m,l}}|^2] \\ =&\frac{P_{\mathrm{T}}}{\tilde{\eta}_l \mathrm{PL}_{k,l,l}}\gamma_{k,l} - \delta_{k,l} = \frac{P_{\mathrm{T}}}{\tilde{\eta}_l \mathrm{PL}_{k,l,l}}\left[\frac{s_l}{K} - \frac{2s_l+\epsilon_l}{K(K+1)}\right] = \frac{P_{\mathrm{T}}}{\tilde{\eta}_l \mathrm{PL}_{k,l,l}}\left[\frac{(K-1)s_l-\epsilon_l}{K(K+1)}\right]\end{aligned} \tag{8.38}$$

where (8.32) is utilized to obtain the third equality. The second term in (8.36) denotes the inter-cell interference, or OCI, and can be formulated as:

$$\begin{aligned}\mathbb{E}[|\check{\mathbf{h}}_{k,l,i}\mathbf{f}_{\mathrm{BB}_{m,i}}|^2] =&\mathbb{E}[\mathrm{tr}\{\check{\mathbf{h}}_{k,l,i}^H \check{\mathbf{h}}_{k,l,i}\mathbf{f}_{\mathrm{BB}_{m,i}}\mathbf{f}_{\mathrm{BB}_{m,i}}^H\}] \\ =&\mathrm{tr}\{\mathbb{E}[\check{\mathbf{h}}_{k,l,i}^H \check{\mathbf{h}}_{k,l,i}]\mathbb{E}[\mathbf{f}_{\mathrm{BB}_{m,i}}\mathbf{f}_{\mathrm{BB}_{m,i}}^H]\} = \frac{1}{K}\mathrm{tr}\{\mathbb{E}[\check{\mathbf{h}}_{k,l,i}^H \check{\mathbf{h}}_{k,l,i}]\mathbb{E}[\mathbf{F}_{\mathrm{BB}_i}\mathbf{F}_{\mathrm{BB}_i}^H]\}\end{aligned} \tag{8.39}$$

The second equality in (8.39) holds because $\check{\mathbf{h}}_{k,l,i}$ and $\mathbf{f}_{\mathrm{BB}_{m,i}}$ are independent, since $\mathbf{f}_{\mathrm{BB}_{m,i}}$ is only related to $\check{\mathbf{H}}_{i,i}$ which is independent of $\check{\mathbf{h}}_{k,l,i}$ when $l \neq i$ according to (8.2). Note that $\mathbf{F}_{\mathrm{BB}_i} = \check{\mathbf{H}}_{i,i}^H(\check{\mathbf{H}}_{i,i}\check{\mathbf{H}}_{i,i}^H + \xi_i\mathbf{I}_K)^{-1}$, the second expectation in (8.39) can be recast as:

$$\begin{aligned}\mathbb{E}[\mathbf{F}_{\mathrm{BB}_i}\mathbf{F}_{\mathrm{BB}_i}^H] =&\mathbb{E}[\check{\mathbf{H}}_{i,i}^H(\check{\mathbf{H}}_{i,i}\check{\mathbf{H}}_{i,i}^H + \xi_l\mathbf{I}_K)^{-2}\check{\mathbf{H}}_{i,i}] \\ =&\mathbb{E}[\check{\mathbf{H}}_{i,i}^H(\mathbf{U}\boldsymbol{\Lambda}\mathbf{U}^H + \xi_l\mathbf{I}_K)^{-2}\check{\mathbf{H}}_{i,i}] = \mathbb{E}[\check{\mathbf{H}}_{i,i}^H\mathbf{U}(\boldsymbol{\Lambda} + \xi_l\mathbf{I}_K)^{-2}\mathbf{U}^H\check{\mathbf{H}}_{i,i}]\end{aligned} \tag{8.40}$$

where the second equality stems from $\check{\mathbf{H}}_{i,i}\check{\mathbf{H}}_{i,i}^H = \mathbf{U}\boldsymbol{\Lambda}\mathbf{U}^H$. For the case $N_{\mathrm{T}}^{\mathrm{RF}} = K$ considered in this work, it follows from SVD that $\check{\mathbf{H}}_{i,i} = \mathbf{U}\boldsymbol{\Lambda}^{1/2}\mathbf{V}^H$. Conse-

quently, (8.40) is transformed to:

$$\begin{aligned}\mathbb{E}[\mathbf{F}_{\mathrm{BB}_i}\mathbf{F}_{\mathrm{BB}_i}^H] =&\mathbb{E}[\mathbf{V}\mathbf{\Lambda}^{1/2}\mathbf{U}^H\mathbf{U}(\mathbf{\Lambda}+\xi_l\mathbf{I}_K)^{-2}\mathbf{U}^H\mathbf{U}\mathbf{\Lambda}^{1/2}\mathbf{V}^H]\\ =&\mathbb{E}[\mathbf{V}\mathbf{\Lambda}^{1/2}(\mathbf{\Lambda}+\xi_l\mathbf{I}_K)^{-2}\mathbf{\Lambda}^{1/2}\mathbf{V}^H]\end{aligned} \tag{8.41}$$

For the first expectation in (8.39), let

$$\check{\mathbf{H}}_{l,i} = [\check{\mathbf{H}}_{1,l,i}^H, \check{\mathbf{H}}_{2,l,i}^H, ..., \check{\mathbf{H}}_{K,l,i}^H,]^H \tag{8.42}$$

one can denote $\check{\mathbf{H}}_{l,i}^H\check{\mathbf{H}}_{l,i} = \mathbf{Q}^H\mathbf{\Sigma}\mathbf{Q}$, where $\mathbf{\Sigma} = \mathrm{diag}(\sigma_1, ..., \sigma_K)$, then the trace in (8.39) becomes:

$$\begin{aligned}\varkappa_i =&\mathrm{tr}\{\mathbb{E}[\check{\mathbf{h}}_{k,l,i}^H\check{\mathbf{h}}_{k,l,i}]\mathbb{E}[\mathbf{F}_{\mathrm{BB}_i}\mathbf{F}_{\mathrm{BB}_i}^H]\}\\ =&\frac{1}{K}\mathrm{tr}\{\mathbb{E}[\check{\mathbf{H}}_{l,i}^H\check{\mathbf{H}}_{l,i}]\mathbb{E}[\mathbf{F}_{\mathrm{BB}_i}\mathbf{F}_{\mathrm{BB}_i}^H]\} = \frac{1}{K}\mathbb{E}[\mathrm{tr}\{\mathbf{Q}^H\mathbf{\Sigma}\mathbf{Q}\mathbf{V}\mathbf{\Lambda}^{1/2}(\mathbf{\Lambda}+\xi_i\mathbf{I}_K)^{-2}\mathbf{\Lambda}^{1/2}\mathbf{V}^H\}]\\ =&\frac{1}{K}\mathbb{E}[\mathrm{tr}\{\mathbf{V}^H\mathbf{Q}^H\mathbf{\Sigma}\mathbf{Q}\mathbf{V}\mathbf{\Lambda}^{1/2}(\mathbf{\Lambda}+\xi_i\mathbf{I}_K)^{-2}\mathbf{\Lambda}^{1/2}\}] = \frac{1}{K}\mathbb{E}\left[\sum_{k=1}^{K}\sum_{a=1}^{K}\sigma_a|w_{a,k}|^2\frac{\lambda_k}{(\lambda_k+\xi_i)^2}\right]\end{aligned} \tag{8.43}$$

where $w_{a,k}$ denotes the (a,k)-th entry of the unitary matrix $\mathbf{QV}$. Let $r = |w_{a,k}|^2$, then the PDF of r is given by [156]:

$$f_r(r) = (K-1)(1-r)^{K-2}, \quad 0 \le r \le 1 \tag{8.44}$$

which implies

$$\mathbb{E}[|w_{a,k}|^2] = \int_0^1 r(K-1)(1-r)^{K-2}dr = \frac{1}{K} \tag{8.45}$$

Therefore,

$$\begin{aligned}\varkappa_i =& \frac{1}{K}\mathbb{E}\left[\sum_{k=1}^{K}\sum_{a=1}^{K}\sigma_a\mathbb{E}[|w_{a,k}|^2]\frac{\lambda_k}{(\lambda_k+\xi_i)^2}\right]\\ =& \frac{1}{K^2}\mathbb{E}\left[\sum_{k=1}^{K}\sum_{a=1}^{K}\sigma_a\frac{\lambda_k}{(\lambda_k+\xi_i)^2}\right] = \frac{1}{K^2}\mathbb{E}_\sigma\left[\sum_{a=1}^{K}\sigma_a\right]\mathbb{E}_\lambda\left[\sum_{k=1}^{K}\frac{\lambda_k}{(\lambda_k+\xi_i)^2}\right]\\ \approx& \frac{1}{K}\tilde{\eta}_i\int_0^\infty \sigma f_{\sigma_{\text{arb}}}(\sigma)d\sigma\end{aligned} \tag{8.46}$$

where the approximation follows from (8.33). Based on (8.17), the integral in (8.46) can be recast as:

$$\varpi = \int_0^\infty \sigma f_{\sigma_{\text{arb}}}(\sigma)d\sigma = \frac{1}{K}\sum_{n=1}^{K}\int_0^\infty \sigma\frac{d_n^{c_n}\sigma^{c_n-1}e^{-d_n\sigma}}{\Gamma(c_n)}d\sigma = \frac{1}{K}\sum_{n=1}^{K}\frac{\Gamma(c_n+1)}{d_n\Gamma(c_n)} \tag{8.47}$$

Plugging (8.47) and (8.34) into (8.46) results in:

$$\varkappa_i = \frac{1}{K}\tilde{\eta}_i\varpi \tag{8.48}$$

Combining the results in (8.38), (8.39), and (8.48), the expected per-user interfer-

ence in (8.36) is expressed as:

$$\begin{aligned}\varsigma_{k,l} =& \frac{P_{\mathrm{T}}}{\tilde{\eta}_l \mathrm{PL}_{k,l,l}} \left[\frac{(K-1)s_l - \epsilon_l}{K(K+1)} \right] + \sum_{\substack{i=1 \\ i \neq l}}^{L} \frac{P_{\mathrm{T}} \varkappa_i}{\tilde{\eta}_i \mathrm{PL}_{k,l,i}} \\ =& \frac{P_{\mathrm{T}}}{\tilde{\eta}_l \mathrm{PL}_{k,l,l}} \left[\frac{(K-1)s_l - \epsilon_l}{K(K+1)} \right] + \sum_{\substack{i=1 \\ i \neq l}}^{L} \frac{P_{\mathrm{T}} \tilde{\eta}_i \varpi}{K \tilde{\eta}_i \mathrm{PL}_{k,l,i}} \\ =& \frac{P_{\mathrm{T}}}{\tilde{\eta}_l \mathrm{PL}_{k,l,l}} \left[\frac{(K-1)s_l - \epsilon_l}{K(K+1)} \right] + \sum_{\substack{i=1 \\ i \neq l}}^{L} \frac{P_{\mathrm{T}} \varpi}{K \mathrm{PL}_{k,l,i}}\end{aligned} \tag{8.49}$$

which will be used in (8.50) to calculate the expected per-user SINR.

8.2.5 Expected Per-User SINR and Ergodic Per-Cell Spectral Efficiency

Combining the expected per-user signal power $\delta_{k,l}$ in (8.32) and the expected per-user interference power $\varsigma_{k,l}$ in (8.49), the expected per-user SINR in (8.5) can be expressed as:

$$\mathbb{E}[\mathrm{SINR}_{k,l}] \approx \frac{\delta_{k,l}}{\varsigma_{k,l} + N_0} \tag{8.50}$$

The expected ergodic spectral efficiency for cell l can be approximated from $\mathbb{E}[\mathrm{SINR}_{k,l}]$ in (8.50) as:

$$\mathbb{E}[R_l] = \mathbb{E}\left[\sum_{k=1}^{K} \log_2(1 + \mathrm{SINR}_{k,l}) \right] \approx \sum_{k=1}^{K} \log_2\big(1 + \mathbb{E}[\mathrm{SINR}_{k,l}]\big) \tag{8.51}$$

It is noteworthy that (8.51) arouses an approximation instead of an upper bound via

Jensen's inequality, as the value of $\mathbb{E}[\text{SINR}_{k,l}]$ is itself an approximation [234, 245]. The generality of the results derived above is worth mentioning. *The analysis methodology derived above is applicable for any link SNR and channel model, including potential special cases such as the presence of a fixed LOS component in the channel (as long as the necessary eigenvalue densities are known).* If there is a change in the transmit or the receive dimension, then the analytical approach is still valid, however, the approximated gamma distributed eigenvalue densities need to be re-fitted. This is because of the mathematical complexity of finding closed–form expressions when using such an advanced channel model as well as the additional presence of RF beamforming.

8.2.6 Numerical Results and Discussion

The accuracy of the derived expected per-user SINR in (8.50) and expected per-cell spectral efficiency in (8.51) is evaluated in this subsection through comparison with numerical results for the three-cell homogeneous network introduced in Section 8.1 with three users per cell, along with the HBF architecture in Fig 8.3. In the simulations, the number of TP antennas was 256, the number of UE antennas was one, the number of streams per UE is one, the number of RF chains at each TP was three, and the cell radius was 200 m. For each channel model, 500 random channel realizations were carried out for each set of parameter settings. It is assumed that the carrier frequency is 28 GHz with a 100 MHz RF bandwidth and OFDM modulation with narrowband frequency-flat fading sub-carriers.

The CDFs of simulated and approximated expected per-user SINR and per-cell spectral efficiency are illustrated in Fig. 8.6. The expected SINR and spectral efficiency curves denote (8.5) (for simulated CDF) or (8.50) (for approximated CDF)

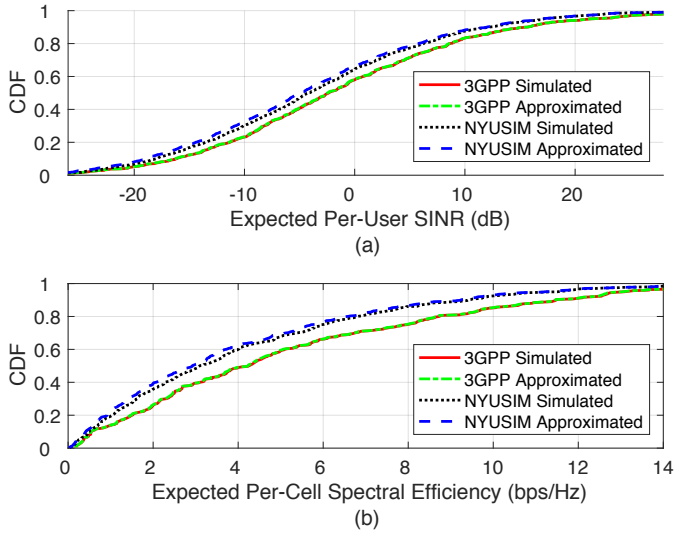

Figure 8.6: CDFs of (a) expected per-user SINR and (b) expected per-cell spectral efficiency, with a cell radius of 200 m, a cell-edge SNR of 5 dB, and three users per cell.

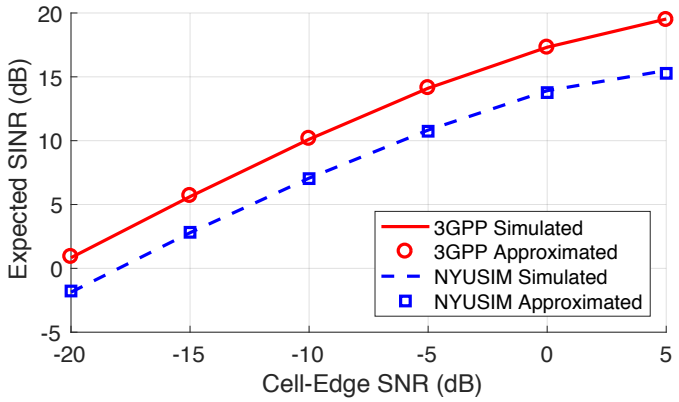

Figure 8.7: Expected per-user SINR versus cell-edge SNR with a cell radius of 200 m and three users per cell.

and (8.51), respectively, where the expectation is taken over the small-scale fading with the distribution representing the randomness in user location (i.e., large-scale path loss and shadow fading). It is observed from Fig. 8.6 that the derived SINR and spectral efficiency approximations closely follow the corresponding simulated values over the entire probability range. Furthermore, the expected per-user SINR as a function of the cell-edge SNR is illustrated in Fig. 8.7, where the average is performed globally over both the link gains and the multipath fading. As shown by Fig. 8.7, *for both 3GPP and NYUSIM models, the analytical expressions remain sufficiently accurate over the entire cell-edge SNR range investigated, revealing the tightness and generality of the derived SINR approximations.* The spectral efficiencies between 3GPP and NYUSIM in Fig. 8.6 do not differ much because there is only one stream per user, the difference will be larger for multi-stream per user, as will be shown later in this chapter.

8.3 Multi-Cell Multi-User Multi-Stream Hybrid Beamforming

In this section, multi-cell multi-user HBF schemes when multiple streams are transmitted from each TP to each of its serving users are investigated. As the analytical derivation for the expected per-user SINR is extremely cumbersome and even intractable for the multi-stream-per-user case, numerical simulations are utilized to evaluate the performance of various multi-cell HBF approaches. Furthermore, it is found through simulations that the spectral efficiency obtained by using the TP HBF architecture in Fig. 8.3 is lower than using the structure shown in Fig. 8.8, as demonstrated in Table 6.16, due to the increased IUI in the

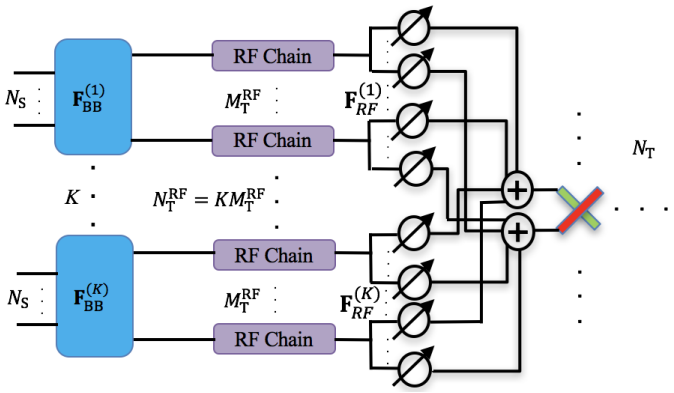

Figure 8.8: Multi-cell HBF architecture at the TP in each cell. N_S denotes the number of data streams per user in each cell, K is the number of users in each cell, N_T^{RF} represents the total number of RF chains at each TP, M_T^{RF} is the number of RF chains connected to the baseband precoder for one user, and N_T denotes the number of TP antenna elements in each cell. In this multi-cell multi-stream work, N_S varies from 1 to 4, K is either 3 or 12, $M_T^{RF} = 4$ which equals the number of RF chains at each UE, $N_T^{RF} = KM_T^{RF}$ which is either 12 or 48, and $N_T = 256$.

former. Therefore, the HBF architecture in Fig. 8.8 is used for multi-stream-per-user beamforming, where at each TP the N_T^{RF} RF chains are divided into K subsets with M_T^{RF} RF chains (fixed at four in this work due to channel sparsity [51]) in each subset, such that the total number of TP RF chains is $N_T^{RF} = KM_T^{RF}$. Additionally, there is a baseband digital precoder which is connected to a subset dedicated to a user in the home cell. The URA architecture at each UE is illustrated in Fig. 8.9, where there are N_R antennas and N_R^{RF} RF chains at each UE, and all the RF chains are connected to all the antennas.

For TP i and user k in cell l, the $N_R \times N_T$ downlink channel is denoted as $\mathbf{H}_{k,l,i}$, the $N_T \times M_T^{RF}$ RF precoding matrix is $\mathbf{F}_{\mathrm{RF}_{k,l}}$, and the $M_T^{RF} \times N_S$ baseband precoding matrix is $\mathbf{F}_{\mathrm{BB}_{k,l}}$. The $N_R \times N_R^{RF}$ RF combining matrix and the $N_R^{RF} \times N_S$ baseband combining matrix is $\mathbf{W}_{\mathrm{RF}_{k,l}}$ and $\mathbf{W}_{\mathrm{BB}_{k,l}}$, respectively. The received signal

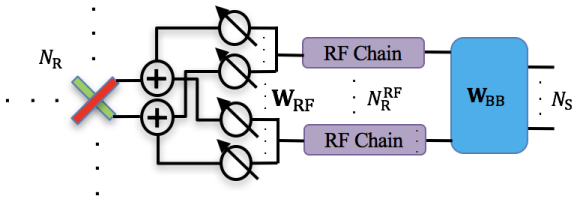

Figure 8.9: Multi-cell HBF architecture at each UE. N_S denotes the number of data streams per UE, N_R^{RF} represents the number of RF chains at each UE, and N_R denotes the number of UE antenna elements. In this multi-cell multi-stream work, N_S varies from 1 to 4, $N_R^{RF} = 4$, and $N_R = 8$.

at user k in cell l is formulated as:

$$\begin{aligned}\mathbf{y}_{k,l} = & \underbrace{\sqrt{\frac{P_t}{\eta_{k,l}\mathrm{PL}_{k,l,l}}}\mathbf{W}_{\mathrm{BB}_{k,l}}^H\mathbf{W}_{\mathrm{RF}_{k,l}}^H\mathbf{H}_{k,l,l}\mathbf{F}_{\mathrm{RF}_{k,l}}\mathbf{F}_{\mathrm{BB}_{k,l}}\mathbf{s}_{k,l}}_{\text{Desired Signal}} \\ & + \underbrace{\sum_{\substack{(m,i)\\ \neq(k,l)}}\sqrt{\frac{P_t}{\eta_{m,i}\mathrm{PL}_{k,l,i}}}\mathbf{W}_{\mathrm{BB}_{k,l}}^H\mathbf{W}_{\mathrm{RF}_{k,l}}^H\mathbf{H}_{k,l,i}\mathbf{F}_{\mathrm{RF}_{m,i}}\mathbf{F}_{\mathrm{BB}_{m,i}}\mathbf{s}_{m,i}}_{\text{Interference}} \\ & + \underbrace{\mathbf{W}_{\mathrm{BB}_{k,l}}^H\mathbf{W}_{\mathrm{RF}_{k,l}}^H\mathbf{n}_{k,l}}_{\text{Noise}}\end{aligned} \tag{8.52}$$

where P_t represents the transmit power for each user in Watts, and is assumed to be constant regardless of the number of users per cell and the cell radius. $\mathrm{PL}_{k,l,i}$ denotes the large-scale distance-dependent path loss in Watts, including shadow fading, from TP i to user k in cell l, $\eta_{k,l} = ||\mathbf{F}_{\mathrm{RF}_{k,l}}\mathbf{F}_{\mathrm{BB}_{k,l}}||_F^2$ is a scaling factor to satisfy the per-user transmit power constraint $||\sqrt{P_t}\mathbf{F}_{\mathrm{RF}_{k,l}}\mathbf{F}_{\mathrm{BB}_{k,l}}/\sqrt{\eta_{k,l}}||_F^2 = P_t$. $\mathbf{s}_{k,l}$ represents the desired transmitted signal for user k in cell l with $\mathbb{E}[\mathbf{s}_{k,l}\mathbf{s}_{k,l}^H] = \mathbf{I}_{N_S}$, and $\mathbf{n}_{k,l} \sim \mathcal{CN}(\mathbf{0}, N_0\mathbf{I}_{N_R})$ is circularly symmetric complex Gaussian noise with variance N_0. The spectral efficiency of user k in cell l is calculated as in (8.53) [117], where the interference term $\mathbf{D}$ in (8.53) is given by:

$$R_{k,l} = \log_2 \Bigg| \mathbf{I}_{N_\mathrm{S}} + \frac{P_\mathrm{t}}{\eta_{k,l}\mathrm{PL}_{k,l,l}} \big(\mathbf{W}^H_{\mathrm{BB}_{k,l}} \mathbf{W}^H_{\mathrm{RF}_{k,l}} (N_0 \mathbf{I}_{N_\mathrm{R}} + \mathbf{D}) \mathbf{W}_{\mathrm{RF}_{k,l}} \mathbf{W}_{\mathrm{BB}_{k,l}} \big)^{-1} \times \mathbf{W}^H_{\mathrm{BB}_{k,l}} \breve{\mathbf{H}}_{k,l,k,l} \mathbf{F}_{\mathrm{BB}_{k,l}} \mathbf{F}^H_{\mathrm{BB}_{k,l}} \breve{\mathbf{H}}^H_{k,l,k,l} \mathbf{W}_{\mathrm{BB}_{k,l}} \Bigg| \tag{8.53}$$

$$\mathbf{D} = \sum_{\substack{(m,i) \\ \neq (k,l)}} \frac{P_\mathrm{t}}{\eta_{m,i}\mathrm{PL}_{k,l,i}} \mathbf{H}_{k,l,i} \mathbf{F}_{\mathrm{RF}_{m,i}} \mathbf{F}_{\mathrm{BB}_{m,i}} \mathbf{F}^H_{\mathrm{BB}_{m,i}} \mathbf{F}^H_{\mathrm{RF}_{m,i}} \mathbf{H}^H_{k,l,i} \tag{8.54}$$

Note that the spectral efficiency in (8.53) is formulated based on Shannon theory assuming ideal encoding and decoding functions and serves as an upper bound of the achievable rate [246]. Non-ideal/more practical encoding and decoding may be used in reality which results in lower spectral efficiency compared to (8.53). Additionally, for all the multi-cell HBF approaches henceforth, it is assumed that no power control is performed.

8.3.1 Baseline Case — No Coordination Among Cells

Let us first consider the interference-ignorant baseline case where there is no TP coordination among cells. Assuming only local CSI is available at each TP, a reasonable precoding scheme is eigenmode transmission [235]. User k in cell l will be treated as the desired user in all the subsequent multi-cell HBF design. Let us define the effective channel matrix $\breve{\mathbf{H}}_{k,l,k,l} \in \mathbb{C}^{N^{\mathrm{RF}}_\mathrm{R} \times M^{\mathrm{RF}}_\mathrm{T}}$ for user k in cell l as $\frac{1}{\sqrt{\mathrm{PL}_{k,l,l}}} \mathbf{W}^H_{\mathrm{RF}_{k,l}} \mathbf{H}_{k,l,l} \mathbf{F}_{\mathrm{RF}_{k,l}}$, where the RF precoding and combining matrices $\mathbf{F}_{\mathrm{RF}_{k,l}}$ and $\mathbf{W}_{\mathrm{RF}_{k,l}}$ are designed such that $||\mathbf{W}^H_{\mathrm{RF}_{k,l}} \mathbf{H}_{k,l,l} \mathbf{F}_{\mathrm{RF}_{k,l}}||^2_F$ is maximized to enhance SNR. The RF beamforming approach in Eqs. (12)-(14) proposed in [171] is applied to obtain $\mathbf{F}_{\mathrm{RF}_{k,l}}$ and $\mathbf{W}_{\mathrm{RF}_{k,l}}$, in which the codebooks for $\mathbf{F}_{\mathrm{RF}_{k,l}}$ and $\mathbf{W}_{\mathrm{RF}_{k,l}}$

consist of the TP and UE antenna array response vectors corresponding to the angles-of-departure (AoDs) and angles-of-arrival (AoAs) associated with the desired user, respectively [117]. The baseband precoding matrix $\mathbf{F}_{\mathrm{BB}_{k,l}}$ is composed of the dominant N_{S} right singular vectors obtained from the SVD of $\check{\mathbf{H}}_{k,l,k,l}$, and the baseband combining matrix $\mathbf{W}_{\mathrm{BB}_{k,l}}$ is constituted by the dominant N_{S} left singular vectors obtained from the SVD of $\check{\mathbf{H}}_{k,l,k,l}\mathbf{F}_{\mathrm{BB}_{k,l}}$.

8.3.2 Leakage-Suppressing and Signal-Maximizing Precoding

A coordinated scheduling/beamforming CoMP scheme named leakage-suppressing and signal-maximizing precoding (LSP) is proposed herein, where the RF precoder is aimed at mitigating the dominant leakage to all the other users while enhancing the strength of the desired signal. The precoding matrix at TP l for user k in cell l is designed as follows. First, the cascaded leakage channel matrix consisting of all the channel matrices except the one for user k in cell l is obtained through CSI exchange among TPs as:

$$\tilde{\mathbf{H}}_{k,l} = \left[\frac{1}{\sqrt{\mathrm{PL}_{1,1,l}}}\mathbf{H}_{1,1,l}^{T}, ..., \frac{1}{\sqrt{\mathrm{PL}_{k-1,l,l}}}\mathbf{H}_{k-1,l,l}^{T}, \ \frac{1}{\sqrt{\mathrm{PL}_{k+1,l,l}}}\mathbf{H}_{k+1,l,l}^{T}, ..., \frac{1}{\sqrt{\mathrm{PL}_{K,L,l}}}\mathbf{H}_{K,L,l}^{T} \right]^{T} \tag{8.55}$$

The columns of RF beamforming matrices at each TP and UE are selected from pre-defined beamforming codebooks that consist of antenna array response vectors $\mathbf{a}_{\mathrm{T}}$ and $\mathbf{a}_{\mathrm{R}}$ at the TP and UE, respectively. The matrix $\mathbf{A}_{\mathrm{T}}$ and $\mathbf{A}_{\mathrm{R}}$ are composed of $\mathbf{a}_{\mathrm{T}}$'s and $\mathbf{a}_{\mathrm{R}}$'s corresponding to the AoDs and AoAs associated with the desired user, respectively [117]. The first column in the RF precoding matrix $\mathbf{F}_{\mathrm{RF}_{k,l}}$ is

chosen from $\mathbf{A}_{\mathrm{T}}$ such that $||\tilde{\mathbf{H}}_{k,l}\mathbf{F}_{\mathrm{RF}_{k,l}}(:,1)||_F^2$ is minimized, whose physical meaning is using the first RF precoding vector at TP l to suppress the leakage to all the other users in all the cells considered. The remaining $M_{\mathrm{T}}^{\mathrm{RF}}-1$ columns in $\mathbf{F}_{\mathrm{RF}_{k,l}}$ are selected from $\mathbf{A}_{\mathrm{T}}$ to maximize $||\mathbf{H}_{k,l,l}\mathbf{F}_{\mathrm{RF}_{k,l}}(:,2:M_{\mathrm{T}}^{\mathrm{RF}})||_F^2$, the physical meaning of which is utilizing the remaining $M_{\mathrm{T}}^{\mathrm{RF}}-1$ RF precoding vectors to maximize the desired signal power to user k in cell l. Then the baseband precoding matrix $\mathbf{F}_{\mathrm{BB}_{k,l}}$ is designed by taking the SVD of $\mathbf{H}_{k,l,l}\mathbf{F}_{\mathrm{RF}_{k,l}}$ and setting $\mathbf{F}_{\mathrm{BB}_{k,l}}$ as $\mathbf{V}(:,1:N_{\mathrm{S}})$ where $\mathbf{V}(:,1:N_{\mathrm{S}})$ represents the first N_{S} dominant right singular vectors of $\mathbf{H}_{k,l,l}\mathbf{F}_{\mathrm{RF}_{k,l}}$.

For the design of the hybrid combining matrix at user k in cell l, first, the optimum fully digital combining matrix is obtained by taking the SVD of $\mathbf{H}_{k,l,l}\mathbf{F}_{\mathrm{RF}_{k,l}}\mathbf{F}_{\mathrm{BB}_{k,l}}$, and setting the columns of the combining matrix to be the dominant N_{S} left singular vectors. Then the RF and baseband combining matrices are designed according to Algorithm 1 on Page 1505 of [117] based on the optimum fully digital combining matrix.

As extensions of LSP, if sufficient channel diversity exists, more than one precoding vector could be used for suppressing leakage when designing the precoding matrix at each TP.

8.3.3 SLNR-Based Precoding

The third multi-cell HBF strategy is an SLNR-based scheme incorporating coordinated scheduling/beamforming in CoMP. Directly maximizing the SINR over all users in all cells involves a challenging optimization problem with coupled variables, thus the SLNR is utilized as an alternative optimization criterion. In the SLNR-based TP coordination, the effective channel matrix $\check{\mathbf{H}}_{m,i,k,l} \in \mathbb{C}^{N_{\mathrm{R}}^{\mathrm{RF}} \times M_{\mathrm{T}}^{\mathrm{RF}}}$ is defined as $\frac{1}{\sqrt{\mathrm{PL}_{m,i,l}}}\mathbf{W}_{\mathrm{RF}_{m,i}}^H\mathbf{H}_{m,i,l}\mathbf{F}_{\mathrm{RF}_{k,l}}$, and the $(KL-1)N_{\mathrm{R}}^{\mathrm{RF}} \times M_{\mathrm{T}}^{\mathrm{RF}}$ leakage matrix for

TP l communicating with user k in cell l is given by:

$$\tilde{\mathbf{H}}_{k,l} = \left[\breve{\mathbf{H}}_{1,1,k,l}^{T}, ..., \breve{\mathbf{H}}_{k-1,l,k,l}^{T}, \breve{\mathbf{H}}_{k+1,l,k,l}^{T}, ..., \breve{\mathbf{H}}_{K,L,k,l}^{T}\right]^{T} \tag{8.56}$$

The RF precoding and combining matrices $\mathbf{F}_{\mathrm{RF}_{k,l}}$ and $\mathbf{W}_{\mathrm{RF}_{k,l}}$ are designed such that $||\mathbf{W}_{\mathrm{RF}_{k,l}}^{H}\mathbf{H}_{k,l,l}\mathbf{F}_{\mathrm{RF}_{k,l}}||_{F}^{2}$ is maximized, where $\mathbf{F}_{\mathrm{RF}_{k,l}}$ and $\mathbf{W}_{\mathrm{RF}_{k,l}}$ are obtained in the same manner as in the baseline case. The baseband precoding matrix $\mathbf{F}_{\mathrm{BB}_{k,l}}$ is designed to maximize the SLNR as follows [157]. The expected received signal power prior to the baseband combining process is $\mathbb{E}\big[\frac{P_{\mathrm{t}}}{\eta_{k,l}}\mathbf{s}_{k,l}^{H}\mathbf{F}_{\mathrm{BB}_{k,l}}^{H}\breve{\mathbf{H}}_{k,l,k,l}^{H}\breve{\mathbf{H}}_{k,l,k,l}\mathbf{F}_{\mathrm{BB}_{k,l}}\mathbf{s}_{k,l}\big]$, the expected leakage power is $\mathbb{E}\big[\sum\limits_{(m,i)\neq(k,l)}\frac{P_{\mathrm{t}}}{\eta_{k,l}}\mathbf{s}_{k,l}^{H}\mathbf{F}_{\mathrm{BB}_{k,l}}^{H}\breve{\mathbf{H}}_{m,i,k,l}^{H}\breve{\mathbf{H}}_{m,i,k,l}\mathbf{F}_{\mathrm{BB}_{k,l}}\mathbf{s}_{k,l}\big]$, and the expected noise power is $\mathbb{E}\big[\mathbf{n}_{k,l}^{H}\mathbf{W}_{\mathrm{RF}_{k,l}}\mathbf{W}_{\mathrm{RF}_{k,l}}^{H}\mathbf{n}_{k,l}\big]$. The SLNR is hence formulated as in (8.57) [157],

$$\begin{aligned}
\mathrm{SLNR} &\approx \frac{\mathbb{E}\left[\frac{P_{\mathrm{t}}}{\eta_{k,l}}\mathbf{s}_{k,l}^{H}\mathbf{F}_{\mathrm{BB}_{k,l}}^{H}\breve{\mathbf{H}}_{k,l,k,l}^{H}\breve{\mathbf{H}}_{k,l,k,l}\mathbf{F}_{\mathrm{BB}_{k,l}}\mathbf{s}_{k,l}\right]}{\mathbb{E}\left[\sum\limits_{(m,i)\neq(k,l)}\frac{P_{\mathrm{t}}}{\eta_{k,l}}\mathbf{s}_{k,l}^{H}\mathbf{F}_{\mathrm{BB}_{k,l}}^{H}\breve{\mathbf{H}}_{m,i,k,l}^{H}\breve{\mathbf{H}}_{m,i,k,l}\mathbf{F}_{\mathrm{BB}_{k,l}}\mathbf{s}_{k,l}\right] + \mathbb{E}\big[\mathbf{n}_{k,l}^{H}\mathbf{W}_{\mathrm{RF}_{k,l}}\mathbf{W}_{\mathrm{RF}_{k,l}}^{H}\mathbf{n}_{k,l}\big]} \\
&= \frac{\mathrm{tr}\left(\frac{P_{\mathrm{t}}}{\eta_{k,l}}\mathbf{F}_{\mathrm{BB}_{k,l}}^{H}\breve{\mathbf{H}}_{k,l,k,l}^{H}\breve{\mathbf{H}}_{k,l,k,l}\mathbf{F}_{\mathrm{BB}_{k,l}}\right)}{\mathrm{tr}\left(\sum\limits_{(m,i)\neq(k,l)}\frac{P_{\mathrm{t}}}{\eta_{k,l}}\mathbf{F}_{\mathrm{BB}_{k,l}}^{H}\breve{\mathbf{H}}_{m,i,k,l}^{H}\breve{\mathbf{H}}_{m,i,k,l}\mathbf{F}_{\mathrm{BB}_{k,l}}\right) + N_0\mathrm{tr}\big(\mathbf{W}_{\mathrm{RF}_{k,l}}\mathbf{W}_{\mathrm{RF}_{k,l}}^{H}\big)} \\
&= \frac{\mathrm{tr}\left(\mathbf{F}_{\mathrm{BB}_{k,l}}^{H}\breve{\mathbf{H}}_{k,l,k,l}^{H}\breve{\mathbf{H}}_{k,l,k,l}\mathbf{F}_{\mathrm{BB}_{k,l}}\right)}{\mathrm{tr}\left(\mathbf{F}_{\mathrm{BB}_{k,l}}^{H}\tilde{\mathbf{H}}_{k,l}^{H}\tilde{\mathbf{H}}_{k,l}\mathbf{F}_{\mathrm{BB}_{k,l}}\right) + \frac{\eta_{k,l}}{P_{\mathrm{t}}}N_0\mathrm{tr}\big(\mathbf{W}_{\mathrm{RF}_{k,l}}\mathbf{W}_{\mathrm{RF}_{k,l}}^{H}\big)} \\
&= \frac{\mathrm{tr}\left(\mathbf{F}_{\mathrm{BB}_{k,l}}^{H}\breve{\mathbf{H}}_{k,l,k,l}^{H}\breve{\mathbf{H}}_{k,l,k,l}\mathbf{F}_{\mathrm{BB}_{k,l}}\right)}{\mathrm{tr}\left(\mathbf{F}_{\mathrm{BB}_{k,l}}^{H}\left(\tilde{\mathbf{H}}_{k,l}^{H}\tilde{\mathbf{H}}_{k,l} + \gamma\mathbf{I}_{M_{\mathrm{T}}^{\mathrm{RF}}}\right)\mathbf{F}_{\mathrm{BB}_{k,l}}\right)}
\end{aligned} \tag{8.57}$$

The SLNR in (8.57) is used as an optimizing criterion to calculate the optimal

baseband precoding matrix $\mathbf{F}_{\mathrm{BB}_{k,l}}$, where $\tilde{\mathbf{H}}_{k,l}$ is given by (8.56), and the second equality in (8.57) holds since $\mathbb{E}[\mathbf{s}_{k,l}\mathbf{s}_{k,l}^H] = \mathbf{I}_{N_\mathrm{S}}$ and $\mathbb{E}[\mathbf{n}_{k,l}\mathbf{n}_{k,l}^H] = N_0\mathbf{I}_{N_\mathrm{R}}$. And γ satisfies:

$$\mathrm{tr}(\gamma\mathbf{F}_{\mathrm{BB}_{k,l}}^H\mathbf{F}_{\mathrm{BB}_{k,l}}) = \frac{\eta_{k,l}}{P_\mathrm{t}}N_0\mathrm{tr}(\mathbf{W}_{\mathrm{RF}_{k,l}}\mathbf{W}_{\mathrm{RF}_{k,l}}^H) \tag{8.58}$$

The optimal $\mathbf{F}_{\mathrm{BB}_{k,l}}$ that maximizes the SLNR in (8.57) can be derived similarly to the precoding matrix in [157] and is composed of the leading N_S columns of $\mathbf{T}_{k,l}$ which contains the generalized eigenvectors of the pair $\left\{\breve{\mathbf{H}}_{k,l,k,l}^H\breve{\mathbf{H}}_{k,l,k,l}, \ \tilde{\mathbf{H}}_{k,l}^H\tilde{\mathbf{H}}_{k,l} + \gamma\mathbf{I}_{M_\mathrm{T}^\mathrm{RF}}\right\}$. $\mathbf{W}_{\mathrm{BB}_{k,l}}$ is designed as a matched filter at the receiver [157]:

$$\mathbf{W}_{\mathrm{BB}_{k,l}} = \frac{\breve{\mathbf{H}}_{k,l,k,l}\mathbf{F}_{\mathrm{BB}_{k,l}}}{||\breve{\mathbf{H}}_{k,l,k,l}\mathbf{F}_{\mathrm{BB}_{k,l}}||_F} \tag{8.59}$$

8.3.4 Generalized Maximum-Ratio Precoding

The fourth HBF strategy is generalized maximum-ratio (GMR) transmission that belongs to coordinated scheduling/beamforming in CoMP, and has the same RF precoding, RF combining, and baseband combining procedures as the baseline. In contrast to conventional maximum ratio (MR) transmission where the precoder is designed based on the channel matrix $\mathbf{H}$, GMR transmission uses the effective, RF-filtered channel $\mathbf{HF}_\mathrm{RF}$ to design the baseband precoder. In the GMR-based approach, the effective channel for user k in cell l after RF precoding and combining is denoted as the $N_\mathrm{R}^\mathrm{RF} \times M_\mathrm{T}^\mathrm{RF}$ matrix $\breve{\mathbf{H}}_{m,i,k,l}$ defined as

$$\breve{\mathbf{H}}_{m,i,k,l} = \frac{1}{\sqrt{\mathrm{PL}_{m,i,l}}}\mathbf{W}_{\mathrm{RF}_{m,i}}^H\mathbf{H}_{m,i,l}\mathbf{F}_{\mathrm{RF}_{k,l}} \tag{8.60}$$

and the $KLN_\mathrm{R}^\mathrm{RF} \times M_\mathrm{T}^\mathrm{RF}$ concatenated effective channel matrix is:

$$\tilde{\mathbf{H}}_{k,l} = [\breve{\mathbf{H}}_{1,1,k,l}^T, ..., \breve{\mathbf{H}}_{k,l,k,l}^T, ..., \breve{\mathbf{H}}_{K,L,k,l}^T]^T \tag{8.61}$$

If $N_\mathrm{S} = N_\mathrm{R}^\mathrm{RF}$, then the baseband precoding matrix can be set as the $N_\mathrm{S}(K(l -$

$1)+k-1)+1$th to the $N_{\mathrm{S}}(K(l-1)+k)$th columns of $\overline{\mathbf{F}_{\mathrm{BB}}}$ yielded by the GMR transmission matrix:

$$\overline{\mathbf{F}_{\mathrm{BB}}} = \tilde{\mathbf{H}}_{k,l}^{H} \tag{8.62}$$

Or equivalently

$$\mathbf{F}_{\mathrm{BB}_{k,l}} = \check{\mathbf{H}}_{k,l,k,l}^{H} \tag{8.63}$$

Eq. (8.63) shows that GMR essentially requires no coordination among TPs. However, it should be noted that GMR only works for the situation where $N_{\mathrm{S}} = N_{\mathrm{R}}^{\mathrm{RF}}$, and will not work otherwise due to matrix dimension mismatch. All the other proposed algorithms work for any situations where $N_{\mathrm{S}} \leq N_{\mathrm{R}}^{\mathrm{RF}}$. In practice, the dimension issue is easily accounted for by turning off the unnecessary RF chains.

8.3.5 Feasibility of Zero-Forcing Precoding

Another popular multi-user precoding method besides maximum ratio is ZF [247, 248], thus it is reasonable to consider whether ZF precoding is feasible in the system setup herein. Analogous to GMR introduced in the previous subsection, let us assume the RF precoding, RF combining, and baseband combining schemes are the same as those in the GMR-based HBF method, and that $N_{\mathrm{S}} = N_{\mathrm{R}}^{\mathrm{RF}}$, then the baseband precoding matrix for user k in cell l $\mathbf{F}_{\mathrm{BB}_{k,l}}$ is composed of the $N_{\mathrm{S}}(K(l-1)+k-1)+1$th to the $N_{\mathrm{S}}(K(l-1)+k)$th columns of $\overline{\mathbf{F}_{\mathrm{BB}}}$ given by the generalized ZF matrix:

$$\overline{\mathbf{F}_{\mathrm{BB}}} = \tilde{\mathbf{H}}_{k,l}^{H}(\tilde{\mathbf{H}}_{k,l}\tilde{\mathbf{H}}_{k,l}^{H})^{-1} \tag{8.64}$$

where $\tilde{\mathbf{H}}_{k,l}$ is given by (8.61) with the dimension $KLN_{\mathrm{R}}^{\mathrm{RF}} \times M_{\mathrm{T}}^{\mathrm{RF}}$, hence $\tilde{\mathbf{H}}_{k,l}\tilde{\mathbf{H}}_{k,l}^{H}$ has the dimension $KLN_{\mathrm{R}}^{\mathrm{RF}} \times KLN_{\mathrm{R}}^{\mathrm{RF}}$ with a rank of $M_{\mathrm{T}}^{\mathrm{RF}}$ which is smaller than $KLN_{\mathrm{R}}^{\mathrm{RF}}$. Therefore, $\tilde{\mathbf{H}}_{k,l}\tilde{\mathbf{H}}_{k,l}^{H}$ is rank deficient thus not invertible, hence *ZF precod-*

ing is not feasible for the proposed multi-cell system due to dimension constraints. Alternatively, the rank deficiency problem will not exist if ZF is done at the receiver side, which, however, requires that each user has the CSI of all TPs to all users, and this is too much overhead for the user hence not feasible, either.

While RZF can be used to avoid the rank deficiency issue in ZF, the optimal regularization parameter remains to be solved for multi-cell multi-stream scenarios, which is outside the scope of this technical report. Further, the performance of RZF approximates MR for low SNRs and ZF for high SNRs, thus it is sufficient to study MR and ZF.

8.4 Simulation Results and Analysis

Using the multi-cell MU-MIMO HBF procedures proposed above and the system layout and settings demonstrated in Section 8.1, spectral efficiency is studied using both the 3GPP [66] and NYUSIM [51] channel models via MATLAB simulations. It is assumed that there are $N_{\mathrm{R}}^{\mathrm{RF}}$ RF chains at each UE, and each TP communicates with each UE via N_{S} ($N_{\mathrm{S}} \leq N_{\mathrm{R}}^{\mathrm{RF}}$) data streams. For each channel model, 400 random channel realizations were carried out where 27 channel matrices were generated in each channel realization for the three-user-per-cell case (hence resulting in 10800 channel matrices in total), which represent the channel matrices between each TP and each UE in the three cells; while 100 random channel realizations were carried out where 108 channel matrices were generated in each channel realization for the 12-user-per-cell case (hence resulting in 10800 channel matrices in total). In each channel realization, UE locations in each cell are randomly and uniformly generated with T-R separation distances ranging from 10 m to the cell radius.

The cell radius is set to 50 m and 200 m, respectively, where the 200 m radius is obtained by assuming that 95% of the area in each cell has a signal-to-noise ratio (SNR) larger than or equal to 5 dB, and the upper bound of the T-R separation distance is calculated based on this assumption and is rounded to 200 m for both models for fair comparison [51, 66], while the 50 m radius is chosen for comparison purposes.

Beam patterns generated by the baseline, LSP, and SLNR-based precoding matrices in an example channel realization are illustrated in Fig. 8.10, where the cell radius is 50 m, there are three users per cell and two streams per user. *It is seen from Fig. 8.10 that the SLNR-based precoding is able to generate six distinct main beams each for one stream at one user. In the baseline and LSP beam patterns, however, some of the main beams are much weaker than in the SLNR case, and some main beams are accompanied with a side beam that may cause interference to other streams or other users, hence reducing spectral efficiency. The difference in beam patterns will give rise to difference in spectral efficiency to be analyzed below.*

The CDFs of per-user spectral efficiency in the three-cell MU-MIMO system using both 3GPP [66] and NYUSIM [51] models are illustrated in Fig. 8.11 for different cell radii and user numbers with two steams per user. Fig. 8.11 shows that for both 3GPP and NYUSIM models, the SLNR-based HBF outperforms all the other HBF schemes, revealing its effectiveness in suppressing both intra-cell and inter-cell interference and noise. Another distinguishing feature is that LSP does not outperform the baseline case for the 3GPP model, which is probably due to the fact that LSP spends part of the transmit power on suppressing leakage, thus leaving less power for signal transmission compared to the baseline case. While for NYUSIM, LSP renders comparable performance relative to the baseline case as

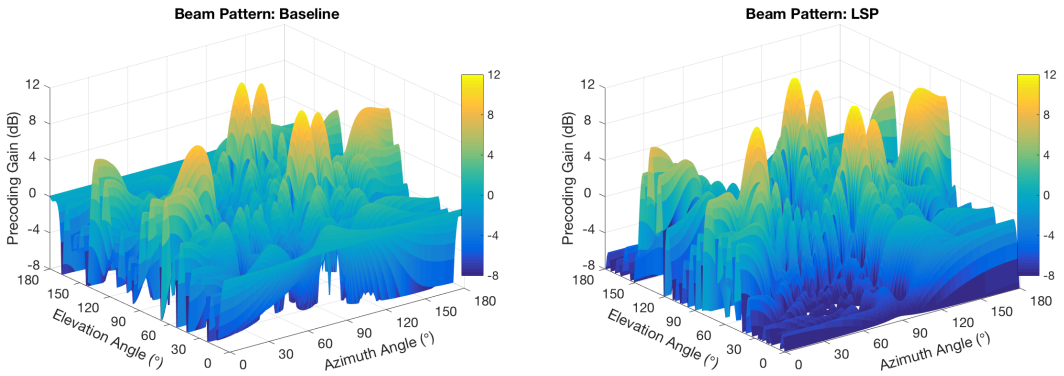

(a) Baseline

(b) LSP

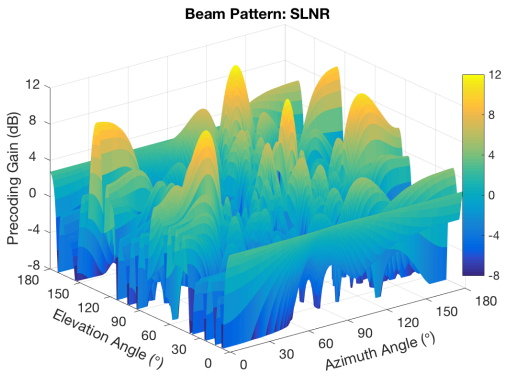

(c) SLNR

Figure 8.10: Beam patterns in an example channel realization generated by the (a) baseline, (b) LSP, and (c) SLNR-based precoding matrices at one TP. The cell radius is 50 m, there are three users per cell and two streams per user.

Table 8.2: Multi-cell per-user spectral efficiency at the 50% CDF point in Fig. 8.11 using the SLNR-based HBF.

Per-User Spectral Efficiency (bps/Hz)	50 m Cell Radius (3GPP/NYUSIM)	200 m Cell Radius (3GPP/NYUSIM)
3 UEs Per Cell	8.8 / 10.2	5.3 / 8.8
12 UEs Per Cell	2.6 / 3.0	1.4 / 2.6

compared to the 3GPP model, since the NYUSIM channel has a stronger dominant eigenchannel than 3GPP (see Fig. 6.4), thus LSP appears to be much more effective when using the NYUSIM channel model, since the dominant leakage is stronger. Furthermore, using NYUSIM leads to higher spectral efficiency as compared to the 3GPP model, likely due to the stronger two dominant eigenmodes per user yielded by NYUSIM channel matrices. This implies that it is important to design a proper beamforming approach (e.g., the SLNR-based approach) to make CoMP superior to the non-CoMP case, since some coordinated beamforming methods (e.g., LSP) may not yield higher spectral efficiency than the baseline. Table 8.2 summarizes the per-user spectral efficiency at the 50% CDF point in Fig. 8.11 using the SLNR-based HBF, which shows that *NYUSIM can provide up to 86% more spectral efficiency than the 3GPP channel model.*

When comparing Figs. 8.11(a) and 8.11(b), or Figs. 8.11(c) and 8.11(d), it is noticeable that for the same cell radius, the spectral efficiency gap between the SLNR approach and the baseline decreases as the user number increases. This phenomenon can be explained by Fig. 8.12 which depicts the average signal power and interference power (averaged over users) for different user numbers using the SLNR method and the baseline for the 50 m cell radius as an example. Fig. 8.12 shows that for either the SLNR approach or the baseline, when the user number increases from three to 12, the average signal power remains almost the same, while

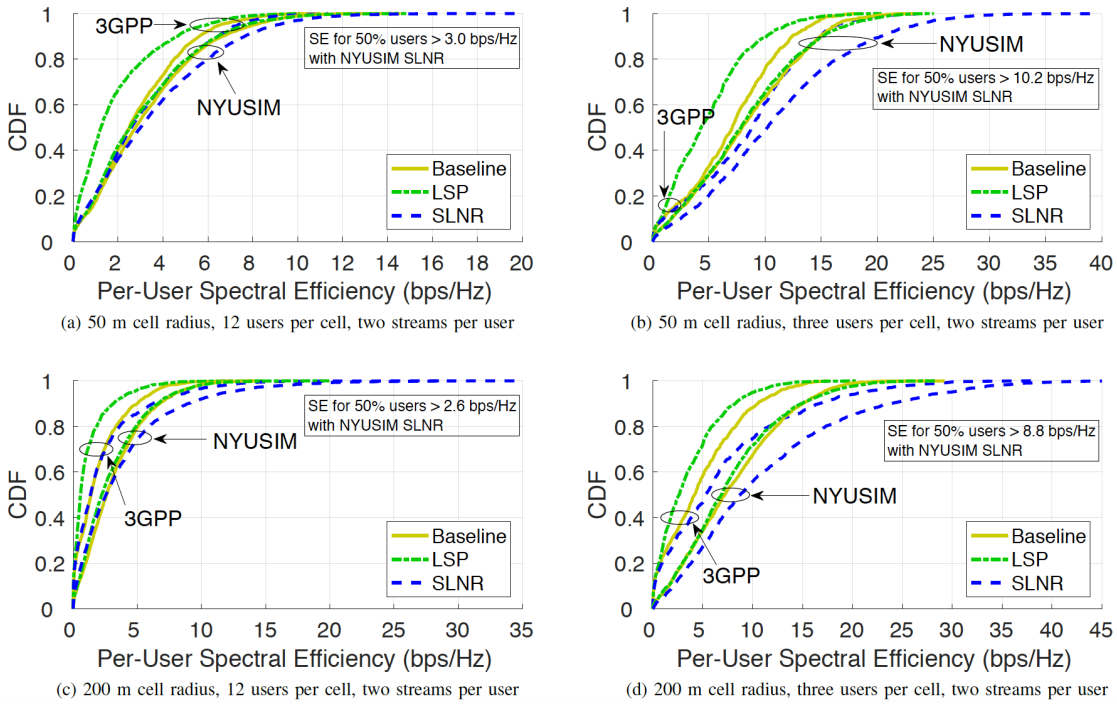

(a) 50 m cell radius, 12 users per cell, two streams per user

(b) 50 m cell radius, three users per cell, two streams per user

(c) 200 m cell radius, 12 users per cell, two streams per user

(d) 200 m cell radius, three users per cell, two streams per user

Figure 8.11: CDFs of the spectral efficiency per user with (a) a 50 m cell radius and 12 users per cell, (b) a 50 m cell radius and three users per cell, (c) a 200 m cell radius and 12 users per cell, and (d) a 200 m cell radius and three users per cell, in the three-cell multi-user MIMO system using the HBF algorithms proposed in this chapter for 3GPP [66] and NYUSIM [51] channel models. Baseline means no coordination among TPs, LSP denotes leakage-suppressing and signal-maximizing precoding, and SLNR represents SLNR-based precoding. There is one TP per cell, and the users in each cell are distributed uniformly and randomly with T-R separation distances ranging from 10 m to the cell radius [66]. There are four RF chains and two streams per user, and 48 and 12 TP RF chains for 12 and three users per cell, respectively.

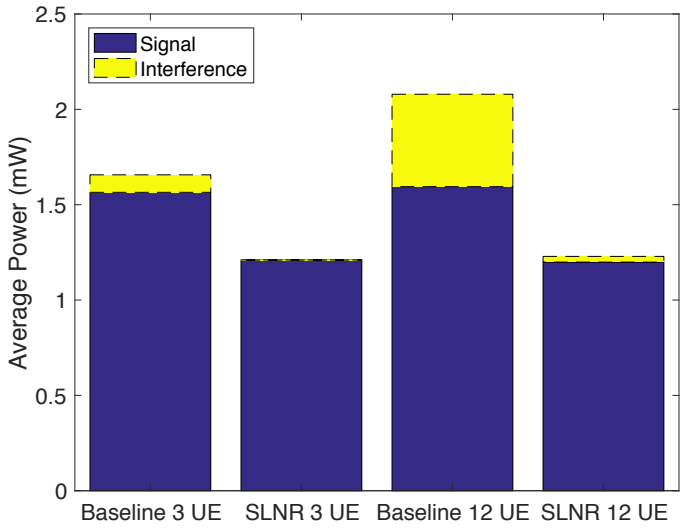

Figure 8.12: Average signal power and average interference power generated from the NYUSIM channel model for the three-cell system with a cell radius of 50 m, where the average is taken over users. There are two streams and four RF chains per user, and 48 and 12 TP RF chains for 12 and three users per cell, respectively.

the average interference power increases, and the ratio of the interference power in the baseline to that in the SLNR scheme is smaller in the 12-user case than in the three-user case (about 16 versus 140), since the interference power in the SLNR method approaches zero for the three-user case. Therefore, the corresponding SINR gap and hence the spectral efficiency gap is smaller in the 12-user case.

Moreover, it is observable by comparing Figs. 8.11(a) and 8.11(c), or Figs. 8.11(b) and 8.11(d), that for the majority (about 70%-90%) of the users, the spectral efficiency for the 200 m cell radius is lower than the 50 m cell radius for any of the proposed HBF schemes with the same user number per cell and the same transmit power per user, except for the peak spectral efficiency. This indicates that the effect of interference does not dictate the spectral efficiency, but rather coverage/SNR matters most, since the 200 m cell radius corresponds to weaker interference but

has lower spectral efficiency in most cases.

Next, the case where each TP communicates with each of its home-cell users via one and four data streams is considered, along with the two-stream-per-user case. As $N_{\mathrm{S}} = N_{\mathrm{R}}^{\mathrm{RF}}$ in the four-stream-per-user case, GMR is tractable hence is considered herein. Fig. 8.13 depicts the 10%, 50%, and 90% CDF points of spectral efficiency for both 3GPP and NYUSIM models for one-stream, two-stream, and four-stream cases with a cell radius of 50 m and three users per cell. As unveiled by Fig. 8.13, SLNR yields the highest spectral efficiency except for the 10% CDF point in Fig. 8.13(c), where GMR outperforms all the other HBF schemes since GMR intrinsically maximizes the received signal power hence is more efficient when the SNR is low. For the single-stream case in Fig. 8.13(a), RZF is inferior to the baseline at low and medium SNRs (represented by the 10% and 50% CDF points) but outperforms the baseline at high SNRs (represented by the 90% CDF point), because the RZF method demonstrated in Section 8.2 is more like ZF due to the small regulation factor in (8.25) (on the order of 10^{-16}), hence the RZF method is more efficient in high SNR regions since it focuses more on mitigating interference instead of noise. Interestingly, the eigenmode beamforming scheme in the baseline case exhibits better performance as the number of streams increases, especially for the 3GPP channel model, likely due to its capability to focus all the transmit power onto strongest eigenmodes, and that the third and fourth eigenmodes in the 3GPP model are mostly stronger than those in NYUSIM (see Fig. 6.4). Figs. 8.11 and 8.13 indicate that the spectral efficiency performance of the four HBF strategies proposed in this chapter depend upon the interference and SNR level. Furthermore, TP coordination (e.g., SLNR) generally provides higher spectral efficiency than the no-coordination case (e.g., up to 67% more spectral efficiency for the weakest 5%

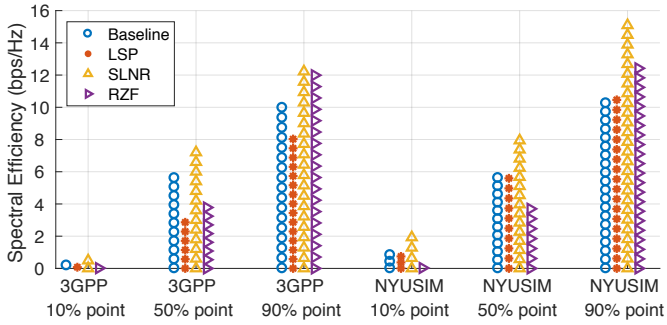

(a) One stream per user, 50 m cell radius, three users per cell

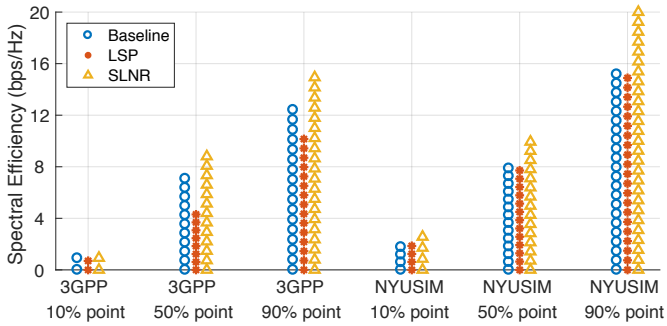

(b) Two streams per user, 50 m cell radius, three users per cell

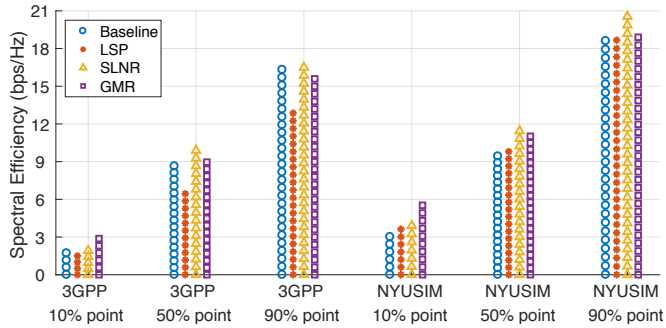

(c) Four streams per user, 50 m cell radius, three users per cell

Figure 8.13: CDFs of the per-user spectral efficiency of the three-cell multi-user MIMO system using the HBF algorithms proposed in this chapter for 3GPP [66] and NYUSIM [51] channel models for the cases of (a) one stream, (b) two streams, and (c) four streams per user. Baseline means no coordination among TPs, LSP denotes leakage-suppressing and signal-maximizing precoding, SLNR represents SLNR-based precoding, RZF refers to regularized zero-forcing for the single-stream-per-user case, and GMR represents generalized maximum ratio precoding. The users in each cell are distributed uniformly and randomly with T-R separation distances ranging from 10 m to 50 m.

of users), thus is worth using in mmWave multi-cell networks.

8.5 Concluding Remarks

This chapter focused on multi-cell multi-user communication in mmWave systems, derived analytical expressions for expected SINR and spectral efficiency for the single-stream-per-user case, and proposed and compared four HBF algorithms for the multi-stream-per-user case based on the assumption that base stations in different cells have full CSI and can exchange the CSI, but not the user data, among each other, such that they can take into account both intra-cell and inter-cell interference when designing precoding matrices.

Numerical results show that *the derived multi-cell analytical expected SINR and spectral efficiency have good accuracy and analytical tractability, and the analysis framework is applicable to any link SNR and channel model, as long as the necessary eigenvalue densities are known.* SLNR-based CoMP generally provides higher spectral efficiency than the no-coordination case (e.g., up to 67% higher spectral efficiency for the weakest 5% of users), thus is worth using in mmWave multi-cell networks. LSP shows minimal improvement over the baseline. Furthermore, the behaviors of the four proposed multi-stream HBF approaches are affected by the interference and SNR level, which are themselves influenced by the cell radius, the number of users per cell, and the number of streams per user. Specifically, *a smaller cell radius and fewer users per cell usually give rise to higher per-user spectral efficiency given a constant transmit power for each user. Moreover, it is critical to maintain coverage in mmWave systems when the cell radius is relatively large (e.g., 200 m).*

Chapter 9

Conclusions and Future Work

9.1 Thesis Summary

The technical report has focused on investigation and comparison of 5G channel models, and multi-cell multi-user analog-digital HBF approaches for mmWave MIMO systems. *Channel models have a penetrating impact on numerous aspects of wireless systems ranging from system design to performance evaluation, and different channel models can lead to substantially varied predictions on diverse channel performance metrics and hardware requirements, thus it is critical to develop and use an accurate channel model able to generate realistic temporal and spatial channel responses.* This technical report has presented a novel 5G channel simulator, NYUSIM, including its underlying channel model, the development of GUI, generation of output files, and its diverse applications. Then the technical report systematically compared the 3GPP and NYUSIM channel models, demonstrated their different evaluation results, and analyzed the reason for the discrepancies. Furthermore, *a general analytical framework has been provided to*

study the multi-cell spectral efficiency performance in the presence of both intra-cell and inter-cell interference. Particularly, *eigenvalue distributions for channels after RF precoding in a multi-cell multi-user system with a single stream per user are investigated for both signal and interference channels in NLOS environments, which has never done in the prior literature*, and tight analytical approximations of the expected per-user SINR, and expected per-cell sum spectral efficiency, under the condition of a bank of analog phase shifters for the analog precoding and RZF processing for digital beamforming. Numerical results for multi-cell multi-stream networks show that benefits of multi-cell coordination depend on the underlying channel model and the interference and noise levels.

9.2 Future Work

The work conducted throughout the technical report motivate further investigations in unexplored research fields directly related to the contents of the technical report, which are identified and discussed below:

- Currently NYUSIM only contains the channel models for UMi, UMa, and RMa scenarios, without indoor scenarios. It is worth developing a channel model for indoor environments, such as the indoor office, and integrating it into NYUSIM.

- The eigenvalue densities in the multi-cell multi-user systems are developed for *NLOS* channels only in this technical report (Chapter 8). It is worth investigating the eigenvalue densities for LOS and LOS-NLOS combined channels. As indicated in [242] and Chapter 8 of this technical report, LOS paths are likely to induce additional spatial correlation to eigenvalue densities,

thus the eigenvalue densities for LOS and LOS-NLOS combined channels can be obtained by adding extra correlation terms to the eigenvalue densities for NLOS channels.

- The eigenvalue densities in the multi-cell multi-user systems are developed for a transmission point antenna array with 256 elements and a single receive antenna in Chapter 8. If there is a change in the transmit or the receive dimension, then the analytical approach is still valid, but the approximated gamma distributed eigenvalue densities need to be re-fitted. This can be done using the eigenvalue density fitting method in Chapter 8.

- The analytical framework for the multi-cell system is done in Chapter 8 for the situation with a single stream per user. It will be valuable to explore the possibility of conducting similar analysis for the multi-stream-per-user case, although this is highly challenging since it involves an optimization problem with coupled variables and matrices.

Bibliography

[1] F. Boccardi *et al.*, "Five disruptive technology directions for 5G," *IEEE Communications Magazine*, vol. 52, pp. 74–80, Feb. 2014.

[2] T. S. Rappaport, S. Sun, R. Mayzus, H. Zhao, Y. Azar, K. Wang, G. N. Wong, J. K. Schulz, M. Samimi, and F. Gutierrez, "Millimeter wave mobile communications for 5G cellular: It will work!," *IEEE Access*, vol. 1, pp. 335–349, May 2013.

[3] Federal Communications Commission, "Spectrum frontiers rules identify," Jul. 2016.

[4] S. Rangan, T. S. Rappaport, and E. Erkip, "Millimeter-wave cellular wireless networks: potentials & challenges," in *IEEE Proceedings*, vol. 102, Mar. 2014.

[5] Cisco, "Cisco visual network index: Global mobile traffic forecast update," Tech. Rep. 20162021 white paper, Mar. 2017.

[6] M. Shafi, A. F. Molisch, P. J. Smith, T. Haustein, P. Zhu, P. D. Silva, F. Tufvesson, A. Benjebbour, and G. Wunder, "5G: A tutorial overview of standards, trials, challenges, deployment, and practice," *IEEE Journal on Selected Areas in Communications*, vol. 35, pp. 1201–1221, Jun. 2017.

[7] G. P. Fettweis, "The tactile internet: Applications and challenges," *IEEE Vehicular Technology Magazine*, vol. 9, pp. 64–70, Mar. 2014.

[8] J. G. Andrews, S. Buzzi, W. Choi, S. V. Hanly, A. Lozano, A. C. K. Soong, and J. C. Zhang, "What will 5G be?," *IEEE Journal on Selected Areas in Communications*, vol. 32, pp. 1065–1082, Jun. 2014.

[9] C. X. Wang, F. Haider, X. Gao, X. H. You, Y. Yang, D. Yuan, H. M. Aggoune, H. Haas, S. Fletcher, and E. Hepsaydir, "Cellular architecture and key technologies for 5G wireless communication networks," *IEEE Communications Magazine*, vol. 52, pp. 122–130, Feb. 2014.

[10] X. Ge, H. Cheng, M. Guizani, and T. Han, "5G wireless backhaul networks: challenges and research advances," *IEEE Network*, vol. 28, pp. 6–11, Nov. 2014.

[11] S. Hur, T. Kim, D. J. Love, J. V. Krogmeier, T. A. Thomas, and A. Ghosh, "Millimeter wave beamforming for wireless backhaul and access in small cell networks," *IEEE Transactions on Communications*, vol. 61, pp. 4391–4403, Oct. 2013.

[12] M. Rumney, "Testing 5G: Time to throw away the cables," *Microwave Journal*, Nov. 2016.

[13] T. L. Marzetta, "Noncooperative cellular wireless with unlimited numbers of base station antennas," *IEEE Transactions on Wireless Communications*, vol. 9, pp. 3590–3600, Nov. 2010.

[14] F. Rusek, D. Persson, B. K. Lau, E. G. Larsson, T. L. Marzetta, O. Edfors, and F. Tufvesson, "Scaling up MIMO: Opportunities and challenges with

very large arrays," *IEEE Signal Processing Magazine*, vol. 30, pp. 40–60, Jan. 2013.

[15] E. G. Larsson, O. Edfors, F. Tufvesson, and T. L. Marzetta, "Massive MIMO for next generation wireless systems," *IEEE Communications Magazine*, vol. 52, pp. 186–195, Feb. 2014.

[16] L. Lu, G. Y. Li, A. L. Swindlehurst, A. Ashikhmin, and R. Zhang, "An overview of massive MIMO: Benefits and challenges," *IEEE Journal of Selected Topics in Signal Processing*, vol. 8, pp. 742–758, Oct. 2014.

[17] T. L. Marzetta, "Massive MIMO: An introduction," *Bell Labs Technical Journal*, vol. 20, pp. 11–22, 2015.

[18] E. Bjrnson, E. G. Larsson, and T. L. Marzetta, "Massive MIMO: ten myths and one critical question," *IEEE Communications Magazine*, vol. 54, pp. 114–123, Feb. 2016.

[19] V. Jungnickel, K. Manolakis, W. Zirwas, B. Panzner, V. Braun, M. Lossow, M. Sternad, R. Apelfrojd, and T. Svensson, "The role of small cells, coordinated multipoint, and massive MIMO in 5G," *IEEE Communications Magazine*, vol. 52, pp. 44–51, May 2014.

[20] Federal Communications Commission, "Spectrum Frontiers Report and Order and Further Notice of Proposed Rulemaking: FCC16-89," July 2016.

[21] T. S. Rappaport, "Spectrum Frontiers: The New World of Millimeter-Wave Mobile Communication," *Invited keynote presentation, The Federal Communications Commission (FCC) Headquarters*, Mar. 10 2016.

[22] X. Cheng, B. Yu, L. Yang, J. Zhang, G. Liu, Y. Wu, and L. Wan, "Communicating in the real world: 3D MIMO," *IEEE Wireless Communications*, vol. 21, pp. 136–144, Aug. 2014.

[23] W. Roh, et al, "Millimeter-wave beamforming as an enabling technology for 5G cellular communications: theoretical feasibility and prototype results," *IEEE Communications Magazine*, vol. 52, pp. 106–113, Feb. 2014.

[24] S. Sun, T. S. Rappaport, R. W. Heath, A. Nix, and S. Rangan, "MIMO for millimeter-wave wireless communications: beamforming, spatial multiplexing, or both?," *IEEE Communications Magazine*, vol. 52, pp. 110–121, Dec. 2014.

[25] G. Xu, Y. Li, J. Yuan, R. Monroe, S. Rajagopal, S. Ramakrishna, Y. H. Nam, J. Y. Seol, J. Kim, M. M. U. Gul, A. Aziz, and J. Zhang, "Full dimension MIMO (FD-MIMO): Demonstrating commercial feasibility," *IEEE Journal on Selected Areas in Communications*, vol. 35, pp. 1876–1886, Aug. 2017.

[26] J. Zhang, Y. Zhang, Y. Yu, R. Xu, Q. Zheng, and P. Zhang, "3-D MIMO: How much does it meet our expectations observed from channel measurements?," *IEEE Journal on Selected Areas in Communications*, vol. 35, pp. 1887–1903, Aug. 2017.

[27] N. Bhushan, J. Li, D. Malladi, R. Gilmore, D. Brenner, A. Damnjanovic, R. T. Sukhavasi, C. Patel, and S. Geirhofer, "Network densification: the dominant theme for wireless evolution into 5G," *IEEE Communications Magazine*, vol. 52, pp. 82–89, Feb. 2014.

[28] K. Sundaresan, M. Y. Arslan, S. Singh, S. Rangarajan, and S. V. Krishnamurthy, "Fluidnet: A flexible cloud-based radio access network for small

cells," *IEEE/ACM Transactions on Networking*, vol. 24, pp. 915–928, Apr. 2016.

[29] P. K. Agyapong, M. Iwamura, D. Staehle, W. Kiess, and A. Benjebbour, "Design considerations for a 5G network architecture," *IEEE Communications Magazine*, vol. 52, pp. 65–75, Nov. 2014.

[30] J. G. Andrews, X. Zhang, G. D. Durgin, and A. K. Gupta, "Are we approaching the fundamental limits of wireless network densification?," *IEEE Communications Magazine*, vol. 54, pp. 184–190, Oct. 2016.

[31] S. Y. Lien, S. L. Shieh, Y. Huang, B. Su, Y. L. Hsu, and H. Y. Wei, "5G new radio: Waveform, frame structure, multiple access, and initial access," *IEEE Communications Magazine*, vol. 55, no. 6, pp. 64–71, 2017.

[32] P. Banelli, S. Buzzi, G. Colavolpe, A. Modenini, F. Rusek, and A. Ugolini, "Modulation formats and waveforms for 5G networks: Who will be the heir of OFDM?: An overview of alternative modulation schemes for improved spectral efficiency," *IEEE Signal Processing Magazine*, vol. 31, pp. 80–93, Nov. 2014.

[33] N. Michailow, M. Matthé, I. S. Gaspar, A. N. Caldevilla, L. L. Mendes, A. Festag, and G. Fettweis, "Generalized frequency division multiplexing for 5th generation cellular networks," *IEEE Transactions on Communications*, vol. 62, pp. 3045–3061, Sep. 2014.

[34] F.-L. Luo and C. Zhang, *Major 5G Waveform Candidates: Overview and Comparison*. Wiley-IEEE Press, 2016.

[35] C. J. Zhang *et al.*, "New waveforms for 5G networks," *IEEE Communications Magazine*, vol. 54, pp. 64–65, Nov. 2016.

[36] C. J. Hansen, "WiGiG: Multi-gigabit wireless communications in the 60 GHz band," *IEEE Wireless Communications*, vol. 18, pp. 6–7, Dec. 2011.

[37] ITU-R, "Technical feasibility of IMT in bands above 6 GHz," Tech. Rep. M 2376-0, July 2015.

[38] F. Giannetti, M. Luise, and R. Reggiannini, "Mobile and personal communications in the 60 GHz band: A survey," *Wireless Personal Communications*, vol. 10, no. 2, pp. 207–243, 1999.

[39] T. S. Rappaport, J. N. Murdock, and F. Gutierrez, "State of the art in 60-GHz integrated circuits and systems for wireless communications," *Proceedings of the IEEE*, vol. 99, pp. 1390–1436, Aug. 2011.

[40] F. Gutierrez, S. Agarwal, K. Parrish, and T. S. Rappaport, "On-chip integrated antenna structures in CMOS for 60 GHz WPAN systems," *IEEE Journal on Selected Areas in Communications*, vol. 27, pp. 1367–1378, October 2009.

[41] C. Park and T. S. Rappaport, "Short-range wireless communications for next-generation networks: UWB, 60 GHz millimeter-wave WPAN, and ZigBee," *IEEE Wireless Communications*, vol. 14, pp. 70–78, Aug. 2007.

[42] R. C. Daniels and R. W. Heath, "60 GHz wireless communications: emerging requirements and design recommendations," *IEEE Vehicular Technology Magazine*, vol. 2, pp. 41–50, Sept. 2007.

[43] A. Siligaris, O. Richard, B. Martineau, C. Mounet, F. Chaix, R. Ferragut, C. Dehos, J. Lanteri, L. Dussopt, S. D. Yamamoto, R. Pilard, P. Busson, A. Cathelin, D. Belot, and P. Vincent, "A 65-nm CMOS fully integrated transceiver module for 60-GHz wireless HD applications," *IEEE Journal of Solid-State Circuits*, vol. 46, pp. 3005–3017, Dec. 2011.

[44] S. Bronckers, A. Roc'h, and B. Smolders, "Wireless receiver architectures towards 5G: Where are we?," *IEEE Circuits and Systems Magazine*, vol. 17, pp. 6–16, thirdquarter 2017.

[45] J. B. Andersen, T. S. Rappaport, and S. Yoshida, "Propagation measurements and models for wireless communications channels," *IEEE Communications Magazine*, vol. 33, pp. 42–49, Jan. 1995.

[46] J. Medbo, P. Kyosti, K. Kusume, L. Raschkowski, K. Haneda, T. Jamsa, V. Nurmela, A. Roivainen, and J. Meinila, "Radio propagation modeling for 5G mobile and wireless communications," *IEEE Communications Magazine*, vol. 54, pp. 144–151, Jun. 2016.

[47] T. S. Rappaport, Y. Xing, G. R. MacCartney, Jr., A. F. Molisch, E. Mellios, and J. Zhang, "Overview of millimeter wave communications for fifth-generation (5G) wireless networks-with a focus on propagation models," *IEEE Transactions on Antennas and Propagation, Special Issue on 5G.* to appear Dec. 2017.

[48] T. S. Rappaport, S. Sun, and M. Shafi, "Investigation and comparison of 3GPP and NYUSIM channel models for 5G wireless communications," in

2017 IEEE 86th Vehicular Technology Conference (VTC-Fall), pp. 1–5, Sep. 2017.

[49] S. Sun, G. R. MacCartney, M. K. Samimi, and T. S. Rappaport, "Synthesizing omnidirectional antenna patterns, received power and path loss from directional antennas for 5G millimeter-wave communications," in *2015 IEEE Global Communications Conference (GLOBECOM)*, pp. 1–7, Dec. 2015.

[50] S. Sun, T. S. Rappaport, T. A. Thomas, A. Ghosh, H. C. Nguyen, I. Z. Kovcs, I. Rodriguez, O. Koymen, and A. Partyka, "Investigation of prediction accuracy, sensitivity, and parameter stability of large-scale propagation path loss models for 5G wireless communications," *IEEE Transactions on Vehicular Technology*, vol. 65, pp. 2843–2860, May 2016.

[51] S. Sun, G. R. MacCartney, and T. S. Rappaport, "A novel millimeter-wave channel simulator and applications for 5G wireless communications," in *2017 IEEE International Conference on Communications (ICC)*, May 2017.

[52] M. K. Samimi and T. S. Rappaport, "3-D millimeter-wave statistical channel model for 5G wireless system design," *IEEE Transactions on Microwave Theory and Techniques*, vol. 64, pp. 2207–2225, Jul. 2016.

[53] S. Sun, T. S. Rappaport, M. Shafi, P. Tang, J. Zhang, and P. J. Smith, "Propagation models and performance evaluation for 5G millimeter-wave bands," *submitted to IEEE Transactions on Vehicular Technology*, Jan. 2018.

[54] T. S. Rappaport, G. R. MacCartney, Jr., M. K. Samimi, and S. Sun, "Wideband millimeter-wave propagation measurements and channel models for

future wireless communication system design (Invited Paper)," *IEEE Transactions on Communications*, vol. 63, pp. 3029–3056, Sep. 2015.

[55] S. Sun and T. S. Rappaport, "Millimeter wave MIMO channel estimation based on adaptive compressed sensing," in *2017 IEEE International Conference on Communications Workshops (ICC Workshops)*, pp. 47–53, May 2017.

[56] S. Sun, T. S. Rappaport, M. Shafi, and H. Tataria, "Analytical framework of hybrid beamforming in multi-cell millimeter-wave systems," *submitted to IEEE Transactions on Wireless Communications*, Feb. 2018.

[57] S. Sun, T. S. Rappaport, and M. Shafi, "Hybrid beamforming for 5G millimeter-wave multi-cell networks," in *Proceedings of the IEEE Conference on Computer Communications Workshops (INFOCOM WKSHPS)*, Apr. 2018.

[58] G. R. MacCartney, Jr., S. Sun, T. S. Rappaport, Y. Xing, H. Yan, J. Koka, R. Wang, and D. Yu, "Millimeter wave wireless communications: New results for rural connectivity," in *Proceedings of the 5th Workshop on All Things Cellular: Operations, Applications and Challenges: in conjunction with MobiCom 2016*, ATC '16, (New York, NY, USA), pp. 31–36, ACM, Oct. 2016.

[59] G. R. MacCartney and T. S. Rappaport, "Rural macrocell path loss models for millimeter wave wireless communications," *IEEE Journal on Selected Areas in Communications*, vol. 35, pp. 1663–1677, Jul. 2017.

[60] S. Nie, G. R. MacCartney, Jr., S. Sun, and T. S. Rappaport, "72 GHz millimeter wave indoor measurements for wireless and backhaul communications,"

in *2013 IEEE 24th International Symposium on Personal Indoor and Mobile Radio Communications (PIMRC)*, pp. 2429–2433, Sep. 2013.

[61] G. R. MacCartney, T. S. Rappaport, S. Sun, and S. Deng, "Indoor office wideband millimeter-wave propagation measurements and channel models at 28 and 73 GHz for ultra-dense 5G wireless networks," *IEEE Access*, vol. 3, pp. 2388–2424, Oct. 2015.

[62] T. S. Rappaport, G. R. MacCartney, S. Sun, H. Yan, and S. Deng, "Small-scale, local area, and transitional millimeter wave propagation for 5G communications," *IEEE Transactions on Antennas and Propagation*, vol. 65, pp. 6474–6490, Dec. 2017.

[63] J. Ryan, G. R. MacCartney, and T. S. Rappaport, "Indoor office wideband penetration loss measurements at 73 GHz," in *2017 IEEE International Conference on Communications Workshops (ICC Workshops)*, pp. 228–233, May 2017.

[64] A. F. Molisch, *Wireless communications*, vol. 34. John Wiley & Sons, 2012.

[65] A. Goldsmith, *Wireless communications*. Cambridge university press, 2005.

[66] 3GPP, "Study on channel model for frequencies from 0.5 to 100 GHz," TR 38.901 V14.3.0, 3rd Generation Partnership Project (3GPP), Dec. 2017.

[67] T. S. Rappaport, *Wireless Communications: Principles and Practice*. Upper Saddle River, NJ: Prentice Hall, second ed., 2002.

[68] S. Sun, H. Yan, G. R. MacCartney, Jr., and T. S. Rappaport, "Millimeter wave small-scale spatial statistics in an urban microcell scenario," in *2017*

IEEE International Conference on Communications (ICC), pp. 1–7, May 2017.

[69] M. K. Samimi, G. R. MacCartney, S. Sun, and T. S. Rappaport, "28 GHz millimeter-wave ultrawideband small-scale fading models in wireless channels," in *2016 IEEE 83rd Vehicular Technology Conference (VTC2016-Spring)*, pp. 1–6, May 2016.

[70] M. K. Samimi, S. Sun, and T. S. Rappaport, "MIMO channel modeling and capacity analysis for 5G millimeter-wave wireless systems," in *2016 10th European Conference on Antennas and Propagation (EuCAP)*, pp. 1–5, Apr. 2016.

[71] M. R. Akdeniz, Y. Liu, M. K. Samimi, S. Sun, S. Rangan, T. S. Rappaport, and E. Erkip, "Millimeter wave channel modeling and cellular capacity evaluation," *IEEE Journal on Selected Areas in Communications*, vol. 32, pp. 1164–1179, Jun. 2014.

[72] J. Ko, Y.-J. Cho, S. Hur, T. Kim, J. Park, A. F. Molisch, K. Haneda, M. Peter, D.-J. Park, and D.-H. Cho, "Millimeter-wave channel measurements and analysis for statistical spatial channel model in in-building and urban environments at 28 ghz," *IEEE Transactions on Wireless Communications*, 2017.

[73] S. Hur, S. Baek, B. Kim, Y. Chang, A. F. Molisch, T. S. Rappaport, K. Haneda, and J. Park, "Proposal on millimeter-wave channel modeling for 5G cellular system," *IEEE Journal of Selected Topics in Signal Processing*, vol. 10, pp. 454–469, Apr. 2016.

[74] H. L. Bertoni, *Radio propagation for modern wireless systems*. Pearson Education, 1999.

[75] I. Recommendation, "Itu-r m. 1225,," *Guidelines for evaluation of radio transmission technologies for IMT-2000*, 2000.

[76] ITU-R, "M. 2135: guidelines for evaluation of radio interface technologies for imt-advanced," 2008.

[77] F. Huang, L. Tian, Y. Zheng, and J. Zhang, "Propagation characteristics of indoor radio channel from 3.5 ghz to 28 ghz," in *Vehicular Technology Conference (VTC-Fall), 2016 IEEE 84th*, pp. 1–5, IEEE, 2016.

[78] G. R. Maccartney, T. S. Rappaport, M. K. Samimi, and S. Sun, "Millimeter-wave omnidirectional path loss data for small cell 5G channel modeling," *IEEE Access*, vol. 3, pp. 1573–1580, 2015.

[79] S. Sun, G. R. MacCartney, and T. S. Rappaport, "Millimeter-wave distance-dependent large-scale propagation measurements and path loss models for outdoor and indoor 5G systems," in *2016 10th European Conference on Antennas and Propagation (EuCAP)*, pp. 1–5, Apr. 2016.

[80] S. Sun, T. A. Thomas, T. S. Rappaport, H. Nguyen, I. Z. Kovacs, and I. Rodriguez, "Path loss, shadow fading, and line-of-sight probability models for 5G urban macro-cellular scenarios," in *2015 IEEE Globecom Workshops (GC Wkshps)*, pp. 1–7, Dec. 2015.

[81] K. Haneda, N. Omaki, T. Imai, L. Raschkowski, M. Peter, and A. Roivainen, "Frequency-agile pathloss models for urban street canyons," *IEEE Transactions on Antennas and Propagation*, vol. 64, pp. 1941–1951, May 2016.

[82] T. A. Thomas, M. Rybakowski, S. Sun, T. S. Rappaport, H. Nguyen, I. Z. Kovacs, and I. Rodriguez, "A prediction study of path loss models from 2-73.5 GHz in an urban-macro environment," in *2016 IEEE 83rd Vehicular Technology Conference (VTC Spring)*, pp. 1–5, May 2016.

[83] S. O. Rice, "Statistical properties of a sine wave plus random noise," *Bell Labs Technical Journal*, vol. 27, no. 1, pp. 109–157, 1948.

[84] A. A. Saleh and R. Valenzuela, "A statistical model for indoor multipath propagation," *IEEE Journal on selected areas in communications*, vol. 5, no. 2, pp. 128–137, 1987.

[85] A. F. Molisch and F. Tufvesson, "Propagation channel models for next-generation wireless communications systems," *IEICE Transactions on Communications*, vol. 97, no. 10, pp. 2022–2034, 2014.

[86] International Telecommunications Union (ITU), "Guidelines for evaluation of radio interface technologies for IMT-2020," REP. Revision 2 to Document 5D/TEMP/347-E, Niagara Falls, Canada, Jun. 2017.

[87] A. Alkhateeb and R. W. Heath, "Frequency selective hybrid precoding for limited feedback millimeter wave systems," *IEEE Transactions on Communications*, vol. 64, pp. 1801–1818, May 2016.

[88] E. K. Smith, "Centimeter and millimeter wave attenuation and brightness temperature due to atmospheric oxygen and water vapor," *Radio Science*, vol. 17, no. 06, pp. 1455–1464, 1982.

[89] H. J. Liebe, "An updated model for millimeter wave propagation in moist air," *Radio Science*, vol. 20, no. 5, pp. 1069–1089, 1985.

[90] ITU-R, "Specific attenuation model for rain for use in prediction methods, propagation in non-ionized media," Tech. Rep. P.838-3, 2005.

[91] ITU-R, "Attenuation by atmospheric gases," Tech. Rep. P.676-8, 2009.

[92] H. Zhao, R. Mayzus, S. Sun, M. Samimi, J. K. Schulz, Y. Azar, K. Wang, G. N. Wong, F. Gutierrez, and T. S. Rappaport, "28 GHz millimeter wave cellular communication measurements for reflection and penetration loss in and around buildings in new york city," in *2013 IEEE International Conference on Communications (ICC)*, pp. 5163–5167, Jun. 2013.

[93] X. Chen, L. Tian, P. Tang, and J. Zhang, "Modelling of human body shadowing based on 28 ghz indoor measurement results," in *Vehicular Technology Conference (VTC-Fall), 2016 IEEE 84th*, pp. 1–5, IEEE, 2016.

[94] WP5D, ITUR, "Framework and overall objectives of the future development of imt for 2020 and beyond," *Draft New Recommendation ITU*, 2015.

[95] S. Han, I. Chih-Lin, Z. Xu, and C. Rowell, "Large-scale antenna systems with hybrid analog and digital beamforming for millimeter wave 5G," *IEEE Communications Magazine*, vol. 53, pp. 186–194, Jan. 2015.

[96] Y. Zeng and R. Zhang, "Millimeter wave MIMO with lens antenna array: A new path division multiplexing paradigm," *IEEE Transactions on Communications*, vol. 64, pp. 1557–1571, Apr. 2016.

[97] Y. Wang, Z. Shi, L. Huang, Z. Yu, and C. Cao, "An extension of spatial channel model with spatial consistency," in *Vehicular Technology Conference (VTC-Fall), 2016 IEEE 84th*, pp. 1–5, IEEE, 2016.

[98] Y. Tan, C. X. Wang, J. . Nielsen, and G. F. Pedersen, "Comparison of stationarity regions for wireless channels from 2 GHz to 30 GHz," in *2017 13th International Wireless Communications and Mobile Computing Conference (IWCMC)*, pp. 647–652, Jun. 2017.

[99] X. Yin, C. Ling, and M.-D. Kim, "Experimental multipath-cluster characteristics of 28-ghz propagation channel," *IEEE Access*, vol. 3, pp. 3138–3150, 2015.

[100] S. Y. Seidel, K. Takamizawa, and T. S. Rappaport, "Application of second-order statistics for an indoor radio channel model," in *IEEE 39th Vehicular Technology Conference*, pp. 888–892 vol.2, May 1989.

[101] S. Jaeckel, L. Raschkowski, K. Brner, and L. Thiele, "QuaDRiGa: A 3-D multi-cell channel model with time evolution for enabling virtual field trials," *IEEE Transactions on Antennas and Propagation*, vol. 62, pp. 3242–3256, Jun. 2014.

[102] Y. Yu, Y. Liu, W. J. Lu, and H. B. Zhu, "Propagation model and channel simulator under indoor stair environment for machine-to-machine applications," in *2015 Asia-Pacific Microwave Conference*, vol. 2, pp. 1–3, Dec. 2015.

[103] T. S. Rappaport, S. Y. Seidel, and K. Takamizawa, "Statistical channel impulse response models for factory and open plan building radio communicate system design," *IEEE Transactions on Communications*, vol. 39, pp. 794–807, May 1991.

[104] Wireless Valley Communications, Inc. *SMRCIM Plus 4.0 (Simulation of Mobile Radio Channel Impulse Response Models) Users Manual*, Aug. 1999.

[105] V. K. Rajendran, J. N. Murdock, A. Duran, and T. S. Rappaport, "Concepts and implementation of a semantic web archiving and simulation system for rf propagation measurements," in *2011 IEEE Vehicular Technology Conference (VTC Fall)*, pp. 1–5, Sep. 2011.

[106] V. Fung, T. S. Rappaport, and B. Thoma, "Bit error simulation for pi/4 DQPSK mobile radio communications using two-ray and measurement-based impulse response models," *IEEE Journal on Selected Areas in Communications*, vol. 11, pp. 393–405, Apr. 1993.

[107] J. I. Smith, "A computer generated multipath fading simulation for mobile radio," *IEEE Transactions on Vehicular Technology*, vol. 24, pp. 39–40, Aug. 1975.

[108] R. H. Clarke, "A statistical theory of mobile-radio reception," *The Bell System Technical Journal*, vol. 47, pp. 957–1000, Jul. 1968.

[109] T. P. Krauss and M. D. Zoltowski, "Oversampling diversity versus dual antenna diversity for chip-level equalization on cdma downlink," in *Proceedings of the 2000 IEEE Sensor Array and Multichannel Signal Processing Workshop. SAM 2000 (Cat. No.00EX410)*, pp. 47–51, 2000.

[110] L. Liu, C. Oestges, J. Poutanen, K. Haneda, P. Vainikainen, F. Quitin, F. Tufvesson, and P. D. Doncker, "The COST 2100 MIMO channel model," *IEEE Wireless Communications*, vol. 19, pp. 92–99, Dec. 2012.

[111] A. F. Molisch, H. Asplund, R. Heddergott, M. Steinbauer, and T. Zwick, "The COST259 directional channel model-part i: Overview and methodology,"

IEEE Transactions on Wireless Communications, vol. 5, pp. 3421–3433, Dec. 2006.

[112] V. Nurmela *et al.*, "Deliverable D1.4: METIS Channel Models," Tech. Rep. ICT-317669, METIS, Feb. 2015.

[113] R. J. Weiler *et al.*, "Quasi-deterministic millimeter-wave channel models in MiWEBA," *EURASIP Journal on Wireless Communications and Networking*, Dec. 2016.

[114] WINNER II D1.1.2 V1.2, "WINNER II Channel Models," Tech. Rep. IST-4-027756, Sep. 2007.

[115] "Test environments and channel models," tech. rep., Annex 1 to section 5.11, chapter 5, Doc 5D/Temp/238, 17, Nov. 2016.

[116] B. Mondal, T. A. Thomas, E. Visotsky, F. W. Vook, A. Ghosh, Y. h. Nam, Y. Li, J. Zhang, M. Zhang, Q. Luo, Y. Kakishima, and K. Kitao, "3D channel model in 3GPP," *IEEE Communications Magazine*, vol. 53, pp. 16–23, Mar. 2015.

[117] O. E. Ayach, S. Rajagopal, S. Abu-Surra, Z. Pi, and R. W. Heath, "Spatially sparse precoding in millimeter wave mimo systems," *IEEE Transactions on Wireless Communications*, vol. 13, pp. 1499–1513, Mar. 2014.

[118] R. W. Heath, N. Gonzlez-Prelcic, S. Rangan, W. Roh, and A. M. Sayeed, "An overview of signal processing techniques for millimeter wave MIMO systems," *IEEE Journal of Selected Topics in Signal Processing*, vol. 10, pp. 436–453, Apr. 2016.

[119] A. Alkhateeb, O. E. Ayach, G. Leus, and R. W. Heath, "Channel estimation and hybrid precoding for millimeter wave cellular systems," *IEEE Journal of Selected Topics in Signal Processing*, vol. 8, pp. 831–846, Oct. 2014.

[120] E. J. Candes and T. Tao, "Decoding by linear programming," *IEEE Transactions on Information Theory*, vol. 51, pp. 4203–4215, Dec. 2005.

[121] D. E. Berraki, S. M. D. Armour, and A. R. Nix, "Application of compressive sensing in sparse spatial channel recovery for beamforming in mmwave outdoor systems," in *2014 IEEE Wireless Communications and Networking Conference (WCNC)*, pp. 887–892, Apr. 2014.

[122] A. Alkhateeb, G. Leus, and R. W. Heath, "Limited feedback hybrid precoding for multi-user millimeter wave systems," *IEEE Transactions on Wireless Communications*, vol. 14, pp. 6481–6494, Nov. 2015.

[123] W. U. Bajwa, J. Haupt, A. M. Sayeed, and R. Nowak, "Compressed channel sensing: A new approach to estimating sparse multipath channels," *Proceedings of the IEEE*, vol. 98, pp. 1058–1076, Jun. 2010.

[124] G. Destino, M. Juntti, and S. Nagaraj, "Leveraging sparsity into massive MIMO channel estimation with the adaptive-LASSO," in *2015 IEEE Global Conference on Signal and Information Processing (GlobalSIP)*, pp. 166–170, Dec. 2015.

[125] S. Malla and G. Abreu, "Channel estimation in millimeter wave MIMO systems: Sparsity enhancement via reweighting," in *2016 International Symposium on Wireless Communication Systems (ISWCS)*, pp. 230–234, Sep. 2016.

[126] Z. Gao, L. Dai, and Z. Wang, "Channel estimation for mmwave massive MIMO based access and backhaul in ultra-dense network," in *2016 IEEE International Conference on Communications (ICC)*, pp. 1–6, May 2016.

[127] R. Zhang, H. Zhao, S. Jia, and C. Shan, "Joint channel estimation algorithm based on structured compressed sensing for fdd multi-user massive mimo," in *2016 IEEE 13th International Conference on Signal Processing (ICSP)*, pp. 1202–1207, Nov. 2016.

[128] P. N. Jayanthi and S. Ravishankar, "Sparse channel estimation for mimo-ofdm systems using compressed sensing," in *2016 IEEE International Conference on Recent Trends in Electronics, Information Communication Technology (RTEICT)*, pp. 1060–1064, May 2016.

[129] Z. Marzi, D. Ramasamy, and U. Madhow, "Compressive channel estimation and tracking for large arrays in mm-wave picocells," *IEEE Journal of Selected Topics in Signal Processing*, vol. 10, pp. 514–527, Apr. 2016.

[130] Z. Gao, L. Dai, Z. Wang, and S. Chen, "Spatially common sparsity based adaptive channel estimation and feedback for fdd massive mimo," *IEEE Transactions on Signal Processing*, vol. 63, pp. 6169–6183, Dec. 2015.

[131] S. Park and R. W. Heath, "Spatial channel covariance estimation for mmwave hybrid mimo architecture," in *2016 50th Asilomar Conference on Signals, Systems and Computers*, pp. 1424–1428, Nov. 2016.

[132] J. Mo, P. Schniter, N. G. Prelcic, and R. W. Heath, "Channel estimation in millimeter wave MIMO systems with one-bit quantization," in *2014 48th*

Asilomar Conference on Signals, Systems and Computers, pp. 957–961, Nov. 2014.

[133] J. Rodrguez-Fernndez, N. Gonzlez-Prelcic, and R. W. Heath, "Channel estimation in mixed hybrid-low resolution mimo architectures for mmwave communication," in *2016 50th Asilomar Conference on Signals, Systems and Computers*, pp. 768–773, Nov. 2016.

[134] J. Choi, J. Mo, and R. W. Heath, "Near maximum-likelihood detector and channel estimator for uplink multiuser massive MIMO systems with one-bit ADCs," *IEEE Transactions on Communications*, vol. 64, pp. 2005–2018, May 2016.

[135] P. Schniter and A. M. Sayeed, "A sparseness-preserving virtual MIMO channel model," in *Proc. Conf. on Information Sciences and Systems*, pp. 36–41, Mar. 2004.

[136] H. Huang, K. Liu, R. Wen, Y. Wang, and G. Wang, "Joint channel estimation and beamforming for millimeter wave cellular system," in *2015 IEEE Global Communications Conference (GLOBECOM)*, pp. 1–6, Dec. 2015.

[137] P. A. Eliasi, S. Rangan, and T. S. Rappaport, "Low-rank spatial channel estimation for millimeter wave cellular systems," *IEEE Transactions on Wireless Communications*, vol. PP, no. 99, pp. 1–1, 2017.

[138] Y. Han and J. Lee, "Asymmetric channel estimation for multi-user millimeter wave communications," in *2016 International Conference on Information and Communication Technology Convergence (ICTC)*, pp. 4–6, Oct. 2016.

[139] I. Chafaa and M. Djeddou, "Improved channel estimation in mmwave communication system," in *2017 Seminar on Detection Systems Architectures and Technologies (DAT)*, pp. 1–5, Feb. 2017.

[140] P. Schniter and A. Sayeed, "Channel estimation and precoder design for millimeter-wave communications: The sparse way," in *2014 48th Asilomar Conference on Signals, Systems and Computers*, pp. 273–277, Nov. 2014.

[141] A. M. Sayeed, "Deconstructing multiantenna fading channels," *IEEE Transactions on Signal Processing*, vol. 50, pp. 2563–2579, Oct. 2002.

[142] C. Huang, L. Liu, C. Yuen, and S. Sun, "A LSE and sparse message passing-based channel estimation for mmwave mimo systems," in *2016 IEEE Globecom Workshops (GC Wkshps)*, pp. 1–6, Dec. 2016.

[143] K. N. R. S. V. Prasad, E. Hossain, and V. K. Bhargava, "Energy efficiency in massive MIMO-based 5G networks: Opportunities and challenges," *IEEE Wireless Communications*, vol. 24, no. 3, pp. 86–94, 2017.

[144] B. D. V. Veen and K. M. Buckley, "Beamforming: a versatile approach to spatial filtering," *IEEE ASSP Magazine*, vol. 5, pp. 4–24, Apr. 1988.

[145] P. Xia, R. W. Heath, and N. Gonzalez-Prelcic, "Robust analog precoding designs for millimeter wave MIMO transceivers with frequency and time division duplexing," *IEEE Transactions on Communications*, vol. 64, pp. 4622–4634, Nov. 2016.

[146] X. Zhang, A. F. Molisch, and S.-Y. Kung, "Variable-phase-shift-based rf-baseband codesign for MIMO antenna selection," *IEEE Transactions on Signal Processing*, vol. 53, pp. 4091–4103, Nov. 2005.

[147] P. Sudarshan, N. B. Mehta, A. F. Molisch, and J. Zhang, "Channel statistics-based RF pre-processing with antenna selection," *IEEE Transactions on Wireless Communications*, vol. 5, pp. 3501–3511, Dec. 2006.

[148] X. Yu, J. C. Shen, J. Zhang, and K. B. Letaief, "Alternating minimization algorithms for hybrid precoding in millimeter wave MIMO systems," *IEEE Journal of Selected Topics in Signal Processing*, vol. 10, pp. 485–500, Apr. 2016.

[149] Z. Li, S. Han, and A. F. Molisch, "Hybrid beamforming design for millimeter-wave multi-user massive MIMO downlink," in *2016 IEEE International Conference on Communications (ICC)*, pp. 1–6, May 2016.

[150] R. Mndez-Rial, C. Rusu, N. Gonzlez-Prelcic, A. Alkhateeb, and R. W. Heath, "Hybrid MIMO architectures for millimeter wave communications: Phase shifters or switches?," *IEEE Access*, vol. 4, pp. 247–267, 2016.

[151] X. Gao, L. Dai, S. Han, C. L. I, and R. W. Heath, "Energy-efficient hybrid analog and digital precoding for mmwave MIMO systems with large antenna arrays," *IEEE Journal on Selected Areas in Communications*, vol. 34, pp. 998–1009, Apr. 2016.

[152] M. N. Kulkarni, A. Ghosh, and J. G. Andrews, "A comparison of MIMO techniques in downlink millimeter wave cellular networks with hybrid beamforming," *IEEE Transactions on Communications*, vol. 64, pp. 1952–1967, May 2016.

[153] H. Tataria, P. J. Smith, and P. A. Dmochowski, "On the general analysis of coordinated regularized zero-forcing precoding: An application to two-

tier small-cell networks," *IEEE Transactions on Communications*, vol. 65, pp. 3133–3150, Jul. 2017.

[154] M. Costa, "Writing on dirty paper," *IEEE Transactions on Information Theory*, vol. 29, pp. 439–441, May 1983.

[155] X. Gao, O. Edfors, F. Rusek, and F. Tufvesson, "Linear pre-coding performance in measured very-large MIMO channels," in *2011 IEEE Vehicular Technology Conference (VTC Fall)*, pp. 1–5, Sep. 2011.

[156] C. B. Peel *et al.*, "A vector-perturbation technique for near-capacity multiantenna multiuser communication-part I: channel inversion and regularization," *IEEE Transactions on Communications*, vol. 53, pp. 195–202, Jan. 2005.

[157] M. Sadek, A. Tarighat, and A. H. Sayed, "A leakage-based precoding scheme for downlink multi-user MIMO channels," *IEEE Transactions on Wireless Communications*, vol. 6, pp. 1711–1721, May 2007.

[158] Q. H. Spencer and M. Haardt, "Capacity and downlink transmission algorithms for a multi-user mimo channel," in *2002 Conference Record of the Thirty-Sixth Asilomar Conference on Signals, Systems and Computers*, vol. 2, pp. 1384–1388, Nov. 2002.

[159] Q. H. Spencer, A. L. Swindlehurst, and M. Haardt, "Zero-forcing methods for downlink spatial multiplexing in multiuser MIMO channels," *IEEE Transactions on Signal Processing*, vol. 52, pp. 461–471, Feb. 2004.

[160] R. Mendez-Rial, C. Rusu, N. Gonzlez-Prelcic, A. Alkhateeb, and R. W. Heath, "Hybrid MIMO architectures for millimeter wave communications: Phase shifters or switches?," *IEEE Access*, vol. 4, pp. 247–267, 2016.

[161] 3GPP, "Coordinated multi-point operation for LTE physical layer aspects," TR 36.819 V11.2.0, 3rd Generation Partnership Project (3GPP), Sep. 2013.

[162] A. F. Molisch, V. Ratnam, S. Han, Z. Li, S. L. H. Nguyen, L. Li, and K. Haneda, "Hybrid beamforming for massive MIMO — A survey," *arXiv:1609.05078*, Sep. 2016.

[163] L. Dai, X. Gao, J. Quan, S. Han, and C. L. I, "Near-optimal hybrid analog and digital precoding for downlink mmwave massive mimo systems," in *2015 IEEE International Conference on Communications (ICC)*, pp. 1334–1339, Jun. 2015.

[164] S. Park, A. Alkhateeb, and R. Heath, "Dynamic subarrays for hybrid precoding in wideband mmWave MIMO systems," *IEEE Transactions on Wireless Communications*, vol. PP, no. 99, pp. 1–1, 2017.

[165] H. Seleem, A. Sulyman, and A. Alsanie, "Hybrid precoding-beamforming design with hadamard rf codebook for mmWave large-scale MIMO systems," *IEEE Access*, vol. PP, no. 99, pp. 1–1, 2017.

[166] A. Adhikary, E. A. Safadi, M. K. Samimi, R. Wang, G. Caire, T. S. Rappaport, and A. F. Molisch, "Joint spatial division and multiplexing for mm-wave channels," *IEEE Journal on Selected Areas in Communications*, vol. 32, pp. 1239–1255, Jun. 2014.

[167] A. Adhikary, J. Nam, J. Y. Ahn, and G. Caire, "Joint spatial division and multiplexing — the large-scale array regime," *IEEE Transactions on Information Theory*, vol. 59, pp. 6441–6463, Oct. 2013.

[168] T. S. Rappaport, R. W. Heath, Jr., R. C. Daniels, and J. N. Murdock, *Millimeter Wave Wireless Communications*. Pearson/Prentice Hall 2015.

[169] X. Yu, J. Zhang, and K. B. Letaief, "Alternating minimization for hybrid precoding in multiuser ofdm mmwave systems," in *2016 50th Asilomar Conference on Signals, Systems and Computers*, pp. 281–285, Nov. 2016.

[170] J. Noh, T. Kim, J. Y. Seol, and C. Lee, "Zero-forcing based hybrid beamforming for multi-user millimeter wave systems," *IET Communications*, vol. 10, no. 18, pp. 2670–2677, 2016.

[171] N. Song, H. Sun, and T. Yang, "Coordinated hybrid beamforming for millimeter wave multi-user massive mimo systems," in *2016 IEEE Global Communications Conference (GLOBECOM)*, pp. 1–6, Dec. 2016.

[172] G. Kwon and H. Park, "A joint scheduling and millimeter wave hybrid beamforming system with partial side information," in *2016 IEEE International Conference on Communications (ICC)*, pp. 1–6, May 2016.

[173] F. Sohrabi and W. Yu, "Hybrid digital and analog beamforming design for large-scale antenna arrays," *IEEE Journal of Selected Topics in Signal Processing*, vol. 10, pp. 501–513, Apr. 2016.

[174] G. Caire, N. Jindal, M. Kobayashi, and N. Ravindran, "Multiuser mimo achievable rates with downlink training and channel state feedback," *IEEE Transactions on Information Theory*, vol. 56, pp. 2845–2866, Jun. 2010.

[175] R. Mndez-Rial, N. Gonzlez-Prelcic, and R. W. Heath, "Adaptive hybrid precoding and combining in mmwave multiuser mimo systems based on

compressed covariance estimation," in *2015 IEEE 6th International Workshop on Computational Advances in Multi-Sensor Adaptive Processing (CAMSAP)*, pp. 213–216, Dec. 2015.

[176] L. F. Lin, W. H. Chung, H. J. Chen, and T. S. Lee, "Energy efficient hybrid precoding for multi-user massive mimo systems using low-resolution adcs," in *2016 IEEE International Workshop on Signal Processing Systems (SiPS)*, pp. 115–120, Oct. 2016.

[177] D. Gesbert, S. Hanly, H. Huang, S. S. Shitz, O. Simeone, and W. Yu, "Multi-cell mimo cooperative networks: A new look at interference," *IEEE Journal on Selected Areas in Communications*, vol. 28, pp. 1380–1408, Dec. 2010.

[178] N. Seifi, R. W. Heath, M. Coldrey, and T. Svensson, "Adaptive multicell 3-d beamforming in multiantenna cellular networks," *IEEE Transactions on Vehicular Technology*, vol. 65, pp. 6217–6231, Aug. 2016.

[179] H. V. Balan, R. Rogalin, A. Michaloliakos, K. Psounis, and G. Caire, "Airsync: Enabling distributed multiuser MIMO with full spatial multiplexing," *IEEE/ACM Transactions on Networking*, vol. 21, pp. 1681–1695, Dec. 2013.

[180] A. Michaloliakos, W. C. Ao, and K. Psounis, "Joint user-beam selection for hybrid beamforming in asynchronously coordinated multi-cell networks," in *2016 Information Theory and Applications Workshop (ITA)*, pp. 1–10, Jan. 2016.

[181] S. Wang, Y. Zhao, S. Zhu, and G. Chen, "SLNR based cascaded interference align precoding in CoMP," in *11th International Conference on Wireless*

Communications, Networking and Mobile Computing (WiCOM 2015), pp. 1–6, Sep. 2015.

[182] T. S. Rappaport, W. Roh, and C. Kyungwhoon, "Smart antennas could open up new spectrum for 5G," *IEEE Spectrum*, Aug. 2014.

[183] G. R. MacCartney, Jr. and T. S. Rappaport, "73 GHz millimeter wave propagation measurements for outdoor urban mobile and backhaul communications in New York City," in *2014 IEEE International Conference on Communications (ICC)*, pp. 4862–4867, June 2014.

[184] T. S. Rappaport, F. Gutierrez, E. Ben-Dor, J. N. Murdock, Y. Qiao, and J. I. Tamir, "Broadband millimeter-wave propagation measurements and models using adaptive-beam antennas for outdoor urban cellular communications," *IEEE Transactions on Antennas and Propagation*, vol. 61, pp. 1850–1859, Apr. 2013.

[185] H. Zhou, "Phased array for millimeter-wave mobile handset," in *2014 IEEE Antennas and Propagation Society International Symposium (APSURSI)*, pp. 933–934, July 2014.

[186] S. Hur, et al, "Synchronous channel sounder using horn antenna and indoor measurements on 28 GHz," in *2014 IEEE International Black Sea Conference on Communications and Networking (BlackSeaCom)*, pp. 83–87, May 2014.

[187] S. Rajagopal, S. Abu-Surra, and M. Malmirchegini, "Channel feasibility for outdoor non-line-of-sight mmwave mobile communication," in *Vehicular Technology Conference (VTC Fall), 2012 IEEE*, pp. 1–6, Sept. 2012.

[188] G. R. MacCartney, Jr., M. K. Samimi, and T. S. Rappaport, "Omnidirectional path loss models at 28 GHz and 73 GHz in New York City," in *2014 IEEE International Symposium on Personal, Indoor and Mobile Radio Communications*, Sept. 2014.

[189] Y. Azar, G. N. Wong, K. Wang, R. Mayzus, J. K. Schulz, H. Zhao, F. Gutierrez, Jr., D. Hwang, and T. S. Rappaport, "28 GHz propagation measurements for outdoor cellular communications using steerable beam antennas in New York City," in *2013 IEEE International Conference on Communications (ICC)*, pp. 5143–5147, June 2013.

[190] "Far field radiation from electric current."

[191] 3GPP TR 25.996, "Spatial channel model for multiple input multiple output (MIMO) simulations," Sep. 2012.

[192] S. Sun, T. S. Rappaport, S. Rangan, T. A. Thomas, A. Ghosh, I. Z. Kovacs, I. Rodriguez, O. Koymen, A. Partyka, and J. Jarvelainen, "Propagation path loss models for 5G urban micro- and macro-cellular scenarios," in *2016 IEEE 83rd Vehicular Technology Conference (VTC Spring)*, pp. 1–6, May 2016.

[193] 3GPP TR 36.873, V12.1.0, "Study on 3D channel model for LTE (release 12)," Mar. 2015.

[194] G. R. MacCartney, Jr. *et al.*, "Path loss models for 5G millimeter wave propagation channels in urban microcells," in *IEEE Global Communications Conference (GLOBECOM)*, pp. 3948–3953, Dec. 2013.

[195] M. Hata, "Empirical formula for propagation loss in land mobile radio services," *IEEE Transactions on Vehicular Technology*, vol. 29, pp. 317–325, Aug. 1980.

[196] M. N. Abdallah, W. Dyab, T. K. Sarkar, M. V. S. N. Prasad, C. S. Misra, A. Lamparez, M. Salazar-Palma, and S. W. Ting, "Further validation of an electromagnetic macro model for analysis of propagation path loss in cellular networks using measured drive test data," in *Antennas and Propagation in Wireless Communications (APWC), 2014 IEEE-APS Topical Conference on*, pp. 429–429, 2014.

[197] A. Alvarez, G. Valera, M. Lobeira, R. P. Torres, and J. L. Garcia, "Ultra wideband channel model for indoor environments," *Journal of Communications and Networks*, vol. 5, pp. 309–318, Dec. 2003.

[198] E. Ben-Dor, T. S. Rappaport, Y. Qiao, and S. J. Lauffenburger, "Millimeter-wave 60 GHz outdoor and vehicle AOA propagation measurements using a broadband channel sounder," in *2011 IEEE Global Telecommunications Conference (GLOBECOM 2011)*, pp. 1–6, Dec. 2011.

[199] T. S. Rappaport, E. Ben-Dor, J. N. Murdock, and Y. Qiao, "38 GHz and 60 GHz angle-dependent propagation for cellular and peer-to-peer wireless communications," in *2012 IEEE International Conference on Communications (ICC)*, pp. 4568–4573, June 2012.

[200] S. Deng, M. K. Samimi, and T. S. Rappaport, "28 GHz and 73 GHz millimeter-wave indoor propagation measurements and path loss models," in *2015 IEEE International Conference on Communication Workshop (ICCW)*, pp. 1244–1250, Jun. 2015.

[201] M. K. Samimi *et al.*, "Probabilistic omnidirectional path loss models for

millimeter-wave outdoor communications," *IEEE Wireless Communications Letters*, vol. 4, pp. 357–360, Aug. 2015.

[202] 3GPP TR 36.814, "Further advancements for E-UTRA physical layer aspect," Mar. 2010.

[203] T. Bai and R. Heath, "Coverage and rate analysis for millimeter-wave cellular networks," *IEEE Transactions on Wireless Communications*, vol. 14, pp. 1100–1114, Feb. 2015.

[204] K. Haneda *et al.*, "5G 3GPP-like channel models for outdoor urban microcellular and macrocellular environments," *2016 IEEE 83rd Vehicular Technology Conference (VTC Spring)*, May 2016.

[205] M. K. Samimi and T. S. Rappaport, "Local multipath model parameters for generating 5G millimeter-wave 3GPP-like channel impulse response," in *2016 10th European Conference on Antennas and Propagation (EuCAP)*, pp. 1–5, Apr. 2016.

[206] G. R. MacCartney, Jr., S. Sun, T. S. Rappaport, Y. Xing, H. Yan, J. Koka, R. Wang, and D. Yu, "Millimeter wave wireless communications: New results for rural connectivity," in *All Things Cellular16, in conjunction with ACM MobiCom*, Oct. 2016.

[207] "Investigation of prediction accuracy, sensitivity, and parameter stability of large-scale propagation path loss models from 500 MHz to 100 GHz,"

[208] T. S. Rappaport, S. Sun, and M. Shafi, "5G channel model with improved accuracy and efficiency in mmWave bands," *IEEE 5G Tech Focus*, vol. 1, Mar. 2017.

[209] J. C. Liberti and T. S. Rappaport, "Analysis of CDMA cellular radio systems employing adaptive antennas in multipath environments," in *IEEE 46th Vehicular Technology Conference*, vol. 2, pp. 1076–1080, Apr. 1996.

[210] J. Lota, S. Sun, T. S. Rappaport, and A. Demosthenous, "5G uniform linear arrays with beamforming and spatial multiplexing at 28, 37, 64, and 71 GHz for outdoor urban communication: A two-level approach," *IEEE Transactions on Vehicular Technology*, vol. 66, pp. 9972–9985, Nov. 2017.

[211] H. J. Liebe, G. A. Hufford, and M. G. Cotton, "Propagation modeling of moist air and suspended water/ice particles at frequencies below 1000 GHz," *AGARD Conference Proceedings 542*, May 1993.

[212] J. J. A. Lempianen, J. K. Laiho-Steffens, and A. F. Wacker, "Experimental results of cross polarization discrimination and signal correlation values for a polarization diversity scheme," in *IEEE 47th Vehicular Technology Conference*, vol. 3, pp. 1498–1502, May 1997.

[213] H. lin Xiao, S. Ouyang, and Z. ping Nie, "The cross polarization discrimination of MIMO antennas at mobile station," in *International Conference on Communications, Circuits and Systems (ICCCAS)*, pp. 203–206, May 2008.

[214] T. S. Rappaport and S. Deng, "73 GHz wideband millimeter-wave foliage and ground reflection measurements and models," in *2015 IEEE International Conference on Communication Workshop (ICCW)*, pp. 1238–1243, June 2015.

[215] T. S. Rappaport and R. A. Brickhouse, "A simulation of cellular system growth and its effect on urban in-building parasitic frequency reuse," *IEEE Transactions on Vehicular Technology*, vol. 48, pp. 286–294, Jan. 1999.

[216] T. Bai, A. Alkhateeb, and R. W. Heath, "Coverage and capacity of millimeter-wave cellular networks," *IEEE Communications Magazine*, vol. 52, pp. 70–77, Sep. 2014.

[217] A. I. Sulyman, A. T. Nassar, M. K. Samimi, G. R. Maccartney, T. S. Rappaport, and A. Alsanie, "Radio propagation path loss models for 5G cellular networks in the 28 GHz and 38 GHz millimeter-wave bands," *IEEE Communications Magazine*, vol. 52, pp. 78–86, September 2014.

[218] A. I. Sulyman, A. Alwarafy, G. R. MacCartney, T. S. Rappaport, and A. Alsanie, "Directional radio propagation path loss models for millimeter-wave wireless networks in the 28-, 60-, and 73-GHz bands," *IEEE Transactions on Wireless Communications*, vol. 15, pp. 6939–6947, Oct 2016.

[219] Q. H. Abbasi, H. E. Sallabi, E. Serpedin, K. Qaraqe, and A. Alomainy, "Condition number variability of ultra wideband MIMO on body channels," in *2016 International Workshop on Antenna Technology (iWAT)*, pp. 167–169, Feb. 2016.

[220] R. W. Heath and D. J. Love, "Multimode antenna selection for spatial multiplexing systems with linear receivers," *IEEE Transactions on Signal Processing*, vol. 53, pp. 3042–3056, Aug. 2005.

[221] N. Bourbaki, *Elements of Mathematics, Algebra I.* Hermann 1974.

[222] M. Matthaiou, D. I. Laurenson, and C. X. Wang, "Reduced complexity detection for ricean MIMO channels based on condition number thresholding," in *2008 International Wireless Communications and Mobile Computing Conference*, pp. 988–993, Aug. 2008.

[223] New York University *NYUSIM*, 2016.

[224] M. K. Samimi, T. S. Rappaport, and G. R. MacCartney, "Probabilistic omnidirectional path loss models for millimeter-wave outdoor communications," *IEEE Wireless Communications Letters*, vol. 4, pp. 357–360, Aug 2015.

[225] 3GPP, "Technical specification group radio access network; Study on 3D channel model for LTE (Release 12)," TR 36.873 V12.2.0, 3rd Generation Partnership Project (3GPP), Jun. 2015.

[226] 5GCM, "5G channel model for bands up to 100 GHz," technical report, Oct. 2016.

[227] R. He, W. Chen, B. Ai, A. F. Molisch, W. Wang, Z. Zhong, J. Yu, and S. Sangodoyin, "On the clustering of radio channel impulse responses using sparsity-based methods," *IEEE Transactions on Antennas and Propagation*, vol. 64, pp. 2465–2474, Jun. 2016.

[228] B. H. Fleury, M. Tschudin, R. Heddergott, D. Dahlhaus, and K. I. Pedersen, "Channel parameter estimation in mobile radio environments using the SAGE algorithm," *IEEE Journal on Selected Areas in Communications*, vol. 17, pp. 434–450, Mar. 1999.

[229] N. Czink, P. Cera, J. Salo, E. Bonek, J. p. Nuutinen, and J. Ylitalo, "A framework for automatic clustering of parametric mimo channel data including path powers," in *IEEE Vehicular Technology Conference*, pp. 1–5, Sep. 2006.

[230] F. W. Vook *et al.*, "Performance characteristics of 5G mmWave wireless-to-the-home," in *2016 50th Asilomar Conference on Signals, Systems and Computers*, pp. 1181–1185, Nov. 2016.

[231] T. S. Rappaport, R. W. Heath, Jr., R. C. Daniels, and J. N. Murdock, *Millimeter Wave Wireless Communications*. Pearson/Prentice Hall, 2015.

[232] A. Papoulis and S. U. Pillai, *Probability, Random Variables, and Stochastic Processes*. Tata McGraw-Hill, 2002.

[233] C. Ekanadham, D. Tranchina, and E. P. Simoncelli, "Recovery of sparse translation-invariant signals with continuous basis pursuit," *IEEE Transactions on Signal Processing*, vol. 59, pp. 4735–4744, Oct. 2011.

[234] H. Tataria, "Analysis of multiuser cellular systems over heterogeneous channels," *Ph.D. dissertation, Victoria University of Wellington, New Zealand*, 2017.

[235] I. E. Telatar, "Capacity of multi-antenna Gaussian channels," *Europ. Trans. Telecommun.*, vol. 10, pp. 585–596, Nov.-Dec. 1999.

[236] G. Alfano *et al.*, "Capacity of MIMO channels with one-sided correlation," in *2004 IEEE Eight Int. Symp. on Spread Spectrum Tech. and App. (ISSSTA)*, pp. 515–519, Aug. 2004.

[237] G. Alfano *et al.*, "Mutual information and eigenvalue distribution of MIMO ricean channels," in *2004 Int. Symposium on Info. Theory and Applications (ISITA)*, pp. 1–6, Oct. 2004.

[238] M. Chiani and A. Zanella, "Joint distribution of an arbitrary subset of the ordered eigenvalues of wishart matrices," in *2008 IEEE 19th International Symposium on Personal, Indoor and Mobile Radio Communications*, pp. 1–6, Sep. 2008.

[239] A. Zanella *et al.*, "On the marginal distribution of the eigenvalues of wishart matrices," *IEEE Transactions on Communications*, vol. 57, pp. 1050–1060, Apr. 2009.

[240] S. Jin *et al.*, "Ordered eigenvalues of complex noncentral wishart matrices and performance analysis of SVD MIMO systems," in *2006 IEEE International Symposium on Information Theory*, pp. 1564–1568, Jul. 2006.

[241] G. D. Durgin *et al.*, "New analytical models and probability density functions for fading in wireless communications," *IEEE Transactions on Communications*, vol. 50, pp. 1005–1015, Jun. 2002.

[242] H. Tataria *et al.*, "Performance and analysis of downlink multiuser MIMO systems with regularized zero-forcing precoding in Ricean fading channels," in *Proceedings of the IEEE International Conference on Communications*, pp. 1–7, 2016.

[243] P. G. Moschopoulos, "The distribution of the sum of independent gamma random variables," *Ann. Inst. Statist. Math. (Part A)*, vol. 37, pp. 541–544, 1985.

[244] G. Castro *et al.*, "Outdoor-to-indoor empirical path loss models: Analysis for pico and femto cells in street canyons," *IEEE Wireless Communications Letters*, vol. 6, pp. 542–545, Aug. 2017.

[245] T. M. Cover and J. A. Thomas, *Elements of Information Theory*, vol. 3. John Wiley Sons 1991.

[246] C. E. Shannon, "A mathematical theory of communication," *The Bell System Technical Journal*, vol. 27, pp. 379–423, Jul. 1948.

[247] R. Zakhour and S. V. Hanly, "Base station cooperation on the downlink: Large system analysis," *IEEE Transactions on Information Theory*, vol. 58, pp. 2079–2106, Apr. 2012.

[248] J. Mirza *et al.*, "Coordinated regularized zero-forcing precoding for multicell MISO systems with limited feedback," *IEEE Transactions on Vehicular Technology*, vol. 66, pp. 335–343, Jan. 2017.